HAL
open science

High harmonic generation in crystals assisted by local field enhancement in nanostructures

Dominik Franz

▶ **To cite this version:**

Dominik Franz. High harmonic generation in crystals assisted by local field enhancement in nanostructures. Optics / Photonic. Université Paris Saclay (COmUE), 2018. English. NNT : 2018SACLS128 . tel-01830832

High harmonic generation in crystals assisted by local field enhancement in nanostructures

Thèse de doctorat de l'Université Paris-Saclay
préparée à l'Université Paris-Sud

École doctorale n°572 Ondes et matières (EDOM)
Spécialité de doctorat: Optique et Photonique

Thèse présentée et soutenue à Gif-sur-Yvette, le 22 Mai 2018, par

Dominik Franz

Composition du Jury:

Dr. Annie Klisnick   Présidente
Institut des Sciences Moléculaires d'Orsay – France
Dr. Eric Constant   Rapporteur
Institut Lumière Matière – France
Pr. Jan Lüning   Rapporteur
Laboratoire de Chimie Physique – Matière et Rayonnement, Sorbonne Université – France
Pr. Angela Vella   Examinatrice
Groupe de Physique des Matériaux, Université de Rouen – France
Dr. Frédéric Druon   Examinateur
Laboratoire Charles Fabry, Institut d'Optique Graduate School – France
Dr. Hamed Merdji   Directeur de thèse
Laboratoire LIDYL, CEA Saclay – France

Contents

French summary

Le but de cette thèse est d'étudier le processus de la génération d'harmoniques d'ordre élevé (HHG, en anglais high-order harmonic generation) dans les solides et la possibilité d'augmenter son efficacité en exploitant l'exaltation locale du champ générateur dans des nanostructures.

La HHG dans des gaz est connue depuis plusieurs décennies et a été étudiée en détails. Le mécanisme de génération est expliqué par le modèle à trois étapes: ionisation d'un atome de gaz par un faisceau laser intense, accélération de l'électron libéré dans le champ laser et recombinaison de l'électron avec le cœur atomique. La radiation émise lors de ce processus contient des harmoniques d'ordre élevé de la fréquence du fondamental. La HHG dans les solides est démontrée pour la première fois en 2011. Ce phénomène est expliqué par la dynamique électronique induite par le champ laser dans la structure de bandes des cristaux. La dynamique des électrons entre la bande de valence et la bande de conduction (recombinaisons interbandes) et l'accélération des électrons dans la bande de conduction (acceleration intrabande) jouent un rôle important dans la HHG dans les solides. Ces deux processus sont fortement couplés et leur importance relative dépend des paramètres expérimentaux comme la longueur d'onde et les propriétés du cristal. Le processus de la HHG dans les solides est toujours en cours d'investigation et est débattu dans la communauté. Dans cette thèse, nous étudions la génération d'harmoniques dans différents cristaux, comme ZnO, $CaCO_3$ et $CdWO_4$. Nous confirmons que la HHG dépend de la longueur d'onde génératrice et des symmétries cristalline. Outre les cristaux 3D nous étudions la HHG dans des matériaux bidimensionnels comme le graphène. Grâce à sa grande mobilité électronique et sa structure de bandes spécifique, le graphène exalte fortement la HHG par rapport aux cristaux tridimensionnels.

Typiquement des éclairements de l'ordre de $10^{12}\,\mathrm{W/cm^2}$ ou plus sont nécessaires pour susciter la HHG. Ces intensités élevées sont atteintes par l'utilisation de lasers basés sur l'amplification à dérive de fréquence qui génère des impulsions femtosecondes à des énergies μJ ou mJ. Grâce aux progrès récents dans les techniques de nanofabrication, il est possible de fabriquer des nanostructures qui peuvent exalter localement un champ électrique laser par plusieurs ordres de grandeur. Il est donc possible de générer des champs intenses ($> 10^{12}\,\mathrm{W/cm^2}$) à partir de champs de l'ordre de $10^{11}\,\mathrm{W/cm^2}$ obtenus simplement par un oscillateur laser femtoseconde MHz de dimensions et de coût extrêmement modestes. En 2008 et 2011, des travaux précurseurs démontrent la possibilité de coupler plasmonique et champs fort. Les auteurs prétendirent avoir mesuré la HHG dans des gaz à partir d'un oscillateur, l'éclairement élevé nécessaire pour la HHG étant atteint grâce à l'exaltation du faisceau fondamental dans des nanostructures métalliques. Bien que ces travaux furent rapidement invalidés, l'idée fût reprise et des travaux récents ont pu démontrer l'augmentation de l'efficacité de la HHG dans des solides grâce aux effets plasmoniques. En 2016, Han et al. ont

démontré la HHG dans des nanostructures hybrides saphir-or. En 2017, Vampa et al. ont rapporté la HHG jusqu'à l'ordre 9 dans un cristal de silicium et l'augmentation du flux harmonique en déposant des nanoantennes métalliques à la surface du cristal. Dans ce travail, nous étudions l'exaltation de la HHG dans différentes configurations. D'abord, nous analysons différents types de nanostructures, à savoir des bow ties, des nano-trous, des réseaux et des résonateurs. Nous comparons ces structures en utilisant différents critères comme le volume d'exaltation et l'exaltation crête. Différentes longueurs d'onde et cristaux sont utilisés. Une forte exaltation par plusieurs ordres de grandeur est démontrée pour la troisième harmonique. Nous étudions également l'origine de la troisième harmonique. En plus, nous discutons les dommages des nanostructures causés par l'irradiation laser. Nous observons différents types de dommages comme l'ablation induite par la haute intensité locale et à cause des effets thermiques. Des nanostructures semi-conductrices qui confinent la lumière par guidage sub-longueur d'onde ont plusieurs avantages par rapport aux nanostructures métalliques. Des nanocones semi-conducteurs par exemple ont un grand volume d'exaltation, plusieurs ordres de grandeur plus élevé que précédemment démontré, et évitent la fusion observée dans les nanostructures métalliques. En 2017, Sivis et al. ont démontré l'augmentation de l'intensité de H5 d'un laser à $2.0-2.3$ μm dans des nanostructures en ZnO par rapport à une surface de ZnO non-structurée. Dans ce travail, nous répétons une expérience dans des nanocones de ZnO en améliorant le système de détection et la géométrie des nanocones à chaque itération. De plus, nous utilisons différents lasers et adaptons les nanocones en conséquence. La HHG d'un faisceau pompe à 3.1 μm de longueur d'onde jusqu'à l'ordre 15 dans des nanocones de ZnO est démontrée. L'augmentation de l'efficacité de génération d'harmoniques au-dessous et au-dessus du bandgap générées à partir d'impulsions nanojoule issues d'un oscillateur à une cadence de 18.66 MHz et une longueur d'onde de 2.1 μm par plusieurs ordres de grandeur est démontrée, pour la première fois jusqu'à H9. Le facteur d'exaltation dépend de l'intensité du faisceau pompe. Nous étudions également la forte exaltation de la luminescence et proposons des méthodes pour démêler sa contribution de la contribution cohérente.

En outre, nous analysons plusieurs applications de la HHG dans les solides. Les solides offrent des degrés de libertés supplémentaires par rapport aux milieux gazeux. La structuration du milieu non linéaire permet de modifier et de façonner les propriétés spatiales des harmoniques. Premièrement, nous proposons une nouvelle méthode pour déduire la distribution spatiale du champ électrique dans des nanostructures en analysant les dommages induits par laser. Deuxièmement, nous générons des harmoniques qui portent un moment orbital angulaire. Enfin, nous utilisons l'émission du nanocone, qui est cohérente spatialement, pour imager des objets avec une résolution spatiale à l'échelle du nanomètre.

1. Introduction

Sources with large dimensions like free electron lasers (FEL) or synchrotrons deliver coherent X-rays with high flux and adjustable wavelength. These sources are ultra-intense and can deliver hard X-rays with energies up to 100 keV and ultrashort pulse durations (from ps to fs). For example, at a FEL installation in Japan (Sacla), short pulse durations are obtained at 7.1 keV which yields intensities of 10^{20} TW/cm^2 when focused [1]. These sources have a vast field of applications, such as induced transparency by saturable absorption in iron [1]. The high penetration depth of X-rays allows to image non-crystallized biological samples such as living cells [2], organels [3] and virusses [4]. These X-rays yield a high magnetic contrast which is crucial in solid state physics for the study of ultrafast dynamics of magnetic nanometric gratings [5]. However, there exist only few FELs or synchrotrons, and their access is limited, which does not allow the use of coherent X-rays by a large community. High harmonic generation (HHG) appears to be an interesting alternative to synchrotrons and FELs. The great advantage of HHG sources is their tremendously reduced size and price with respect to other coherent X-ray sources. HHG occurs when an amplified laser pulse (pulses out of an oscillator amplified in external laser amplifiers) interacts at high intensity with a nonlinear medium. HHG in gases was first reported in 1988 and is now a well-established method to produce coherent X-rays [6, 7]. HHG in crystals was first reported in 2011 [8]. The group of David Reis observed the generation of high harmonics of a mid-infrared femtosecond beam in a zinc oxide (ZnO) crystal. However, even HHG sources are still bulky and expensive, mostly due to the amplifiers which are necessary to reach the high intensities needed for HHG. A promising route towards HHG with oscillator pulses without additional amplification stages are plasmonic nanostructures. This would reduce a HHG setup tremendously in cost and size. Plasmonic nanostructures allow for the spatial confinement of electromagnetic radiation to sub-wavelength volumes, leading to an enhancement of the local intensity by several orders of magnitude. They have been used in a vast amount of applications to enhance incoherent and coherent radiation in linear and nonlinear processes. Examples are the enhancement of second [9, 10] and third harmonic generation [11, 12], surface enhanced Raman scattering [13] and the enhancement of weak signals emitted by molecules [14]. Furthermore, plasmonic fields can be used to tailor the phase matching properties in nonlinear processes [15]. Different types of nanostructures have been used to confine light, such as bow ties, gratings, tapered waveguides or split ring resonators. First attempts to boost HHG by exploiting plasmonic field enhancement were reported in 2008 by the group of Kim [16]. In their experiment, they focused Ti:sapphire oscillator pulses onto an array of bow ties (Fig. 1.1(a)) that were purged with argon gas. They reported HHG (up to H17) in argon gas at low intensities which do typically not allow to trigger HHG. Since the bow tie nanostructures are expected to enhance the fundamental beam by several orders of magnitude in intensity, Kim et
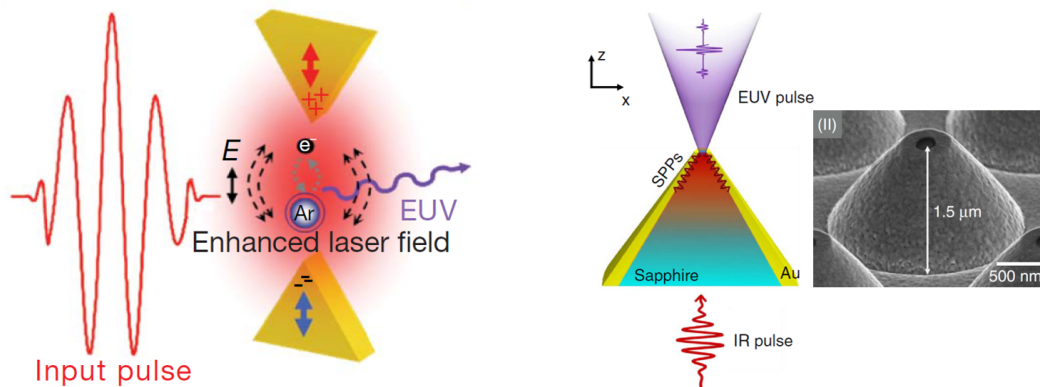
(a) **Enhancement of an** 800 nm **laser in bow tie nanostructures and subsequent enhancement of UV emission from Ar gas, taken from [16].**

(b) **Enhancement of an** 800 nm **laser in sapphire-gold nanostructures and subsequent enhancement of HHG from sapphire, taken from [17].**

Figure 1.1.: HHG with plasmonic enhancement.

al. argued that the intensity threshold for HHG was reached by plasmonic enhancement. They observed the emission of UV photons that were enhanced with respect to the case without nanostructures. However, these obervations were strongly contested by Sivis et al. [18]. They performed an experiment similar to the one of Kim's group [16] in which bow ties purged with a noble gas were exposed to an 800 nm beam and enhanced UV emission was observed. In opposition to Kim, Sivis et al. argue that the emitted radiation is the enhanced incoherent atomic line emission of the gas atoms. While the intensities necessary for HHG are reached due to plasmonic enhancement, the generation volume is limited by the dimension of the bow tie. In the case of a bow tie, the field enhancement occurs close to the tip of the antennas. Hence the field enhancement occurs only in nanoscopic volumes and only few gas atoms can experience it. The small volume should prohibit an efficient conversion from the pump beam to the harmonic radiation.

HHG in solids assisted by plasmonic field enhancement was first reported in 2016 [17]. Han et al. generated high harmonics of an 800 nm driving laser in sapphire-metal nanostructures (Fig. 1.1(b)). While in the case of gases, where the harmonic emission is difficult to distinguish from atomic line emission without additional characterization such as coherence measurements, the UV emission from solids reported in [17] can unambiguously be identified as high-order harmonics. In 2017, the group of Paul Corkum reported on the generation of up to H9 of a 2.1 μm driving laser in bulk silicon and the enhancement for H5, H7, and H9 by the use of gold nanoantenna at the output surface of the crystal [19]. The same group demonstrated recently the generation of up to H9 of a $2.0 - 2.3\,\mu$m driving laser in ZnO nanostructures. Enhancement is reported for H5 from these ZnO nanostructures with respect to a bare ZnO crystal [20].

Thesis outline

The main goal of this thesis is to investigate the possibility of enhanced HHG in solids by exploiting the field enhancement of modest laser intensities in nanostructures. Two types of structures are investigated: Plasmonic nanostructures which enhance electromagnetic radiation by coherent charge oscillations in metal and semiconductor nanostructures which confine the light by subwavelength waveguiding. In addition, we study different aspects of the process of HHG in solids.

This work is separated in three main parts.

Chapter 2 investigates the process of HHG in solids. While HHG in gases is well understood and known for several decades, HHG in solids was first reported in 2011 [8]. The process is still under investigation and under debate in the community. First, we give an introduction to the process of HHG and discuss the state of the art of HHG in both bulk solids and 2D materials. We investigate the generation of high harmonics in different crystals, such as ZnO, $CaCO_3$ and $CdWO_4$. Beside 3-dimensional bulk crystals, we investigate the possibility of HHG in 2D materials such as graphene.

Chapter 3 discusses the enhancement of crystal HHG in plasmonic nanostructures. We discuss different types of plasmonic nanostructures, namely bow ties, nanoholes, gratings and resonators. Different driving wavelengths and crystals are used. Furthermore, we discuss radiation-induced damage of plasmonic nanostructures.

Chapter 4 investigates the capability of semiconductor nanostructures to enhance crystal HHG. We use different driving lasers and study HHG in different nanocone geometries. Besides harmonic enhancement we explore the enhancement of luminescence due to local field enhancement.

In chap. 5, we explore several applications of crystal HHG, such as the possibility to deduce the electric field distribution in nanostructures by analyzing the radiation-induced damage and the possibility to generate solid harmonics that carry an orbital angular momentum. In addition, we image nanoscale objects with harmonic radiation from nanocones.

2. High harmonic generation

In this chapter, the process of high harmonic generation (HHG) in solid state materials is investigated. In sec. 2.1, we give an introduction to the process of HHG. The mechanism and the important parameters of HHG in gases (subsec. 2.1.2), solids (subsec. 2.1.3) and two-dimensional materials (subsec. 2.1.4) are discussed and compared. Table 2.1 at the end of sec. 2.1 summarizes the most important properties of HHG. In sec. 2.2 we study HHG in different nonlinear crystals with different driving wavelengths and repetition rates. In subsec. 2.2.1, we explore numerically the influence of the driving wavelength on HHG by employing a simple one-dimensional model. We then investigate HHG experimentally for different driving wavelengths in the near- and mid-infrared. In subsec. 2.2.2, we describe experiments conducted with a high-repetition rate femtosecond fiber laser at $1.039\,\mu$m wavelength. In subsec. 2.2.3 we study HHG in a $CaCO_3$-crystal. In subsec. 2.2.4, we analyze the fringes that occur in third harmonic spectra generated in $CdWO_4$ and ZnO. In 2.2.5, we generate perturbative and non-perturbative harmonics in ZnO with a $3.1\,\mu$m beam. In sec. 2.3, HHG in graphene is investigated. We study both graphene on a substrate and freestanding graphene suspended on a TEM grid.

2.1. Theory of high harmonic generation

HHG is a nonlinear process in which a high-intensity infrared laser interacts with a nonlinear target and generates high harmonics of the driving laser frequency, i.e. radiation with multiples of the frequency of the driver. HHG is originating from coherent electron motion induced by intense light and is a general feature of driven nonlinear systems. A sketch of a typical harmonic spectrum is shown in Fig. 2.1. It consists of harmonics of low orders that rapidly decrease with increasing order and scale perturbatively with pump intensity, so-called perturbative harmonics (section 2.1.1) and a plateau of high-order harmonics that scale non-perturbatively with pump intensity, called non-perturbative harmonics (sections 2.1.2 - 2.1.4). The plateau ends apruptly at the so-called cutoff frequency. While perturbative harmonics are generated due to multiphoton absorption of the fundamental beam, non-perturbative harmonics originate from tunnel-ionization of an electron. Both processes can occur in the presence of intense laser fields and are efficient in different spectral regions. Keldysh established the so-called Keldysh parameter γ which indicates which process, multiphoton absorption or tunnel ionization, is dominant under the given experimental conditions [21]. It is calculated as:

$$\gamma = \omega \frac{\sqrt{2mV}}{eE} \tag{2.1}$$

Here, ω is the frequency of the laser field, V is the ionization potential of the nonlinear medium and m and e are electronic mass and charge, respectively [21]. Tunnel ioniza-
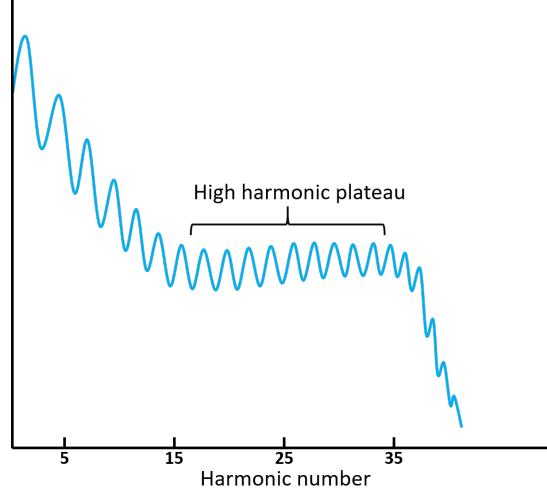
Figure 2.1.: Typical high harmonic spectrum. Rapidly decreasing orders are followed by a plateau of high-order harmonics which ends abruptly at the high harmonic cutoff.

tion occurs for $\gamma < 0.5$ [22].

HHG was first observed in 1977 during the interaction of an intense CO_2 laser with plasma generated from a solid target [23]. Since then, it was observed in gases [6, 7], dielectrics and semiconductors [24, 25], metals [26], thin films [27], superlattices [28], plasmas [29], water droplets [30] and from surfaces [31].
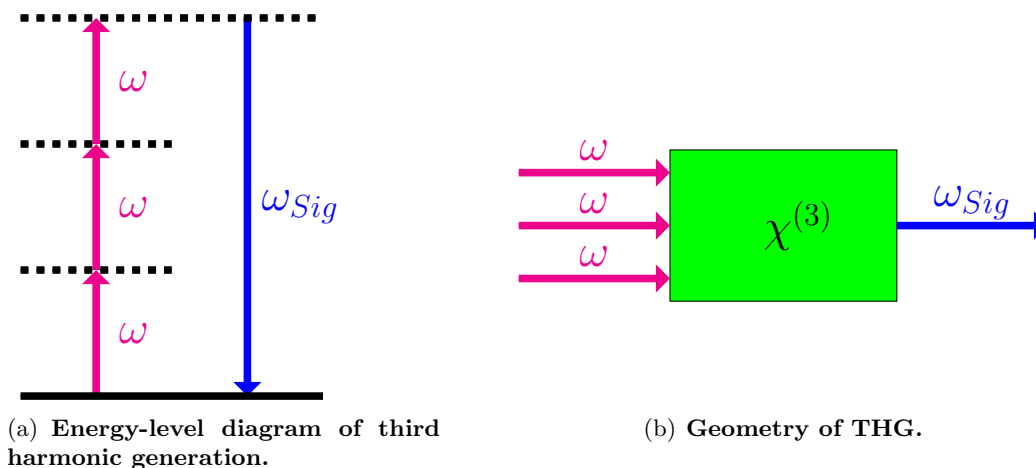
2.1.1. Perturbative harmonic generation

Second harmonic generation was first observed by Franken et al. in 1961 when they focused a ruby laser into a quartz sample [32]. With the development of high-intensity lasers and improved detection systems even higher perturbative harmonics were observed. In 2001, Chin et al. measured the seventh harmonic generated in a ZnSe crystal [33].

Perturbative harmonic generation in crystals (gases) is a nonlinear optical process in which an electron from the valence band (the outer shell) absorbs n photons of a high-intensity mid-infrared driver of frequency ω and emits one photon of frequency $n\omega$. In the case of a solid, the electron is raised to so-called virtual levels in the gap region between valence and conduction bands. This is shown schematically for the case of third harmonic generation in Fig. 2.2. The intense driving laser induces a nonlinear polarization that can be described as

$$P = \epsilon_0 \chi^{(1)} E^1 + \epsilon_0 \chi^{(2)} E^2 + \epsilon_0 \chi^{(3)} E^3 + ... \tag{2.2}$$

$\chi^{(n)}$ are the nonlinear susceptibilities of order n and ϵ_0 is the vacuum permittivity. The nonlinear polarization causes the emission of harmonics. The intensity $I^{(n)}$ of the n-th harmonic with frequency $n\omega$ scales perturbatively with the intensity I(t) of the

(a) **Energy-level diagram of third harmonic generation.**

(b) **Geometry of THG.**

Figure 2.2.: Illustration of the process of perturbative harmonic generation for the case of the third harmonic. An electron is raised through the absorption of three photons of frequency ω to a virtual level in the bandgap region. It then goes back to the valence band by emitting a photon of frequency 3ω.

drive laser as

$$I^{(n)} = \chi^{(n)} I(t)^n, \text{n... harmonic order.} \tag{2.3}$$

The probability of absorbing n photons decreases as the order of the process increases which leads to a rapid decrease of the harmonic yield (Fig. 2.1). Harmonics scale perturbatively as long as their energy is smaller than the ionization potential for the case of a gas or the bandgap in the case of a solid. Perturbative harmonics are generated throughout the nonlinear crystal and add up coherently. Since their energy is smaller than the bandgap, they do not suffer from absorption. Their generation is mainly limited by crystal dispersion and imperfect phase matching conditions. While for inversion symmetric media the even orders of the susceptibilities vanish and only odd harmonics can be generated, in media with no inversion symmetry, as it is the case for example at surfaces, even harmonics can be generated.

2.1.2. Non-perturbative harmonic generation in gases

HHG in gases is known for 30 years and has been extensively studied. It was discovered almost simultaneously at CEA Saclay [7] and the University of Illinois [6]. Both research groups observed the emission of high harmonics of the driving laser frequency by different noble gas atoms (Xe, Kr, and Ar) that were exposed to intense, ultrashort infrared pump pulses. This process was described in 1993 by Paul Corkum by a model comprising three steps: tunnel ionization, acceleration of the electron wavepacket in the continuum and recombination. Before the interaction, the Coulomb potential is unperturbed. The atomic potential is then lowered by the field of the driving laser which yields a finite probability for an electron to tunnel through the potential well (Fig. 2.3). In the next step, the released electron is accelerated in the continuum by the laser field, and, when the field reverses direction, the electron is accelerated back and can recombine with the parent ion by emitting the energy that it gained during

11
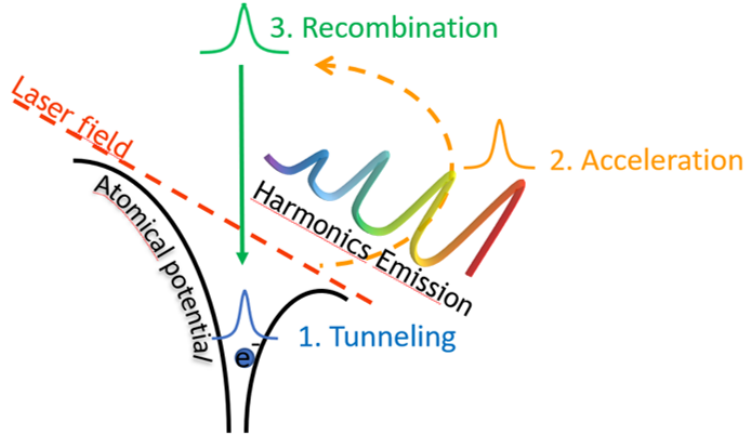
Figure 2.3.: Three step model of HHG in gases: An electron is released from the atom (1. step: ionization), accelerated in the laser field (2. step: acceleration) and eventually recombines with it (3. step: recombination).

this subcycle electronic acceleration process as XUV radiation. The energy of the emitted radiation is proportional to the kinetic energy of the electron. The bandwidth of the emitted spectrum depends on many parameters, such as the laser intensity, and supports attosecond pulse durations. The process is repeated every half-cycle of the driving laser which leads to the emission of a train of attosecond pulses. The Fourier transform of this train of attosecond pulses yields a high harmonic spectrum in the spectral domain. In other words, high harmonics are interference fringes in broadband spectra due to the interference of subsequently emitted broadband attosecond pulses. HHG in gases is used nowadays to produce isolated attosecond pulses from single-cycle driving pulses, where the spectrum of the generated coherent radiation ranges from the visible to soft X-rays. This was first demonstrated by the group of Krausz in 2001 [34]. In 1994 Lewenstein et al. proposed a pure quantum mechanical model for HHG for the case of high laser fields and low frequencies (strong field approximation) [35]. For HHG in gases, intensities in the range $10^{13} - 10^{15} \, \mathrm{W/cm^2}$ are required to trigger HHG. In experiments, the HHG yield is maximized by tuning the gas pressure in order to achieve a balance between generation efficiency, phase matching and reabsorption. Due to the symmetry of the process only odd harmonics are generated. However, in gases even harmonics can be generated when the symmetry of the process is broken, as is the case for molecules with non-symmetric electronic orbitals or when adding a second light field to the driving laser.

In the following we discuss several important aspects of HHG in gases, namely the wavelength and ellipticity dependences, conversion efficiency and phase matching.

Wavelength dependence

The highest frequency in the harmonic spectrum, also referred to as high harmonic cutoff, can be calculated as $\hbar\omega = \mathrm{I_p} + 3.2\,\mathrm{U_p} = \mathrm{I_p} + 3.2\,\mathrm{e^2E^2}/(4\mathrm{m}\omega^2)$ [36]. Here, $\mathrm{I_p}$ is

the ionization potential, U_p the ponderomotive energy, e the elementary charge, m the electron mass, and $\hbar$ the reduced Planck constant. It can be seen that the cutoff of the high harmonic spectrum increases as the square of the driving wavelength and as the square of the electric field strength. Historically, wavelengths around 800 nm were used as a driving source. Recently, mid-IR sources attracted interest in the community. Mid-IR wavelengths extend the cutoff due to the quadratic wavelength scaling of the ponderomotive energy [37]. Hower, the counterpart of this advantageous behaviour which allows to go further to the XUV is that the HHG efficiency decreases dramatically with increasing wavelength. While theory predicts a decrease in efficiency that goes with $\lambda^{(-5-6)}$[38], experiments show an even steeper decrease of $\lambda^{(-6-7)}$ [39].

Ellipticity dependence

HHG in gases will only occur when the driving laser is linearly or weakly elliptically polarized. When increasing the ellipticity, HHG is quickly turned off. The reason is that the electron that is accelerated in the laser field misses the parent ion when it is accelerated back and cannot recombine with it [40]. The sensitivity of HHG to the ellipticity of the driving laser inreases with the drive wavelength [41]. In the case of atoms, the harmonic yield decreases faster with ellipticity than for molecules [42].

Conversion efficiency

The conversion efficiency from the pump beam to the harmonic radiation is low and depends on many parameters such as the driving wavelength. For example, when using a driving wavelength of $1.55\,\mu$m, the conversion efficiency typically lies in the range 10^{-8} - $5 \cdot 10^{-7}$ for harmonics around 250 eV at pump intensities around $10^{14}\,W/cm^2$. Due to the wavelength dependence of the conversion efficiency, the conversion efficiency is by around one order of magnitude higher when pumped with 800 nm [43]. Lower harmonics in the XUV can reach higher conversion efficiencies between 10^{-5} and $5 \cdot 10^{-4}$ (pumped by 800 nm) with large noble gases atoms. Xenon gas yields the highest conversion efficiency (10^{-4}) for harmonics in the XUV for an 800 nm driver. In argon it is around 10^{-5} and in neon 10^{-7} [43, 44, 45, 46, 47]. Due to different ionization potentials of the noble gas atoms, neon has a higher cutoff than xenon for example (the cutoff depends linearly on I_p).

Phase matching

In order to have an efficient conversion from the pump beam to the harmonic radiation, a fixed phase relation between both needs to be established. The driving laser and the harmonic radiation have to travel nearly at the same phase velocity in the gas. For an 800 nm driving laser, harmonics with energies < 130 eV can be perfectly phase matched by balancing the neutral atom dispersion with the dispersion of the free-electron plasma that is created during the ionization of the gas [48, 49]. In practice, the phase matching condition is achieved by tuning the gas pressure, by varying the length and the size of the interaction region and the focus position in the gas [50]. It was recently demonstrated that the cutoff can be extended by controlling the self-defocusing effect of the pump laser [51]. Shaaran et al. showed that the field gradient of the local

enhancement in plasmonic nanostructures can be used to control the phase matching of high harmonics generated in atoms that are exposed to this field enhancement. The spatial inhomogenity of the plasmonic field affects the electron trajetory and recombination time [52]. Furthermore, phase matching at the nanoscale can be used to tailor the spatio-temporal properties of harmonic radiation [53]. Other phase matching schemes were proposed such as the use of corrugated waveguides for example [54].

2.1.3. Non-perturbative harmonic generation in solids

While HHG in gases is known for three decades now, HHG in solids has been extensively studied only in the last years. HHG in solids was first reported in 2011 when Ghimire et al. focused a $3.25\,\mu$m laser into a $500\,\mu$m thick ZnO crystal [25]. At a vacuum intensity of $5\,\mathrm{TW/cm^2}$ they observed emission of high-order harmonics up to 25th order. There are some striking differences between solids and gases that have an impact on the HHG process and cause different wavelength dependences of the cutoff, the conversion efficiency and the ellipticity dependence [8]. Solids have a density of matter that is by several orders of magnitude higher than in the case of a gas. Furthermore, lattice sites in a crystalline solid are arranged in a periodic manner. Many-body effects due to the crystalline structure of solids play an important role that makes HHG in solids and gases fundamentally different. While in atoms electrons are confined to discrete atomic orbitals, in solids they are delocalized and can move within continuous bands. The formation of bands in a solid state material is due to the overlap of atomic orbitals from different atoms of the crystal. The energy band occupied by the valence electrons is called valence band. In the conduction band, which is separated from the valence band by the bandgap, electrons can freely move. HHG was observed in different dielectric and semiconductor materials such as bulk ZnSe, GaSe, ZnO, MgO, Al_2O_3 [55], in polycristalline and in amorphous SiO_2 [56], in Si thin films [57], in different types of semiconductor superlattices [28], from graphene [58, 59, 60] and MoS_2 monolayer [61] as well as solid Ar and Kr [62]. In addition, HHG was predicted from diamond [63].

The maximum excursion of a semi-classical electron accelerated by an external electric field in a solid can be calculated as $r_{max} = \frac{eE\lambda^2}{4\pi^2mc^2}$ [25]. e and m are the fundamental charge and eletronic mass, respectively. The excursion length grows linearly with the driving electric field and quadratically with wavelength. For the experimental parameters in [25] $r_{max} = 32\,\text{Å}$ which is many times the lattice parameter of the ZnO-crystal used in this experiment. Hence, an electron encounters other lattice sites during its excursion and might recombine with them which might, due to the periodicity of the crystal lattice, lead to the emission of harmonic radiation [64]. However, it was experimentally demonstrated that even amorphous crystals can lead to coherent harmonic emission [56]. This means that the periodicity in a crystal is not a requirement for coherent emission. While in gases the high harmonic cutoff depends on the square of the driving field strength it depends linearly on the field strength for solids [25]. Two different mechanisms that contribute to HHG in crystals are identified.

- **Interband oscillations**: An electron is excited across the bandgap from the valence to the conduction band of a crystal by the laser electric field (Fig. 2.4).

The electron in the conduction band and the hole in the valence band are accelerated in opposite directions within their bands. When the electric field changes sign, electron and hole recombine at the Γ-point (k = 0) by emitting their energy. Interband oscillations resemble the atomic HHG process in some aspects.

- **Intraband oscillations**: This term refers to the acceleration of electrons within the conduction band. While a weak laser field makes the electron oscillate around the center of the Brillouin zone, a sufficiently strong laser field can accelerate electrons towards the edge of the first Brillouin zone where Bragg reflection occurs. The electron momentum jumps to a value with inverse sign and traverses the Brillouin zone again. In real space this acceleration leads to periodic oscillations of the electron wavepacket, so-called Bloch oscillations. The rate $\omega_{\mathrm{B}} = \frac{eEa}{\hbar}$ at which a classical electron travels through the BZ for peak fields E and lattice constant a is called Bloch frequency.

So while in gases the HHG process is fully described by the 3-step model, one has to take into account interband and intraband processes in order to correctly describe HHG in solids. Vampa et al. tried to find analogies between the mechanism of HHG in gases and HHG in solids. On the one hand, the electron ionized from an atom
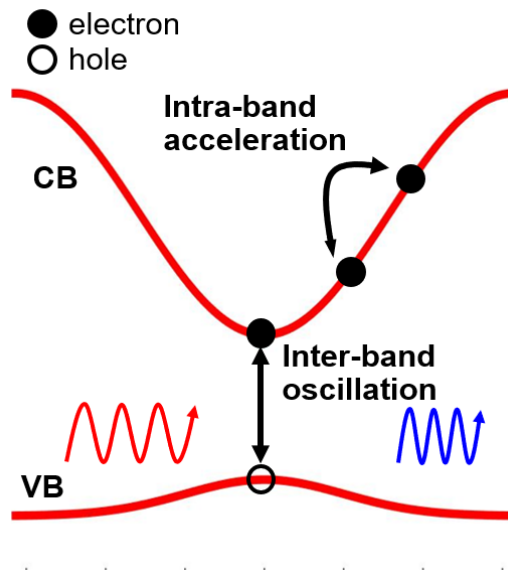

Figure 2.4.: Band structure in a two-band model: An electron that is initially located in the valence band (VB) can be accelerated by an external field to the conduction band (CB), leaving a positively charged hole in the valence band. When the laser field reverses sign, the electron is accelerated back to the valence band and recombines with the hole by emitting the energy that it gained during the oscillation between the two bands (interband oscillation). The oscillations of an electron within the conduction band are called intraband oscillations. Both interband and intraband oscillations contribute to the emission of high harmonics.

undergoes oscillatory motion in the laser field, which can be seen as the counterpart of the oscillation of an electron within the conduction band (intraband oscillation) in solid HHG [65]. However, the oscillations of the electron ionized from an atom in the laser field are not Bloch oscillations. On the other hand, the ionized electron recolliding and recombining with its parent ion can be seen in anology to the interband term in solid HHG where an electron oscillates between valence and conduction band and eventually recombines with its associated hole [65]. There are different theoretical approaches to describe the emission of harmonics from dielectric and semiconductor bulk crystals. For correctly describing the interplay between interband and intraband oscillations a full quantum mechanical approach is needed. This is provided for example by the semiconductor Bloch equations (SBE) [66], the solution of the time dependent many-body Schrödinger equation, or a density matrix approach. Here, we show the main steps of how to derive a harmonic spectrum from the SBE. The coherent emission intensity of a semiconductor excited by a strong laser field is calculated as

$$I_{tot}(\omega) \propto |\mathscr{F}(\frac{\partial P(t)}{\partial t} + J(t))| \propto |\omega P(\omega) + iJ(\omega)|^2 \tag{2.4}$$

Here, $\frac{\partial P(t)}{\partial t} + J(t)$ corresponds to the total current induced by the fundamental laser beam composed of the free current ($J(t)$) and the bound current desribed by the time-derivative of the polarization ($\frac{\partial P(t)}{\partial t}$). The interband oscillation is the induced polarization between valence and conduction band that occurs when an electron-hole pair is created and is taken into account by the bound current. The intraband current which is the current within the conduction band is represented by the induced current. $P(\omega)$ is the Fourier transform of $P(t)$ which can be expressed as

$$\mathbf{P}(t) = \sum_k \mathbf{d}_k p_k(t) + c.c. \tag{2.5}$$

where $\mathbf{d}_k$ is the dipole matrix element and $\mathbf{p}_k$ are the microscopic polarizations. $J(\omega)$ is the Fourier transform of $J(t)$ which can be written as

$$\mathbf{J}(t) = \sum_{k,\lambda \in \{e,h\}} \mathbf{j}_k^\lambda f_k^\lambda(t) \tag{2.6}$$

where $\mathbf{j}_k^\lambda = \frac{e}{\hbar} \nabla_k \epsilon_k^\lambda$ are the current matrix elements and $\mathbf{f}_k$ are the electron and hole occupations. The quantities $\mathbf{p}_k$ and $\mathbf{f}_k$ are solutions of the SBE [66]. The SBE can be written as

$$i\hbar\frac{\partial}{\partial t}p_k = (\epsilon_k^e + \epsilon_k^h - i\gamma)p_k - (1 - f_k^e - f_k^h)\left[\mathbf{d}_k \cdot \mathbf{E} + \sum_{q \neq k} V_{k-q}p_q + |e|E \cdot \nabla_k p_k\right] \tag{2.7}$$

$$\hbar\frac{\partial}{\partial t}f_k^\lambda = -2Im\left[(\mathbf{d}_k \cdot \mathbf{E} + \sum_{q \neq k} V_{k-q}p_q)p_k^\star\right] + |e|E \cdot \nabla_k f_k^\lambda) \tag{2.8}$$

The terms proportional to $\mathbf{d}_k$ describe interband processes, the terms containing derivatives ∇_k describe intraband processes [66]. ϵ_k^e and ϵ_k^h are the single-particle energies

for electrons and holes, respectively, and γ is a dephasing parameter.

Koch and Golde solved the semiconductor Bloch equations 2.7 and 2.8 for a GaAs nanostructure and a two-band model [67], [68]. The results of the simulations show that, when considering only interband effects, HHG is more efficient than when considering only intraband effects. However, it is the modulation of the interband polarization by the intraband current that strongly enhances HHG [69]. In contrast to HHG from gases, the microscopic mechanism underlying HHG from solids is still controversial and under debate in the attosecond community. The different approaches to explain HHG in solids converge towards a unified theory. Several approaches have been made to determine experimentally the relative importance of interband and intraband oscillations.

- The harmonic spectra emitted by the nonlinear interband current are predicted to exhibit atto-chirp, whereas those resulting from intraband Bloch oscillations do not [70]. You et al. found by measuring the atto-chirp of the harmonic spectrum of MgO that HHG is dominated by interband processes. However, this might be different for other crystals and experimental parameters [71].

- The linear scaling of the cutoff can be explained by taking into account intraband oscillations [25]. A typical high harmonic spectrum and the scaling of the cutoff with electric field are shown in Fig. 2.5(a).

- Luu et al. [27] generate high harmonics in a thin film of polycrystalline SiO_2. Their results are best reproduced by simulations that only take into account intraband currents and not interband currents.

- HHG driven by longer wavelengths is dominated by intraband oscillations, HHG driven by shorter wavelengths by interband oscillations [72, 73]. According to Vampa et al. [72], at short laser wavelengths, i.e., between 1.0 and 5.0 μm, the main contribution to the harmonic spectrum is from interband transitions. The wavelength-dependences of interband and intraband contributions are shown in Fig. 2.5(b).

So it as a complex interplay between interband and intraband oscillations that causes the generation of high harmonics, where the importance of both contributions is strongly influenced by material properties such as the bandstructure and the dipole-matrix elements, as well as the properties of the exciting radiation such as the frequency and the waveform. This complex interplay leads to a great sensitivity of the spectrum to small variations in the electronic band structure [8]. For not too strong excitation electrons explore only the near-parabolic region of the Brillouin zone. This is why for weak laser fields, it was found that the magnitude of the interband contribution is larger than that of the intraband contribution [74]. Tancogne-Dejean et al. found that high harmonics are generated by two competing terms, namely the spatial variation of the total electronic density and the gradient of the electron-nuclei potential [74]. So an increasing harmonic yield is expected for strong spatial fluctuations of the electron-nuclei potential, as can be realized at surfaces or interfaces [74].

In the following we discuss several important aspects of solid HHG, namely the wave-
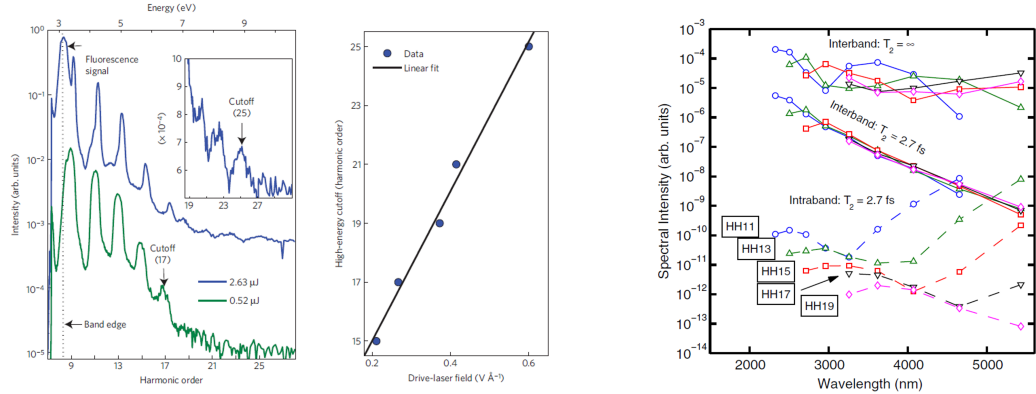
(a) **Typical high harmonic spectrum and linear cutoff scaling with electric field (taken from [8]).**

(b) **Wavelength-dependence of the interband and intraband contribution in HHG (taken from [72]).**

Figure 2.5.: Typical high harmonic spectrum with cutoff scaling and the wavelength-dependence of interband and intraband oscillations in HHG.

length and intensity dependence, damage issues and phase matching, conversion efficiency and ellipticity dependence.

Wavelength dependence

Solid HHG strongly depends on the driving wavelength. It was shown theoretically that the cutoff energies of interband and intraband energies exhibit essentially different wavelength dependences. While the cutoff of intraband HHG is wavelength independent, the cutoff energy of interband HHG depends linearly on the laser wavelength [75]. Mid-infrared HHG driven by wavelengths between 1.0 and 5.0 μm seems to be dominated by interband oscillations [72, 73]. The interband current drops exponentially with increasing laser wavelength (following $\lambda^{-11.4 \pm 2.9}$ according to [76]) and the intraband contribution will be dominant for harmonic emission at longer wavelength (Fig. 2.6(a)). The decrease of the interband contribution can be understood when considering that a longer driving wavelength requires more photons to overcome the bandgap and to drive the interband transition. While [76] claim that the overall HHG yield decreases, according to [77], for longer wavelengths (in the Terahertz range) the intraband current grows and becomes eventually more important than the interband contribution.

Ellipticity dependence

The ellipticity dependence of solid HHG is complex. You et al. demonstrated experimentally that HHG in MgO is turned off when increasing the ellipticity (as it is the case for gases) starting from a linear polarization and turned on again for high ellipticity values close to circular polarization [64]. Tancogne-Dejean et al. found that interband and intraband mechanisms exhibit a different ellipticity dependence. Fur-

18
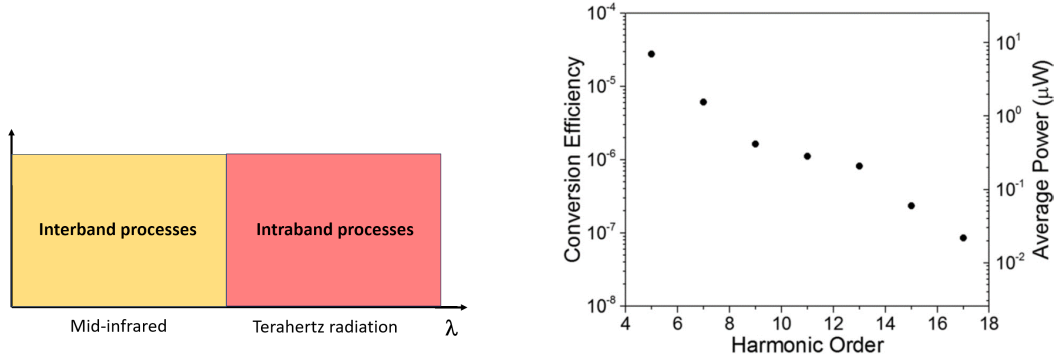
(a) **Interband processes are dominant in the MIR, intraband processes in the Terahertz regime [72, 73, 76, 77].**

(b) **High harmonic conversion efficiency vs. harmonic order (taken from [80]).**

Figure 2.6.: **Wavelength-dependence of interband and intraband processes and high harmonics conversion efficiency vs. harmonic order.**

thermore, harmonics of different orders are not affected equally by ellipticity. The change in harmonic intensity is explained by the fact that for different ellipticities the delocalized electron experiences different parts of the Brillouin zone [74]. It was shown that it is not necessarily a linear polarization that yields the highest cutoff [78]. For more details we refer to [78].

Conversion efficiency

Typical densities of solids are by several orders of magnitudes higher than gas densities. On the one hand this behaviour might be advantegeous since in solids much more emitters contribute to the HHG process compared to a gas. On the other hand, reabsorption in solids is strong and limits the efficient interaction region to several tens of nanometers to several hundreds of nanometers. For Si for example, which has been used recently for HHG [19] and which has a bandgap of 1.17 eV, wavelengths around 500 nm are attenuated to 0.98 and 0.84 after propagation distances of 10 and 100 nm, respectively [79]. However, wavelengths around 200 nm are attenuated much more to 0.17 and $2 \cdot 10^{-8}$ after propagation distances of 10 and 100 nm, respectively [79]. The effective propagation distance decreases with shorter wavelengths and depends on the material parameters. Harmonics generated deeper inside the crystal cannot be observed since they are entirely absorbed. So in experiments the laser focus is often placed at the output surface of the crystal in order to maximize the harmonic yield. Luu et al. found that a quartz crystal is, under the same experimental conditions, by one order of magnitude more efficient in generating harmonics than argon or krypton gas [81]. Gholam-Mirzaei et al. generated high-order harmonics from a $3.8\,\mu$m driving laser in a ZnO crystal [80]. Conversion efficiencies for H11 and H13 which correspond to wavelengths of around 300 nm are of the order of 10^{-7} and 10^{-6} for H17 which corresponds to 220 nm (Fig. 2.6(b)). Calculated conversion efficiencies generated by a $3.25\,\mu$m driving laser in ZnO are 10^{-7} for 250 nm and 10^{-15} for 130 nm [82]. Conversion

efficiencies for harmonics in the soft X-ray range were not reported yet.

Phase matching

For solid perturbative harmonic generation different phase matching schemes exist. The most common method is to use birefringent crystals such that the fundamental beam and the harmonic beam travel at the same velocity throughout the crystal which allows a coherent buildup of the harmonic radiation. Another method is quasi phase matching, where the refractive index of the material is varied periodically. However, non-perturbative harmonics are typically absorbed within a few tens or hundreds of nanometers. This is of the order the wavelength of the harmonic radiation and corresponds to a fraction of the pump wavelength which is typically in the NIR or MIR. Up to now, phase matching is not considered for non-perturbative HHG in solids.

Intensity scaling

While harmonics with an energy smaller than the bandgap (below-bandgap harmonics) scale perturbatively with pump intensity (eq. 2.3), harmonics with an energy close to and higher than the bandgap (above-bandgap harmonics) scale non-perturbatively with pump intensity (eq. 2.9) [80, 8].

$$I^{(n)} = I(t)^q, q \neq n... \text{harmonic order.} \tag{2.9}$$

Kim et al. found that non-perturbative harmonics H7, H9, H11, H13 of an 800 nm driving laser generated in sapphire have coefficients of q = 3.8, 6.0, 8.3 and 5.0, respectively, where q is the exponent of eq. 2.9 [55]. The exponent q does not correspond to the harmonic order n as it would for perturbative harmonics. On the other hand, q does not increase steadily with harmonic order. While q increases from H7 to H11, it jumps again to a small value at H13. No relation between q and n was determined yet. Typical intensities needed for HHG in solids are $10^{11} - 10^{14}$ W/cm² [8, 71], which is about one order of magnitude less than for HHG in gases. When using longer driving wavelength, higher intensities can be applied without causing damage. The intensities required for HHG in solids depend strongly on the crystal properties. Intensities required for MgO for example lie by a factor of 10 higher than for ZnO [8, 71]. Solid HHG typically starts to saturate at intensities of around 1 TW/cm² [8, 80].

Damage threshold

For too high intensity, irreversible crystal damage occurs and the harmonic yield decreases. The threshold intensity where damage occurs depends on the crystal properties and on the laser parameters such as the wavelength and the repetition rate. Fig. 2.7 shows the time-scales of laser-material interaction. While for kHz repetition rate heat deposited by laser pulses can dissipate before the subsequent pulse arrives, this is not possible any more at multiple MHz repetition rates. Heat accumulates in the crystal and eventually causes damage [83]. Typically, higher intensities can be used without causing damage when using longer wavelengths since at longer wavelengths more photons are necessary for electrons to overcome the bandgap. When using MHz
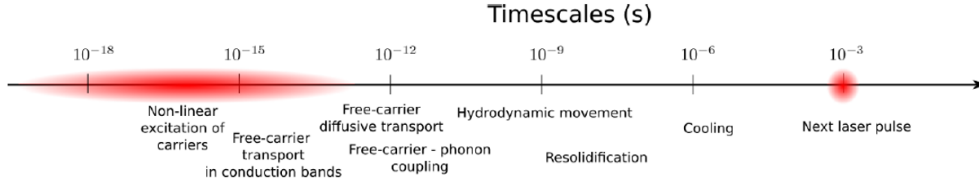
Figure 2.7.: Time-scales of the laser-material interaction of the example of silicon irradiated by a 100 fs laser at intensity close to modification regime (repetition rate is taken equal to 1 kHz here), taken from [83].

repetition rates, thermal damage occurs since the heat dissipation time is longer than the time difference between the arrival times of two subsequent pulses (Fig. 2.7). You et al. used peak field strengths of 10^{14} W/cm^2 without observing damage in MgO and amorphous SiO$_2$ [71, 56]. This was achieved by using long driving wavelength, low repetition rate (kHz), short pulse durations and materials with a high bandgap. Gholam-Mirzaei et al. observed crystal damage in ZnO (bandgap 3.3 eV) for intensities above 1.4 TW/cm^2 for a driving wavelength of 3.8 μm, 50 kHz repetition rate and a pulse duration of 100 fs [80]. Kim et al. observed a decrease of the harmonic photon flux over 30 min for a driving wavelength, repetition rate, pulse duration and peak intensity of 800 nm, 75 MHz, 12 fs and 1.3 TW/cm^2 [84]. They attribute this decrease to internal structural modification of the specimen by the accumulated heat without causing severe damage. Lee et al. investigated harmonic generation with a fiber laser (1550 nm, 93.4 MHz, 60 fs) and observed a decrease of the harmonic signal after a few minutes of irradiation [85]. However, when blocking the laser and irradiating again after a certain recovery time, the signal rose up to the initial value, indicating that no permanent damage occured.

2.1.4. High harmonic generation in 2D materials

Two dimensional (2D) materials offer a unique possibility to investigate the pure HHG process without propagation effects as they occur naturally in bulk crystals. Their thickness typically varies from several Å to several nm and they can be produced either freestanding on a grid or on substrates and have different electronic properties compared to bulk crystals. HHG in 2D materials was first reported in 2016. Liu et al. observed odd and even high harmonics up to seventeenth order generated in a monolayer of MoS$_2$ on a fused silica substrate from a 4 μm pump beam at a pump intensity of few TW/cm^2 [61]. A monolayer of MoS$_2$ consists of two hexagonal layers of S-atoms surrounding a central hexagonal layer of Mo-atoms with trigonal prismatic coordination and has a direct bandgap of 1.8 eV [61].

Since we investigate HHG in graphene in the frame of this thesis we will discuss its most important properties briefly. Graphene is a monolayer of carbon atoms packed in a two-dimensional honeycomb lattice (Fig. 2.8(a)). It has a bandgap of 0 eV and its band structure exhibits linear dispersion which is described by the Dirac cone (Fig. 2.8(b)). Their is no gap as it would be the case in insulators and no partially-filled
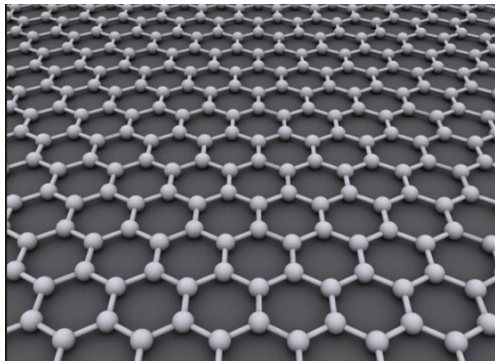
(a) **The structure of graphene is the honeycomb lattice (image taken from www.gralon.net).**
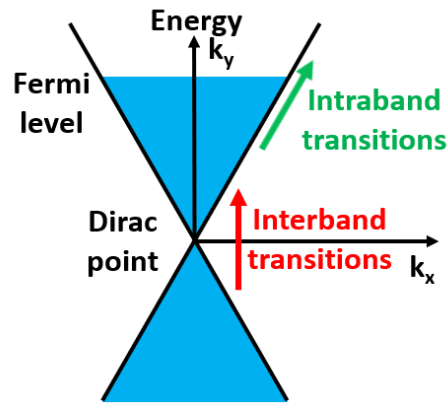
(b) **The bandstructure of graphene is described by the Dirac cone.**

Figure 2.8.: Electronic and structural properties of graphene. Graphene is a two-dimensional material that occurs in the honeycomb lattice. Its band structure is described by the Dirac cone.

bands, as it would be the case for metals. A direct consequence of the Dirac cone is that electrons in graphene have all the same velocity and no inertia. The combination of the zero-bandgap and the linear dispersion of graphene leads to an instantaneous response of free carriers to the optical field [60]. Each carbon layer possesses 3 electrons that are bound with the nearest neighbor atom electrons, thus creating chemical sp^2-bonds. Furthermore, each atom has a fourth electron that is delocalized on the whole graphene layer. It allows for the conduction of an electrical current. Few-layer graphene or monolayer graphene on a substrate can have significanty different properties from freestanding graphene such as a non-zero bandgap. These unique electronic properties make graphene highly interesting for HHG. Savostianova et al. found that third harmonic generation from graphene on a suitable substrate can be by several orders of magnitudes stronger than third harmonic generation from freestanding graphene [86]. Hendry et al. calculated that the third-order susceptibility of a graphene monolayer is 10^8 times stronger than in bulk dielectric materials [87]. So graphene has high potential to efficiently generate high harmonics. Since 2017, HHG in graphene was reported by several research groups.

- Yoshikawa et al. generated harmonics up to the 9th order in a graphene monolayer on a substrate using 0.26 eV pump pulses at $1\,\mathrm{TW/cm^2}$ [58].

- Baudisch et al. generated up to the fifth harmonic in a 5-monolayer of graphene on a CaF_2 substrate at few $\mathrm{GW/cm^2}$ intensity from $3.1\,\mu\mathrm{m}$ wavelength [60].

- Taucer et al. observed up to the fifth harmonic from monolayer graphene and up to the seventh harmonic from few-layer graphene. They used a pump of

$3.1 - 3.9\,\mu\text{m}$ wavelength at 0.5 - 0.6 TW/cm^2. The fifth harmonic has a broader spectrum for the few layer compared to the monolayer [59].

In monolayer graphene strong harmonic generation at modest field amplitudes occurs due to an interplay of the interband and intraband dynamics, which has similarities to HHG in bulk crystals. Applied laser fields lead to interband dynamics by inducing transitions between the bands, while the subsequent driving of the carriers within their bands by the same fields leads to intraband dynamics [88]. Interband and intraband transitions control the absorption of electromagnetic radiation in graphene. In contrast to HHG in gases or solids, HHG in monolayers does not require phase matching since there are no propagation effects. Beside the generation of odd harmonics, even harmonics can be generated in monolayers since (similar to the surface of bulk crystals) the inversion symmetry is broken. The generation of odd harmonics is significantly more efficient compared to that from an equivalent layer in the bulk [61]. The introduction of a slight bandgap in the graphene dispersion effectively enhances the nonlinear response compared to that of gapless graphene [87].
In the following we discuss several important aspects of HHG in 2D materials, namely the ellipticity dependence, conversion efficiency, damage threshold and intensity scaling.

Ellipticity dependence

While some groups observe that HHG is maximum for linear polarization, another group reports the maximum for circular polarization. This behaviour is ruled by the reciprocal space symmetries [89].

- Lui et al. observed that harmonic generation in MoS$_2$ is maximum for linear polarization and is quickly turned off when increasing the ellipticity [61].

- Baudisch et al. found that for harmonic generation in 5-monolayer graphene the third harmonic yield decreases rapidly with increasing ellipticity [60]. They found that the free carriers lower the refractive index and cause a spectral blue shift that is proportional to the optical frequency. The blue shift is maximum for linear polarization (2 percent) and decreases to less than 0.3 percent for circular polarization [60].

- Yoshikawa et al. observed that all harmonics generated in graphene vanish for circular polarization ($\epsilon = 1$) [58]. An elliptically polarized pump ($\epsilon = 0.32$) enhances seventh and ninth harmonics compared to linear polarization ($\epsilon = 0$).

- Taucer et al. observed HHG in freestanding graphene and in graphene on a substrate. HHG is quickly turned off when ellipticity increases [58].

Conversion efficiency

Electrons in an isolated monolayer of MoS$_2$ experience greatly enhanced electron-hole Coulomb interactions. Liu et al. reported that the generation efficiency of odd harmonics per material layer is higher for monolayers with respect to bulk crystals

[61]. This is due to correlation effects in the monolayer. No quantitive information is available about the conversion efficiency.

Damage threshold

The damage threshold of 2D materials depends strongly on whether a monolayer or few-layers are used and whether the 2D material is freestanding or on a substrate. The damage threshold can be increased by using a suitable substrate [90]. In the following, we give a few examples for the damage threshold of different materials at different intensities. The damage threshold for 5-monolayer graphene on a CaF_2 substrate is reported to be $5\,\mathrm{GW/cm^2}$ for $3\,\mu\mathrm{m}$ wavelength and 160 kHz repetition rate. For mono- and few-layer graphene on a sapphire substrate the damage threshold is $0.55\,\mathrm{TW/cm^2}$ when using $3-4\,\mu\mathrm{m}$ pulses at 100 Hz repetition rate [59]. Liu et al. used monolayer MoS_2 on a fused silica substrate for HHG. At a wavelength of $4\,\mu\mathrm{m}$ and an intensity of $2.5\,\mathrm{TW/cm^2}$ no damage was reported [61].

Intensity scaling

High harmonics generated in 2D materials scale non-perturbatively with pump intensity. However, only few systematic studies have been carried out and a systematic theory for the intensity scaling is not available yet. We give a few examples in the following. Cui et al. observed that above-bandgap third harmonic generation in monolayer and multilayer ReS_2 on a BK7 substrate scales perturbatively with pump intensity $(I^{(3)} = I(t)^3)$ [91]. Zhou observed that below-bandgap second harmonic generation in monolayer GaSe scale almost perturbatively with pump intensity $(I^{(2)} = I(t)^{2.1})$ [92]. Liu et al. found that for HHG in monolayer MoS_2 the harmonic intensity of representative orders (H7, H9, H12, H13) scales as $I^{(7,9,12,13)} = I(t)^{3.3}$, where n = 3.3 for all harmonic orders [61]. The behaviour deviates strongly from the one for perturbative harmonics. Taucer et al. generated harmonics in graphene with $3-4\,\mu\mathrm{m}$ pump wavelength. Theory and experiment both show a non-perturbative scaling approximately characterized by $I^{(5,7)} = I(t)^2$ for H5 and H7 [59]. Yoshikawa et al. observed that H5 generated in graphene scales as $I^{(5)} = I(t)^2$ [58].

Table 2.1 compares the most important properties of HHG in different kind of media, namely in gases, bulk crystals and 2D materials.

	Generation mech.	λ- and E-scaling of cutoff	λ-scaling of conv. efficiency	Conversion efficiency	Ellipticity dependence
HHG in gases	3-step model	$\sim \lambda^2$ $\sim E^2$	$\lambda^{(-5-6)}$	0.8 μm pump 250 eV: 10^{-7} XUV: 10^{-5}	$\epsilon = 0$: HHG max, $\epsilon \uparrow$: HHG $\downarrow$ $\epsilon \to 1$: HHG $\to 0$
HHG in solids	interband oscillations, intraband oscillations	intraband cutoff λ-independent, interband cutoff $\sim \lambda$ $\sim E$	$\lambda^{(-11.4\pm2.9)}$	3-4 μm pump 350 nm: 10^{-6} 230 nm: 10^{-7} 130 nm: 10^{-15}	$\epsilon = 0$: HHG max, $\epsilon \uparrow$: HHG $\downarrow$, $\epsilon \to 1$: HHG complicated
HHG in 2D mat.	interband oscillations, intraband oscillations	n/a	n/a	n/a	inconsistent observations

Table 2.1.: Comparison of the generation mechanism, wavelength dependence of the cutoff, generation efficiency and ellipticity dependence of HHG in gases, bulk solid state materials and 2D materials.

2.2. High harmonic generation in different nonlinear crystals

In this section, we investigate HHG in different crystals and with different laser systems with respect to repetition rate and central wavelength. In subsec. 2.2.1, we study numerically the influence of the driving wavelength on HHG by employing a simple one-dimensional model. We then investigate HHG experimentally with different driving wavelengths in the near- and mid-infrared. In subsec. 2.2.2, we conduct experiments with a high-repetition rate femtosecond fiber laser at $1.039\,\mu m$ wavelength. The aim was to study HHG in ZnO. In subsec. 2.2.3 we explore HHG in a $CaCO_3$-crystal and we analyze the dependence of harmonic generation on the angle between polarization and crystal axes. In subsec. 2.2.4, we analyze the fringes that we observed in third harmonic spectra from ZnO and $CdWO_4$. In subsec. 2.2.5, we generate perturbative and non-perturbative harmonics in ZnO with a $3.1\,\mu m$ beam. We analyze the intensity-dependence of different harmonic orders. In sec. 2.3, we study HHG in graphene on a substrate and in freestanding graphene suspended on a TEM grid.

2.2.1. TDSE-simulations of the wavelength-dependence of HHG

The simulations presented in this chapter were made by Dr. Thierry Auguste at CEA Saclay. A periodic potential $V(x) = -0.37(1 + \cos(2\pi x/a_0))$ with a lattice constant of $a_0 = 0.42\,nm$ which is a typical value of semiconductor crystals is used to model a 1d solid. The harmonic spectrum is calculated by solving the time-dependent Schrödinger equation (TDSE). This periodic potential corresponds to a bandgap of about 4.2 eV. The band structure of this potential is shown in Fig. 2.9(a). The calculation includes 51 bands or Bloch states for each k value. Since the lowest band (band 1) is deeply bound and very flat, the second band is used as the initially populated valence band.
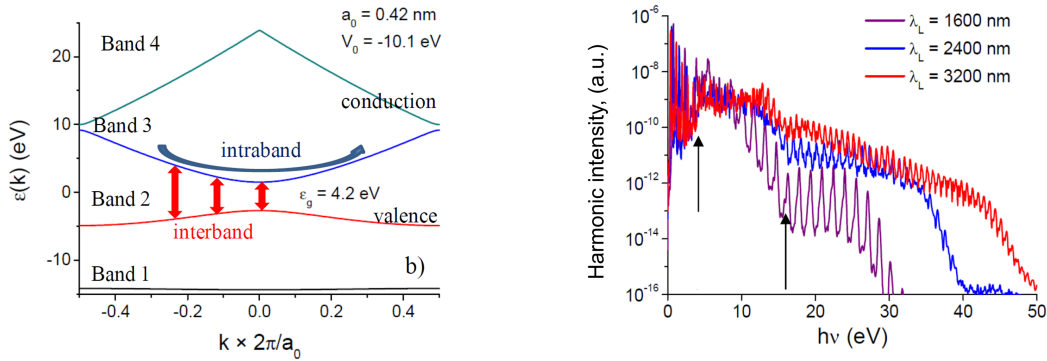
(a) **Resulting band structure and scheme of interband and intraband dynamics. The second band is considered as the valence band and the third band as the conduction band.**

(b) **High harmonic spectra of different laser induced currents calculated by solving the TDSE. The black arrows indicate the minimum and maximum bandgap energies in the first Brillouin zone.**

Figure 2.9.: **Band structure of a 1d chain of atomic potentials and generated high harmonic spectrum.**

The laser pulse has a $\cos^4$-envelope in its electric field, with a full width at half maximum pulse duration of 8 optical cycles. The harmonic spectrum is calculated as the modulus square $|J(\omega)|^2$ of the Fourier transform of the time-dependent current $J(t)$. Fig. 2.9(b) shows the calculated harmonic spectra using different laser wavelength of $1.6\,\mu m$, $2.4\,\mu m$ and $3.2\,\mu m$ at an intensity of $10^{12}\,W/cm^2$. The harmonic spectrum exhibits both a perturbative regime with harmonic orders up to 5, 7 and 9 for driving wavelength of 1600 nm, 2400 nm and 3200 nm, respectively. After the perturbative orders we observe a plateau which is highly dependent on the pump wavelength. The cutoff extends to higher frequencies when increasing the pump wavelength. It has been demonstrated by similar calculations using only the valence band and the first conduction band that the plateau is well reproduced. This good reproduction indicates that the plateau comes from the dynamics involving only the valence and the first conduction band in those parameter regimes. The plateau is due to interband transitions, and the harmonics can be generated with photon energies well above the maximum bandgap energy. The increase of the cutoff frequency with driving wavelength is consistent with the scaling law listed in tab. 2.1.

2.2.2. High harmonic generation with a high-repetition rate $1.039\,\mu m$ beam

In this experiment, we investigate harmonic generation with a high repetition rate fiber laser source at $1.039\,\mu m$ wavelength in ZnO, MgO and Al_2O_3. The experiment was made in November/December 2015 at Institut d'Optique Graduate School (IOGS), Palaiseau, in the group of Marc Hanna.

Laser system and experimental setup

The fiber laser has a central wavelength of 1039 nm, a pulse duration of less than 50 fs and a repetition rate of 100 kHz. The laser is focused into the sample (normal incidence) where a maximum intensity of $22\,TW/cm^2$ is achieved. The harmonics are detected in transmission where they are either focused into an Ocean Optics spectrometer (for H3 and H5) or detected by a combination of a grating and a photomultiplier. The setup is placed in a vacuum chamber, in order to avoid harmonics absorption by air. After the laser, two polarizers and a half-waveplate ensure the laser polarization and attenuation. In order to have a small focal spot, we enlarge the fundamental beam with a telescope by using a convergent lens (f = +400 mm) and a divergent lens (f = -75 mm). A pair of fused-silica wedges are employed to compensate the dispersion of all material in the beam path. A UV fused silica lens (f = +75 mm) is used to focus the beam into the sample which yields a beam waist of $19\,\mu m$ (FWHM). The focal spot has been measured with the knife-edge method. Different filters can be used to filter the third and fifth harmonic beam. By using a flip mirror, the harmonic beam can alternatively be guided to a setup for the detection of higher harmonics in the UV. More details about the laser system can be found in app. C.

Measurements

First, we carry out some measurements with the third harmonic. We point out that at a driving wavelength of 1039 nm, the third harmonic from ZnO is an above-bandgap

(a) **Pump intensity spectrogram of H3.**　　　(b) **Ellipticity dependence of H3.**
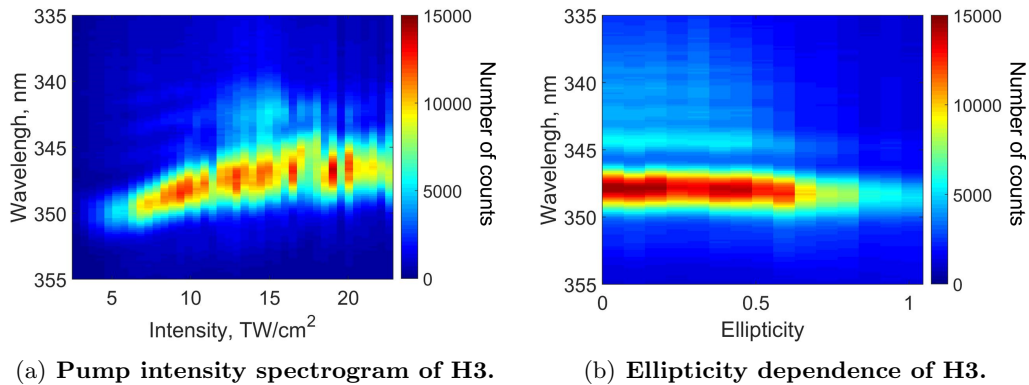
Figure 2.10.: Intensity- and ellipticity-dependence of H3.

harmonic and suffers from strong absorption in the crystal. Fig. 2.10(a) shows the measured third harmonic spectrum in dependence on the pump intensity. We observe a strong increase of the third harmonic with pump intensity. Saturation starts at around $8\,\mathrm{TW/cm^2}$. Fig. 2.10(b) shows the measurement of the third harmonic signal in dependence on the ellipticity of the pump beam. As expected, the signal is maximum at linear polarization and stronly decreases towards circular polarization. Surprisingly, the detection of higher harmonics, even the fifth harmonic, turned out to be difficult. There are several possible reasons:

- The presence of a non-negligible pre-pulse of few milliwatt in the pump pulse which induces electronic perturbations in the HHG process. With a FROG measurement such a side pulse was identified. However, it was not determined whether it was a pre- or a post-pulse.

- The high repetition rate of 100 kHz can affect the crystal thermalization and thus the thermal conductivity of the material [93]. This means that between two optical pulses, the local heat accumulation inhibits electronic relaxation and decreases the electron mobility (Fig. 2.7).

In order to push our study further, we used an automized program that moved the sample permanently perpendicular to the beam direction. When placing the photo-multiplier directly behind the crystal (without grating), a signal was measured only when moving the crystal constantly. This indicates indeed that some crystal damage occurs and that a signal reappeared when moving to a pristine spot on the sample. The same phenomenon was observed when using other nonlinear crystals such as sapphire and MgO. The study was not pushed further due to limited beamtime, but the results hold promise that HHG in solids with a high-repetition rate fiber laser is possible [94].

2.2.3. High harmonic generation with a $2.0\,\mu m$ beam in $CaCO_3$

In this experiment, we investigate HHG in a $CaCO_3$ [100] crystal. We study the generation in dependence on the angle between polarization direction and crystalline orientation. In comparison to the experiment described in subsec. 2.2.2, we now use a laser with lower repetition rate and longer wavelength in order to reduce damage effects. The experiment was carried out in January - March 2016 in the SOFOCKLE laboratory of Dr. Christian Cornaggia at CEA Saclay. The simulations were made by Dr. Nicolas Tancogne-Dejean.

Laser system and experimental setup

The experiment was performed with the idler of a Ti:sapphire pumped (repetition rate 3 kHz, pulse duration 40 fs and pulse energy $700\,\mu J$) TOPAS optical parametric amplifier (OPA). Repetition rate, pulse duration and maximum pulse energy of the idler are 3 kHz, 100 fs and $120\,\mu J$, respectively. The signal has a maximum pulse energy of $110\,\mu J$. A layout of the setup is shown in Fig. 2.11. Parasitic signals from the OPA in the visible are removed from the idler by the use of a high-pass filter (cutoff at 1500 nm). A half-wave plate and a polarizer are used to adjust the pulse energy. The idler is tunable in wavelength in the range 1600 nm - 2400 nm. The signal is centered at 1350 nm. A telescope with a convex mirror (f = 400 mm) and a concave mirror (f = 200 mm) is used in order to expand the beam before focusing. The beam is focused into the sample (normal incidence) with a plano-convex lens with (f = 200 mm) focal length, the beam size in the focus is $100\,\mu m$ at FWHM. We work at a peak intensity of $3\,TW/cm^2$. The harmonics are detected in transmission by focusing them with an off-axis parabola into an imaging spectrometer.
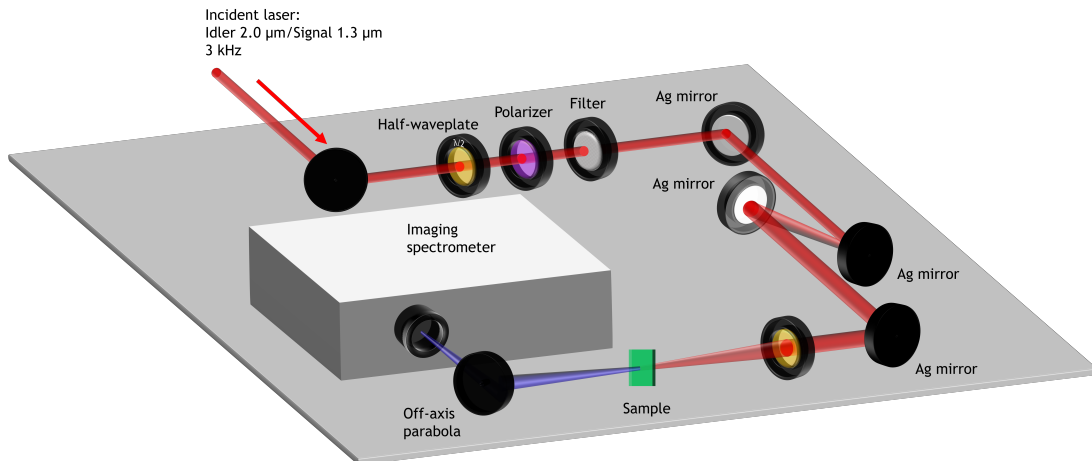
Figure 2.11.: Experimental setup.

Sample

For our experiments, we use a $500\,\mu$m thick $CaCO_3$ [100] crystal. Details about the crystal structure are given in Fig. 2.12. The lattice constants of $CaCO_3$ are 0.50 nm/ 1.71 nm and the bandgap is 6 eV.
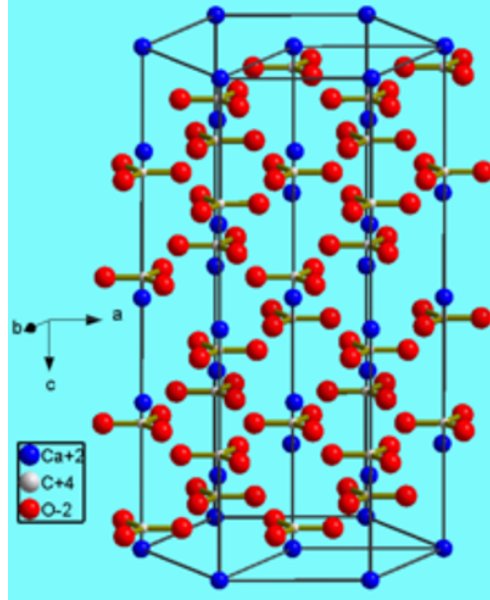
Figure 2.12.: The crystal structure of $CaCO_3$ **is trigonal − Hexagonal Scalendohedral (image taken from www.quora.com).**

Measurements

In this experiment the idler is centered at 2050 nm. We detect up to the ninth harmonic. Since in this experiment we were limited by the absorption in air we could not detect higher harmonics. Spectra of H3, H5, H7 and H9 generated in $CaCO_3$ are shown in Fig. 2.13(a) - (d). The spectrum of H9 is modulated because H9 is weak and close to the noise level. The harmonics were measured for a laser polarization perpendicular to the c-axis ([001]-direction). We then change the angle between polarization and crystal axes by turning the crystal perpendicular to the propagation axis. The measured harmonic signals in dependence on the crystal orientation are shown as blue crosses in Fig. 2.14. The insets in Figs. 2.14(a) - (d) show a zoom on the parts of the curve that have low counts. During a full turn of 360°, we observe two global (at 0° and 180°) and two local maxima (at 90° and 270°) for H3. The local maxima appear when the polarization is parallel to the [001] axis. For H5, the two global maxima appear at the same angles as for H3. However, the two local maxima are much smaller than for H3. In addition, side-maxima on both sides of the local maxima appear (see inset in Fig. 2.14(b)). For H7 and H9, which are below-bandgap harmonics as H3 and H5, two global maxima still appear at the same position as for H3 and H5. However, instead of a local maximum a minimum appears when the laser polarization is aligned

30

(a) **Spectrum of H3.**

(b) **Spectrum of H5.**

(c) **Spectrum of H7.**
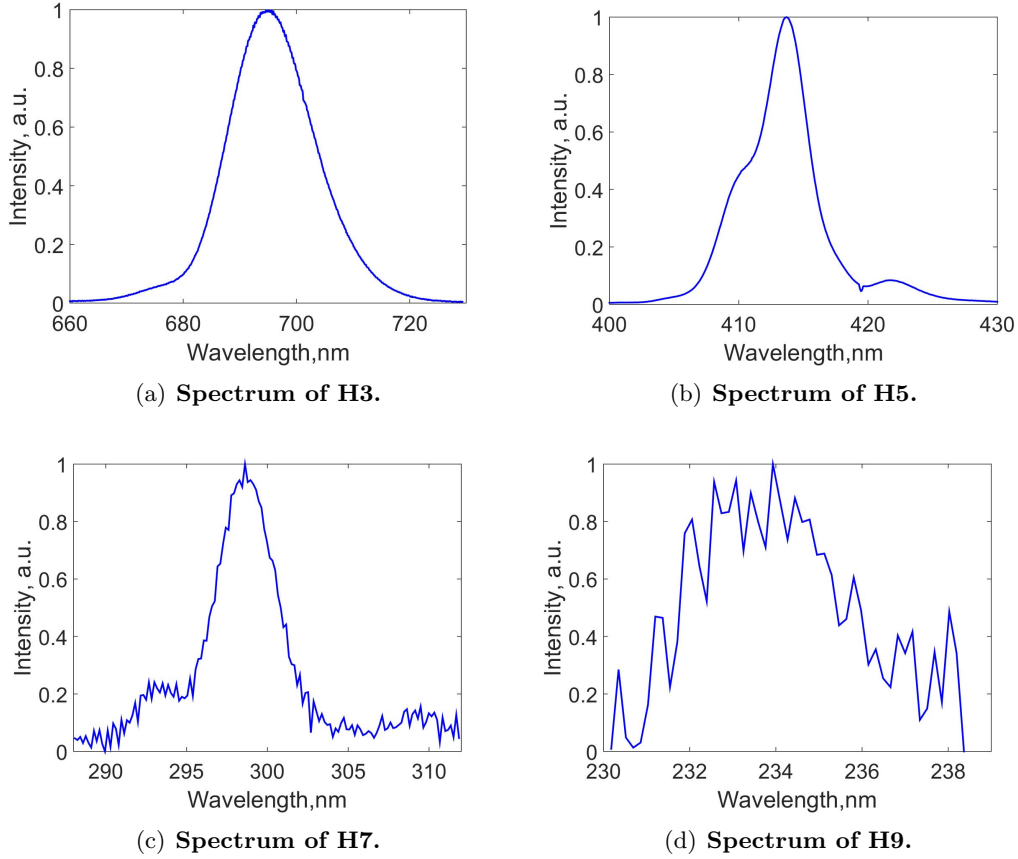
(d) **Spectrum of H9.**

Figure 2.13.: Harmonic spectrum of $CaCO_3$ generated at $3\,TW/cm^2$.

along the [001] axis. So the behaviour of H7 and H9 is different from H3. Using an ab initio approach based on time-dependent density-functional theory (TDDFT) [74], we started to investigate the microscopic origin of the strong anisotropy observed in the harmonic yield from $CaCO_3$ using a linear polarization. Effects stemming from the full electronic structure (valence and conduction bands) and the real crystal structure are properly accounted for. We did not take into account macroscopic effects such as phase matching. The result of the simulations is shown as red circles in Figs. 2.14. The strong anisotropy of the harmonic yield is captured by our preliminary TDDFT results for 0° and 90°, corresponding to polarizations parallel an perpendicular to the cristallographic direction [001]. $CaCO_3$ is strongly birefringent, which makes the polarization elliptical upon propagation. The polarization state changes many times between $\epsilon = 0$ and $\epsilon = 1$ while the beam propagates in the $500\,\mu$m thick $CaCO_3$ crystal. Ellipticity of the fundamental beam can strongly affect harmonic generation, as was discussed in sec. 2.1. However, even without taking these effects into account, the TDDFT simulations are able to reproduce the global behaviour of the harmonic yield in dependence on the crystalline orientation.

You et al. [95] investigated nonperturbative harmonic generation in MgO and observed

(a) **Polar plot of H3.**

(b) **Polar plot of H5.**

(c) **Polar plot of H7.**

(d) **Polar plot of H9.**
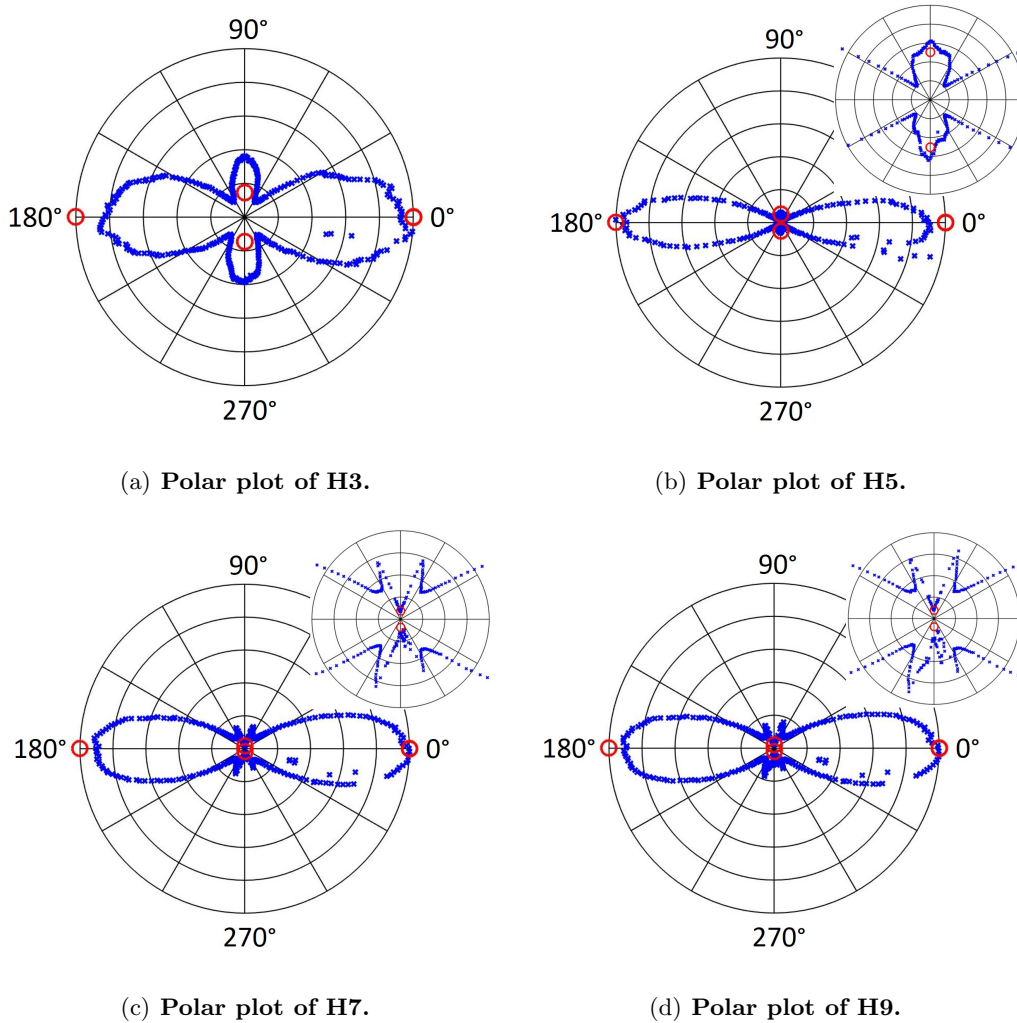
Figure 2.14.: Harmonic generation (H3, H5, H7, H9) in $CaCO_3$ in dependence on the angle between polarization and crystalline axes.

a strong dependence of the harmonic generation efficiency on the angle between polarization and crystal axes. The relative strength of the maxima appearing at certain angles changes for different harmonic orders. The change in efficiency in dependence on the angle can be explained by the sensitiviy of HHG to interatomic bonding. It is the microscopic valence electron density that determines the optical, electronic, structural and thermal properties of materials [95].

2.2.4. Modulations in third-harmonic spectra

In different experiments carried out in the frame of this thesis we observed modulations in third harmonic spectra. As an example we show the third harmonic generated
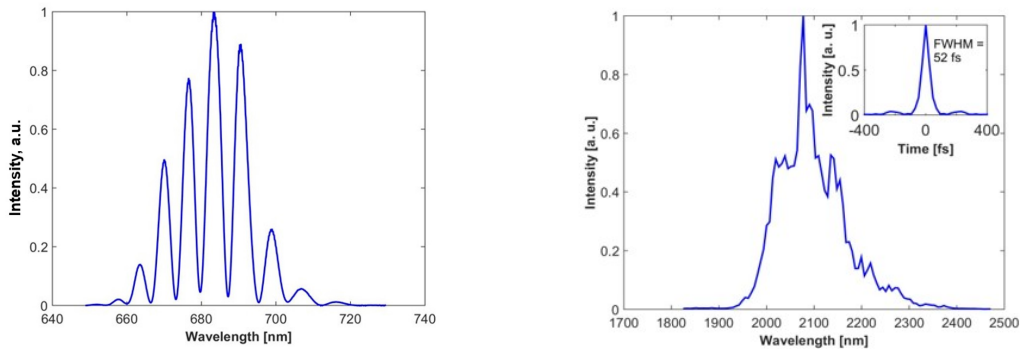
(a) **The third harmonic of a 2100 nm beam exhibits strong and equally spaced spectral modulations.**

(b) **The fundamental spectrum (measured before the crystal) exhibits sharp spikes with irregular spacing.**

Figure 2.15.: The third harmonic spectrum exhibits strong modulations that do not appear in the fundamental spectrum.

in $CdWO_4$ (Fig. 2.15(a)) from a $2.1\,\mu$m beam (Fig. 2.15(b)). The third harmonic is strongly modulated. The modulations are equally spaced and cannot be found in the spectrum of the fundamental beam. This means that the fringes are not transferred from the fundametal beam to the harmonics beam but rather created during harmonic generation. In this subsection we discuss the origin of these fringes.

Mlejnek et al. [96] explain the occurence of fringes for the case of second harmonic generation. The fundamental beam impinging on the nonlinear crystal generates two harmonic beams. The first one is generated at the boundary between the linear medium (air or vacuum) and the nonlinear crystal and propagates in the crystal with the group velocity set by the material dispersion at the harmonic wavelength. The second harmonic wave is generated throughout the crystal and, since it is driven by the nonlinear polarization, propagates at the velocity of the fundamental beam. Since both components of the harmonic beam propagate at different group velocities, they separate when propagating in the crystal under phase-mismatch conditions. The interference of these temporally separated pulses causes fringes in the harmonic spectrum [96]. Such fringes in third harmonic spectra were already discussed by [97]. In principle such spectral fringes could appear in all below-bandgap harmonic spectra. However, this kind of phenomenon is not possible for above-bandgap harmonics since they are absorbed inside the crystal. The fringe spacing is calculated according to

$$\Delta\lambda = \frac{\lambda^2}{c\Delta t} = \frac{\lambda^2}{c \cdot d \cdot (1/v_{g,\omega} - 1/v_{g,3\omega})} \tag{2.10}$$

, where Δt is the temporal separation between both harmonic pulses at the crystal output surface, d is the crystal thickness and $v_{g,\omega}$ and $v_{g,3\omega}$ are the group velocities of the fundamental and the third harmonic beam, respectively. The group velocity is calculated as $v_g = \frac{c}{n} \cdot (1 + \frac{\lambda}{n}\frac{dn}{d\lambda})$. So the thicker the crystal, the higher the temporal separation Δt between both pulses. We see from eq. 2.10 that the wavelength spacing

33

$\Delta\lambda$ is inversely proportional to the temporal separation Δt. For very thin crystals, Δt is small which leads to a large fringe spacing. The spacing can be larger than the bandwidth of the harmonic beam such that the fringes cannot be observed. Even the opposite case is possible. For thick crystals Δt can have high values which leads to a small $\Delta\lambda$ that cannot be resolved by the detection system.

There are other possibilities that can lead to the appearence of fringes in harmonic spectra. [98, 99] report on pulse splitting of the fundamental beam at high intensity due to nonlinear effects. The pulse splitting of the fundamental leads to pulse splitting of the harmonics beam which eventually leads to spectral modulations of both the fundamental beam and the harmonic beam. We believe that pulse splitting of the fundamental beam does not occur in our case. In the following we compare the fringe spacing observed in third harmonic spectra from ZnO and CdWO$_4$ to the spacing calculated by eq. 2.10.

Fringes in third harmonic spectra from ZnO

In the experiment described in sec. 3.2 the third harmonic spectrum from bare ZnO exhibits fringes. We try to identify the origin of these fringes. The experiment was carried out in August/September 2015 at Pulse Institute at Stanford University in the group of Prof. David Reis.

Laser system and experimental setup

We use the idler of an OPA at a wavelength of $2.0\,\mu$m, 70 fs pulse duration, 1 kHz repetition rate and a maximum pulse energy of $150\,\mu$J. The beam is focused into the sample (normal incidence) and the harmonic radiation is measured in transmission. The peak intensity in the focus is $0.1\,$TW/cm^2. For more details about the laser system and the experimental setup we refer to the sec. 3.2.

Measurement

We investigate the spectal modulations of the third harmonic generated in a $500\,\mu$m ZnO crystal from a $2.0\,\mu$m beam. We generate the third harmonic in two different setups at similar peak intensities. Once a reflective objective with an extremely short focal length is used. The corresponding third harmonic spectrum is shown in Fig. 2.16(a). The third harmonic spectrum is very smooth. In the second setup, an off-axis parabola with a focal length of f = 15 cm is used. The corresponding third harmonic spectrum is shown in Fig. 2.16(b). The spectrum exhibits strong spectral modulations. This is consistent with the theory discussed above that the spectral fringes are due to the interference of a 'free' component of the third harmonic generated at the crystal input surface and a 'driven' component generated throughout the crystal. When using the setup with the short focal length, the beam divergence angle is high. This means that the Rayleigh length is very short (it is estimated to be $15\,\mu$m) and, since the focal position is at the output surface of the crystal, the beam diameter at the input surface will be large and the intensity considerably lower than at the output surface. The intensity at the input surface might not be sufficient to trigger third harmonic generation. This means that the surface harmonic necessary to generate the spectral fringes
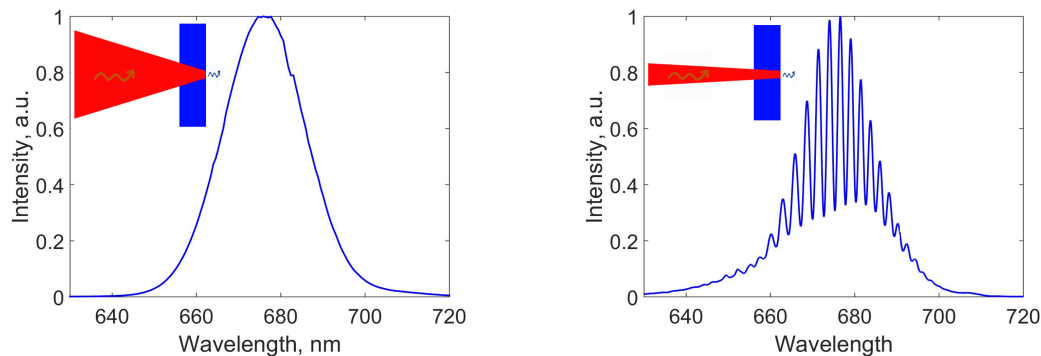
(a) **Third harmonic generated when focused with a reflective objective of shsort focal length.**

(b) **Third harmonic generated when focused with an off-axis parabola of 15 cm focal length.**

Figure 2.16.: Third harmonic generation from ZnO.

is not generated. However, when focusing with the parabola of f = 15 cm focal length, the Rayleigh length is much larger (it is estimated to be 4 mm). As a consequence, the peak intensity does not change considerably along the crystal (500 μm thickness). We expect a strong third harmonic from the input surface, which yields due to interference with the bulk contribution the fringes observed in Fig. 2.16(b). The spectrometer used in the setup with the large focal length was not calibrated in wavelength. However, by comparing the bandwidth of the generated third harmonic to the third harmonic spectrum generated in the setup with the short focal length, we estimate the fringe spacing to be 3 nm. With n(2000 nm) = 1.92, n(667 nm) = 1.98, $\frac{dn}{d\lambda}|_{\lambda=2000\,nm} = -1.296 \cdot 10^{-5}$ and $\frac{dn}{d\lambda}|_{\lambda=667\,nm} = 2.233 \cdot 10^{-4}$ we obtain by using eq. 2.10 a fringe spacing of 4.6 nm, which is in acceptable agreement with the estimated value of 3 nm for the measured third harmonic spectrum [100]. We conclude that the fringes observed in the third harmonic spectrum are due to the interference of 'free' and 'driven' components generated at the input surface and in the bulk.

Fringes in third harmonic spectra from $CdWO_4$

In this experiment we generate the third harmonic in $CdWO_4$. We vary the wavelength of the pump beam and analyze a change in the fringe spacing of the third harmonic spectra.

Laser system and experimental setup

The experiment was performed with the idler of an optical parametric amplifier. In this experiment, we change the wavelength of the idler in the range 1600 nm - 2100 nm. In addition, we use the signal of the OPA at 1350 nm. Repetition rate and pulse duration are 3kHz and 100 fs. The laser is focused into the sample (normal incidence) and the harmonics are measured in transmission. The peak intensity is $3\,TW/cm^2$ in the focus.

35

For more details about the laser system and the experimental setup we refer to sec. 2.2.3.

Sample

For our experiments, we use a $500\,\mu$m thick $CdWO_4$ [001] crystal. The lattice constants of $CdWO_4$ are $1.43\,$nm/$1.02\,$nm/$0.66\,$nm and the bandgap is $4\,$eV. The crystal structure of $CdWO_4$ is monoclinic prismatic.

Measurement

The third harmonic generated at different driving wavelengths (1320 nm, 1620 nm, 1640 nm, 1780 nm, 1980 nm, 2100 nm) is shown in Fig. 2.17. We see that all third harmonic spectra exhibit modulations. Both the fringe spacing and the fringe visibility increases with the driving wavelength. We extract the wavelength-dependent refractive-index of $CdWO_4$ from [101]. By using eq. 2.10 we obtain for the driving wavelengths 1320 nm, 1620 nm, 1640 nm, 1780 nm, 1980 nm, 2100 nm a fringe spacing of the third harmonic of 0.5 nm, 1.3 nm, 2.0 nm, 3.1 nm, 4.7 nm. Fig. 2.18 shows the calculated fringe spacing in blue and the measured fringe spacing in red. The offset at short wavelength is a factor of 2.0 and at long wavelength a factor of 1.5. We explain this offset by the fact that $CdWO_4$ is a biaxial cristal and that the refractive index used for the calculations is for a polarization parallel to the crystal-axis 'a'. However,

(a) **Third harmonic of 1320 nm.**

(b) **Third harmonic of 1620 nm.**

(c) **Third harmonic of 1640 nm.**

(d) **Third harmonic of 1780 nm.**

(e) **Third harmonic of 1980 nm.**

(f) **Third harmonic of 2100 nm.**
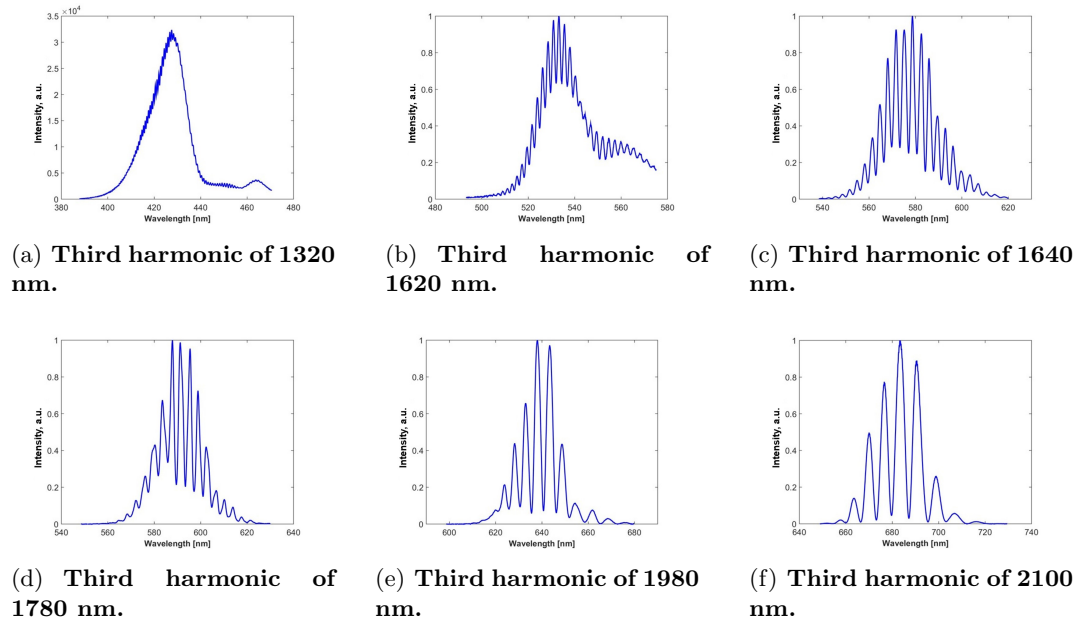
Figure 2.17.: Third harmonic generation for different driving wavelength (1320 nm, 1620 nm, 1640 nm, 1780 nm, 1980 nm, 2100 nm). The harmonic spectra exhibit fringes.
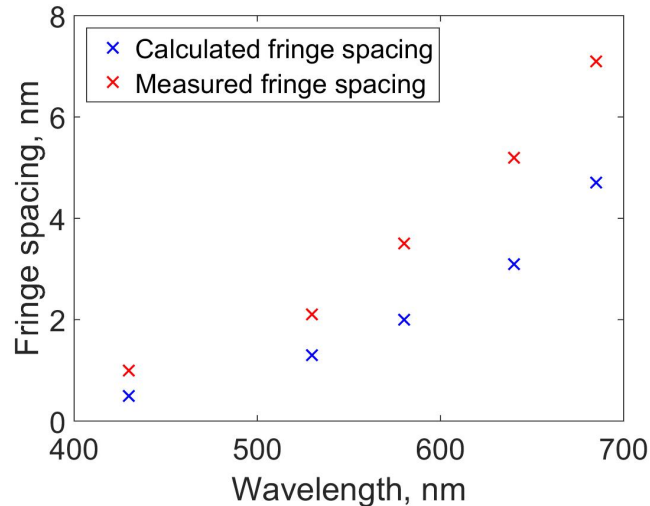
Figure 2.18.: Fringe spacing in third harmonic spectra vs. third harmonic wavelength. The measured values are shown in red and the calculated values in blue.

in the measurement the angle between polarization direction and axis 'a' is not known. We conclude that the spectral modulations in the third harmonic spectrum are due to the interference of 'free' and 'driven' components generated at the input surface and in the bulk.

2.2.5. High harmonic generation with a $3.1 \, \mu m$ beam in ZnO

In this subsection, we investigate the intensity scaling of below-bandgap and above-bandgap harmonics generated in ZnO by a $3.1 \, \mu m$ beam. It was part of the experiment described in sec. 4.3. The experiment was carried out at IOGS (Institute d'Optique Graduate school) in the group of Dr. Marc Hanna in March/April 2017.

Laser system and experimental setup

The laser is an OPCPA system delivering an idler at $3.1 \, \mu m$ wavelength and an energy of $10 \, \mu J$ per pulse at 125 kHz repetition rate. The laser is focused into the sample (normal incidence) and the harmonics are measured in transmission. The peak intensity in the focus is in the range of $0.04 - 0.5 \, TW/cm^2$. Different harmonics orders were selected with tranmission filters. More details about the filters used in this experiment can be found in app. D. For more details about the laser system and the experimental setup we refer to sec. 4.3 and to [102].

Measurements

We investigate the harmonic yield of H5, H7 and H9, H11, H13 as well as the fluorescence in dependence on the pump intensity. The coupling of the fluorescence to the spectrometer was not optimized separately. The fluorescence was rather detected as

a parasitic signal during the measurement of H9. The intensity-scaling is shown in Fig. 2.19. The corresponding harmonic spectra are shown as insets. We did not study

(a) **Power law of H5.**

(b) **Power law of H7.**

(c) **Power law of H9.**

(d) **HPower law of H11.**

(e) **Power law of H13.**

(f) **Power law of fluorescence.**
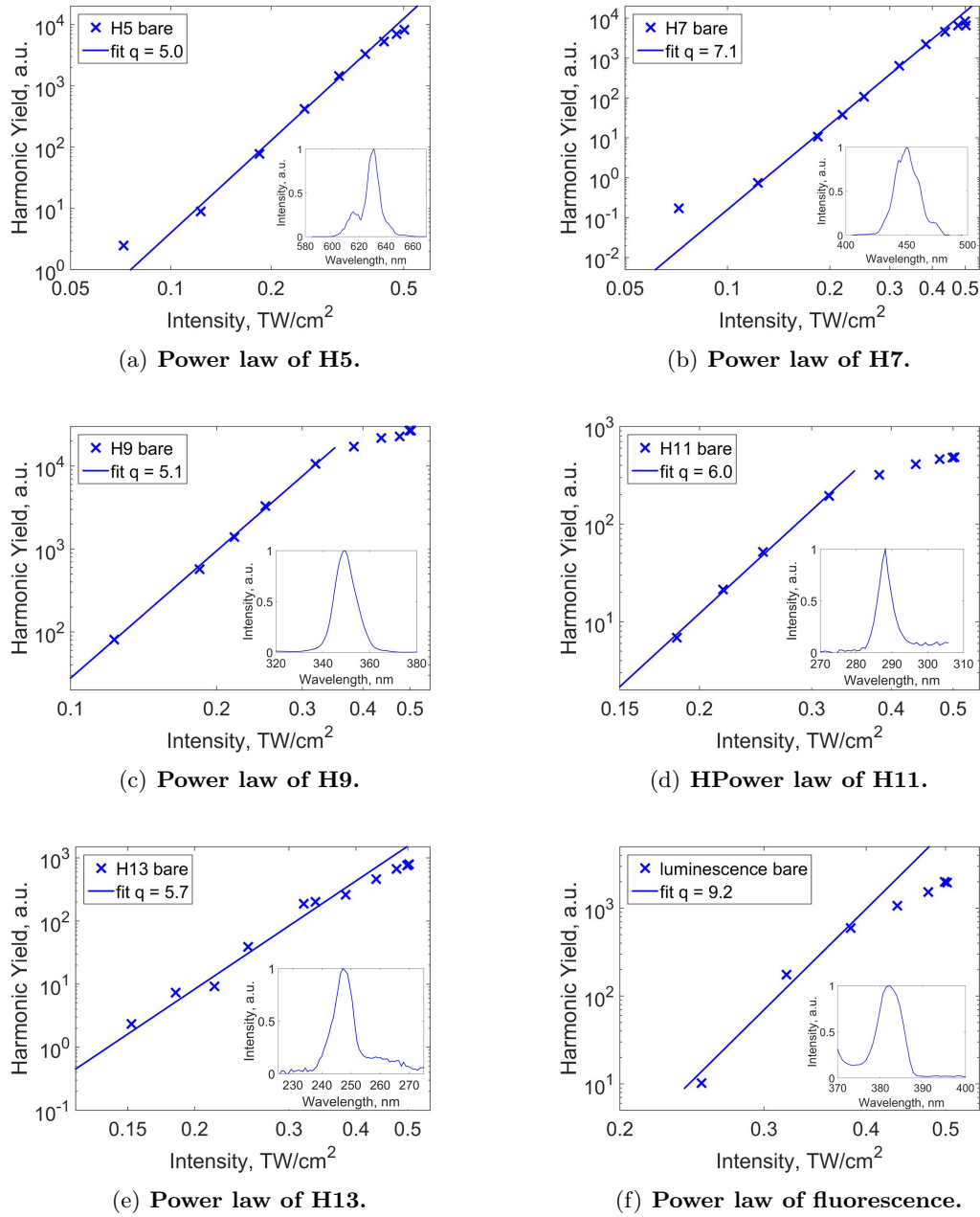
Figure 2.19.: **High harmonics (H5, H7, H9, H11, H13) and the luminescence generated from ZnO. We investigate the dependence of different harmonic orders on the pump intensity. The harmonic spectra are shown as insets. The spectra shown in the inset were measured at $0.24\,\mathrm{TW/cm^2}$ for H5, H7, H9, H11, H13 and at $0.31\,\mathrm{TW/cm^2}$ for the fluorescence.**

H3 since it was beyond the detection range of our spectrometer. The measurement of H5 is shown in Fig. 2.19(a). Detection starts at an intensity of $0.07\,\mathrm{TW/cm^2}$. It grows steadily with increasing pump intensity and starts to saturate at $0.4\,\mathrm{TW/cm^2}$. It can be well fitted with the polynomial of eq. 2.3. We obtain q = 5.0 which is in excellent agreement with what we expect for a perturbative harmonics of fifth order. As H5, H7 is detected for intensities higher than $0.07\,\mathrm{TW/cm^2}$ and starts to saturate at $0.4\,\mathrm{TW/cm^2}$. When fitting eq. 2.3 we obtain q = 7.1, which is close to what is expected for a perturbative process of seventh order. H9, H11 and H13 are above-bandgap harmonics. Saturation starts at around $0.4\,\mathrm{TW/cm^2}$. When fitting eq. 2.9 we obtain q = 5.1, 6.0, 5.7 for harmonics H9, H11 and H13, respectively. We see that they scale non-perturbatively with pump intensity. The luminescence of ZnO is located at 385 nm. The intensity-dependent fluorescence measurement is shown in Fig. 2.19(f). We expect a perturbative scaling for the luminescence. At least 8 - 9 photons of $3.1\,\mu\mathrm{m}$ are necessary to overcome the bandgap. We obtain a value of q = 9.2, which is in good agreement with the expected value.

2.3. High harmonic generation in graphene

In this section, we investigate HHG in graphene. The experiment was carried out in September/October 2017 at CEA Saclay. We study HHG with two different samples:

- trilayer graphene on a quartz substrate

- freestanding trilayer graphene suspended on a TEM grid

Laser system and setup

The laser used in this experiment is an oscillator with a pre-amplifier from NOVAE. The operating wavelength is $2.1\,\mu$m, the pulse duration 85 fs, the maximum pulse energy 8.7 nJ and the repetition rate 18.66 MHz. The laser is focused with an off-axis parabola (f = 25 mm) to a spot size of $5.9\,\mu$m (FWHM). We work at normal incidence. The pulse energy can be attenuated by means of a half-waveplate and a polarizer. The intensity range used in this experiment is $0.01 - 0.08\,\mathrm{TW/cm^2}$. The harmonic radiation is measured in transmission with a spectrometer and a CMOS camera. More details about the experimental setup and the laser system can be found in sec. 4.4 and in app. C, respectively.

Measurements

Here we present the harmonic measurements made with both graphene on a substrate and freestanding graphene.

Trilayer graphene on quartz substrate

The sample is a $500\,\mu$m thick quartz substrate with trilayer graphene at the output surface of the quartz crystal. We measure a complete harmonic spectrum which comprises H3, H5, H7 and H9. H3 (Fig. 2.20(a)) was measured with a spectrometer and H5 (Fig. 2.20(b)), H7 (Fig. 2.20(c)) and H9 (Fig. 2.20(d)) with a combination of a CMOS camera and transmission filters. The camera was suited for the higher harmonics since they are weak and the camera is more sensitive than the spectrometer. We observe that the overall harmonic yield decreases fast over time. We performed a systematic study of the harmonic signal time evolution of H3 which has the highest detection yield. The temporal evolution of H3 at an intensity of $0.014\,\mathrm{TW/cm^2}$ is shown in Fig. 2.20(e). H3 decreases and tends towards a constant value which is reached after 8 minutes. We conclude that at the beginning of the measurement we have a strong third harmonic signal from the graphene trilayer. The graphene layer starts to damage (on the one hand due to the high peak intensity and on the other hand due to the average power) which leads to a decrease of the third harmonic signal. After a few minutes, the graphene trilayer is totally damaged. The constant signal that remains comes from the quartz substrate. We perform similar measurements for different peak intensities in the range $0.010 - 0.078\,\mathrm{TW/cm^2}$. The result is shown in Fig. 2.20(f). It turns out that the higher the pump intensity the higher the harmonic signal from
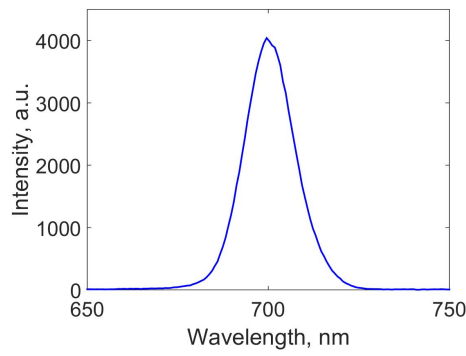
(a) **Spectrum of H3.**
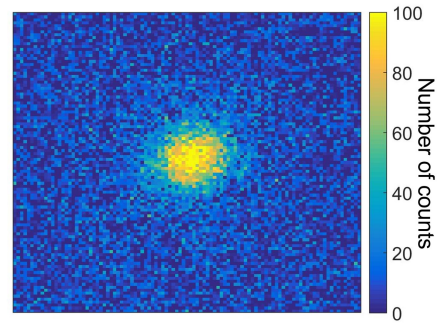
(b) **Spectrum of H5.**
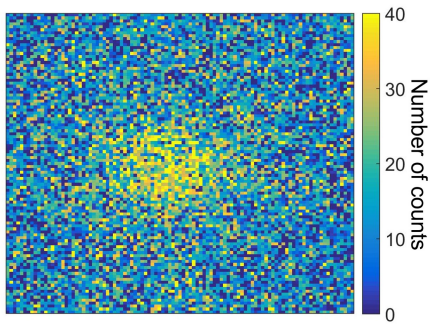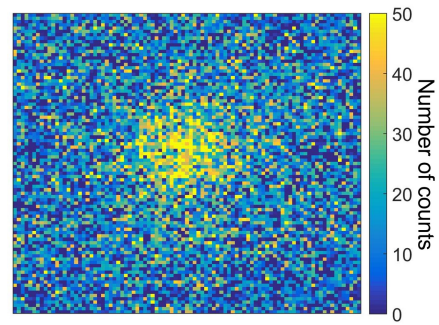
(c) **Spectrum of H7.**

(d) **Spectrum of H9.**
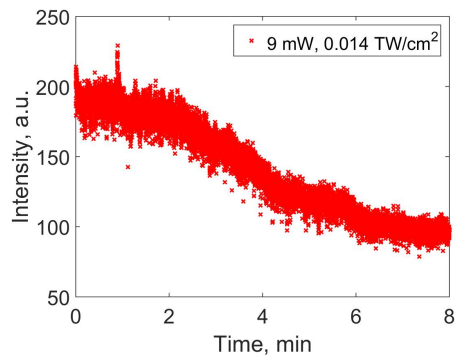
(e) **Temporal decrease of H3 at an intensity of** $0.014\,\mathrm{TW/cm^2}$.
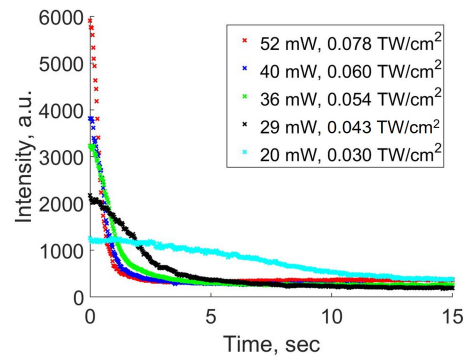
(f) **Temporal decrease of H3 generated at different intensities in the range** $0.030 - 0.078\,\mathrm{TW/cm^2}$.

Figure 2.20.: (a) - (d) Harmonic orders H3, H5, H7 and H9 measured from trilayer graphene on a quartz substrate. (e), (f) Temporal evolution of H3 from graphene.

graphene and the faster the damage. At $0.078\,\mathrm{TW/cm^2}$ a constant value is reached after $\sim 3\,\mathrm{s}$. When decreasing the intensity by $30\,\%$ to $0.054\,\mathrm{TW/cm^2}$, it takes $14\,\mathrm{s}$ until the intensity reaches a constant value. Hence the damage time depends in a highly
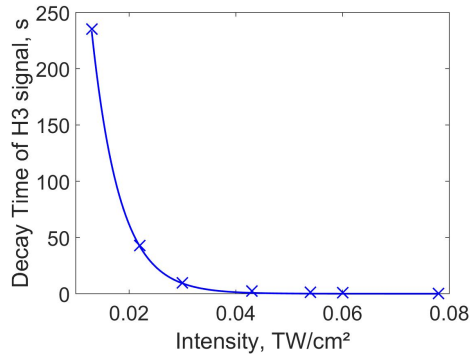
(a) **Intensity-dependent decay time of H3 from graphene. We define the decay time as the time during which H3 looses half of its maximum power with respect to the background from the quartz substrate.**
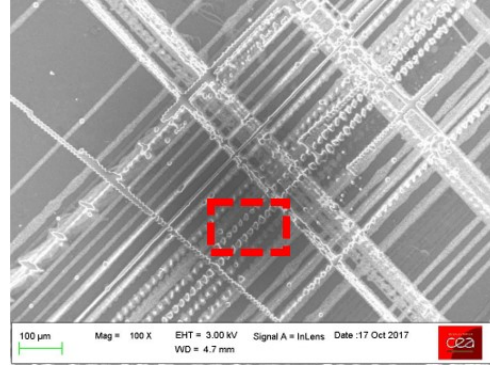
(b) **SEM-image of the damaged graphene layer. The dark areas correspond to the undamaged graphene layer. The white lines correspond to the illuminated areas where damage occured.**

Figure 2.21.: (a) Intensity-dependent decay time of H3 and (b) SEM-image of damaged graphene sample.

nonlinear way on the pump intensity. The intensity-dependent decay time is plotted in Fig. 2.21(a). The decay time decreases exponentially from 240 s at $0.01\,\mathrm{TW/cm^2}$ to 0.4 s at $0.078\,\mathrm{TW/cm^2}$. For making systematic measurements with the harmonic radiation the sample needs to be moved permanently in order to illuminate a fresh graphene spot before the harmonic signal decreases due to damage. We believe that even harmonics higher than H9 are generated. However, in the frame of this experiment we were limited by our detection systems and the absorption in air. From the quartz substrate no harmonic higher than H3 was observed. This shows on the one hand that it is indeed the graphene layer that generates harmonics. On the other hand the graphene layer enhances third harmonic radiation with respect to the substrate. After irradiation, we analyzed the graphene surface with a scanning electron microscope. The result is shown in Fig. 2.21(b). The dark areas correspond to the undamaged graphene layer. The white lines correspond to the illuminated areas where damage occured. We see that each line consists of individual burned points. Indeed, during optimization of the harmonic radiation we moved the sample permanently with an automized program in order to refresh the illuminated spot. During such scans the detected harmonic signals were stable. The holes in Fig. 2.21(b) correspond to the illuminated areas.

Freestanding trilayer graphene suspended on a TEM grid

In order to investigate HHG from only graphene without any substrate we study HHG in trilayer graphene suspended on a TEM-grid which consists of an array of holes in a metallic film. The diameter and the periodicity of the holes are $2\,\mu\mathrm{m}$ and $10\,\mu\mathrm{m}$, respectively. Due to the small beam diameter in the focus only one hole at once is illuminated. We observe H3 and H5. However, H7 and H9 could not be detected. We
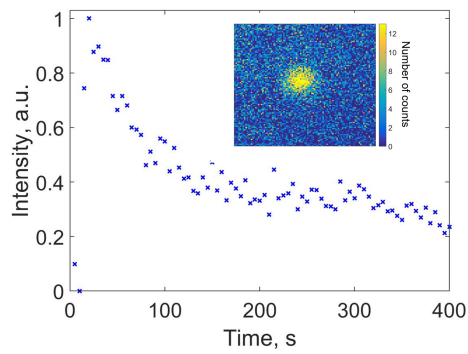
(a) **Temporal evolution of H5. A camera measurement of H5 is shown as an inset.**
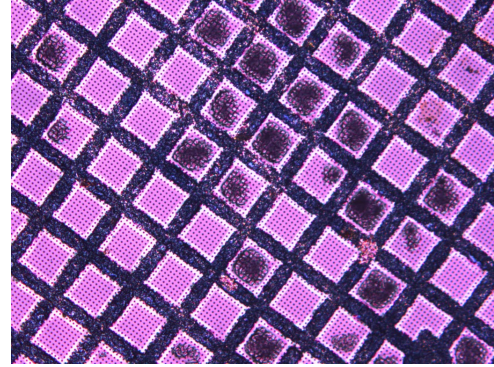
(b) **SEM-image of freestanding graphene on TEM-grid. Each pink square is an array of nanoholes with graphene on top. Damaged areas appear in black.**

Figure 2.22.: Temporal evolution of H5 and SEM-image of freestanding graphene on TEM-grid.

measure the temporal behaviour of H5 at an intensity of $0.03 \, \text{TW/cm}^2$. It decreases steadily over time and is expected to eventually reach zero (Fig. 2.22(a)). The sample after irradiation is shown in Fig. 2.22. Pink areas correspond to the TEM-grids. The laser induced damage appears in black.

Discussion

We generated up to H9 from trilayer graphene on a quartz substrate. We expect that even higher harmonics can be generated. However, in the frame of this experiment we were limited by the absorption of air. H3 from graphene was significantly enhanced
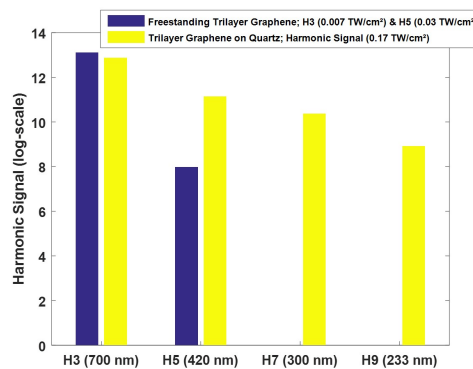
Figure 2.23.: Comparison of harmonic yield from freestanding graphene and graphene on a quartz substrate.

with respect to H3 from the bare substrate. Furthermore, we generated up to H5 from freestanding trilayer graphene suspended on a TEM-grid. In contrast to the first sample (graphene layer on quartz), the second sample (graphene layer on a TEM grid) could not be moved continuously during the measurement since the TEM grid consists of a metallic film with limited aperture sizes. We point out that with a moving sample which ensures a constant harmonic signal even higher harmonic orders might be detectable from sample 2. Fast damage of graphene occured even at low power of the laser for both samples. Fig. 2.23 shows a comparison of harmonic generation from freestanding graphene and from graphene on a quartz substrate. We see that H3 from freestanding graphene is slightly stronger than H3 from graphene on a substrate even though much lower intensity was used ($0.007\,\mathrm{TW/cm}^2$ for freestanding graphene and $0.17\,\mathrm{TW/cm}^2$ for graphene on a substrate).

Conclusion of chap. 2

In this chapter, we studied HHG in different solid state materials. The role of different wavelengths and materials with respect to bandgap and lattice constants was investigated. Simulations of HHG using the time-dependent Schrödinger equation confirmed an extension of the harmonic cutoff with increasing laser wavelength. However, in experiments we mostly worked in air and we were not able to access the harmonic cutoff. We investigated harmonic generation in different 3D crystals. We studied HHG in $CaCO_3$ and found that the harmonic yield strongly depends on the relative orientation of crystalline axes and polarization direction. Simulations based on the TDDFT approach well reproduced the measurements. This confirms that the harmonic generation efficiency depends on the laser polarization and the crystal structure. In a separate experiment, we analyzed the spectral fringes that were observed in third harmonic spectra from different crystals such as ZnO and $CdWO_4$. It turned out that the fringes are due to the interference of a third harmonic pulse generated at the input surface and a third harmonic pulse generated in the bulk rather than due to pulse splitting of the fundamental beam. Furthermore, we generated high harmonics in a ZnO crystal from a $3.1\,\mu m$ beam and investigated the power law. We confirm that below-bandgap harmonics scale perturbatively with pump intensity and that the first three above-bandgap harmonics (H9, H11, H13) scale non-perturbatively with pump intensity. Furthermore, we studied HHG in 2D materials. It turned out that H3 generated in trilayer graphene on a quartz substrate is strongly enhanced with respect to bare quartz. While a graphene trilayer on a quartz substrate generated up to H9, the bare quartz substrate only generated H3. It turns out that graphene damages quickly at high intensities. We observe an intensity-dependent decay time of H3 that varies between a few seconds and several minutes. In order to investigate HHG in 'pure' graphene without substrate that can lead to effects such as bandgap opening we analyed HHG in freestanding graphene on a TEM grid. In this configuration we generated up to H5.

3. High harmonic generation assisted by plasmonic enhancement in metallic nanostructures

In this chapter, we study the enhancement of HHG in plasmonic nanostructures as well as radiation-induced damage in plasmonic nanostructures. In the following, several experiments are presented. In sec. 3.1, we give an introduction to the domain of plasmonic enhancement and the concept of HHG assisted by plasmonic field enhancement is presented. In sec. 3.2, we explore the possibility to enhance HHG in a plasmonic grating. In sec. 3.3 and 3.4, we investigate the enhancement of HHG in two different types of nanostructures, namely nanoholes and a grating resonator. In sec. 3.5, we study HHG in bow tie nanoantennas on a sapphire crystal and we determine the origin of the harmonic generation. Due to limitations in the detection systems we were mostly limited to measurements of the third harmonic. In sec. 3.6, radiation-induced damage and reshaping in different types of metallic nanostructures, namely bow ties and nanoholes, are analyzed. Different mechanisms of radiation-induced damage are identified.

3.1. Theory of plasmonic enhancement

Plasmonics is the study of the interaction between an electromagnetic field and free electrons in a metal. The electric component of the light excites free electrons to make collective oscillations. A plasmon is a quantum of a plasma oscillation. So plasmons are collective oscillations of the free electron gas density in a metal. At optical frequencies, plasmons can couple with a photon to create another quasiparticle called plasmon polariton. Most of their properties can be derived from Maxwell's equations. Plasmons can be described in the classical picture as the oscillation of a free electron density with respect to a background of fixed positive ions inside the metal. They can exist at surfaces and in bulk. Due to Ohmic losses heat is generated that can lead to melting of plasmonic structures. The interaction of light with metal can be tailored and greatly enhanced by properly designing the geometry of metallic nanostructures. Due to the nature of plasmons, field enhancement occurs in subwavelength volumes.

Bulk plasmon

We consider a gas of free electons of mass m and density N that can freely propagate against a background of positively charged nuclei. We neglect electron-electron interaction and the lattice potential. When an external field $E(t) = E_0 e^{-i\omega t}$ is applied, the electrons will oscillate. The oscillations are damped by collisions which is taken into

account phenomenologically by the damping factor γ. The equation of motion for an electron oscillating in an electric field E is:

$$m\,\ddot{x} + m\gamma\,\dot{x} = -eE(t) \tag{3.1}$$

The solution is $x(t) = x_0 e^{-i\omega t}$, where x_0 is the complex amplitude of the oscillation that contains the phase shift between the driving field and the electronic response. We obtain

$$x(t) = \frac{e}{m(\omega^2 + i\gamma\omega)} E(t) \tag{3.2}$$

The displaced electrons create a polarization $P = -Nex$. The dielectric displacement can be written as:

$$D = \epsilon_0 E + P = \epsilon_0 \epsilon E = \epsilon_0 E \left(1 - \frac{Ne^2/(m\epsilon_0)}{\omega^2 + i\gamma\omega}\right) \tag{3.3}$$

By defining the plasma frequency as $\omega_{\mathrm{p}} = \sqrt{Ne^2/\epsilon_0 m}$, we can write the dielectric constant as

$$\epsilon(\omega) = 1 - \frac{Ne^2/\epsilon_0 m}{\omega^2} = 1 - \frac{\omega_p^2}{\omega^2} \tag{3.4}$$

For transverse waves the dispersion relation is $k^2 = \epsilon\omega^2/c^2$. By substituting this into eq. 3.4, we obtain:

$$\omega(k) = \sqrt{\omega_p^2 + k^2 c^2} \tag{3.5}$$

From eq. 3.5 we see that $\omega(\mathrm{k}) > \omega_{\mathrm{p}}$, which means that for $\omega(\mathrm{k}) < \omega_{\mathrm{p}}$ no propagation is possible. For $\omega(\mathrm{k}) > \omega_{\mathrm{p}}$ propagation occurs with a group velocity $v_g = \frac{d\omega}{dk}$. Bulk plasmons are longitudinal waves, so they cannot be excited by electromagnetic waves (which are transverse) under direct illumination.

Surface plasmon

For a dielectric/metal interface, electromagnetic radiation incident on the interface can excite electron oscillations called surface plasmon polaritons (SPP). They are confined to surfaces and interact strongly with light. This coupling is only possible when the wavevector of the incident radiation matches that of the SPP. The negative real part and positive but small imaginary part of the dielectric function $\epsilon(\omega)$ enables the resonant excitation of the plasmon. Solving the Maxwell equations yields [103]

$$k_{SPP} = k_0 * \sqrt{\frac{\epsilon_D \epsilon_M}{\epsilon_D + \epsilon_M}} \tag{3.6}$$

k_{SPP} is the wavevector of the plasmon and k_0 the wavevector of the incident light. ϵ_{D} an ϵ_{M} are the dielectric constants of the dielectric material and the metal, respectively. A schematic of a SPP is shown in Fig. 3.1(a). Plasmonic oscillations are damped, the propagation distance can be calculated according to

$$L = \frac{\lambda}{4\pi} * \sqrt{\frac{\epsilon_m \epsilon_d}{\epsilon_m \cdot \epsilon_d}} \tag{3.7}$$

(a) **Surface plasmon polariton.**

(b) **Localized surface plasmon.**
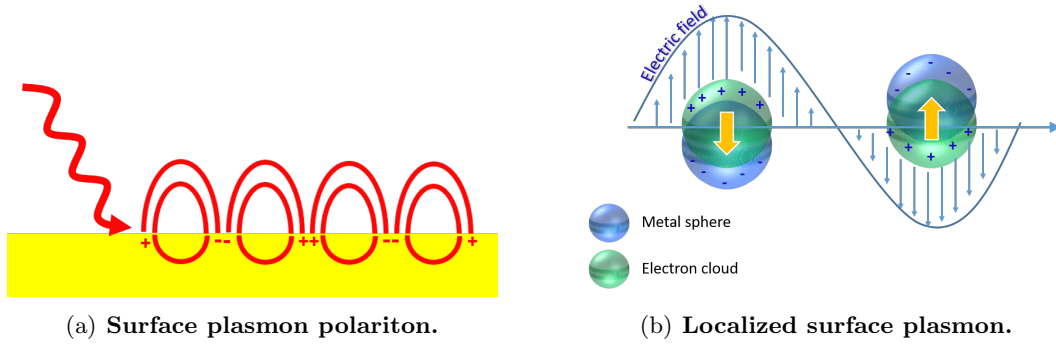
Figure 3.1.: Two types of plasmons are shown schematically: The surface plasmon polariton (SPP) and the localized surface plasmon (LSP).

As an example, typical values for L for excitation wavelengths of $0.8\,\mu$m, $2.0\,\mu$m, $3.2\,\mu$m at a ZnO-gold interface are $96\,\mu$m, $35\,\mu$m, $28\,\mu$m [104]. In order to minimize damping, ohmic absorption should be as low as possible. Ohmic losses are proportional to the imaginary part of the permittivity $\mathrm{Im}(\epsilon(\omega))$. From Fig. 3.2(a) can be seen that the losses are comparably low in the visible and strongly increase towards the mid-infrared. Losses occur close to the surface of the metal within the skin-depth which can be calculated according to

$$\delta_{skin}(\omega) = \frac{\lambda\sqrt{|Re(\epsilon(\omega))|}}{2\pi Im(\epsilon(\omega))} \tag{3.8}$$

There are different techniques to achieve coupling of light to plasmons, such as the Kretschmann configuration. Another common method is to use plasmonic nanostructures.
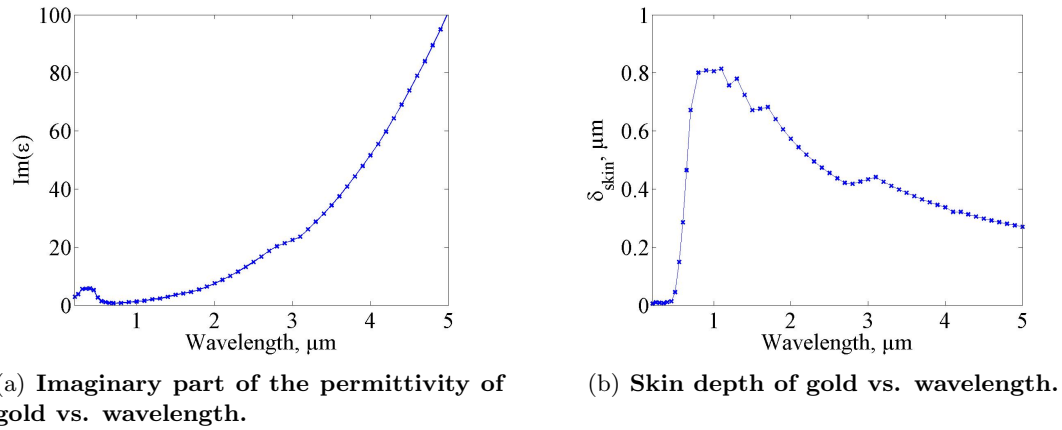
(a) **Imaginary part of the permittivity of gold vs. wavelength.**

(b) **Skin depth of gold vs. wavelength.**

Figure 3.2.: Optical properties of gold.

Bow tie   **Grating**   **Split-ring resonator**
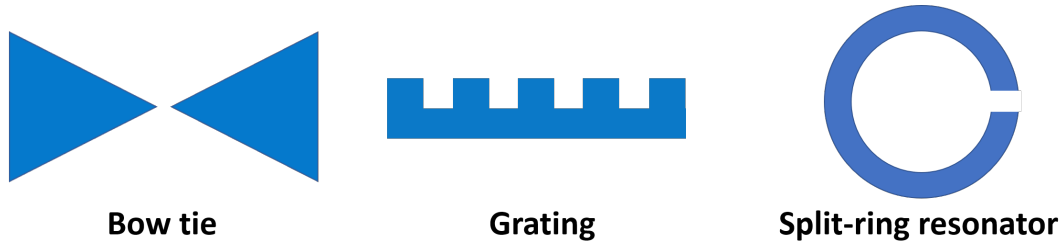
Figure 3.3.: Schematic representation of three commonly used nanostructures: Bow tie, plasmonic grating and split ring resonator.

Plasmonic nanostructures

Plasmonic nanostructures are metallic structures with sub-micrometer sizes. Their size and geometry can be tailored in order to resonate at a certain wavelength. They can enhance the electric field by several orders of magnitude and confine it to sub-wavelength volume below the diffraction limit. There is a vast amount of nanostructures and applications. We will dicuss three of them in more detail.

- The **bow tie** (Fig. 3.3) consists of 2 metallic triangles with the tips pointing towards each other and separated by a gap. Each of these triangles can be considered as an antenna the resonance wavelength of which is approximately twice the antenna length. Each antenna enhances an incident electric field close to the resonance wavelength where the main enhancement occurs close to the corners of the triangles due to the lightning rod effect. The highest enhancement occurs in the gap, where the electric field can be enhanced by several orders of magnitude.

- A **plasmonic grating** (Fig. 3.3) consists of several parallel nanorods separated by a gap, where the gap size is general smaller than the wavelength. Incident light can be enhanced locally in each groove by LSP. Propagating SPPs on the gold surface between two grooves can lead to additional enhancement. In contrast to a bow tie, the enhancement volume is much larger for a plasmonic grating.

- A **split ring resonator (SPR)** consists of a metallic ring with a gap. Incident light can be strongly enhanced in the gap region but even inside the ring. Since the split ring resonator can be considered as a bended antenna, the resonance wavelength is approximately equal two twice the perimeter. The gap behaves like a capacitor. Increasing the gap width decreases the capacitance which in turn increases the resonance frequency. Asymmetric split ring resonators with two gaps were proposed which yield homogeneous enhancement inside the ring rather than high peak enhancement in the gap [105].

Field enhancement in plasmonic nanostructures has applications in different fields, such as the enhancement of incoherent emission of molecules [14] but even the enhancement of coherent nonlinear processes such as four-wave mixing [106], second [9, 10] and third harmonic generation [11, 12] as well as HHG [107, 19].

Introduction to high harmonic generation assisted by plasmonic enhancement

HHG is a highly nonlinear process that scales non-perturbatively with the intensity of the drive laser. Intensities required to trigger HHG in solids lie in the range $10^{11} - 10^{14}\,\mathrm{W/cm^2}$, which are not directly acessible when focusing the output of a femtosecond oscillator. Chirped pulse amplification allows to boost nanojoule oscillator pulses to μJ and mJ-energies yielding peak intensities that exceed $10^{14}\,\mathrm{W/cm^2}$ when focused.

HHG in gases assisted by plasmonic enhancement

Plasmonic nanostructures were successfully used to enhance a laser electric field locally (sec. 3.1). The group of Kim investigated the possibility to reach the high intensities required for HHG in gases by enhancing modest drive laser intensities of $10^{11}\,\mathrm{W/cm^2}$ locally in plasmonic nanostructures [108]. In their experiment, they focused pulses of a Ti:sapphire oscillator at 800 nm wavelength onto plasmonic nanostructures that were purged with a noble gas. They used a tapered waveguide structure produced on a cantilever (Fig. 3.4(a)) and bow tie nanoantennas on a sapphire substrate (Fig. 3.4(b)) and purged them with xenon and argon gas, respectively [108, 109]. Both nanostructures enhance the fundamental intensity by several orders of magnitude. The group of Kim observed the emission of UV photons that were enhanced with respect to the case without nanostructures. In these two experiments they measured up to H43 and H17, respectively. The spectrum measured by [108] is shown in Fig. 3.5.

However, this report of plasmonically enhanced gas-HHG is challenged by Sivis et al. [18]. They performed an experiment similar to the one of Kim's group [109]. Bow ties

(a) **Tapered waveguide.**   (b) **Bow tie.**
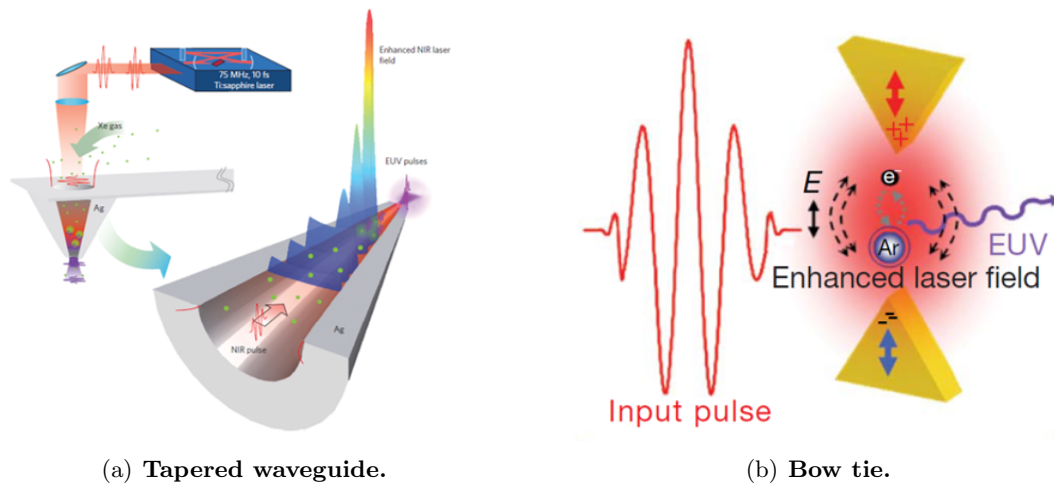
Figure 3.4.: An infrared laser beam is enhanced locally in nanostructures that are purged with noble gas which is the nonlinear medium for HHG (pictures taken from [108, 109]).
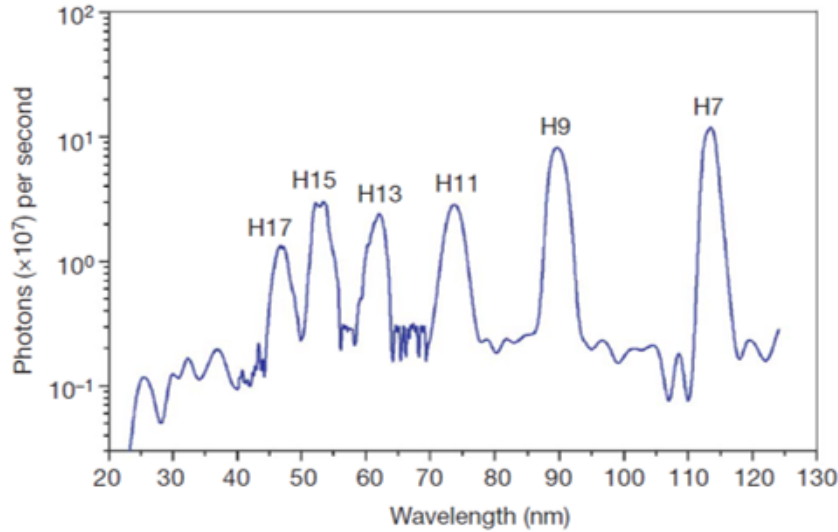
Figure 3.5.: Spectrum measured by [108]. While the group of Kim interpretes this as enhanced harmonic emission, Sivis et al. argue that it is enhanced atomic line emission.

on a sapphire substrate were exposed to an 800 nm beam at $1.5 \cdot 10^{11} \mathrm{W/cm}^2$ and they observed enhanced UV emission. In opposition to Kim, Sivis et al. argue that the emitted radiation is enhanced incoherent atomic line emission of the gas atoms. While the intensities necessary for HHG are reached, the interaction volume is far too small. In the case of a bow tie, the field enhancement occurs close to the tip of the antennas. So the field enhancement occurs only in nanoscopic volumes and only few gas atoms can experience it. The small volume should prohibit an efficient conversion from the pump beam to the harmonic radiation. Furthermore, as was shown by Shaaran et al., a steep gradient of the plasmonic enhancement, as it occurs close to the tip of bow tie antennas, might prohibit HHG [52]. The electron accelerated in the electric field might not recombine with its parent ion. Sivis et al. identify the emitted wavelengths as the atomic line emission of the noble gas atoms. A possibility to determine whether the enhanced UV emission is harmonic radiation or atomic line emission would be to slightly shift the laser wavelength. This would lead to a shift in the harmonic spectrum which corresponds to multiples of the drive frequency. However, the atomic line emission does not depend on the drive frequency, but on the energy level of the respective atoms. Another possibility would be to measure the coherence of the UV radiation. In contrast to harmonic radiation atomic line emission is incoherent.

HHG in solids assisted by plasmonic enhancement

The first report about HHG in solids assisted by plasmonic field enhancement is from 2016 [107]. The group of Kim generated up to H13 of an 800 nm driving laser in sapphire-metal nanostructures. The structures are truncated sapphire-cones with a
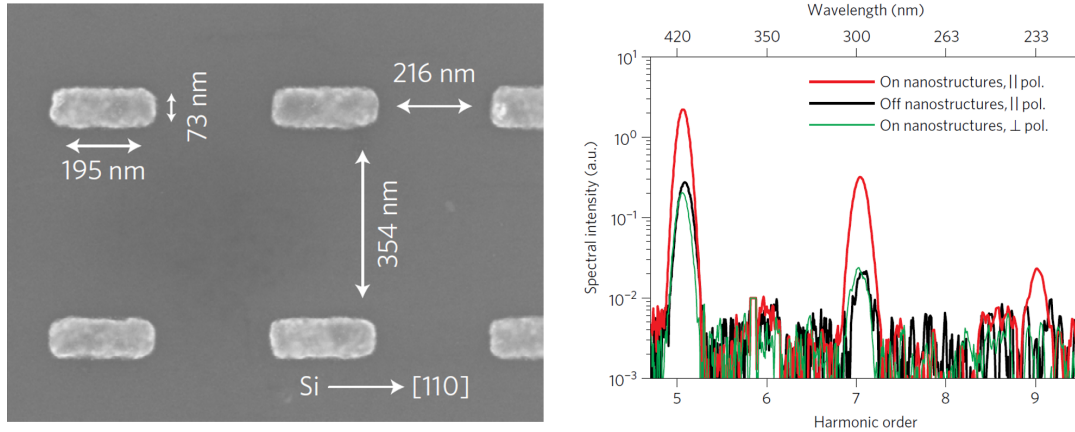
Figure 3.6.: SEM-image of gold nanoantenna on a silicon crystal (left picture) and emitted harmonic spectrum (right picture), taken from [110]. H5, H7 and H9 are enhanced with respect to the bare crystal (black curve) when using gold nanoantenna with a polarization along the antenna axis (red curve). For a polarization perpendicular to the antenna axis the enhancement is switched off and the harmonic yield (green curve) drops to the level of the harmonics from the bare crystal.

gold layer on top [107]. In opposition to gases, the harmonic radiation from solids can be spectrally distinguished from the incoherent luminescence. While in gases many different emission lines are observed which correspond to electronic transitions between different atomic shells and orbitals, solids mainly emit excitonic luminescence, e.g. from defect states or from the band edge. In 2017, the group of Paul Corkum reported on the enhancement of harmonics up to H9 from a $2.1\,\mu$m beam [110]. Harmonics are generated in a silicon crystal, where the field enhancement occurs in nanoantennas on top of the crystal. A SEM-image of the nanostructures of the sample and a spectrum are shown in Fig. 3.6. So while in gases enhancement of harmonics assisted by plasmonic enhancement was not unambiguously shown yet, plasmonically enhanced solid HHG was demonstrated.

3.2. HHG in ZnO assisted by plasmonic enhancement in nanocavity gratings

The goal of this experiment, performed at PULSE Institute at Stanford University in the group of Prof. David Reis in September 2015, was to generate high harmonics of a $2.0\,\mu$m beam in a ZnO crystal and to investigate harmonic enhancement by exploiting the local enhancement of the pump beam in plasmonic nanocavity gratings at the crystal surface. We will describe the limitations of this first proposed nanostructure design.

Laser system and experimental setup

The pump beam for harmonic generation is the idler from a Ti:sapphire seeded (50 fs pulse duration, 1 kHz repetition rate, and 2.8 mJ energy per pulse) COHERENT-OPA with a wavelength of $2.0\,\mu$m, a maximum pulse energy of $150\,\mu$J and a pulse duration of 70 fs. The experimental setup is shown in Fig. 3.7. The beam is focused with a $90°$-off-axis parabola to a spot size of approximately $100\,\mu$m at FWHM, which yields an intensity of $0.1\,\mathrm{TW/cm^2}$. The pulses are focused to the output surface of the ZnO crystal to the nanostructured sample side (normal incidence) and the harmonics are emitted in transmission. They are collimated by a second off-axis parabola and focused into an imaging spectrometer for detection by a third off-axis parabola. The pulse energy can be varied by using a half-wave plate and a polarizer. In this experiment an energy of $1\,\mu$J is used. An additional half-wave plate allows for the change of the laser polarization.
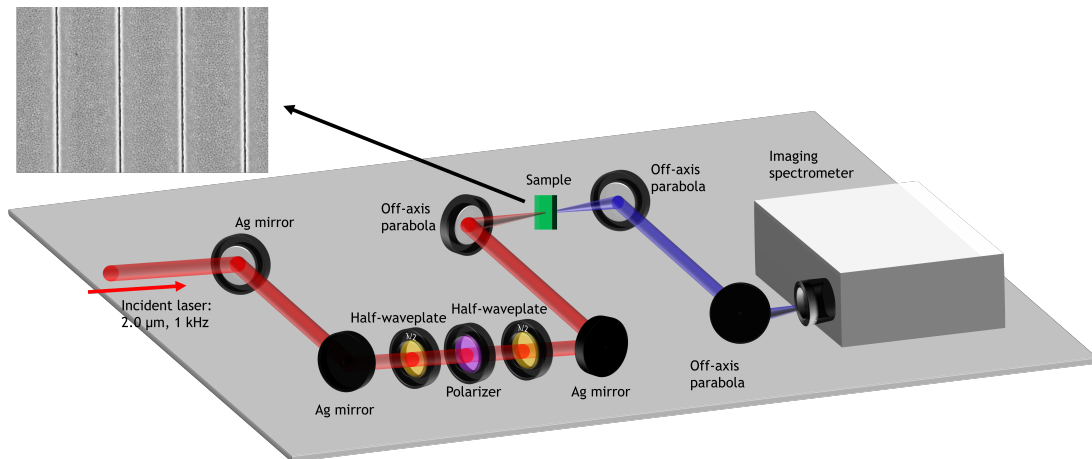
Figure 3.7.: Experimental setup: The pump beam is focused into the sample (normal incidence, shown in green) with the plasmonic grating at its output surface. The harmonics are measured in transmission with an imaging spectrometer. An SEM-image of the sample surface is shown as an inset.

FDTD simulations and sample properties

The sample is a $500\,\mu$m thick ZnO [0001] crystal with a gold grating at one surface. The periodicity of the grating is $1.5\,\mu$m and the groove width is 100 nm. For the fabrication of the nanostructures a 5 nm thick chromium layer is deposited on the crystal surface via sublimation and a 170 nm thick gold film via atomic vapor deposition on top of the chromium layer. The grating structure is etched into the metallic layer using focused ion beam milling (FIB, see app. A). A SEM-image of the plasmonic grating is shown as an inset in Fig. 3.7. Fig. 3.8(a) - 3.8(d) show the intensity enhancement calculated via FDTD simulations with Lumerical solutions for a $2.0\,\mu$m beam in a gold grating with the indicated parameters. The white lines indicate the boundaries of the grating. For TM-polarization, the laser intensity is enhanced by a factor of 2.7 in the crystal below the grating and a part of the incident wave is transmitted (Fig. 3.8(a)). The highest enhancement in the crystal does not occur below the grooves but
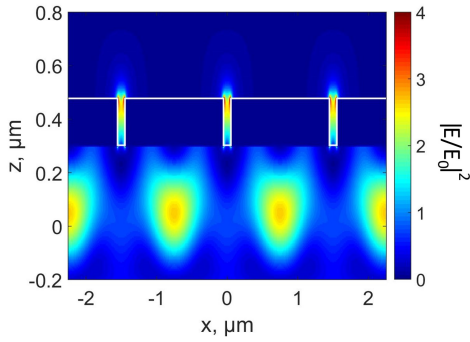
(a) **Intensity enhancement in grating and crystal for TM-polarization (polarization perpendicular to the groove direction).**
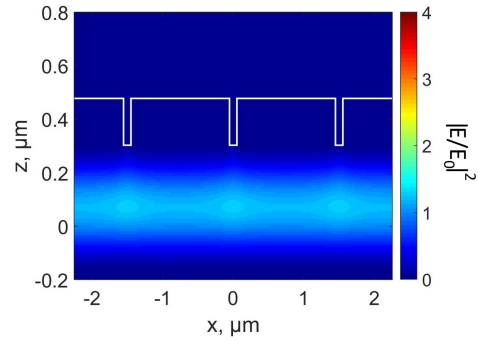
(b) **Intensity enhancement in grating and crystal for TE-polarization (polarization parallel to the groove direction).**
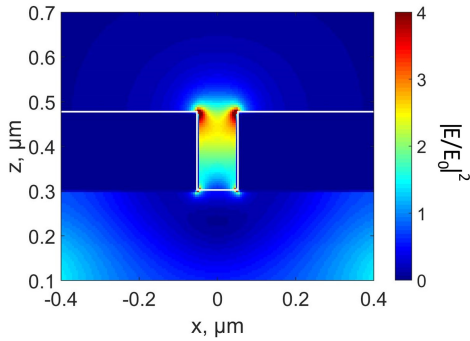
(c) **Intensity enhancement in grating and crystal for TM-polarization, zoom on one groove.**
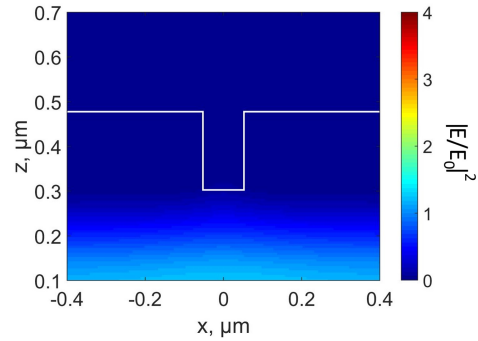
(d) **Intensity enhancement in grating and crystal for TE-polarization, zoom on one groove.**

Figure 3.8.: Simulated intensity enhancement of a $2.0\,\mu$m beam in the plasmonic grating.

between two grooves. For TE-polarization, the enhancement in the crystal is 1.3 (Fig. 3.8(c)). At this polarization, the incident wave rather sees the grating as a flat surface and is mostly reflected while for TM-polariation extraordinary optical transmission occurs [111, 112]. Fig. 3.8(c) and 3.8(d) are a zoom on one single groove for both polarizations.

Measurements

We carry out measurements of the harmonic radiation from both the bare ZnO crystal and from the nanostructures. From the bare crystal we observe H3, H5, H7 and H9. From the nanostructures, however, only H3 and H5 are detected and they are significantly weaker than from the bare crystal. This strong attenuation is due to the 175 nm thick metallic layer that the third harmonic has to pass through when it exits the crystal $(T(170\,\mathrm{nm\,Au}) \cdot T(5\,\mathrm{nm\,Cr})|_{675\mathrm{nm}} = 6.3 \cdot 10^{-6})$. For analyzing whether some small enhancement occurs despite the strong subsequent attenuation we measure the polarization-dependent yield of H3. The result is shown in Fig. 3.9(a). The third harmonic intensity from the bare crystal (red curve) varies weakly with the polarization (by a factor of 1.4), there are 2 maxima at 52° and 142°. Since the third harmonic from the bare crystal is supposed to have constant intensity for all polarizations (The infrared beam should not experience any birefringence effects when propagating along the [0001] axis. If there was any dependence of the harmonic yield on the crystal symmetry, it is expected to be sixfold in the [0001] cut.), this polarization dependence is attributed to the polarization dependence of the spectrometer. The third harmonic from the plasmonic grating (blue curve) depends strongly on the polarization, the maxima are by a factor of ≈ 40 stronger than the minima. So there is a strong interaction between the radiation and the gold grating. The polarization-dependence of the
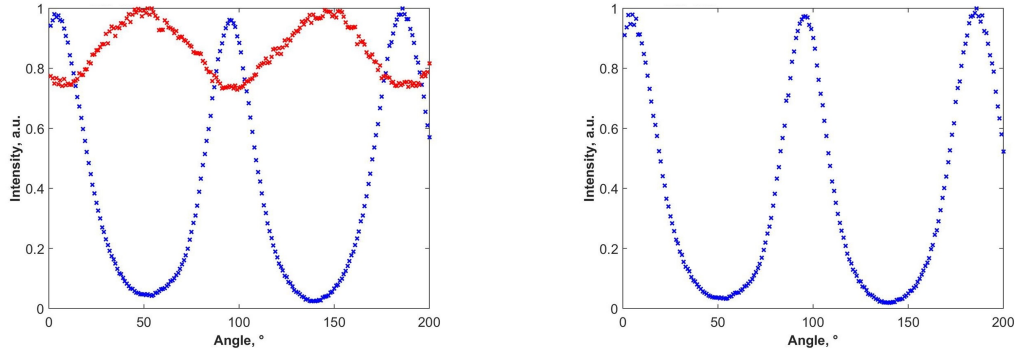
(a) **Third harmonic from crystal with grating (blue) and third harmonic from bare crystal (red). Both curves are normalized to 1. The maxima (minima) of the blue curve correspond TM- (TE-) polarization.**

(b) **Third harmonic from crystal with grating normalized to the spectrometer response.**

Figure 3.9.: Polarization-dependent third harmonic intensity

plasmonic grating normalized to the spectromter response is obtained by dividing the curve obtained after the grating (blue curve in Fig. 3.9(a)) by the curve obtained after the bare crystal (which displays the spectrometer response, red curve in Fig. 3.9(a)). The result is shown in Fig. 3.9(b). H3 changes by a factor of ≈ 50 with polarization. We take two aspects into account in order to understand the polarization-dependence of the third harmonic.

- The generation of the third harmonic in ZnO depends on the enhancement of the fundamental beam in the plasmonic grating which in turn depends on the laser polarization.

- The transmission of the third harmonic through the grating and its outcoupling efficiency into air depends on the laser polarization.

The polarization-dependent third harmonic intensity is expected to scale as $\propto \cos(\alpha)^6$ with α being the angle of the polarization relative to the grating structure (see inset in Fig. 3.10). The exponent of the cosine can be understood as follows: In third harmonic generation, the generated third harmonic field depends on the cube of the driving field $\propto \cos(\alpha)^3$. This yields an exponent of 6 when considering intensity instead of electric field $\propto \cos(\alpha)^6$. We simulated (Lumerical solutions) the transmission of a monochromatic wave at the third harmonic wavelength (670 nm) through the grating in dependence on the polarization. The result is shown by the blue curve in Fig. 3.10. For TM-polarization the transmission is maximum, for TE-polarization it reaches a minimum. This behaviour can be explained when considering that the grating acts as
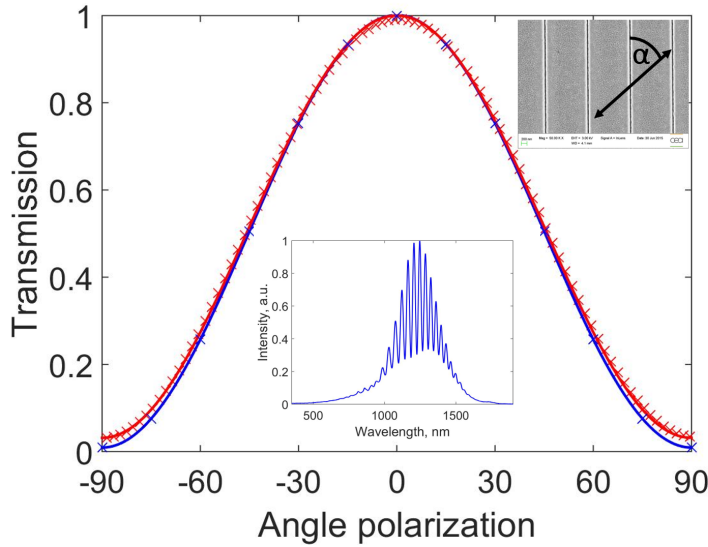
Figure 3.10.: Polarization-dependent transmission through the plasmonic grating. The blue curve corresponds to the transmission at 670 nm (wavelength of H3) calculated with FDTD calculations and the red curve to the transmission of a diode (630 nm wavelength). The third harmonic spectrum is shown as an inset.

a wire-grid polarizer [113]. A polarization parallel to the grooves generates an alternating current along each groove which radiates waves in all directions. The emitted waves have an opposite phase with respect to the incident wave, hence incident and emitted waves add up destructively behind the grating, so there is no transmission. If the polarization is perpendicular to the grooves, the electrons cannot move with the electric field vector, so no alternating current is induced which means that the wave can be transmitted through the grating [113]. The transmission follows a $\cos(\alpha)^2$-behaviour as expected for a wire-grid polarizer. The $\cos(\alpha)^2$-behaviour is confirmed when measuring the polarization-dependent transmission of a diode at 632 nm wavelength (red curve in Fig. 3.10). The ratio of TM- to TE-transmission is 30 for the measurement and 110 for the calculation. When taking into account both the polarization-dependent enhancement of the fundamental beam and the polarization-dependent transmission of the third harmonic through the grating, we expect that the polarization-dependent yield of H3 scales as $\propto \cos(\alpha)^6 \cdot \cos(\alpha)^2 = \cos(\alpha)^8$. A $\cos(\alpha)^8$-fit (red curve) to the measured polarization-dependent third harmonic yield (blue curve) is shown in Fig. 3.11(a). There is a remarkable difference in shape between the measured curve and the $\cos(\alpha)^8$-fit, which leads to the conclusion that the polarization-dependent third harmonic yield cannot be understood by only taking into account plasmonic enhancement of the fundamental and the polarizing effect of the grating on H3. We note that the $\cos(\alpha)^2$-behaviour for the polarization-dependent transmission of a wire grid polarizer is only valid for far-field illumination. Near-field illumination by H3 generated in the vicinity of the grating can have very different polarization-dependent transmission behaviour than far-field illumination. We perform nonlinear FDTD simulations and model third harmonic generation in dependence on the polarization of the pump beam. Such simulations calculate the third harmonics in dependence on the polarization-dependent intensity enhancement of the fundamental beam. When taking into account only the nonlinearity of ZnO and not the nonlinearity of gold we obtain
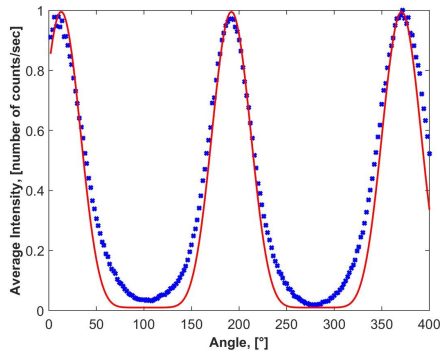
(a) **Fit of a** $cos(\alpha)^8$ **curve (red) to the measured polarization-dependent third harmonic yield (blue).**
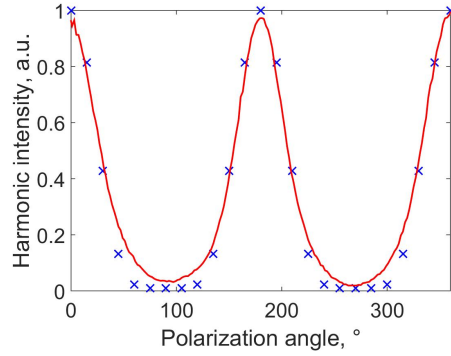
(b) **Simulated third harmonic yield (blue crosses) by taking into account only the nonlinearity of ZnO and measured third harmonic yield (red curve).**

Figure 3.11.: Measured and simulated third harmonic yield.

the blue curve (crosses) shown in Fig. 3.11(b). The shape of this curve is close to the measured curve (red). It does not follow the $\cos(\alpha)^8$-behaviour and is close to the shape of the measured third harmonic (red curve in Fig. 3.11(b)).

In our analysis, we did not take into consideration effects such as the fact that the cross-section of the grooves is slightly conical and that the grooves are slightly smaller at the chromium-ZnO interface than at the gold-air-interface. The impact of conical grooves on enhancement and transmission has not been studied.

Discussion

The goal of this experimental campaign was to enhance high harmonics by exploiting the local enhancement of the infrared pump beam in nanostructures. The harmonic enhancement could not be observed since H3 and H5 from the nanostructures are by two orders of magnitude weaker than the H3 and H5 from the bare crystal. However, when taking into account that the harmonic signal is only emitted through the 'gold-free' parts of the grating, we find that only $100/1500 = 6 - 7\%$ of the harmonic signal are transmitted. Furthermore, in the simulations of the intensity enhancement we saw that the main part of the enhancement occurs below the gold surface between the grooves. So the strongest parts of the third harmonic are absorbed by the gold, while only the weaker parts are transmitted. We conclude that the third harmonic is indeed enhanced, however, it is strongly attenuated due to the thick gold layer and the small groove openings. This strong attenuation is due to the 175 nm thick metallic layer that the third harmonic has to pass through when it exits the crystal. Future nanostructure geometries should use a thinner gold layer and an optimized geometry. H7 and H9 were only detected from the bare crystal and not from the nanostructures. Besides the enhancement properties of the fundamental beam, the outcoupling properties of the nanostructures have to be optimized down to short wavelengths.

3.3. HHG in ZnO assisted by plasmonic enhancement in nanoholes

In this section, we study the plasmonic enhancement of harmonic generation from gold nanoholes on a ZnO crystal. We were limited to the measurement of H3 (which is an above-bandgap harmonic) due to our detection systems. The experiment was conducted in September 2016 at Hanover University in the group of Prof. Milutin Kovacev.

Laser system and experimental setup

We use a Ti:sapphire femtosecond oscillator that delivers pulses with 8 fs pulse duration centered at 820 nm, with a repetition rate of 100 MHz, and an energy of 0.8 nJ per pulse. A double mirror optical system is used to enlarged the beam which is then focused using an off-axis parabola of 100 mm focal length. We work at normal incidence. The focal spot has a diameter of $7\,\mu$m (FWHM). At the focus, the laser intensity did not exceed $0.25\,$TW/cm^2. In transmission, the THG signal is monochromatized and focused by a toroidal grating on a photon multiplier (PMT) capable of single photon counting (Hamamatsu H8259-09), used in combination with a photon counter (Scientific Research SR400) and an exit slit. A schematic of the experimental setup is shown in Fig. 3.12.
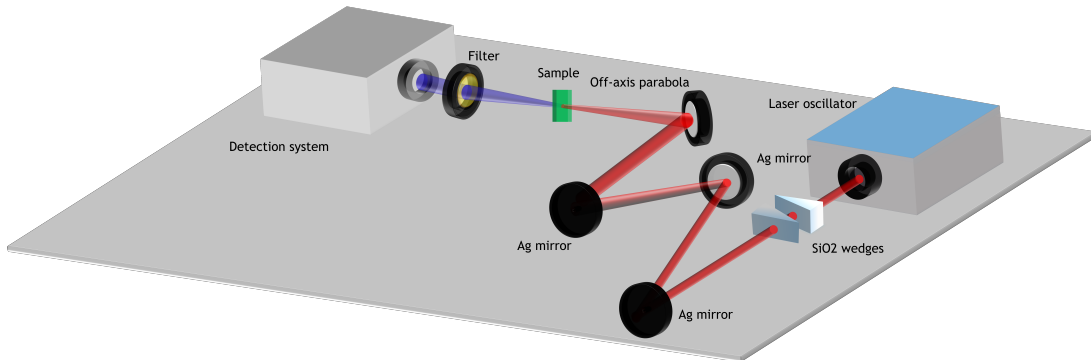
Figure 3.12.: Experimental setup. The laser is focused into the sample and the third harmonic is measured in transmission.

FDTD simulations and sample properties

We investigate a bilayer structure composed of a thin ZnO crystal and a gold layer with a 2D array of nanoholes. Nanoholes were fabricated by patterning a 40 nm Au film deposited on a $500\,\mu$m thick ZnO crystal using focused ion beam (FIB) milling (app. A). The parameters d (hole diameter) and p (distance between two holes) have been varied in the ranges $250 - 450\,$nm and $240 - 360\,$nm, respectively. In this configuration, we are set below the fundamental wavelength so that extraordinary transmission occurs
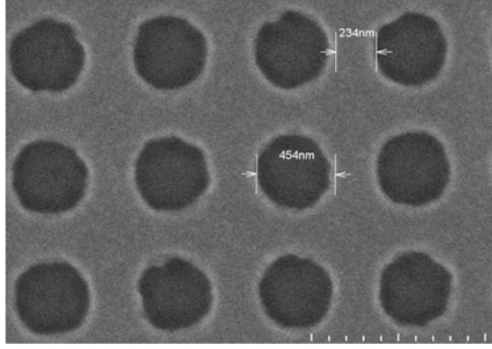
(a) **SEM-images of an array of nanoholes with d = 450 nm and p = 240 (array 1).**
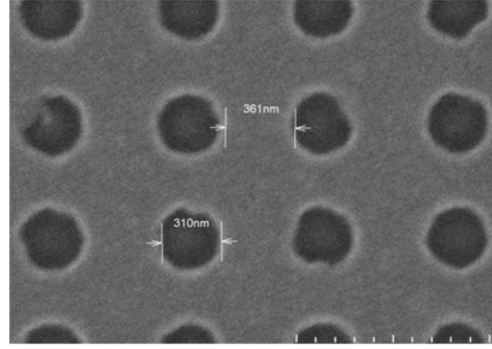
(b) **SEM-images of an array of nanoholes with d = 310 nm and p = 360 (array 2).**
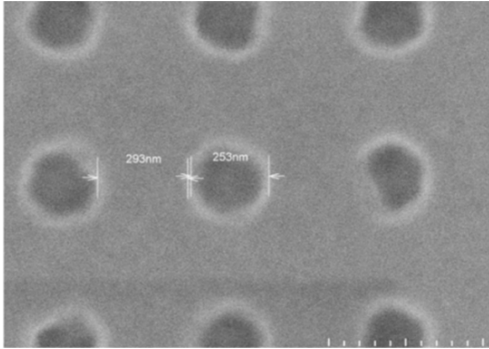
(c) **SEM-images of an array of nanoholes with d = 250 nm and p = 290 (array 3).**
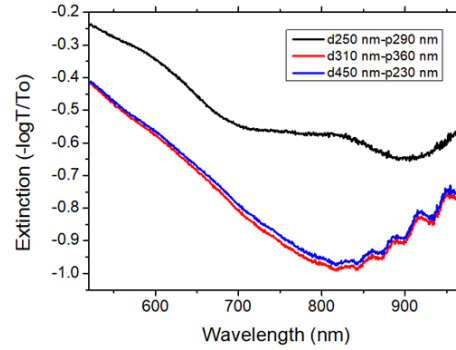
(d) **Extinction measurements of the nanoholes array structures for various hole diameters and periodicities.**

Figure 3.13.: We show SEM-images arrays of nanoholes with three different parameters and an extinction spectrum of these three arrays.

[111, 112]. Figs. 3.13(a) - 3.13(c) show scanning electron microscopy (SEM) images of various nanohole arrays used in the experiment. Array 1 with d = 450 nm has the largest transmission (around $34\,\%$), and has been used for most measurements. In Fig. 3.13(d) measurements of our structures using a transmission optical microscope coupled to a micro-spectrometer using a multimode optical fibre as confocal filtering are shown. The experimental extinction spectrum is defined as $-\log(T/T_0)$, with T being the transmission through the nanostructures and T_0 the transmission outside the nanostructures. In Fig. 3.13(d), the measured negative values are a clear indication of extraordinary transmission. All structures show a large resonance between 700 and 900 nm matching well our laser wavelength of 820 nm. FDTD-simulations show that the enhancement in the nanohole array has a low polarization dependence. The enhancement of the electric field is maximum for full TE- or TM-polarizations (Fig. 3.14(a)) and decreases by only $3\,\%$ at $45°$ (minimum enhancement). Additionally, due to the strong symmetry of the nanoholes, the shape of the electric field distribution inside the crystal is almost identical for all angles Fig. 3.14(b)). In Fig. 3.14(a) we show

(a) **Simulation of field enhancement for array 1 at 820 nm wavelength 5 nm below the surface.**

(b) **FDTD simulations of the electric field enhancement versus polarization angle.**

(c) **Intensity enhancement at 70 nm below the surface at 820 nm wavelength.**
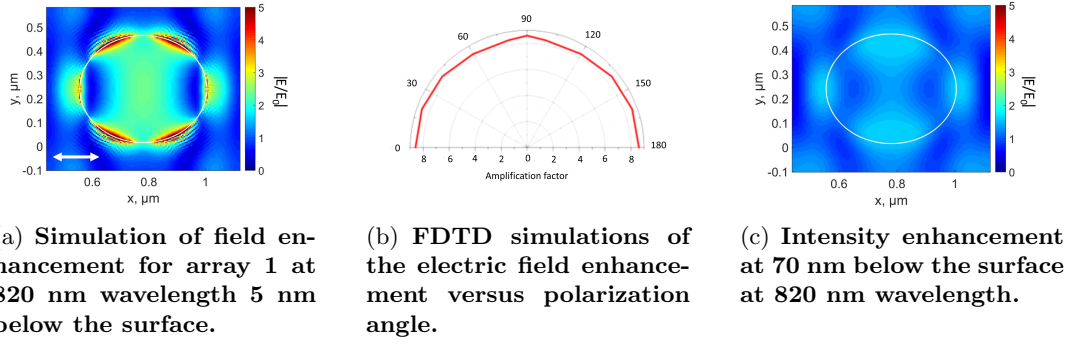
Figure 3.14.: FDTD simulations of the field enhancement for array 1.

FDTD simulations of the xy electric field distribution calculated at a wavelength of 820 nm 5 nm below the ZnO crystal surface in the case of array 1. We can see 4 localized areas with a maximum electric field enhancement factor up to 5 (25 in intensity) and a large enhancement area in the center of the crystal of up to 3 (9 in intensity). The smooth gradient with a reasonable enhancement factor provides a good condition for HHG [52]. Fig. 3.14(c) shows the case when we monitor the electric field 70 nm below the crystal surface. The large enhancement in the center disappears and only a corona enhances the electric field by a factor around 2.5 (6.25 in intensity). Since the laser spectrum extends to even longer wavelengths, we investigated the enhancement at a wavelength of 900 nm. We observe that the enhancement still occurs with about the same values as at a wavelength of 820 nm but with a different spatial distribution.

Measurements

We measure H3 from the bare crystal and from the nanoholes for different intensities. The result is shown In Fig. 3.15(a). The third harmonic signal increases with the laser intensity for both the bare crystal (blue curve) and the nanoholes array (red curve) but with a much steeper gradient in the latter case. The third harmonic signal from the nanoholes is normalized to the open space of the nanoholes which is $34\,\%$. The enhancement factor (black curve) has also an exponential growth and tends to saturate around a value of 12 at intensities above $10^{11}\mathrm{W/cm^2}$.

We have then explored the sustainability of the nanoholes. The third harmonic signal decreases exponentially over time but with a reasonable time span of 40 minutes as shown in Fig. 3.15(a). The damages in the nanoholes are discussed in more detail in sec. 3.6.2.
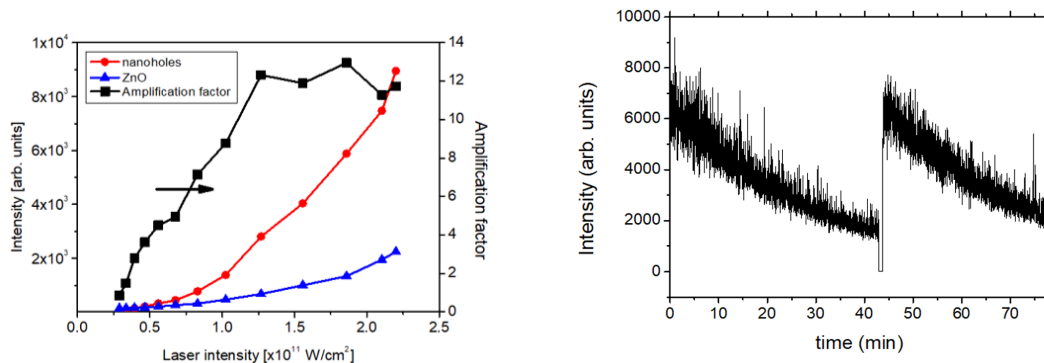
(a) **Third harmonic signal as a function of the driving laser intensity for array 1 (red), the bare crystal (blue) and the amplification factor (black).**

(b) **The third harmonic signal decreases with irradiation time.**

Figure 3.15.: Third harmonic signal measured from the bilayer structure after normalization to the hole transmission.

Discussion

We observed an increase of the third harmonic from the nanoholes by a factor of 12 compared to the bare crystal after normalization to the hole transmission. Compared to our previous experiment described in sec. 3.2, we greatly increased the outcoupling efficiency of the third harmonic. The nanoholes have a low polarization dependence and a good sustainable operating time, in the range of few 10s of minutes. We point out that the third harmonic from ZnO is an above-bandgap harmonic for our wavelength. This holds promise that even higher above-bandgap harmonics are generated and can be measured with an improved detection system.

3.4. HHG in SiO_2 assisted by plasmonic enhancement in a Fabry-Perot grating resonator

In this section, we investigate harmonic generation in a Metal-Dielectric-Metal (MDM) nanostructure. In this experiment, we were limited to the measurement of H3 due to our detection systems. H3 is a below-bandgap harmonic, however, it can be used to validate the potential of the structure to enhance above-bandgap harmonics. The experiment was made in September 2016 at Hanover University in the group of Prof. Milutin Kovacev. Details about the experimental setup can be found in sec. 3.3.

FDTD simulations and sample properties

The sample is a Fabry-Perot resonator with a gold layer on one side and a gold grating on the other side. Fig. 3.16(a) shows a schematic of this MDM-structure. We sputtered by physical vapor deposition a 10 nm Au film on top of a sapphire substrate, followed by the deposition of a 180 nm SiO_2 thin film, and the fabrication of Au gratings using electron beam lithography. Fig. 3.16(b) shows a SEM-image of the gold grating. In contrast to previous works on similar configurations, the MDM arrangement allows much higher volumes of electromagnetic field enhancement inside the nonlinear medium compared to other hybrid structures. The outcoupling efficiency of the third harmonic is increased with respect to the plasmonic grating descibed in sec. 3.2. If we consider a focal spot of 10 μm the dielectric volume influenced by the enhanced electromagnetic field is equal to $18\,\mu m^3$ in our interface compared to $2\,\mu m^3$ in the work of Shibanuma et al. [114], and few $100\,nm^3$ for nano-antennas with nanometric gap sizes [115]. Finite difference time domain (FDTD) calculations using Lumerical Solutions (app. B) have been performed to optimize the local enhancement factor of the electromagnetic field at 820 nm. In Fig. 3.16(c) we see that the maximum intensity enhancement reaches a factor of 11, localized in a relatively large volume of the dielectric thin film. However, when considering TE-polarization (Fig. 3.16(c)), we can see that the enhancement effect is almost switched off. The maximum intensity enhancement is less than 4. To validate our simulations we performed experimental extinction measurements. The experimental extinction spectrum is defined as $-\log(T/T_0)$, with T being the transmission through the nanostructures and T_0 the transmission outside of the nanostructures. Fig. 3.16(e) shows the experimental extinction spectra which presents a broad resonance around 820 nm, matching well the driving laser central wavelength.
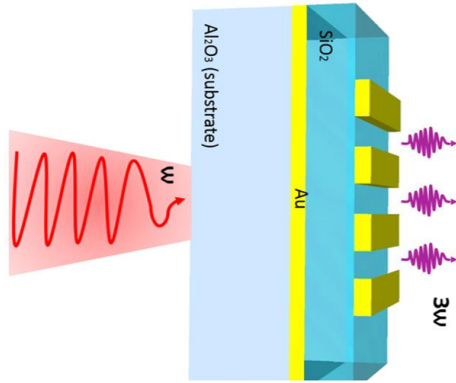
(a) **Schematic of the experimental configuration used for harmonic measurements, 180 nm SiO_2 thin film sandwiched between 20 nm high Au gratings and 10 nm Au film deposited on a Sapphire substrate.**
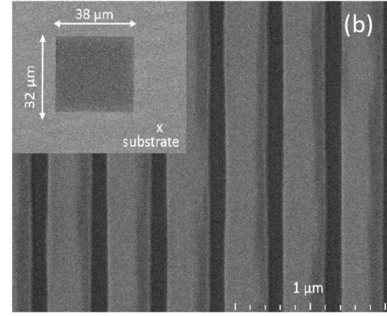
(b) **Scanning Electron Microscopy image showing the grating dimensions with 260 nm width and 130 nm gap, in the inset another SEM-image showing one full array of nano-gratings with 32 x 35 μm size.**
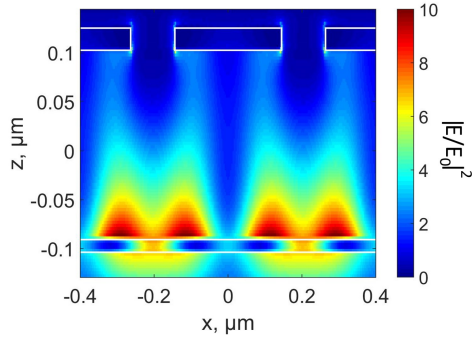
(c) **FDTD simulations of the intensity enhancement 820 nm in TM-mode.**
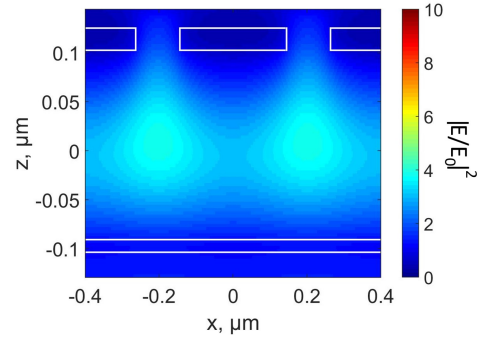
(d) **FDTD simulations of the intensity enhancement 820 nm in TE-mode.**
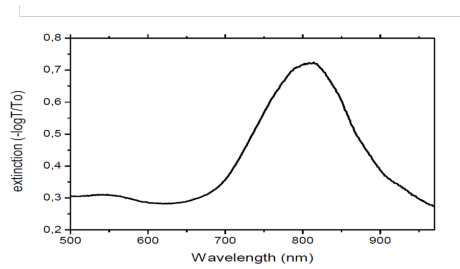
(e) **Experimental extinction spectrum $(-\log(T/T_0))$ of the nanostructure.**

Figure 3.16.: Schematic and SEM-image showing the grating dimensions with 260 nm width and 130 nm gap. We show FDTD simulations of the intensity enhancement and experimental extinction spectra of the MDM structure.

Measurements

The fundamental beam is focused into the sample (normal incidence) and the third harmonic is measured in transmission. The third harmonic signal from both the bare SiO_2 film and the MDM structure are shown in Fig. 3.17(a). The ratio of the harmonic signal from the nanostructures to the harmonics signal from the bare SiO_2-film gives the harmonic enhancement factor which reaches a factor 10. When we take into account
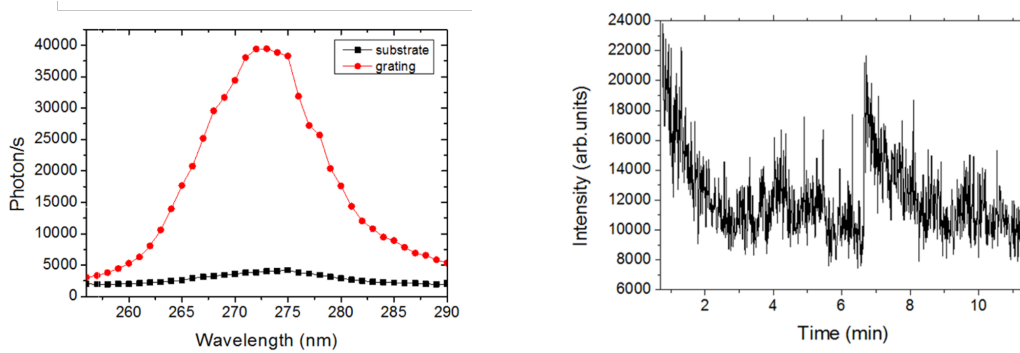
(a) **Third harmonic from the nanostructures and the bare thin film Au/SiO_2 with the fundamental in TM-polarization.**

(b) **Third harmonic as a function of irradiation time in TM-mode.**
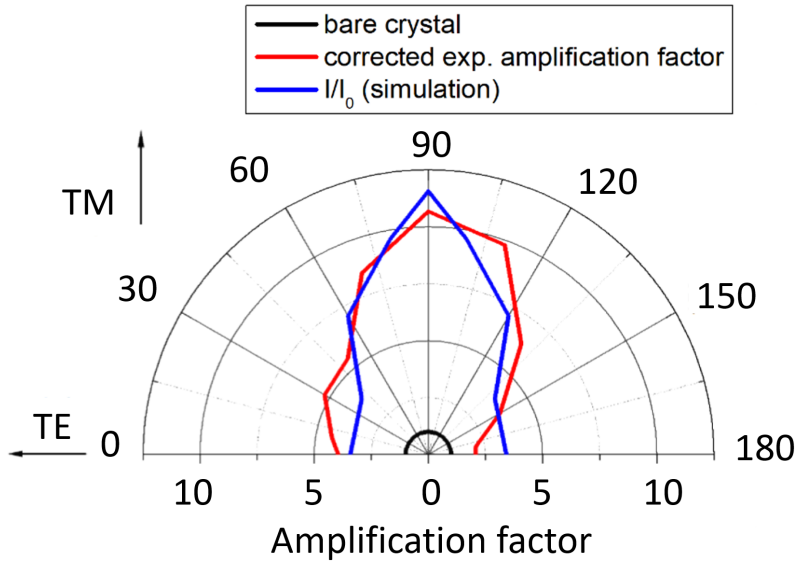
(c) **Experimental third harmonic signal as a function of fundamental polarization state from the bare crystal (black curve) and the plasmonic structure (red curve). The blue curve shows the simulated intensity enhancement as a function of the polarization angle of the laser.**

Figure 3.17.: Third harmonic signal measured from the bilayer structure.

that the gold film only transmits $18\,\%$ of the third harmonic signal and that the open space between two gold rods transmits the harmonic signal without attenuation, the enhancement factor of H3 rises to 21. We observe a fast decay of the harmonic signal during only a few minutes (Fig. 3.17(b)) indicating damage of the nanostructures, which might be due to three possible reasons.

- The plasmonic enhancement can lead to ablation of the surface of the nanogratings, i.e. the 20-nm-thick nanogrooves above the SiO_2 layer. However, the SEM-image of the sample after laser irradiation shows no visible near-field ablation and deposition of material at the surface.

- The optical breakdown of the SiO_2 layer can modify the dielectric structure. Given the ultrashort pulse duration of 8 fs, the optical breakdown of SiO_2 requires the laser peak intensity of $> 100\,\mathrm{TW/cm^2}$. However, in our experiments, from the FDTD-based numerical simulation, we estimate that the peak intensity is only enhanced by one order of magnitude, i.e. from 0.25 to $2.5\,\mathrm{TW/cm^2}$, which is well below the damage threshold of SiO_2.

- The 10-nm gold layer absorbs a part of the 800 nm pump beam which might expand and lead to thermal damage which destroys the Fabry-Perot resonator. The peak intensity inside this layer reaches $2.5\,\mathrm{TW/cm^2}$, corresponding to a fluence of $200\,\mathrm{J/m^2}$. This value already exceeds the photothermal damage threshold ($\sim 100\,\mathrm{J/m^2}$) of the gold film. The damage inside this embedded layer would explain that we cannot observe damage from the top-view SEM-image. Furthermore, heat might be transferred from the gold layer to the SiO_2.

In addition, we studied the harmonic yield in dependence on the laser polarization. The blue curve displayed on Fig. 3.17(c) shows the FDTD simulation of the electric field enhancement versus the laser polarisation angle. The plasmonic resonance from the nano-gratings highly depends on the polarization direction of the incident light and is maximum in TM-mode. The red and black curves shown in Fig. 3.17(c) show the experimental third harmonic signal from the nano-gratings and from the bare SiO_2-film versus the laser polarization angle, respectively. The harmonic signal from the bare crystal is constant for all polarization angles. The third harmonic signal emitted from the nano-gratings shows a strong enhancement for TM-polarization while almost no enhancement is observed for TE-polarization. This confirms the plasmonic origin of the harmonic enhancement.

Discussion

In conclusion, we have enhanced the third harmonic generated in a gold-SiO_2-grating resonator with respect to a bare gold-SiO_2 film. Compared to the structures reported in secs. 3.2 and 3.3, the grating-resonator has a large enhancement volume inside the optically active medium. The MDM shows a strong polarization dependence and a short lifetime of 6 minutes. This kind of nanostructures holds promise to enhance even higher harmonics. Varying the thickness of the gold- and the SiO_2-films can influence the third harmonic signal stability and the enhancement volume.

3.5. HHG in sapphire assisted by plasmonic enhancement in bow ties

In this section, we study enhancement of harmonic generation in sapphire assisted by plasmonic field enhancement in gold bow tie nanoantennas [107, 116]. Furthermore, we try to determine whether the harmonics originate mostly from the sapphire crystal or from the gold bow ties. For more details about this experiment we refer to [117]. The experiment was made in collaboration with the group of Prof. Milutin Kovacev at Hanover University. The experimental setup and the system parameters are described in detail in sec. 3.3.

Sample

The sample consists of a $400\,\mu$m thick sapphire crystal with bow tie gold nanostructures at its surface. The bow tie antennas were produced by focused ion beam milling (app. A). We use two different kind of bow tie samples. The first bow tie consists of two isolated triangles (Fig. 3.18 (a), (b)). The second kind of bow tie is called diabolo antenna and uses a thin gold connector between the two triangles (Fig. 3.18 (c), (d)) [118]. The length, thickness, apex angle, and radius of curvature of a single Au triangle nanostructure are 200 nm, 120 nm, 30°, and 20 nm respectively. The gap distance of the bow tie is 20 nm. For the diabolo antennas, the bow tie feedgap is connected by an
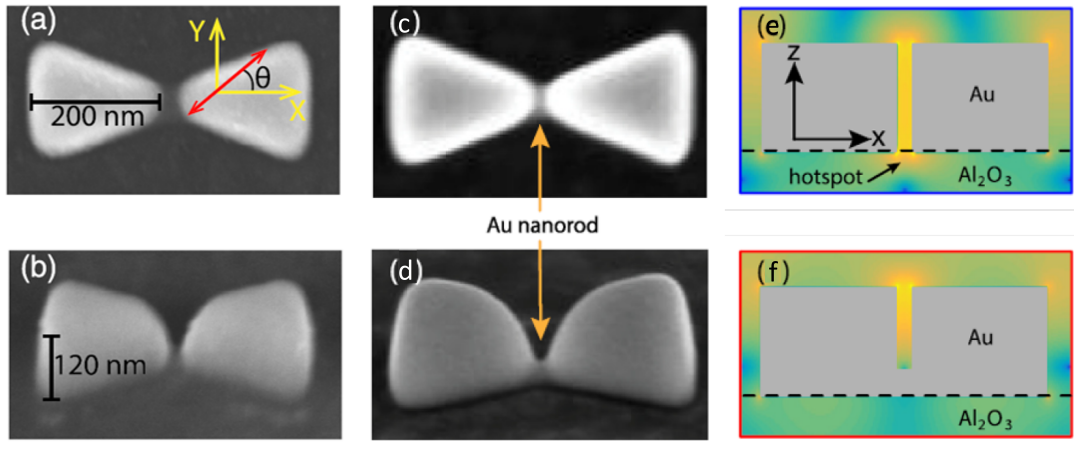
Figure 3.18.: SEM-images of a gold bow tie nanoantenna: (a) top view and (b) perspective view of a bow tie antenna. The red arrow indicates the direction of laser polarization. The crossing angle between the laser polarization and long-axis of the dimeric antennas, i.e., x-axis, is defined as θ. (c) Top and (d) perspective view SEM-images of a so-called diabolo antennas [118]. A thin gold nanorod electrically connects the facing tips. (e) and (f) show FDTD simulations made with MEEP (app. B) of the field enhancement of bow ties and diabolo antennas, respectively. It can be seen that the presence of the gold nanorod in the diabolo antennas pushes the hotspot to be far away from the sapphire crystal.

(a) Bow tie: 2 nm below air-gold surface

(b) Diabolo: 2 nm below air-nanorod surface

(c) Bow tie: 2 nm below gold-sapphire interface

(d) Doabolo: 2 nm below gold-sapphire interface
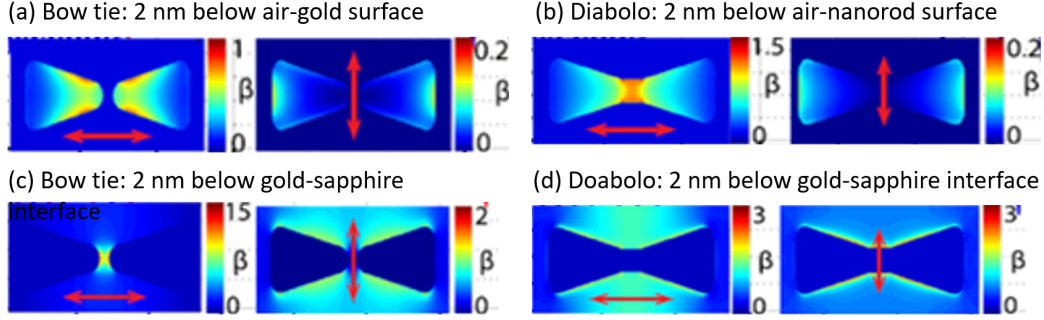
Figure 3.19.: FDTD simulations of the electric field enhancement at 800 nm for the laser polarization parallel (left) and perpendicular (right) to the long antenna axis. (a) Inside gold, 2 nm below the air-bow tie (b) Inside gold, 2 nm below the air-nanorod interface (c) Inside sapphire, 2 nm below the bow tie-sapphire interface (d) Inside sapphire, 2 nm below the bow tie-sapphire interface. Here, β denotes the electric field enhancement factor, ($|E/E_0|$).

Au nanorod with a width of 30 nm and a thickness of 35 nm. The nanostructures were arranged in square arrays of 12 μm x 12 μm, with a spacing of 500 nm in the x-direction and 20 nm nm in the y-direction. In the focus the laser illuminates approximately 250 antennas at the same time. Fig. 3.19 shows the field enhancement for the bow tie in gold 2 nm below the gold-air interface (Fig. 3.19(a)) and for the diabolo antennas in gold 2 nm below the interconnector-air-interface (Fig. 3.19(b)). For $\theta = 90°$, the field enhancement is low in both configurations. For $\theta = 0°$ the field enhancement is higher for both kind of bow ties with respect to $\theta = 90°$. It is by factor of 1.5 higher for the diabolo antennas with respect to the bow ties and is strongly concentrated in the interconnector. The gold triangle acts as a funnel which reinforces the optical current density into the interconnector [119]. Fig. 3.19 shows the field enhancement for the bow tie in sapphire 2 nm below the sapphire-air interface (Fig. 3.19(c)) and for the diabolo antennas in sapphire 2 nm below the gold-air-interface (Fig. 3.19(d)). For $\theta = 0°$, high enhancement (factor 15) occurs in the sapphire crystal when considering standard bow ties. However, for the case of the diabolo antennas, the enhancement is shifted away from the crystal such that almost no enhancement occurs in sapphire (factor 3). For $\theta = 90°$, the enhancement decreases considerably for the bow tie (factor of 2) and does almost not change for the diabolo antenna.

Measurements

We perform a z-scan measurement with bare sapphire, sapphire with bow ties and sapphire with diabolo antennas at its surface. The results are shown in Fig. 3.20. The inset of Fig. 3.20(a) illustrates the experimental approach. The laser propagates from left to right. Fig. 3.20(a) plots the measured third harmonic intensity from bare Al_2O_3 as a function of the focal position. Two maxima appear with a spatial separation of 400 μm, which corresponds to the crystal thickness. The lower harmonic emission from
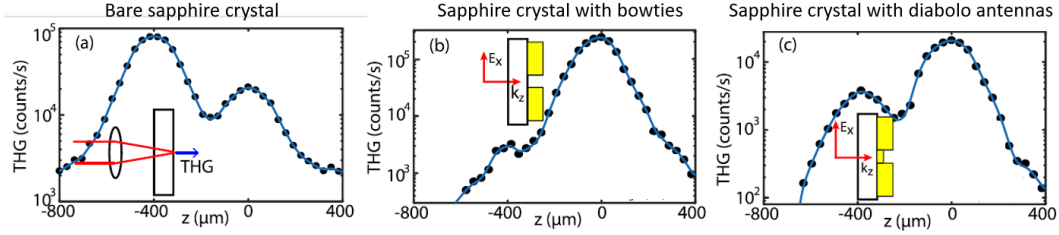
Figure 3.20.: Intensity of third harmonic emission from the three samples (bare sapphire, sapphire with bow ties and sapphire with diabolo antennas) versus the laser focus position. The inset shows the experimental setting from a side view. The laser propagates from left to right, i.e., along the z-axis. The back (left) surface corresponds to the position of -400μm. Intensity of third harmonic emission from (a) the bare sapphire crystal, (b) sapphire with bow tie antennas at the output surface and (c) sapphire with diabolo antennas at the output surface versus the laser focus position. z = 0 corresponds to the laser focus at the front surface.

the back (right) surface with respect to the front (left) one is caused by an increased pulse duration due to the propagation of the laser through the dispersive sapphire crystal (group velocity dispersion GVD $= 58\,\text{fs}^2/$mm at 800 nm [120]) which leads to lower intensity. Figure 3.20(b) shows the third harmonic intensity from a bow tie array versus focal position. The laser is polarized along the x-axis. We observe that the third harmonic emitted from the back surface which is nanostructured with bow ties is drastically enhanced with respect to the bare sapphire crystal (Fig. 3.20(a)). From the z-scan result of the diabolo array (Fig. 3.20(c)), an enhanced of the third harmonic from the back surface is also found. However, its enhancement factor with respect to the front surface is by one order of magnitude lower than that of the bow tie array. This indicates that the interconnector of the diabolo antenna might contribute to the THG enhancement, but its yield efficiency is much weaker than that of the sapphire crystal which is located at the optical hotspot of bow tie feedgap.

We measure the dependence of third harmonic generation for both bow ties on sapphire and diabolo antennas on sapphire. Figs. 3.21(a) and (c) depict the intensity of third harmonic emission (open squares) from a bow tie array and a diabolo antenna array versus θ. The third harmonic emission is normalized to the signal at minimum enhancement ($\theta = \pi/2$). As expected for a third-order process, the third harmonic intensity scales as the cube of the driver intensity (Fig. 3.21(b) and (d) for the bow tie and the diabolo antennas, respectively), $I_{3\omega} \propto I_\omega^3 \propto (E_\omega\cos(\theta))^6$. The measured third harmonic intensity can be well fitted by $\cos^6(\theta)$-function (Fig. 3.21(a) and (c), solid curve). We see that the third harmonic signal is enhanced by a factor of more than 40 for the bow ties and by a factor of less than 3 for the diabolo antennas for $\theta = 0$ with respect to $\theta = \pi/2$. These observations help us to determine the origin the enhanced third harmonic. Two different sources are imaginable:

- the nonlinear third-order susceptibility of the Al_2O_3 crystal.

- the nonlinear third-order susceptibility of the gold antennas.

69
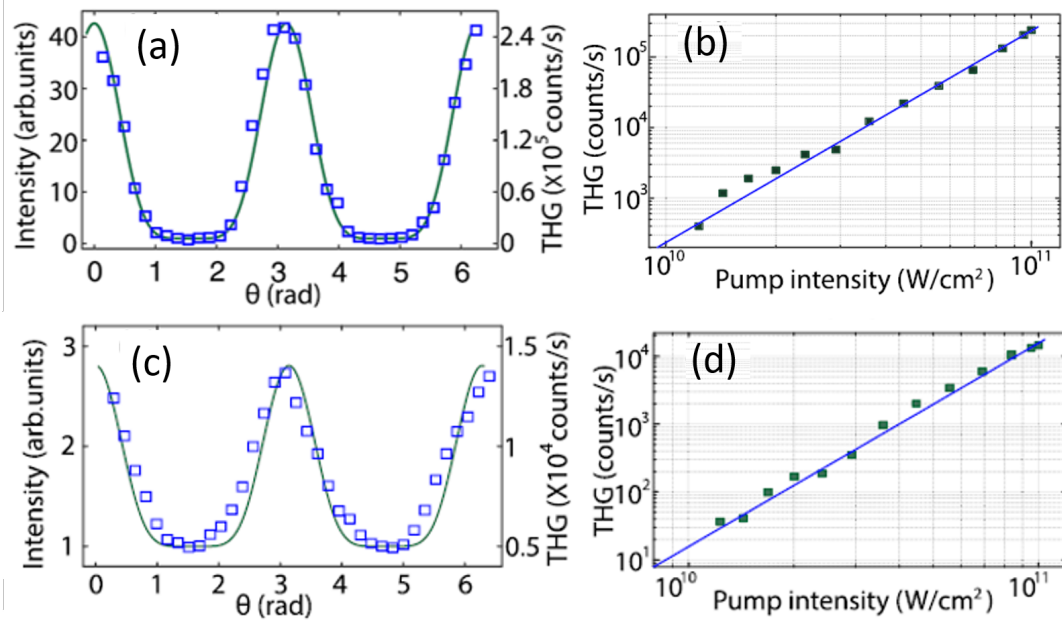
Figure 3.21.: The dependence of third harmonic generation on θ and the pump intensity from the (a), (b) bow tie antennas and (c), (d) diabolo antennas.

The third-order susceptibilities of Au and Al_2O_3 are $\chi^3(Au) \sim 10^{-19} m^2/V^2$ [121] and $\chi^3(Al_2O_3) \sim 10^{-22} m^2/V^2$ [122], respectively. So the third-order susceptibility of gold is by three orders of magnitude stronger than the third-order susceptibility of sapphire. For the diabolo sample, there is no possibility for the gap-sapphire to radiate harmonics. If the third harmonic emission from Au was dominant, by using the interconnector, we should observe an even higher third harmonic intensity counts at $\theta = 0$ than for the standard bow tie on sapphire due to the field enhancement inside Au. Otherwise, the third harmonic should be much lower and its intensity is expected to have a weaker dependence on the laser polarization, as the field inside the sapphire crystal in the gap region is always suppressed by the Au nanorod. Our measurement however clearly confirms that the THG mainly radiates from the exposed sapphire in the optical hot spot of the bow tie, namely, in the antenna gap region. For a discussion about the absence of third harmonic generation from gold we refer to [117].

Discussion

We observed that bow tie antennas enhance third harmonic generation from sapphire by one order of magnitude. We believe that even higher harmonics can be enhanced by bow ties. However, in the frame of this experiment we were limited by our detection system. We used diabolo nanoantennas to identify the origin of third harmonic emission. The sapphire crystal in the gap region of an Au antenna dominates the third harmonic enhancement. We do not observe significant harmonic enhancement from gold itself, which is ascribed to the strong absorption by Au atoms.

3.6. Radiation-induced damage of plasmonic nanostructures

In this section, we study damage and structural modifications of plasmonic nanostructures. In addition to thermal damage, the plasmonic system may also experience other damage channels, such as electron-migration, ion evaporation and surface nonthermal melting. In subsec. 3.6.1, we study the initial increase and subsequent decrease of third harmonic generation due to a self-optimization process of bow ties. Furthermore, we investigate two kinds of damage occuring to bow ties, namely thermal damage and nonlinear optical ablation. In subsec. 3.6.2, we study the morphologic changes occuring to plasmonic nanoholes during laser irradiation and the subsequent decrease of third harmonic generation.

3.6.1. Nonlinear optical ablation and thermal damage of bow ties

In this subsection, we study the damage induced by 820 nm pulses to bow tie antennas and its effect on third harmonic generation. Furthermore, we investigate the morphologic changes happening to different bow tie nanostructures with different thicknesses with and without additional dielectric coating during intense laser irradiation. We investigate the dependence of third harmonic generation in sapphire on the properties of the bow ties at its surface. For further details about this experiment we refer to [115, 123]. The experiment was made in collaboration with the group of Prof. Milutin Kovacev at Hanover University. The experimental setup and the system parameters are described in detail in sec. 3.3.

Sample

We use different kinds of bow tie samples. All of them were fabricated by focused ion beam milling (app. A) on a $400\,\mu$m thick sapphire crystal [0001]. A 3-nm chromium layer is used for better adhesion of the gold dimer antennas on sapphire. The spacing between different bow tie pairs is 500 nm in the x direction and 200 nm in the y direction. They are arranged in square arrays of $12\,\mu$m x $12\,\mu$m size. Enhancement occurs for a laser polarization parallel to the dimeric orientation. We use four different kind of gold bow-tie nanoantennas that differ with respect to thickness, coating, length and apex angle.

1. Type I: Length: 175 nm, Apex angle 30°, thickness: 135 nm, gap size: 10 nm.

2. Type II: Length: 200 nm, Apex angle 40°, thickness: 135 nm, gap size: 10 nm, 5-nm SiO_2 layer on top. A SEM-image of the bow ties is shown in Fig. 3.22(a). FDTD simuations of the field enhancement are shown in Fig. 3.22(b).

3. Type III: Length: 200 nm, Apex angle 40°, thickness: 65 nm, gap size: 10 nm, 5-nm SiO_2 layer on top.

4. Type IV: Length: 200 nm, Apex angle 40°, thickness: 135 nm, gap size: 10 nm. FDTD simuations of the field enhancement are shown in Fig. 3.22(c).
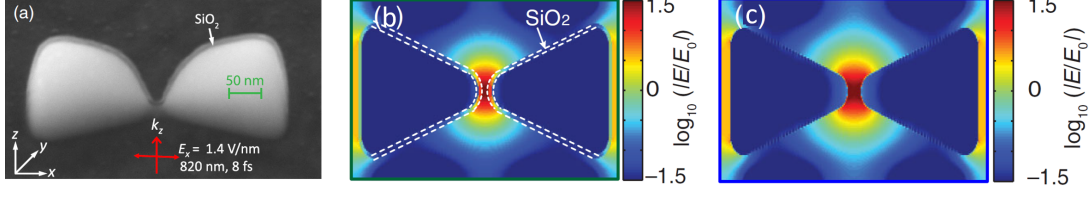
Figure 3.22.: (a) SEM-image of a gold bow tie with a height of 135 nm and 5-nm of SiO_2 on top (type II) (b) FDTD simulations of a gold bow tie with a height of 135 nm and 5-nm of SiO_2 on top (type II) (c) FDTD simulations of a gold bow tie with a height of 135 nm without additional coating (type IV).

We can see in Figs. 3.22(b), (c) that the near-field enhancement is very similar regardless of the SiO_2 coating. The field is enhanced by more than one order of magnitude close to the triangle tips and has a similar shape. The field enhancement for the type I bow tie is very similar and is not shown here.

Measurements

The laser is focused on the bow tie antenna and the third harmonic is measured in transmission. The peak intensity is enhanced from $0.25\,\mathrm{TW/cm^2}$ to $100\,\mathrm{TW/cm^2}$. The measurement is conducted in vacuum ($10^{-3}\,\mathrm{mbar}$). We study the harmonic signal over time in order to probe the modification of the nanostructures (Fig. 3.23(a)) [124]. We observe that under continuous irradiation the harmonic signal decreases within 6 min. When moving to a fresh spot on the sample, the third harmonic increases to its initial maximum, followed by a rapid decrase. In order to get more information about the time span before the decrease of the harmonic signal starts, we expand the time axis (a zoom into the red and green squares in Fig. 3.23(a) are shown in in Figs. 3.23(b) and 3.23(c), respectively.). We see that the third harmonic signal increases during the first 15 s on a new position before the degradation process starts. This observation suggests that some structural modification of the bow ties occurs which first leads to a rapid increase of third harmonic generation followed by a much slower decrease. We
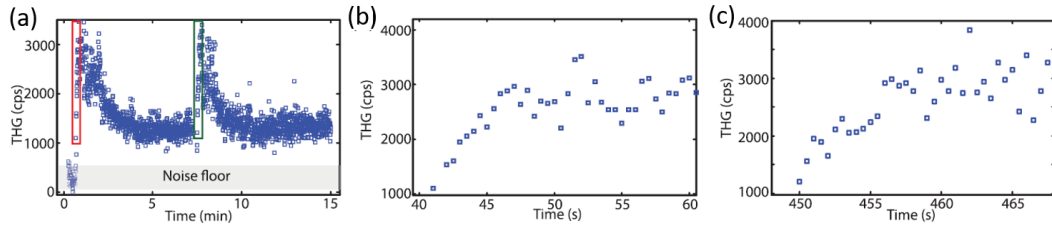
Figure 3.23.: (a) Temporal evolution of third harmonic generation from two pristine nanostructure arrays in vacuum. The squares enclosed in red and green are enlarged in (b) and (c), respectively.

72
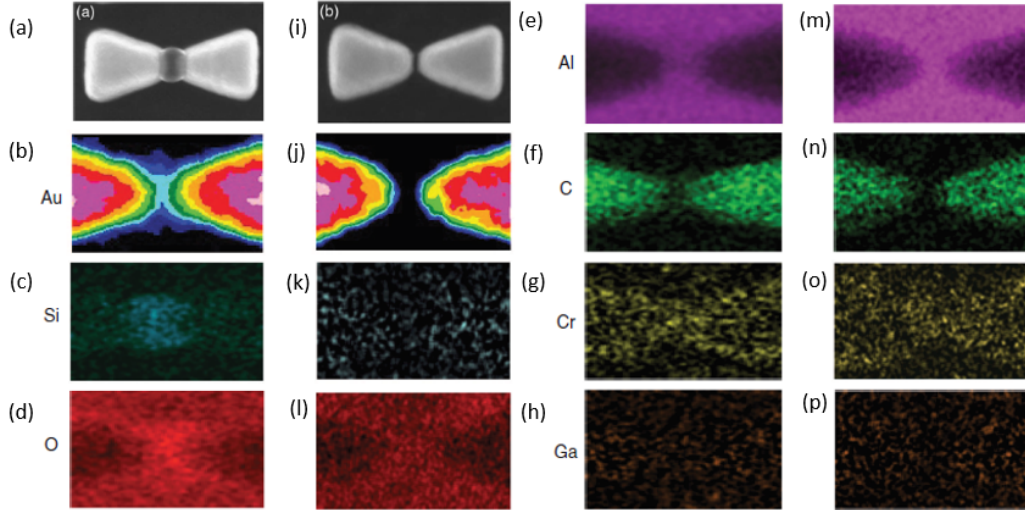
Figure 3.24.: SEM-images of a (a) laser-ablated and (b) pristine gold bowtie antenna. Two-dimensional EDX maps of (c)–(i) laser-ablated antennas and (j)–(p) pristine antennas. The corresponding elements of the rows are Au, Si, O, Al, C, Cr, and Ga, respectively.

compare the SEM-image of a fresh antenna pair (Fig. 3.24(i)) to an irradiated one (Fig. 3.24(a)) and find a strong modification of the feed gap. This finding suggests that structural modification is closely related to the near-field enhancement.

For better understanding the process of reshaping, we analyze the chemical composition of the ablated material. Therefore, we perform a two-dimensional high-resolution energy-dispersive X-ray spectroscopy (EDX) measurement in the gap of the irradiated antennas (Figs. 3.24(b)-3.24(h)), which is then compared to pristine antenna structures (Figs. 3.24(j)–3.24(p)). Analyzing the bow tie nanoantenna in the gap region after irradiation shows that the deposit includes gold (Au, Fig. 33.24(b)), a large amount of silicon (Si, Fig. 3.24(c)), some oxygen (O, Fig. 3.24(d)) and carbon (C, Fig. 3.24(f)). The presence of gold atoms in the gap region substantiates our theory of localized ablation at the antenna tips. The origin of the other materials is discussed in [115]. We performed a similar measurement of third harmonic generation using a pristine pair of bow ties and by purging the setup with nitrogen at atmospheric pressure. The third harmonic signal is found to strongly increase over time up to 10 min (Figs. 3.25(a) and 3.25(b)). This is different in vacuum, where we oberved an increase of the signal over a time span of only 15 sec (Figs. 3.23(b) and (c)). In atmospheric nitrogen, the THG signal reaches its maximum peaks after 25 min illumination time (Fig. 3.25(b)). It is followed by a decrease during 125 min until it saturates. The value at saturation is still by 50 % higher than the initial signal at the beginning of illumination before the reshaping sets in. We link the gradual reduction of harmonic generation to the ablation of the tips of the bow tie. The attenuation rate of third harmonic generation in nitrogen (Fig. 3.25(b)) is about 20 times slower than in vacuum (Fig. 3.23(a)). This indicates that the presence of nitrogen inhibits the removal
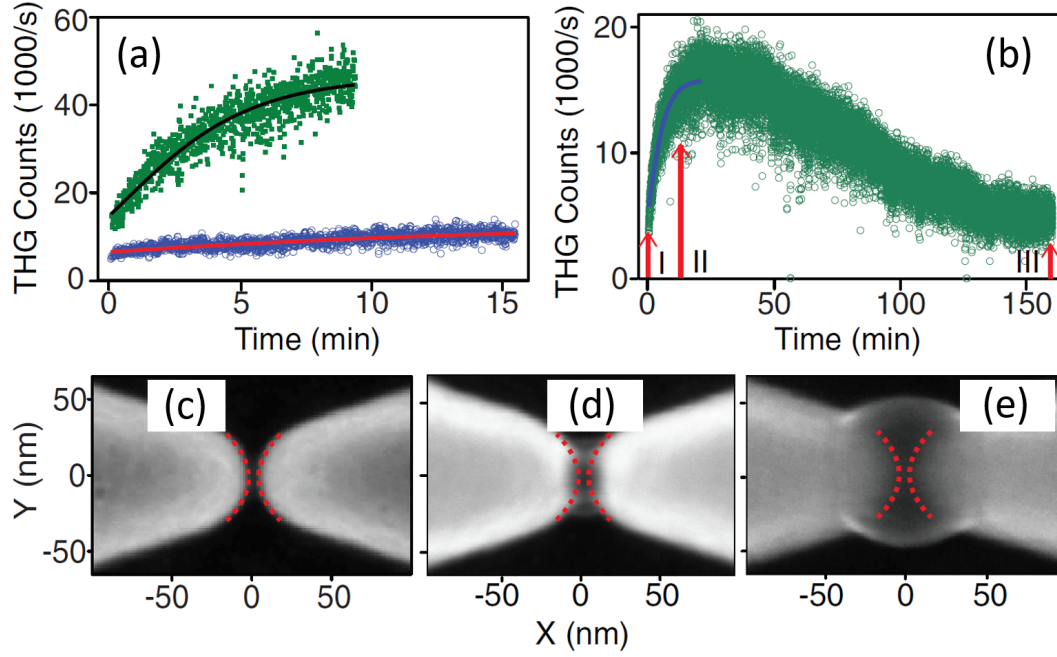
Figure 3.25.: (a) Evolution of third harmonic generation with laser pulse duration of 8 fs (green curve) and 16 fs (blue curve). (b) Third harmonic emission from a pristine array during long-term exposure. It reaches its maximum after 25 min. SEM-image of the tips of nanoantennas after (c) before illumination and (d) after 10 min and (e) after 125 min of exposure, respectively. The dashed curves sketch the initial profile of the tips.

of gold atoms. Fig. 3.25(c) displays bow tie arrays before illumination and after two different illumination times, namely after 10 min (Fig. 3.25(d)) and 125 min (Fig. 3.25(e)). We find that after 10 min of illumination, reshaping only occurs at the apex, and then expands further outward after long-term exposure.

In order to investigate the reshaping of the antenna at different peak intensities while keeping the average power constant, we stretch the pulse duration from 8 to 16 fs. Our findings are shown in Fig. 3.25(a). At lower peak intensity (blue curve), the harmonic signal grows much slower over time than at high peak intensity (green curve), which makes us believe that the reshaping process is weaker at lower peak intensity. We conclude that the reshaping is due to an optical effect at high intensity and not to a thermal effect due to the average power. The maximum enhanced laser fluence in the feed gap is $0.8 \, \mathrm{J/cm^2}$, which suggests that electrostatic ablation is the process mainly responsible for reshaping [115]. The peak intensity at the bowtie tips exceeds $10^{14} \, \mathrm{W/cm^2}$, which can trigger a vast amount of nonlinear optical processes such as electron excitation, photoionization, and electron emission that can lead to ablation of the bow tie antennas [115].

The increase of the third harmonic signal at the beginning of laser irradiation can have several reasons. First, the deposited silicon and silicon oxide in the feed gap can act as a nonlinear optical medium and contribute, in addition to the emission from the sap-

phire substrate, to third harmonic emission [19]. Since the highest field enhancement occurs in the gap region, the deposited silicon and silicon dioxide might experience an even higher intensity than the sapphire substrate. Furthermore, the removal of gold atoms in the center might increase the gap region and change the radius of curvature at the tip, which can lead to an increase of the harmonic yield (Figs. 3.23(b) and 3.23(c)). The reason is that a larger gap with less curved tips can yield a smoother field enhancement that can be more favourable for harmonic generation [52]. When illuminating further, the ablation also occurs off-center (Figs. 3.25(d)) and 3.25(e)). As a consequence, the tips become sharper again which in turn leads to a decrease of harmonic generation. The ablation eventually stops when the field enhancement factor is lower than the ablation threshold. The harmonic signal tends to a constant value (Fig. 3.23(a)) [115]. At atmospheric pressure, the gold atoms will experience collisions with ambient gas molecules, causing a large fraction of the gold atoms to be redirected back to the antenna surfaces. Therefore, the ablation rate at ambient pressure is lower than in vacuum. The observed increase of the THG yield persists for several minutes in nitrogen (Fig. 3.25(b)), while it lasts only 15 s in vacuum (Figs. 3.25(a) and (b)). For more details we refer to [115].

In the next step, we study the effect of an SiO_2 overcoating and of different thicknesses of the bow ties. Fig. 3.26(a) displays the SEM-image of a bow tie of type III after irradiation by 8-fs pulses in vacuum. We see that the gold bow ties melted and now have a spherical shape. However, the remains of the dielectric coating still show a triangular shape. In the next step, we leave the pulse energy constant but increase the duration to 16 fs. It turns out that this does not affect the melting of the thin antennas
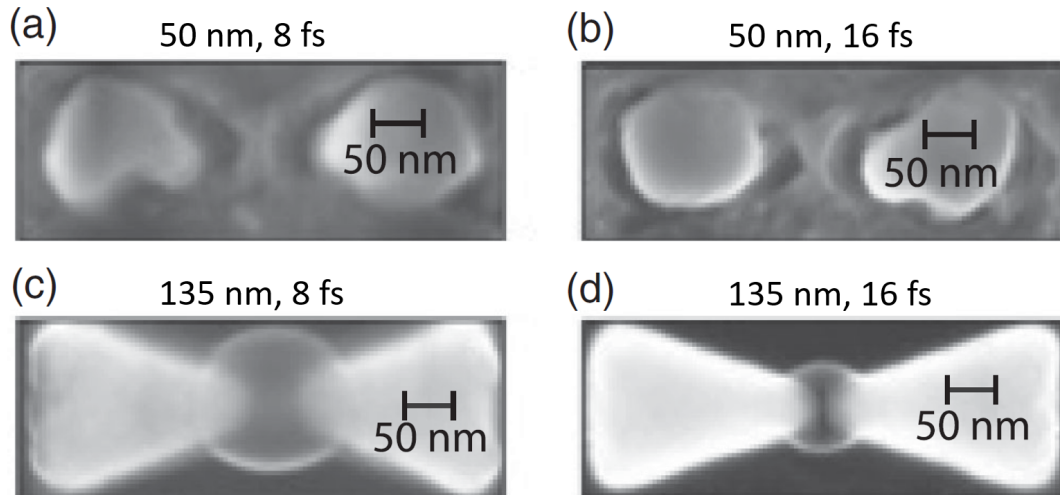
Figure 3.26.: SEM-images of bow tie nanoantennas with different thicknesses and with a 5-nm coating after modification by 8 fs (a),(c) and 16 fs (b),(d) laser pulses of an oscillator. The thickness of the nanoantennas in (a),(b) has been reduced to 50 nm while the thickness in (c),(d) is 135 nm.

as an be seen in Fig. 3.26(b). When using bow ties of type II (increased thickness), we see that the bow tie shape does not change. For 8-fs pulses (Fig. 3.26(c)) a big SiO_2 bubble appears in the gap after irradiation. For 16-fs pulses, the ablation is reduced and the ellipsoidal deposit is much smaller than for 8-fs pulses (Fig. 3.26(c)). EDX measurements reveal that the bubble consists of silicon and oxygen. These two elements originate from the SiO_2 coating, which initially covered the whole surface of the gold bow ties. The element distribution of gold is found to be still bow tie-shaped after laser illumination. The absence of the gold inside the bubble proves that there is no significant ablation of the gold nanostructures, since the SiO_2 coating effectively protects them. Modification of the antenna thickness therefore allows switching between a thermal damage scenario and a nonlinear optical ablation mechanism that depends on the local intensity. There are several promising ways to reduce radiation-induced damage in bow ties, such as the use of pulses with decreased duration or shorter wavelength as well as the use of antenna with an increased thickness.

Fig. 3.27(a) shows the SEM-image of an uncoated gold bow tie (type IV) after 50 min of illumination in vacuum. We observe as for the case with a SiO_2 coating ablation which is confined to the sharpest tips, and no damage is visible in the shanks of the antenna. A zoom onto the gap region in Fig. 3.27(a) is shown enlarged in Fig. 3.27(b) to show the gap region at a tilt angle of 45°. Figs. 3.27(c), (d) show the two-dimensional EDX maps of the gold bow-tie nanoantennas. Compared to the pristine
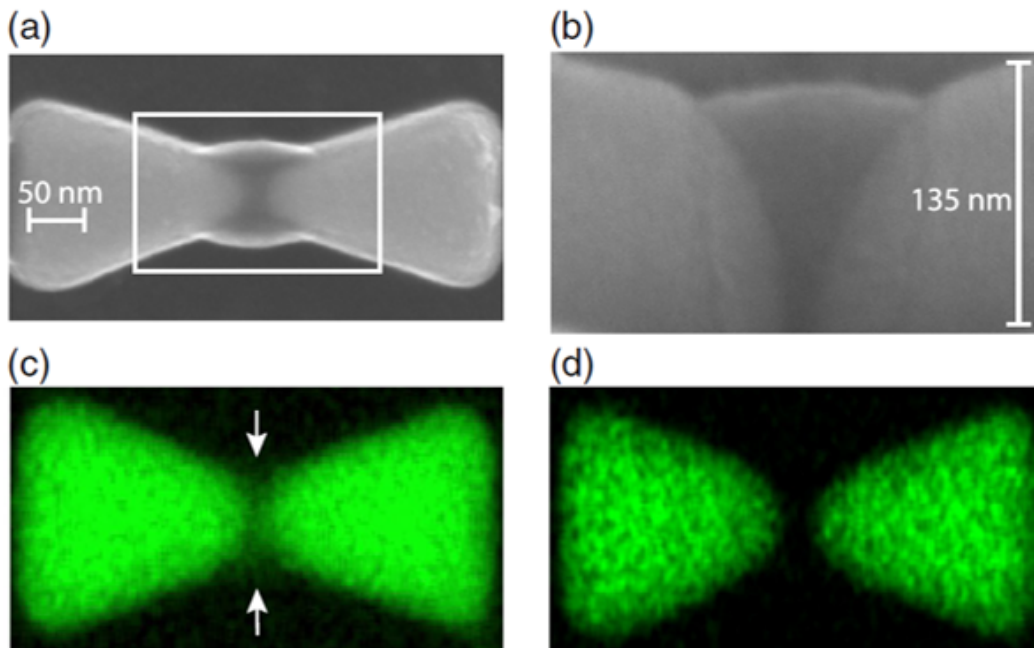
Figure 3.27.: Top-view (a) and enlarged side-view (b) SEM-image of a pure Au nanoantenna after laser ablation. The thickness of the antenna is 135 nm. EDX map showing the Au content of an ablated (c) and pristine (d) Au antenna.
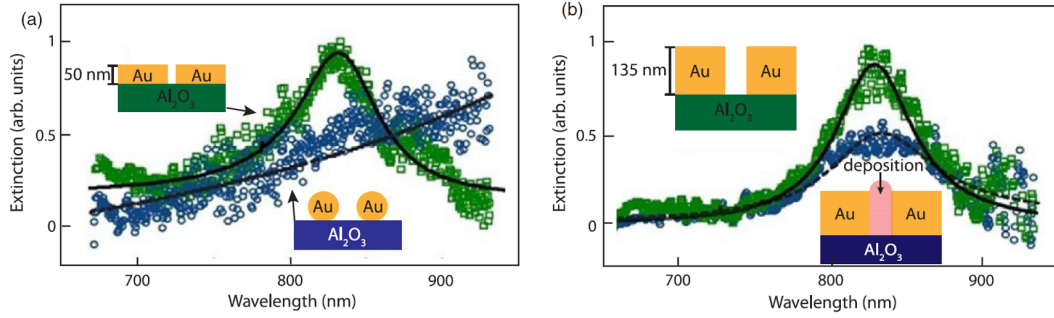
Figure 3.28.: (a) Experimentally measured extinction spectra of plasmon resonant Au nanoantennas (type IV) before (green squares) and after (blue circles) laser irradiation. Thermal melting reshapes the bow-tie nanoantennas into nanospheres, and thus the plasmonic resonance disappears. (b) The increase of heat capacity induces the transition from thermal melting to near-field-enhanced nonthermal ablation, leading to the deposit of a low-density thin film in the feed gap. Extinction spectra of nanoantennas after near-field ablation (blue circles) still show the plasmonic resonance, yet attenuated with respect to the pristine antennas (green squares).

antenna (Fig. 3.27(d)), we see that the deposit in the feed gap, as indicated by the white arrows in Fig. 3.27(c), is indeed gold [125]. We also measure the extinction spectra of pure Au antennas before and after laser modification. The green squares in Fig. 3.28 show a typical plasmonic resonance of pristine nanoantennas centered at 830 nm. As thermal melting completely reshapes the nanoantennas (inset, Fig. 3.28(a)), the plasmonic resonance completely vanishes (blue circles, Fig. 3.28 (a)). In contrast, in
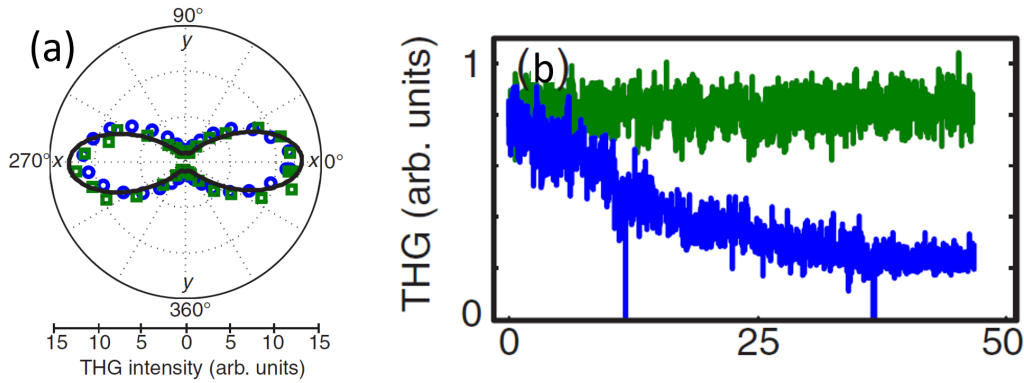
Figure 3.29.: (a) Gap-plasmon-enhanced third harmonic generation from SiO_2-coated (green squares) and metallic (blue circles) antenna as a function of the laser polarized direction. Temporal evolution of the third harmonic signal with long-term irradiation (green curve, coated antenna; blue curve, metallic antenna). (b) Temporal evolution of third harmonic generation with long-term irradiation (green curve, coated antenna; blue curve, metallic antenna).

the case of near-field enhanced ablation, reshaping is limited to the tip region, without modification of other parts of nanoantennas. This mechanism apparently weakens the plasmonic resonance, but does not completely remove it (blue circles, Fig. 3.28(b)). This attenuation may be attributed to the Au deposit in the feed gap [125].

In order to verify the near-field enhancement, we measure third harmonic generation as a function of laser polarization for bow ties of type II and IV (Fig. 3.29(a)). The harmonic intensity is normalized to the signal at $\theta = 90°$. Here, the parameter θ is defined as the crossing angle between the laser polarization and the long axis of the bow tie (x axis). Independently of the presence of an overcoating, we observe that the third harmonic signal shows an enhancement when the laser polarization is parallel to the bow-tie axis, i.e., $\theta = 0°$. Figure 3.29(b) represents the temporal evolution of the harmonic flux for long-term laser irradiation in vacuum. The harmonic emission from pure Au nanoantennas (blue curve) is progressively decreasing with irradiation time. This behavior is attributed to the removal of Au atoms from the tips, resulting in an increase of the radius of curvature and gap size, which decreases the near-field enhancement factor. In contrast, the bow tie with SiO_2 overcoating is capable of maintaining a high third harmonic generation flux for nearly an hour (green curve). These findings appear to be in agreement with the previous observations, i.e., that the coated dielectric nanofilm can efficiently prevent the localized ablation of Au atoms [125].

Discussion

We investigated the structural modifications of bow ties under illumination with sub-TW 800 nm femtosecond pulses. When exposing the nanostructures to the laser, we first observed an increase of third harmonic generation during 15 seconds and a subsequent slow decrease during 6 minutes. Due to the local field enhancement, gold atoms are removed in the center of the bow tie tip which increases the gap region and changes the radius of curvature which leads to an increase of the harmonic yield. When illuminating further, the ablation also occurs off-center which makes the tips sharper again which in turn leads to a decrease of harmonic generation. The ablation eventually stops when the field enhancement factor is lower than the ablation threshold. We found that purging the sample with gas at ambient pressure can slow down the ablation process. For more details we refer to [115]. Furthermore, we studied the morphologic changes happening to different bow tie nanostructures with different thicknesses with and without additional dielectric coating during intense laser irradiation. While thin bow tie antennas (50 nm) suffer from thermal damage, thick ones (170 nm) are reshaped close to the tip. As expected, the thermal damage is independent on the peak intensity. Using 8 fs and 16 fs pulses yields the same result. However, the reshaping of thick antennas is intensity-dependent and is much stronger for shorter laser pulses where SiO_2 is deposited in the feed gap. A 5 nm thin SiO_2 coating prevents gold bow tie antenna from reshaping. Without the coating reshaping was observed. For more details about this experiment we refer to [123].

3.6.2. Structural modification of plasmonic nanoholes

In this subsection, we study the temporal decrease of the third harmonic generated in gold nanoholes on a ZnO crystal. We investigate the physical phenomena behind this temporal attenuation. For further details about this experiment we refer to [125]. The experiment was conducted in collaboration with the group of Prof. Milutin Kovacev at Hanover University. The enhancement properties of the nanoholes were studied in sec. 3.3. The experimental setup, the system parameters and the sample are described in detail in sec. 3.3.

Measurements

For our measurements, we use nanoholes with a diameter of $400\,nm$ and a period of $600\,$nm. The third harmonic signal from the nanoholes decays over an irradiation of 30 minutes. This decrease in harmonic yield (Fig. 3.30(a)) indicates that some structural change of nanostructures took place during the laser irradiation. After 30 minutes of irradiation the transmittance of the nanoholes is reduced by $40\,\%$ of its initial value for the fundamental beam and by $65\,\%$ for the third harmonic.

For determining the origin of the third harmonic we perform FDTD simulations with MEEP (app. B) and compare them to the measurements. Fig. 3.30(b) shows the measured third harmonic spectra emitted from bare ZnO (green curve) and from an array of nanoholes (blue curve). The intensity of the third harmonic emitted from the bare ZnO substrate is calibrated from the ratio of the gold-free aperture area. The signal of the nanoholes is by a factor if 3.5 stronger than the signal from the bare crystal. We simulate the third harmonic from bare ZnO (Fig. 3.30(c), green curve)
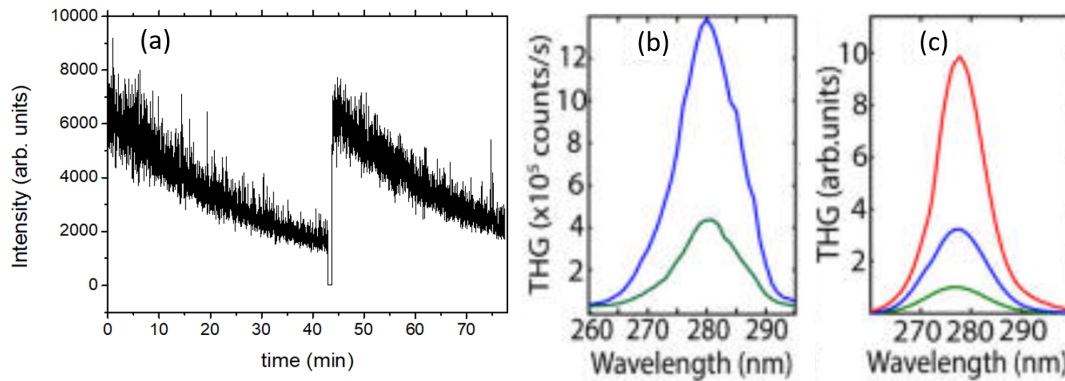
Figure 3.30.: (a) Temporal evolution of the third harmonic emission from the nanoholes. (b) Third harmonic spectra emitted from bare ZnO crystal (green curve) and from an array of nanoholes (blue curve). (c) FDTD simulations of third harmonic spectra from bare ZnO (green curve), from ZnO with gold nanoholes by only taking account the nonlinearity of ZnO (blue curve) and from ZnO with gold nanoholes by taking account the nonlinearity of both ZnO and gold (red curve).
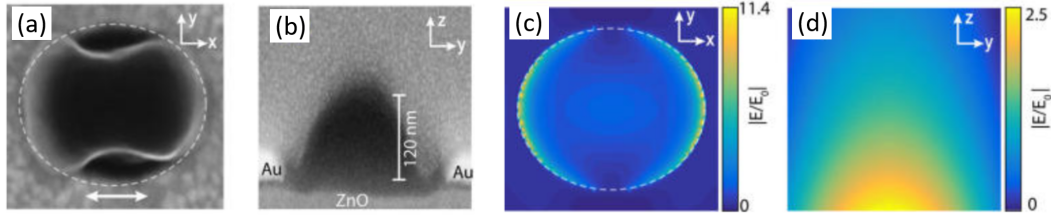
Figure 3.31.: SEM-images in (a) top-view (x-y plane) and (b) cross-sectional-view (y-z plane) of the laser-modified nanohole. FDTD-simulations of the field enhancement of the nanohole in (c) x-y plane at 20 nm above the gold-ZnO interface, and in (d) y-z plane along the bisecting plane of the hole.

and from the nanoholes by taking into account only the nonlinearity of ZnO and not the one of gold ($\chi_{Au}^{(3)} = 0$, Fig. 3.30(c), blue curve). We obtain a third harmonic signal from the nanoholes on ZnO that is three times stronger than that from the bare ZnO crystal, which is close to the experimental result. When we include the nonlinearity of gold into the simulations, we obtain a signal that is significantly stronger than the experimental result (red curve, Fig. 3.30(c)). We conclude that the third harmonic from the nanoholes originates mostly from ZnO and not from gold [125].

SEM-images of one nanohole after 30 min of laser exposure are shown in Fig. 3.31(a) (top view, x-y-plane) and Fig. 3.31 (b) (side view, y-z-plane), respectively. The comparison with the nanoholes before irradiation reveals that the holes after irradiation are filled with a material. The top view (Fig. 3.31 (d)) indicates that the deposit has a lower density than the surrounding material since it is partially transparent. The side view shows that the nanohole is filled with a certain material with an arched shape that sticks out of the surface. Furhermore, when comparing the profile of the deposited material in Figs. 3.31 (a)-(b) to FDTD-simulations of the field enhancement in Figs. 3.31 (c)-(d), we find we find an excellent compliance between both shapes. We made a two-dimensional scan of element maps by means of energy-dispersive X-ray spectroscopy (EDX) in order to determine the chemical elements of the laser-induced deposition. The results in the x-y plane (upper row) and the y-z plane (lower row) are shown in Fig. 3.32. The dashed curves follow the contour of the nanohole. The scan reveals that the dominant chemical element in the material deposited within the nanohole is carbon (C, Fig. 3.32 (a,b)) which accumulates in the center of the nanohole. A small amount of silicon (Si, Fig. 3.32 (c,d)) and oxygen (O, Fig. 3.32 (e,f)) is also observed. The components of gold (Au, Fig. 3.32 (g,h) and zinc (Zn, Fig. 3.32 (i,j)) remain confined to the original nanostructure and substrate. Since no Au and Zn is found in the deposit, we come to the conclusion that no ablation of the nanostructure or the ZnO substrate occured. For a more detailed discussion about the origin of the different elements we refer to [125]. We believe that hydrocarbon molecules, that were deposited during the sample fabrication process on the gold surface, can be cracked under the irradiation of a strong femtosecond laser. The cracking process is strongly related to the photon flux, hence most of the carbon atoms will be generated at the curved surfaces of the Au nanohole, where the highest field enhancement occurs. The
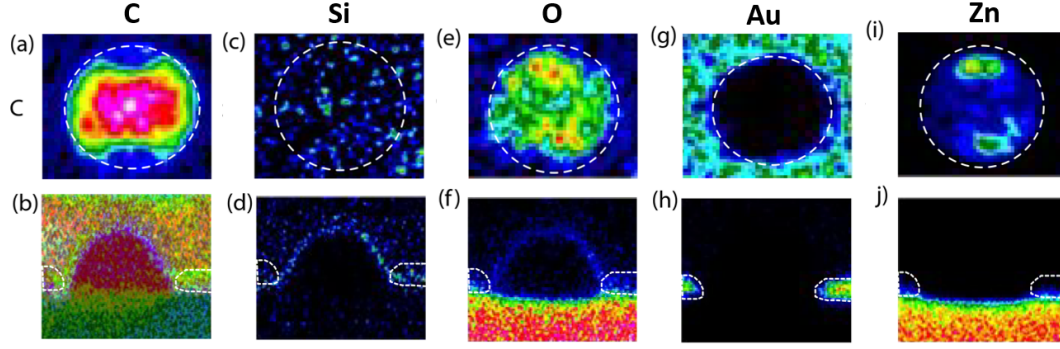
Figure 3.32.: Two-dimensional EDX maps of a gold nanohole after illumination in top-view (a), (c), (e), (g), and (i); and in cross-sectional view (b), (d), (f), (h), and (j). The corresponding elements of the rows from top to bottom are C, Si, O, Au, and Zn, respectively. The dashed curves depict the profile of the Au structure.

laser ablation effect will drive a portion of the carbon atoms to escape from the metal surface.

Figure 3.33 (a) shows the experimentally measured volumes of the carbon deposit inside the nanohole versus the near-field strength. We see that the amount of carbon exponentially increases with the field strength. We explain this as follows: We believe that the near-field enhancement leads to the emission of electrons of the gold surface. The electron emission rate scales exponentially with the electric field strength [126]. The ejection of numerous electrons results in a positively charged surface. Thus, the resultant Coulomb repulsive force can drive the adsorbed carbon ions to escape from the Au film [127]. The ablated carbon atoms will not randomly deposit on the ZnO substrate surface, as the surface plasmons enhanced optical tweezer effect will subsequently act on these atoms. Figure 3.33(b) shows the two-dimensional potential energy distribution resulting from the illumination of an Au nanohole. The atoms would preferentially move to the minimum point at the potential surface, which is close to the Au surface (zone I, Fig. 3.33(b)). However, the charged surface induced electrostatic repulsive force also peaks in this area, which strongly restrains the accumulation of atoms. Therefore, the carbon atoms would rather start to accumulate from the center of the nanohole, where exists a sub-minimum potential energy (zone II, Fig. 3.33(b)) and is absent of optical force, allowing for stable trap of the atoms. Indeed, from the SEM-images (inset I, Fig. 3.33(a)), one can see that the carbon deposit starts to appear in the center of nanohole. After long-term laser illumination, along with the enhanced near-field distribution, the entire optical hotspot inside the nanohole is finally filled by the carbon atoms (insets in Fig. 3.33(a)). The nonlinear harmonic conversion process greatly depends on the near-field, which is significantly sensitive to the local conditions, including the geometry and the surrounding dielectric constant [52]. From the SEM-images and EDX maps we saw that the geometry of the gold nanoholes is not affected by the laser exposure. Furthermore, additional FDTD simulations of the nanoholes with different amounts of carbon show that the field enhancement is almost
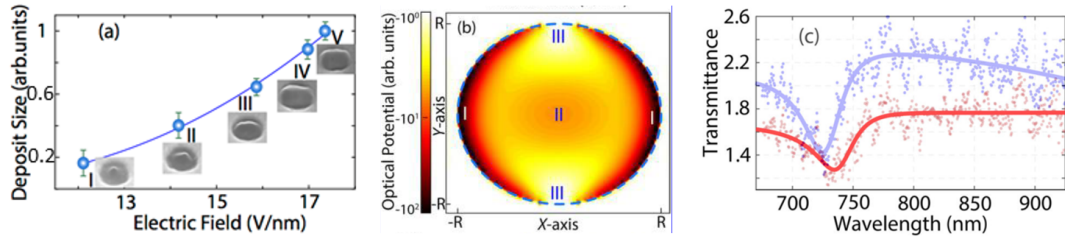
Figure 3.33.: (a) The dependence of the carbon deposit size on the electric near-field strength. Insets (I-V): SEM-images of the nanohole illuminated by different field strength. (b) Numerical simulation of the potential energy distribution of the plasmonically enhanced optical tweezer. Zone I shows two minimum potential wells near the Au curved surface, and zone II depicts a sub-minimum potential surface in the center of the hole. (c) Experimentally measured extraordinary optical transmission of the pristine (blue squares) and the carbon-deposited (green circles) nanoholes.

unaffected by the carbon deposit [125]. In order to investigate the influence of the carbon deposit on the local field enhancement, we compare the linear transmission spectra of the pristine nanoholes and nanoholes with carbon deposit, as shown in Fig. 3.33(c). For the nanoholes with carbon deposit (red curve), the overall optical transmittance is attenuated with respect to the transmission of pristine nanoholes (blue curve), while the plasmonically resonant wavelength does almost not shift. This indicates that the deposit of carbon does not neessarily change the surrounding dielectric constant, and thus the field enhancement stays alomst unaffected. We conclude that the attenuation of optical transmission of both the fundamental and the third harmonic is attributed to the strong absorption of the carbon atoms in these spectral regions.

Discussion

In this work, we investigated the temporal attenuation of third harmonic generation from gold nanoholes on ZnO. We found that carbon atoms were deposited in the gold nanoholes during laser irradiation. The underlying mechanism of carbon deposit is attributed to the cracking of carbon-containing molecules at the gold surface, the emission of electrons which is triggered by the field enhancement in the nanohole, the electron-driven ablation of the carbon atoms and the deposit of carbon in certain regions of the nanohole due to the optical tweezer effect. The attenuation of third harmonic generation is ascribed to the strong absorption of carbon atoms over a broad spectral region.

Conclusion of chap. 3

In this chapter, we studied the enhancement of HHG in crystals by the use of plasmonic nanostructures. We used different nanostructure geometries such as bow ties, nanoholes, gratings and resonators which have different enhancement properties. While bow ties create high field enhancement in a small volume, resonators generate lower enhancement with a smoother field gradient in higher volumes. Nanoholes exhibit a higher enhancement volume than bow ties. Due to detection issues we were limited to the measurement of the third harmonic. First harmonic measurements were made with a $2.0\,\mu$m beam and a ZnO crystal with gold gratings at its surface. We found that the third harmonic yield strongly depends on the polarization of the pump beam. An effective enhancement of the third harmonic could not be observed since this first nanostructure design had important limitations. The used nanograting consisted of a thick gold layer that strongly absorbed harmonic radiation. Furthermore, simulations show that the main field enhancement is located below the gold and not below the apertures which prevents an effective outcoupling of the harmonic radiation. A second generation of plasmonic nanostructures with an improved design (gold nanoholes an ZnO and a gold-SiO_2-gold Fabry-Perot resonator) were used with an 800 nm laser. The effective enhancement factor of the nanholes and the grating resonator with respect to a bare substrate without nanostructures is 12 and 21, respctively. Furthermore, we investigated enhancement of third harmonic generation in sapphire due to the local field enhancement in bow tie nanostructures at the crystal surface. Enhancement values by more than one order of magnitude with respect to a bare sapphire crystal were observed. We studied the origin of third harmonic generation and found that the third harmonic mostly originates from the sapphire crystal and not from the gold itself. We even analyzed the radiation-induced damage of plasmonic nanostructures. Damage can occur due to high average power, but other channels of nanostructure deformation due to high peak intensity are possible (Fig. 2.7). The third harmonic from a sapphire substrate with gold bow ties at its surface first increased and then decreased during laser exposure. This is due to a reshaping of the bow tie that follows the field enhancement. It turns out that bow ties with higher thickness are less susceptible to thermal damage and that higher peak intensity leads to stronger reshaping. A protective SiO_2 film that covers the bow ties can preserve the bow tie shape during laser irradiation. The third harmonic from gold nanoholes steadily decreased over time. This is due to a carbon deposit inside the holes that built up during irradiation and that followed the distribution of the near-field enhancement. The carbon deposit strongly absorbed third harmonic radiation. The shape of the nanoholes, however, remained unchanged.

4. High harmonic generation in semiconductor nanostructures

In this chapter, we study high harmonic generation (HHG) assisted by field enhancement in semiconductor nanostructures. In 2017, the group of Paul Corkum reported on the enhancement of harmonics in ZnO waveguide structures. They generated up to H9 of a beam of $2.0 - 2.3\,\mu$m wavelength in 2D ZnO waveguides and reported on enhancement of H5 in this 2D nanostructure with respect to a bare ZnO crystal [20]. Furthermore, they demonstrated harmonic generation up to H9 from 3D ZnO waveguide structures. In addition, generation of luminescence from the band edge is reported [20]. Incident peak intensities are of the order of $1\,\text{TW/cm}^2$. The simulated enhancement of the fundamental beam in a single nanostructure and the measured spectrum from an array of ZnO nanostructures are shown in Figs. 4.1. Inspired by this work
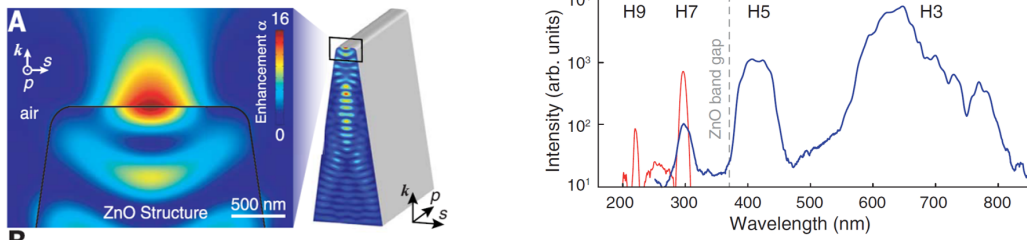
(a) **Simulation of the enhancement of a beam of** $2.0 - 2.3\,\mu$m **wavelength in 2D ZnO nanostructure.**

(b) **Spectrum emitted from 2D ZnO nanostructure.**

Figure 4.1.: Field enhancement in a 2D ZnO nanostructure and spectrum generated in such nanostructures from a $2.0 - 2.3\,\mu$m **beam, taken from [20].**

we performed experiments with similar nanostructures with the goal to demonstrate enhancement for even higher harmonics. We performed three different experiments at ICFO (January/February 2017), at IOGS (March/April 2017) and at CEA (June/July 2017). In order to demonstrate enhancement of high-order harmonics we progressively improved our diagnostics and nanostructure geometries. The most important parameters of these three experiments such as laser wavelength, diagnostics and nanostructure geometries are listed in tab. 4.1. In sec. 4.1, we present the concept of field confinement in semiconductor and dielectric nanostructures. In sec. 4.2, we study the enhancement of harmonics of a $3.2\,\mu$m laser in an array of ZnO nanocones (ICFO). We do this for different cone geometries and wavelengths. Having improved the cone geometry and the detection system, we extend this study to higher harmonic orders by the use of a $3.1\,\mu$m (IOGS). We make spectral and polarization measurements to study the en-

Exp.	Laser	Camera	Spectro	Sample
ICFO	$3.2\,\mu$m 160 kHz	Imaging Source (21BUC03) QE 30% - 50% (380 nm - 850 nm)	Ocean Optics (Maya 2000 pro) QE 50% - 75% (200 nm - 880 nm)	array of ZnO nanocones
IOGS	$3.1\,\mu$m 125 kHz	Photon Lines (PCO) QE 25 % and 40 % (200 nm - 850 nm)	Ocean Optics (QE pro, cooled) QE 45% - 95% (200 nm - 900 nm) 85% at 230 nm	array of ZnO nanocones
CEA	$2.1\,\mu$m 18.66 MHz	Photon Lines PCO QE 25 % − 40 % (200 nm - 850 nm)	Ocean Optics (QE pro, cooled) QE 45% - 95% (200 nm - 900 nm) 85% at 230 nm	isolated truncated ZnO nanocones

Table 4.1.: Comparison of the different parameters of the experiments made at ICFO, IOGS and CEA.

hancement of harmonic radiation and luminescence in an array of ZnO nanocones (sec. 4.3). In sec. 4.4 we use an improved nanocone geometry (truncated nanocones) and investigated enhancement of high harmonics and luminescence of a $2.1\,\mu$m beam (CEA). In order to increase the conversion efficiency from the fundamental beam to the high harmonic radiation the fundamental beam is entirely coupled into one single nanocone. In sec. 5.1 we discuss laser-induced damage of the nanocones observed in the three mentioned experiments.

4.1. Introduction to high harmonic generation assisted by field enhancement in dielectric and semiconductor nanostructures

Semiconductor and dielectric waveguide structures can enhance a laser beam locally, which can greatly enhance nonlinear processes. The origin of the local enhancement are diffraction and scattering effects which occur due to the subwavelength size of the structures. Incoherent and coherent processes can be enhanced at the same time and compete with each other. Dai et al. [128] study luminescence generation and second harmonic generation of a 754 nm driving laser in semiconductor ZnO nanostructures. Second harmonic generation or/and two-photon luminescence were observed. It turns out that different geometries of nanorods enhance different nonlinear process. For single ZnO nanorods, second harmonic generation was observed. No signature of luminescence could be detected (Fig.4.2(a)). When using two nanorods in the geometry shown in Fig. 4.2(b), two-photon luminescence was detected at low intensities in addition to second harmonic generation. The luminescene increased rapidly with increasing pump intensity and became comparable to the second harmonic intensity at high pump intensity of $15\,\mathrm{MW/cm^2}$. For an ensemble of ZnO nanorods (Fig. 4.2(c)), luminescence dominates over second harmonic generation at high pump intensity of $15\,\mathrm{MW/cm^2}$. These three cases shown in Fig. 4.2 might differ with respect to electric field distribution and heat accumulation during laser irradiation which might explain their different behaviour in enhancing nonlinear processes [128]. Furthermore, a reduction of the bandgap might occur due to heat accumulation effects which in turn influences the nonlinear response [128]. In addition, Dai et al. found that the ratio of luminescence generation and second/third harmonic generation depends on the focal spot size [129]. So the relative importance of harmonic generation and luminescence
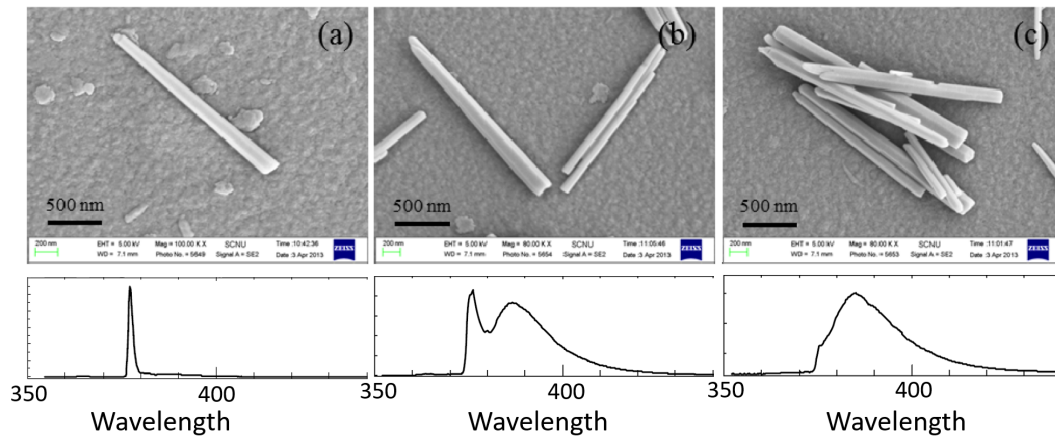
Figure 4.2.: SEM-images and generated nonlinear signal of single (a), double (b) and multiple (c) ZnO nanorods. Pictures taken from [128].

generation is complex and depends on many parameters such as the geometry of the nanostructures and the properties of the exciting laser.

In 2012, Ning et al. [130] demonstrated high field enhancement of a the output of a Nd:YAG laser at 1064 nm wavelength in silicon nitride waveguide gratings (Fig. 4.3). Second harmonic generation in such a grating was shown to be by three orders of magnitude more efficient than second harmonic generation in a flat surface of the same material. In 2008, the same group reported a 5000-fold enhancement of second
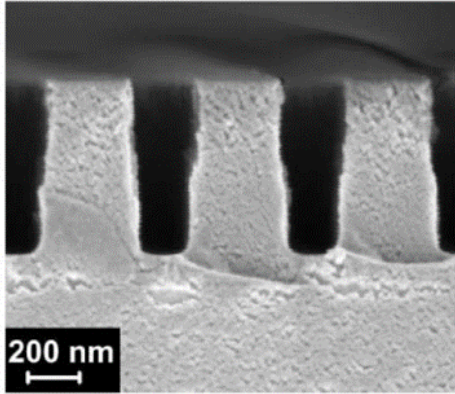
(a) **SEM-image of grating.**
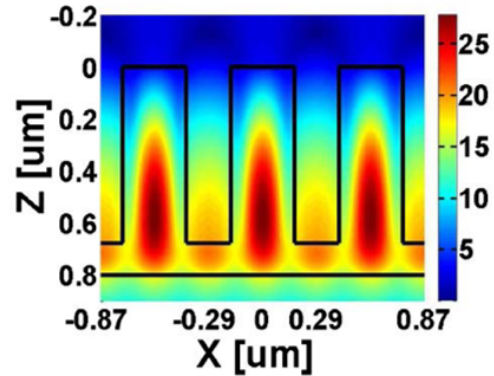
(b) **FDTD simulation of magnetic field enhancement in the grating.**

Figure 4.3.: Strong field enhancement of a laser beam at 1064 nm wavelength in a binary silicon nitride waveguide grating, taken from [130].

harmonic generation in a SiO_2/TiO_2 grating.

As already mentioned above the group of Paul Corkum reported in 2017 the enhancement of H5 of a $2\,\mu$m driving laser in 2D ZnO waveguide structures [131]. While they observed the generation of up to H9, enhancement was reported only for H5.

4.2. Experiment at ICFO: First design

In the experiment described in this section we study enhancement of HHG in an array of ZnO nanocones with different basis sizes and periodicities with an intense femtosecond $3.2\,\mu$m OPCPA system operating at 160 kHz repetition rate. The experiment was carried out at 'The Institute of Photonic Sciences' (ICFO) in Castelldefels, Spain in collaboration with the group of Prof. Jens Biegert in January/February 2017.

Experimental setup

The laser is a $3.2\,\mu$m OPCPA system operating at 160 kHz repetition rate. Pulses have a maximum energy of $130\,\mu$J and a duration of 97 fs. For more details about the laser system we refer to app. C and to [132]. The experimental setup is shown in Fig. 4.4. The pulse energy was attenuated by means of a half-wave plate and a polarizer to energies of only a few micro-joules and focused into the sample on the nanostructured sample side (normal incidence). The focal spot size is $65\,\mu$m (FWHM) and the investigated intensity range is $0.1 - 0.5\,$TW/cm^2. At these intensities, we are set below the ZnO crystal damage threshold. The sample is fixed on a 3D nano-positioning system (Smaract). The harmonic radiation emitted from the nanocones is collimated and different harmonic orders are selected by transmission filters and focused onto a CCD camera (Imaging Source, 21BUC03). Spectral measurements were made with an Ocean Optics spectrometer (Maya 2000 pro). For the spectral measurements the CCD camera as replaced by the spectrometer.
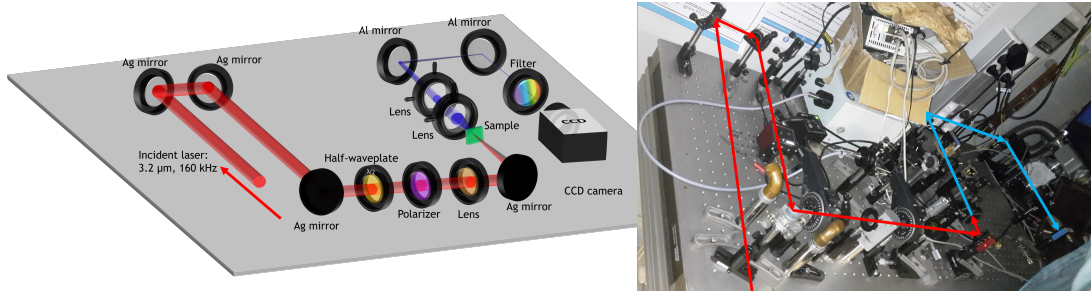
Figure 4.4.: Layout and picture of experimental setup: The pump beam (red) is focused into the sample and the harmonics (blue) are measured in transmission.

FDTD simulations and sample properties

We simulate the enhancement of a $3.2\,\mu$m beam in nanocones with different dimensions by using FDTD simulations with Lumerical Solutions (app. B). In the simulations, x and z are polarization and propagation direction, respectively, and y is the third axis perpendicular to both x and z. We will refer to intensity enhancement (by which we mean the squared modulus of the electric field enhancement) rather than to the field enhancement itself. The height of all nanocones is $6\,\mu$m. The enhancement is

(a) **Enhancement in isolated nanocone in x-z-plane with** $4\,\mu$m **basis.**

(b) **Enhancement in isolated nanocone in y-z-plane with** $4\,\mu$m **basis.**

(c) **Enhancement in isolated nanocone in x-y-plane with** $4\,\mu$m **basis at height of maximum enhancement.**

(d) **Enhancement in nanocone array in x-z-plane with** $4\,\mu$m **basis and** $6\,\mu$m **periodicity.**

(e) **Enhancement in nanocone array in y-z-plane with** $4\,\mu$m **basis and** $6\,\mu$m **periodicity.**

(f) **Enhancement in nanocone array in x-y-plane with** $4\,\mu$m **basis and** $6\,\mu$m **periodicity at height of maximum enhancement.**

(g) **Enhancement in nanocone array in x-z-plane with** $2\,\mu$m **basis and** $3\,\mu$m **periodicity.**

(h) **Enhancement in nanocone array in y-z-plane with** $2\,\mu$m **basis and** $3\,\mu$m **periodicity.**

(i) **Enhancement in nanocone array in x-y-plane with** $2\,\mu$m **basis and** $3\,\mu$m **periodicity at height of maximum enhancement.**

Figure 4.5.: Intensity enhancement of a $3.2\,\mu$m **beam in different types of ZnO nanocones.**

shown as a zoom on one single cone out of the array. The white lines indicate the cone boundaries. Propagation and polarization direction are indicated by $\overrightarrow{k}$- and $\overrightarrow{E}$-vectors, respectively. We define the enhancement volume as the space in which the enhancement exceeds half of the maximum enhancement. Fig. 4.5 shows the simulated intensity enhancement for an isolated ZnO nanocone with a basis of $4\,\mu$m

(a) $\lambda = 0.8\,\mu$m.

(b) $\lambda = 1.2\,\mu$m.

(c) $\lambda = 1.6\,\mu$m.

(d) $\lambda = 2.0\,\mu$m.

(e) $\lambda = 2.4\,\mu$m.

(f) $\lambda = 2.8\,\mu$m.

(g) $\lambda = 3.2\,\mu$m.

(h) $\lambda = 3.6\,\mu$m.

(i) $\lambda = 4.0\,\mu$m.
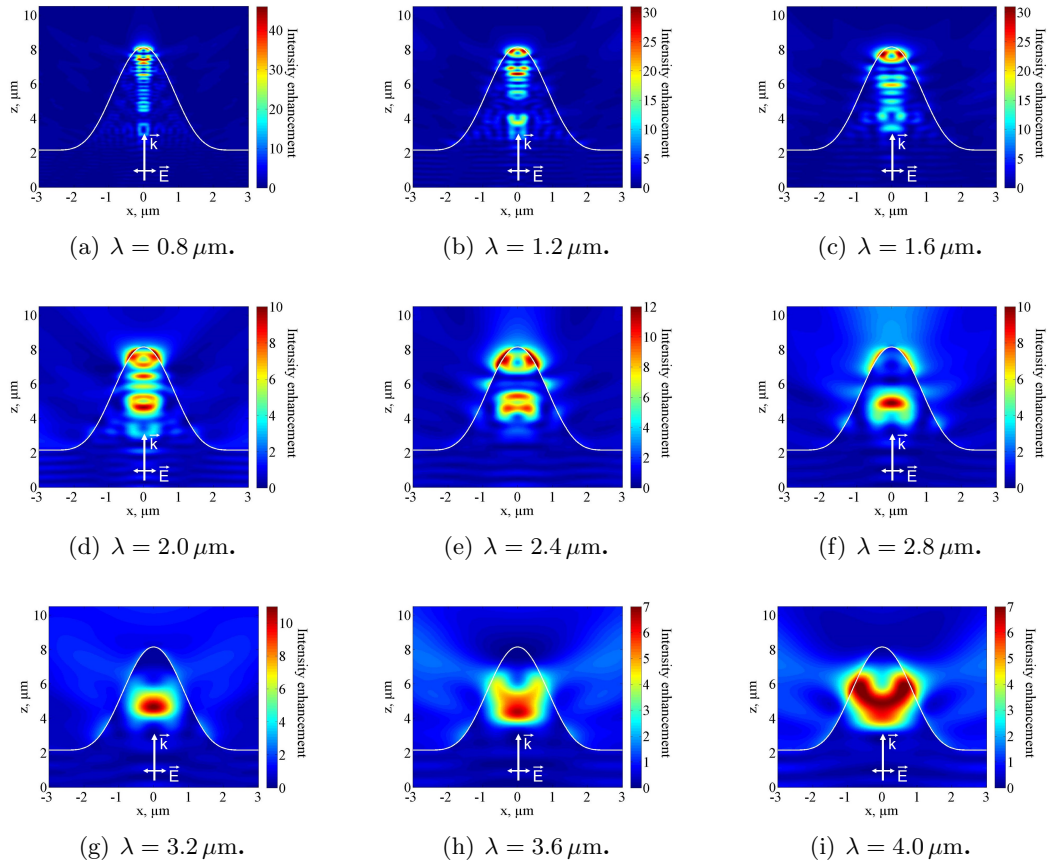
Figure 4.6.: Intensity enhancement of a monochromatic beam of different wavelengths in an isolated ZnO nanocone with a basis of $4.0\,\mu$m.

(Fig. 4.5(a) - 4.5(c)), for an array of ZnO nanocones with a basis of $4\,\mu$m and a periodicity of $6\,\mu$m (Fig. 4.5(d) - 4.5(f)) and for an array of ZnO nanocones with a basis of $2\,\mu$m and a periodicity of $3\,\mu$m (Fig. 4.5(g) - 4.5(i)). For the isolated nanocone, the cone parameters were varied in order to obtain high enhancement in a broad volume. The best result is obtained for a base line of $4\,\mu$m and is shown in Fig. 4.5(a) - 4.5(c). The maximum intensity enhancement is 11 and is located $2.5\,\mu$m above the base line in a volume of $0.15\,\mu m^3$. The enhancement is broader in the direction of the polarization and slightly leaking out of the nanocone, such that there is some enhancement in air. Close to the tip the enhancement factor is 0.3 which corresponds to an attenuation instead on an enhancement. The enhancement in the x-y-plane is shown at the height where maximum enhancement occurs. Figs. 4.5(d) - 4.5(f) show the intensity enhancement for an array of nanocones with a periodicity of $6\,\mu$m. The light is strongly confined when reaching the middle of the nanocones which leads to significant enhancement. The maximum enhancement is 21 and is located at $2.65\,\mu$m height in a volume of $0.10\,\mu m^3$. The leakage is much stronger than for an isolated cone. Close to the tip the enhancement factor is smaller than 1, so the beam

90

is attenuated there instead of being enhanced. So in contrast to an isolated nanocone, an array of nanocones displays higher enhancement in a smaller volume closer to the tip of the nanocone. We attribute these differences to a collective effect between the nanocones. The leakage out of one nanocone can reach a neighbouring nanocone and boost the enhancement there. Fig. 4.5(i) - 4.5(g) show the enhancement of an array of nanocones with $3\,\mu m$ periodicity and a basis size of $2\,\mu m$. One can see that in contrast to the larger nanocones, the wave cannot enter the small nanocones and propagate towards the tip, it is confined at $2.0\,\mu m$ height and strongly leaks out of the cone, the highest enhancement is now outside the cone. In the upper half of the nanocone no enhancement occurs. The enhancement volume is $0.43\,\mu m^3$.

The electric field confinement in the nanocones has been studied as a function of laser wavelength for isolated ZnO nanocones with a $4\,\mu m$ broad basis. Simulations are performed for monochromatic waves with $\lambda = 0.8, 1.2, 1.6, 2.0, 2.4, 2.8, 3.2, 3.6, 4.0\,\mu m$, respectively. The results for the simulated enhancement in the x-z-plane are shown in Fig. 4.6. The maximum intensity enhancement varies from 46 at 800 nm to 7 at $4\,\mu m$. As a general trend shorter wavelengths propagate closer to the tip and show higher enhancement in a smaller volume. A homogeneous mode is found for laser wavelengths longer than $2.8\,\mu m$, especially at $3.2\,\mu m$. Good confinement is achieved at the height where the cone diameter is approximately half of the wavelength.

SEM-images of the two different samples used in this experiment are shown in Fig. 4.7. They were produced by using the focused ion beam (FIB, app. A) technique at CSNSM lab at Orsay. The two samples used in the frame of this experiment are:

- Sample 1: ZnO [0001], 5 mm x 5 mm x 0.5 mm, nanocones with $4\,\mu m$ basis and $6\,\mu m$ periodicity

- Sample 2: ZnO crystal, [11-20], 5 mm x 5 mm x 0.5 mm, nanocones with $4\,\mu m$ - $5\,\mu m$ basis and $6\,\mu m$ periodicity.
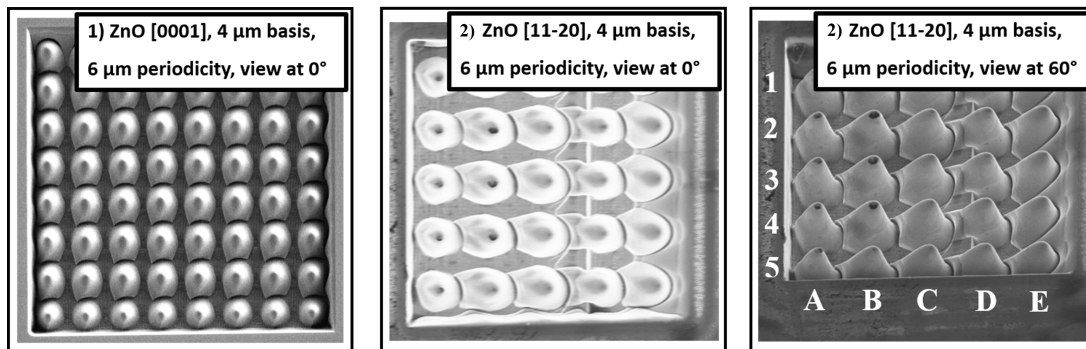
Figure 4.7.: SEM-images of the two samples used in the frame of this experiment. Sample 1: ZnO[0001] nanocones with $4\,\mu m$ basis and $6\,\mu m$ periodicity, view at $0°$, 2: ZnO[1120] nanocones with $4\,\mu m$ basis and $6\,\mu m$, view at $0°$ and $60°$.

Measurements

We carry out harmonic measurements with the two samples shown in Fig. 4.7. The radiation emitted from structure 1 (Fig. 4.7) is imaged on the camera. Figs. 4.8(a), (b), (c) and (d) show harmonic H3 (measured without filter) and the transmission through filters I, II and III, respectively. Filters I, II and III cover the spectral range of H5, H7 and H9, respectively. More details about the filters can be found in app.

(a) **H3.**

(b) **Signal measured with filter I.**

(c) **Signal measured with filter II.**

(d) **Signal measured with filter III.**
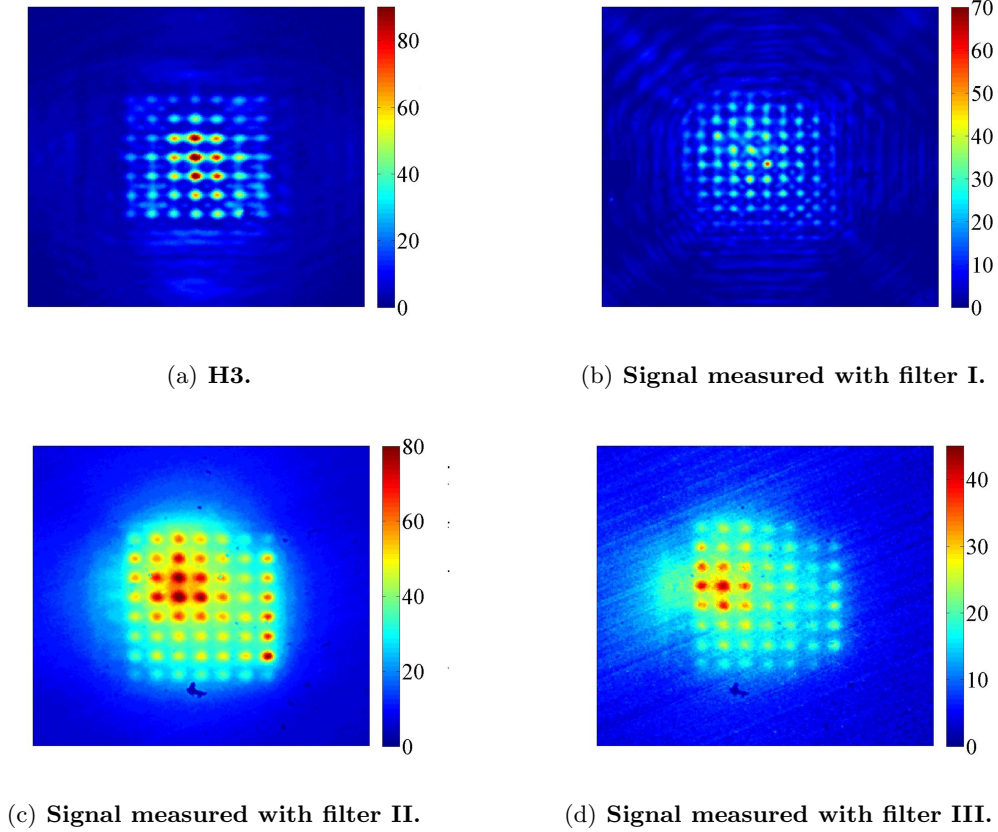
Figure 4.8.: Harmonic H3 (measured without filter) and the transmission through filters I, II and III, respectively, emitted from an 8 x 8 array of nanocones (Structure 1 in Fig. 4.7).

D were used. The goal is to study the harmonic enhancement factors in dependence on the pump intensity. Fig. 4.9 shows the signal measured with filter II from bare ZnO and from the nanocones for two different pump intensities ($0.35\,\mathrm{TW/cm^2}$ and $0.80\,\mathrm{TW/cm^2}$). For low pump intensity ($0.35\,\mathrm{TW/cm^2}$) a weak signal close to the detection limit of the CCD-camera is generated from the bare crystal (Fig. 4.9(a)). The total signal generated at the same pump intensity from the nanocones is by almost one order of magnitude stronger than from the bare crystal. When increasing the pump intensity (($0.80\,\mathrm{TW/cm^2}$), the signal from bare ZnO strongly increases (Fig. 4.9(c)). But the signal from the nanostructures increases much less with respect to weaker
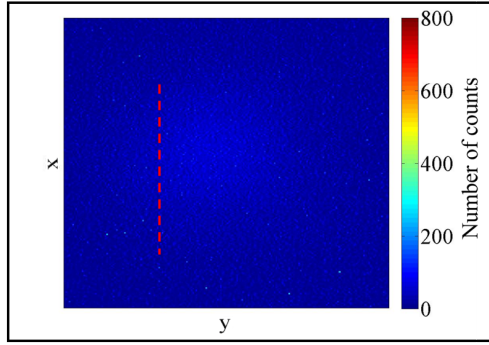
(a) **Signal from bare ZnO at** $0.35\mathrm{TW/cm}^2$**.**
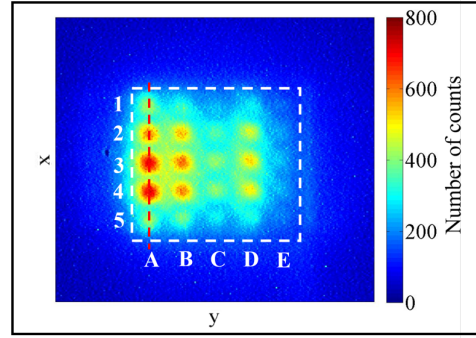
(b) **Signal from nanocones ZnO at** $0.35\mathrm{TW/cm}^2$**.**
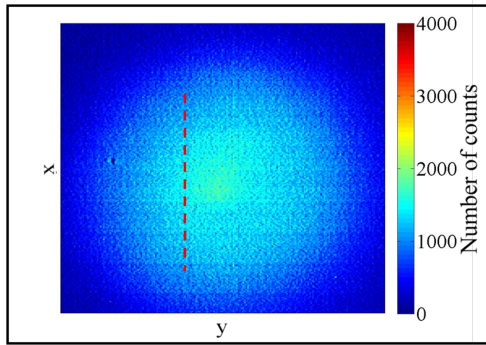
(c) **Signal from bare ZnO at** $0.80\,\mathrm{TW/cm}^2$**.**
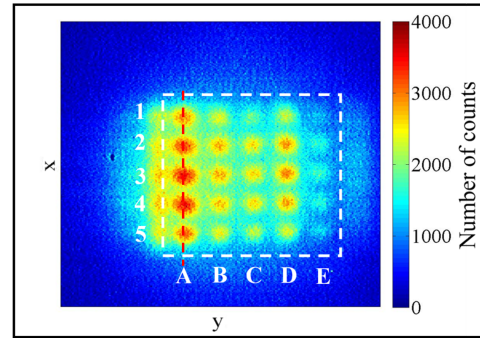
(d) **Signal from nanocones ZnO at** $0.80\,\mathrm{TW/cm}^2$**.**
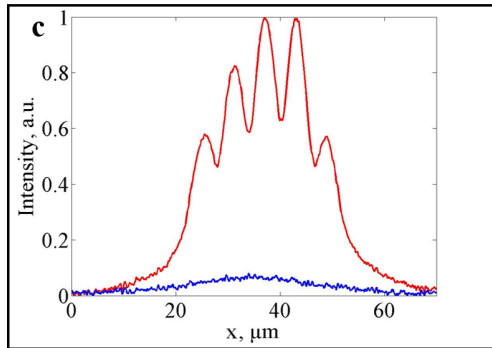
(e) **Intensity lineout along the dashed red line in (c) for** $0.35\,\mathrm{TW/cm}^2$**. The red and blue curves show the lineout for the nanocones and the bare crystal, respectively.**
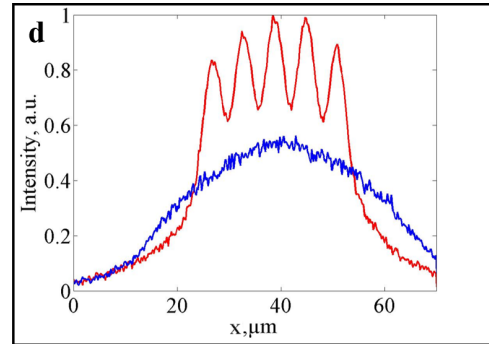
(f) **Intensity lineout along the red dashed line in (d) for** $0.80\,\mathrm{TW/cm}^2$**. The red and blue curves show the lineout for the nanocones and the bare crystal, respectively.**

Figure 4.9.: All images were obtained by imaging the signal transmitted through filter II (which covers the spectral range of H7) on the CCD camera. We compare the signal from the ZnO nanocones and the bare ZnO for different pump intensities.

93
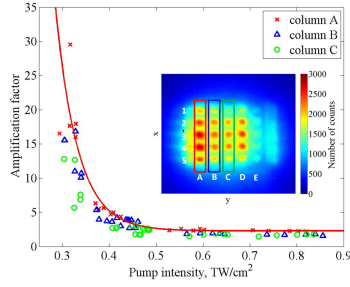
(a) Intensity-dependent enhancement factors for the signal measured with filter II. The enhancement factor of the nanocones with respect to the bare crystal decreases with increasing pump intensity.
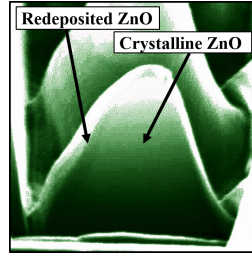
(b) Nanocones in column 5A have a thin layer of re-deposited matter (dark green) with a thickness of up to 300 nm.
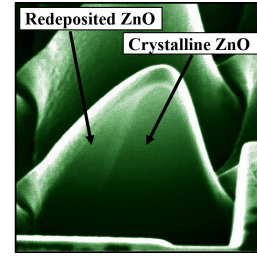
(c) Nanocones in column 5C have a thick layer of redeposited matter (light green) with a thickness of up to $1\,\mu$m.

Figure 4.10.: Intensity dependent enhancement factor for the signal measured with filter II and the impact of redeposition during FIB milling on the enhancement factor. Different columns of nanocones (indicated as A,B,C) show different enhancement factors.

pump intensity. So the enhancement factor is higher for weaker pump intensities which indicates a saturation effect with increasing pump intensity. Figs. 4.9(e) and 4.9(f) show an intensity lineout along column A of the nanocone array (see indications in Fig. 4.9(b) and Fig. 4.9(d)). While at low pump intensity (Fig. 4.9(e)) the signal from the bare crystal (blue curve) is much lower than the signal from the nanocones (red curve), this difference is much less striking for higher pump intensity (Fig. 4.9(f)). We note that the UV signal varies from one nano-source to the other. This is due to the various shapes of the nanocones and to the fact that each nanocone is seeded by a varying local intensity in the laser focal spot. We have studied the enhancement factor as a function of the laser intensity. The intensity-dependent enhancement factors for the signal measured with filter II from nanocones from columns A, B and C are displayed in Fig. 4.10(a). Each column has a given enhancement intensity dependence which is directly related to the sample fabrication process. Indeed, the nanocones milled at later times will deposit atoms on nanocones produced earlier. The amount of re-deposition increases from column A (last patterned column) to column E (first patterned column) and will create a layer (see Fig. 4.10(b) and 4.10(c)) that will affect the light coupling and will scatter the emitted harmonics leading to a lower enhancement. Thus, column A that has almost no re-deposition exhibits the highest enhancement whereas column E shows almost no enhancement. As a general trend, the enhancement factor increases when the nanocones quality increases, as illustrated in Fig. 4 from columns C to A, respectively. In column A, at an intensity of $0.35\,\mathrm{TW/cm^2}$ the local enhancement is high and reaches a maximum of 30 (strong enhancement regime). The enhancement decreases with increasing pump intensity and saturates (weak enhancement regime). Indeed, at high intensity, the signal emission saturates and a plateau is achieved.
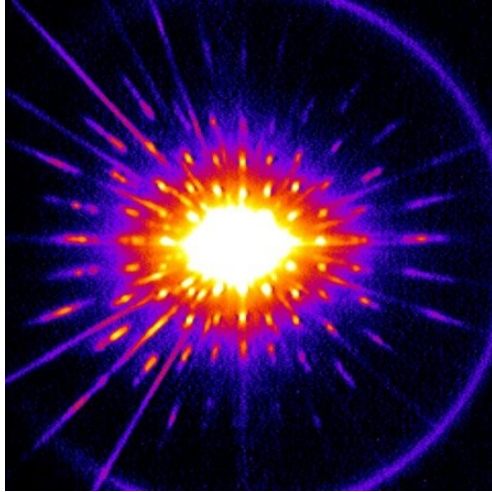
(a) **A plane close to the nanocone array is imaged on the camera for all harmonics and the luminescence.**
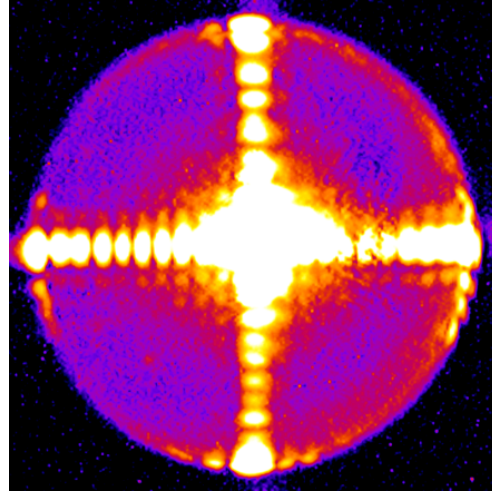
(b) **Signal transmitted through filter II: A plane far from the nanocone array is imaged on the camera.**

Figure 4.11.: Measured far field diffraction pattern of harmonics and luminescence emitted from an array of nanocones.

Although the beam size ($5000 \, \mu\mathrm{m}^2$ at FWHM) was much larger than the coupling base size of the array of nanocones ($300 \, \mu\mathrm{m}^2$) and only a fraction of the beam was enhanced, the total signal emitted by the 25 nanocones measured with filter II was almost one order of magnitude larger in the strong enhancement regime compared to the bare crystal.

The optical system is set to image the far field diffraction patterns produced by the emission of the array of nanocones. This is illustrated by the far field profiles shown in Fig. 4.11. The interaction length along the laser propagation axis is about a micron size so that each nanocone acts as a point-like source. In the far field, the spatial profile is a coherent superposition of the individual nano-sources. Due to the small size of the individual nano-sources, the divergence of the beam is extremely high. The images displayed in Figs. 4.11(a) and 4.11(b) are recorded by imaging different far field planes located after the sample. In Fig. 4.11(a) no filter has been used so that all the harmonics are collected by the detector. In this case, the comb of harmonics leads to a varying period of the interferometric peaks. In Fig. 4.11(b) the transmission through filter II is shown. This leads to regular diffraction peaks from the seventh harmonic signal. The actual data were taken with a low dynamic CCD camera which does not allow applying a phase retrieval algorithm to reconstruct the images of the nanocones. However, the near field imaging spatial resolution was enough to obtain the localization of the array of harmonic nano-sources.

Discussion

We investigated harmonic enhancement in an array of ZnO nanocones with a $3.2\,\mu$m OPCPA system. We found that the signal transmitted through filter II is much stronger from the nanocones than from the bare crystal. This enhancement decreases with increasing pump intensity and eventually saturates. A spectrum measured from bare ZnO [0001] crystal is shown in Fig. 4.12. We identify the third (H3), fifth (H5), seventh

Figure 4.12.: Harmonic spectrum measured from ZnO [0001]. One can see H3 (1030 nm), H5 (635 nm), H7 (442 nm), H9 (344 nm) and the luminescence. The green vertical lines show the transmission bandwidth of filter II (app. D, transmission range from 425 nm - 475 nm) that was used for systematic measurements of H7.

(H7) and ninth (H9) harmonics. We observe further signals that can be identified as incoherent luminescence which consists of two main parts. The first part is centered at 385 nm and corresponds to the band edge of ZnO. The second part is centered at around 500 nm and is related to defect states such as oxygen vacancies [133]. It turns out that the luminescence has a broad bandwidth and that H7 is totally immersed in its tail. The transmission range of filter II is indicated by the vertical green lines. Its bandwidth covers both H7 and the luminescence. So in the frame of this experiment we could not determine whether the enhanced signal measured with filter II is H7 or the luminescene.

Due to our detection system we were limited to H9. In sec. 4.3 we study high harmonic enhancement with an improved detection system and a further improved nanocone geometry in order to demonstrate enhancement of higher harmonic orders. The second generation of nanocones is designed to have high enhancement at the output surface which seems to be more favourable for the enhancement of harmonics. High harmonics generated inside the nanocone are absorbed before being coupled out (above-bandgap harmonics are absorbed within a few tens of nanometers).

4.3. Experiment at IOGS: Second design

We have previously investigated the enhancement of HHG in an array of ZnO nanocones with a $3.2\,\mu$m OPCPA system (sec. 4.2). We showed that the FIB patterning was not optimized and that the nanocones suffered from redeposition which decreased the signal enhancement. Our study focused on H7 which was difficult to disentangle from the luminescence. Furthermore, we were limited by our detection system to H9. In the experiment described in this section we investigate the enhancement of high harmonics of a $3.1\,\mu$m beam in ZnO nanocones with an improved design. Redeposition during FIB milling is strongly reduced and the nanocone geometry was optimized in order to have high enhancement of the fundamental beam at the nanocone-air interface. We use an improved detection system which allows us to detect higher harmonics up to H15 that are far from the luminescence. The experiment was carried out at 'Institut d'Optique Graduate School' (IOGS) in Palaiseau in collaboration with the group of Dr. Marc Hanna in March/April 2017.

Laser system and setup

The laser is an OPCPA system delivering an idler at $3.1\,\mu$m wavelength and an energy of $10\,\mu$J per pulse at 125 kHz repetition rate. For more details about the laser system we refer to the app. C and to [102]. A layout of the experimental setup is shown in Fig. 4.13. The $3.1\,\mu$m pump beam was attenuated to energies in the range $0.1 - 2\,\mu$J and focused to a spot size of focal spot size $63\,\mu$m (FWHM). The focal spot has been measured with the knife-edge method. We work at normal incidence. Intensities lie in the range of $0.04 - 0.5\,\mathrm{TW/cm^2}$. The nanostructures are at the output surface of the crystal. For detection, the harmonic radiation emitted from the nanocones can be focused either onto a CMOS camera (Photon Lines, PCO) or into a spectrometer (Ocean Optics, QE-pro). Both detection devices can be cooled which allows to decrease the noise level and to measure weak signals (tab. 4.1). We focus the harmonics with a
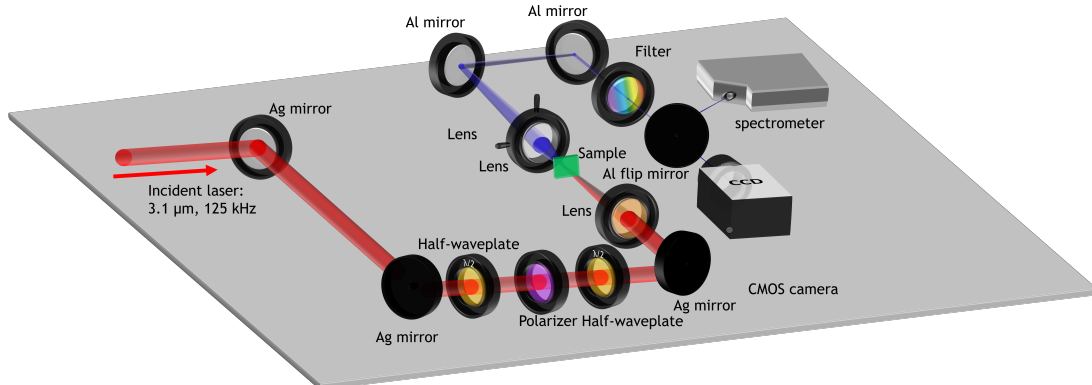
Figure 4.13.: Layout of experimental setup: The pump beam (red) is focused into the sample and the harmonics (blue) are measured in transmission.

lens on a translation stage which means that the coupling of each harmonic needs to be optimized separately. Different harmonic orders are selected by transmission filters. More details about the filters used in this experiment can be found in app. D.

FDTD simulations and sample properties

We simulate the enhancement of a $3.1\,\mu$m beam in ZnO nanocones by using FDTD simulations with Lumerical Solutions (app. B). The optimized design that has high enhancement at the output surface close to the tip is shown in Fig. 4.14. Basis size and

(a) **Enhancement in isolated nanocone in x-z-plane.**

(b) **Enhancement in isolated nanocone in y-z-plane.**

(c) **Enhancement in isolated nanocone in x-y-plane at height of maximum enhancement.**

(d) **Enhancement in array of nanocones with $12\,\mu$m periodicity in x-z-plane.**

(e) **Enhancement in array of nanocones with $12\,\mu$m periodicity in y-z-plane.**

(f) **Enhancement in array of nanocones with $12\,\mu$m periodicity in x-y-plane at height of maximum enhancement.**

Figure 4.14.: Intensity enhancement of a $3.1\,\mu$m beam in ZnO nanocones with $6.5\,\mu$m height and a $7.5\,\mu$m broad basis. We study isolated nanocones (a) - (c) and an array of nanocones with $12\,\mu$m periodicity (d) - (f).

height of the nanocones are $7.5\,\mu$m and $6.5\,\mu$m, respectively. The enhancement in an isolated nanocone in the x-z, y-z and x-y-plane is shown in Figs. 4.14(a), 4.14(b) and 4.14(c), respectively. The intensity enhancement reaches a maximum value of 13 and is located in different fragments in the upper half of the nanocone. The enhancement in the x-y-plane is shown at the height where the maximum enhancement occurs ($5.2\,\mu$m above the base line). The intensity enhancement for an array of nanocones with a periodicity of $12\,\mu$m in the x-z, y-z and x-y-plane is shown (as a zoom on one single cone) in Figs. 4.14(d), 4.14(e) and 4.14(f), respectively. The enhancement is slightly higher than for an isolated cone and reaches a maximum value of 20. However, the

intensity distribution is similar to the isolated case. The maximum enhancement in an array of nanocones occurs as for the isolated case $5.2\,\mu$m above the base line. We conclude that the collective effect is rather small.

The sample used for this measurement is shown in Fig. 4.15. Arrays of 5 nanocones with the dimensions indicated above were produced at the surface of a $500\,\mu$m thick ZnO [0001] crystal by focused ion beam milling (FIB, app. A) at CSNSM lab at Orsay. The fabrication was optimized with respect to the nanocones described in sec. 4.2 such that almost no redeposition of matter occurs. The redeposition was minimized by scanning the ion beam several times over the crystal surface such that the nanostructures were produced gradually rather than in one single run.

(a) **SEM-image taken at** $0°$.

(b) **SEM-image taken at** $45°$.
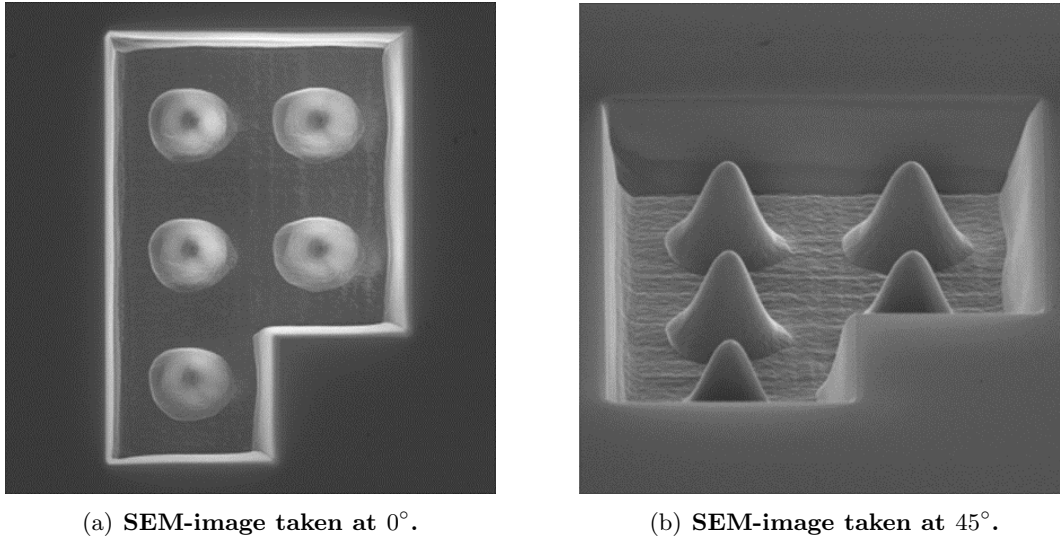
Figure 4.15.: SEM-images of the nanostructures used in this experiment. 5 nanocones with a a height of $6.5\,\mu$m **and a basis of** $7.5\,\mu$m **are arranged in an array with a periodicity of** $12\,\mu$m**.**

Measurements

We use a spectrometer and a CMOS camera with high sensitivity in the UV to analyze the spectrum of the harmonic radiation and the local enhancement of each nanocone.

Spectral measurements

A complete harmonic spectrum from the nanostructures measured at an intensity of $0.5\,\mathrm{TW/cm^2}$ ranging from H3 to H15 is shown in Fig. 4.16. For the measurement, the nanostructures were placed in the center of the beam and each harmonic order was measured separately by the use of an adapted transmission filter (more informations about these filters can be found in app. D). The below-bandgap harmonics H3 - H7 are separated from the above-bandgap harmonics by the luminescence from the band edge
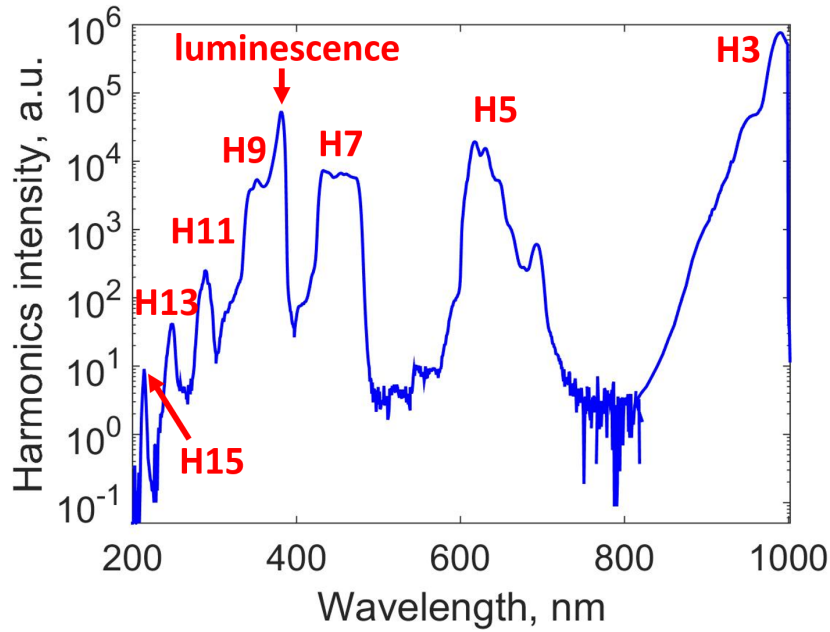
Figure 4.16.: Full harmonic spectrum ranging from H3 to H15 including the photoluminescence at 385 nm generated in an array of ZnO nanocones at a pump intensity of $0.5\,\mathrm{TW/cm^2}$**.**

which is centered at 385 nm. H3 was not entirely covered by the spectral range of the spectrometer. The harmonic intensity is decreasing with increasing harmonic order. The coupling of the luminescence to the spectrometer was not optimized, it was rather detected as a parasitic signal when measuring H9. We note that the luminescence is stronger than H7 and H9. In our systematic studies of the harmonic enhancement factors we mainly focused on H7 and H9.

In the following we show systematic measurements from the bare crystal and from the nanocones made with filters II and III that cover the spectral range of H7 and H9, respectively. We investigate the evolution of the harmonic signal and the luminescence for different pump intensities. The signal measured behind filter II from the bare crystal for four different intensities is shown in Fig. 4.17(a). The curves are all normalized. At low intensity ($0.04\,\mathrm{TW/cm^2}$, blue curve), the threshold for seventh harmonic generation is not reached and H7 cannot be detected. H7 is observed for intensities above $0.1\,\mathrm{TW/cm^2}$. Measurements at $0.18\,\mathrm{TW/cm^2}$ show a signal centered at 450 nm that can clearly be identified as H7 (green curve in Fig. 4.17(a)). However, when increasing the pump intensity further, the signal becomes much broader (red and cyan curve). The nonlinear refractive index (n_2) of ZnO is high, which might lead to distortions of the fundamental beam at high intensity that can inhibit harmonic generation. The red and the cyan curve follow the transmittivity of filter II (dashed magenta curve), which leads us to the conclusion that the total signal is even broadener and only the part covered by the bandwidth of the filter is measured.

When moving on to the nanostructures a signal can be detected even at lowest intensity
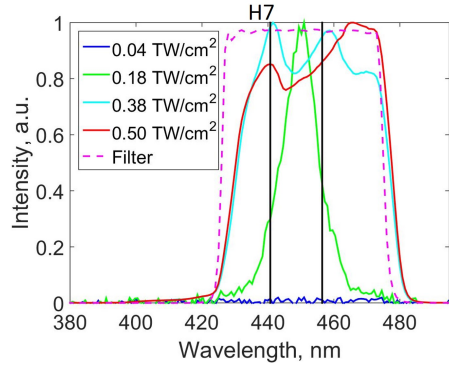
(a) **Measured signal from the bare crystal by employing filter II for different intensities.**
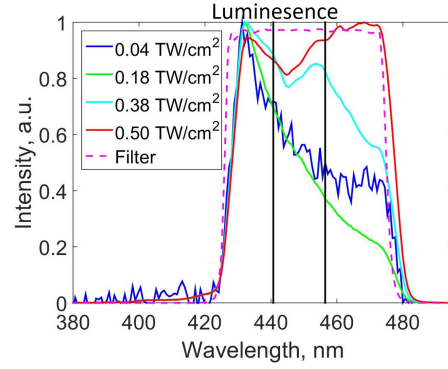
(b) **Measured signal from the nanocones by employing filter II for different intensities.**
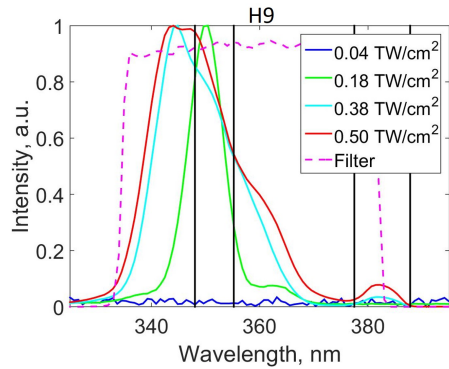
(c) **Measured signal from the bare crystal by employing filter III for different intensities.**
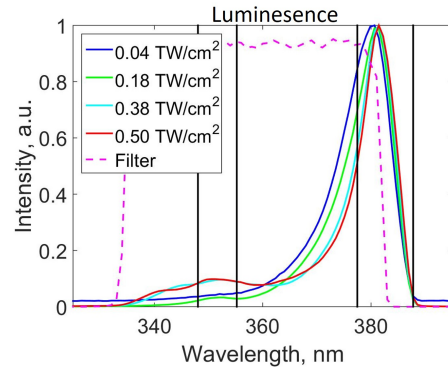
(d) **Measured signal from the nanocones by employing filter III for different intensities.**

Figure 4.17.: Transmission of two different filters (red curve) and measured signal (blue curve).

$(0.04\,\mathrm{TW/cm^2})$ where no signal was measured from the bare crystal. We believe that this signal which steadily decreases in intensity towards longer wavelength is the tail of the luminescence from the band edge transmitted through the filter. We already saw in earlier experiments that the luminescence can be extremely broad (sec. 4.2). The shape of this signal stays unchanged when increasing the intensity to $0.18\,\mathrm{TW/cm^2}$. However, as for the bulk crystal, the signal broadens and is almost identical with the transmittivity curve of filter II.

H9 and luminescence from the bulk crystal for different pump intensities are shown in Fig. 4.17(c). The transmittivity of filter III is represented by the dashed magenta curve. H9 is centered at 357 nm and the luminescence around 38(nm. At low pump intensity $(0.04\,\mathrm{TW/cm^2})$, no signal can be detected (blue curve). When increasing the intensity to $0.18\,\mathrm{TW/cm^2}$, H9 (357 nm) but no luminescence signal is detected. When increasing the intensity further, a weak luminescence signal appears (385 nm).

101
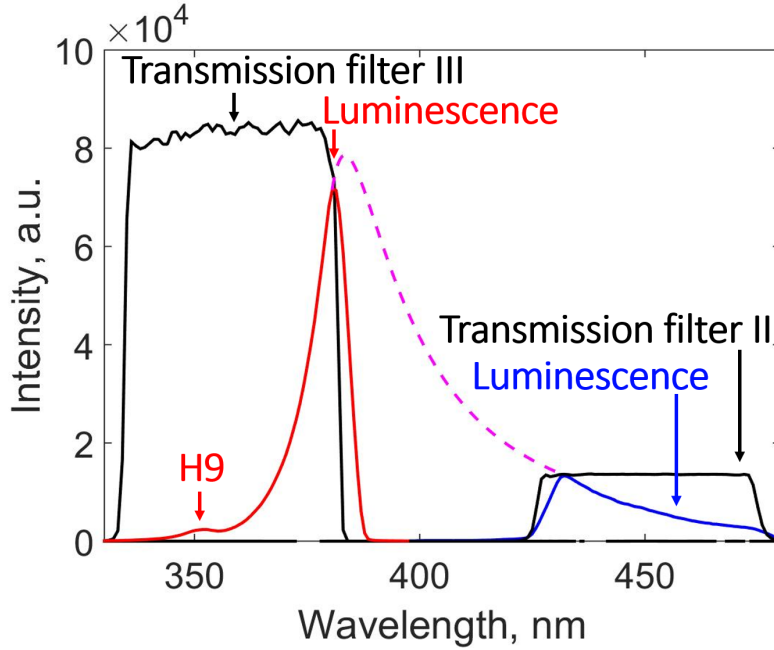
Figure 4.18.: Measurement of H9 (357 nm, red curve) and the luminescence from the band edge (385 nm, red curve) with filter II and of the luminescence from the band edge measured with filter III (blue curve). Both signals were measured at $0.18\,\text{TW/cm}^2$. The magenta dashed line displays a possible shape of the luminescence spectrum.

At the same time, H9 changes shape and broadens. For the entire intensity range H9 is much stronger than the luminescence. At lowest intensity ($0.04\,\text{TW/cm}^2$), a strong luminescence signal and no H9 is detected from the nanostructures (Fig. 4.17(d)). At $0.18\,\text{TW/cm}^2$, H9 appears in the tail of the luminescence. The spectral profile of the luminescence is steepened and slightly shifted to longer wavelengths for increasing intensity. For the entire intensity range, the luminescence is much stronger than H9 when generated in the nanostructures. To emphasize our argument that the signal observed in Fig. 4.17(b) is the luminescence, we plot the signal from the nanocones measured at $0.18\,\text{TW/cm}^2$ with filters II and III (Figs. 4.17(b) and 4.17(d)), respectively, in the same graph. The result is shown in Fig. 4.18. The transmittivity of filters II and III is shown in black. The pink line combines the signals measured with the two different filters and shows a possible shape of the luminescence spectrum. Since during the experiment we were mainly interested in the harmonics, we did not take separate measurements of the luminescence with an adapted filter.

Fig. 4.19 shows the intensity-dependence of different harmonic orders (H5, H7, H9, H11, H13) and of the luminescence both from the bare crystal and from the nanostructures. For the analysis, a small slice around the center of the corresponding spectrum was selected (as shown for H7, H9 and the luminescence by the black vertical lines in Fig. 4.17) and the intensity within this slice was averaged. The integration time of the spectrometer was veried between 5 s and 20 s. So each point in Fig. 4.19 correponds

(a) **H5.** (b) **H7 and luminescence.** (c) **H9 and luminescence.**

(d) **H11.** (e) **H13.** (f) **Luminescence.**
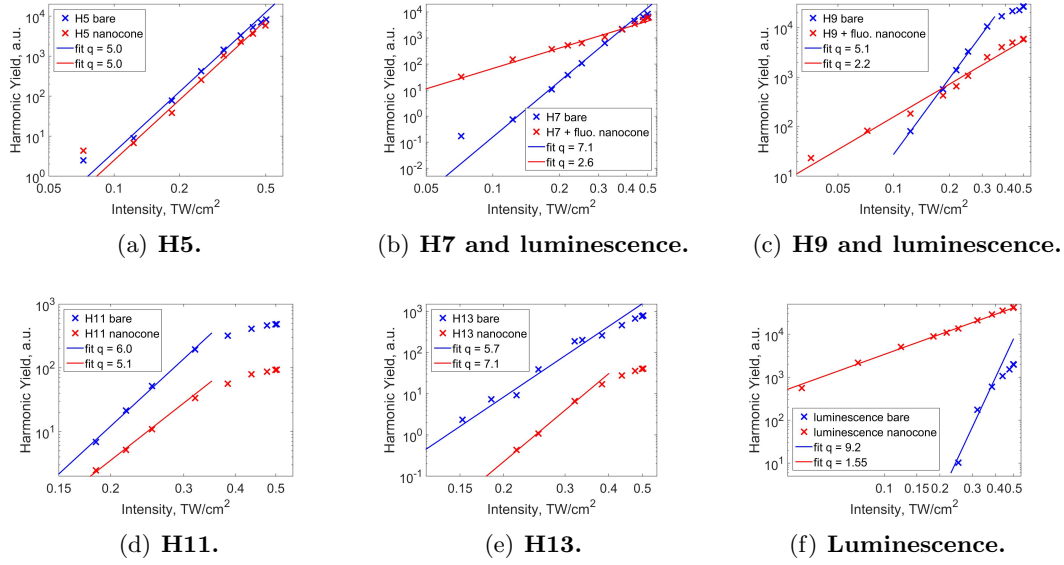
Figure 4.19.: Measurements of harmonic radiation and luminescence from the bare crystal (blue crosses) and the nanocones (red crosses).

to an accumulation of 625000 - 2500000 pulses. H5 from the bare crystal and from the nanostructures are shown as blue and red crosses in Fig. 4.19(a). For this measurement filter I was used. It can be seen that H5 grows with increasing pump intensity. For the whole intensity range that was investigated, H5 is slightly stronger from the bare crystal than from the nanocones. For the below-bandgap harmonics (H3, H5, H7), we expect a perturbative scaling law (eq. 2.3). When fitting the scaling law to the measured values we obtain a value of q = 5.0 for both H5 from the nanostructures and from the bare crystal as expected for a nonlinear signal of fifth order. Around $0.4 \, \mathrm{TW/cm^2}$ generation of H5 starts to saturate. The power dependence of H7 (measured with filter II) is shown in Fig. 4.19(b). The signal from the bare crystal is weaker at low intensities, but becomes stronger than the signal from the nanostructures for intensities higher than $0.4 \, \mathrm{TW/cm^2}$. As was seen in Fig. 4.17(b), it is the luminescence rather than H7 that was enhanced at low intensities. While the luminescence is stronger from the nanocones compared to the bare crystal, it is the opposite case for H7. When fitting a polynomial, we obtain q = 7.1 for the bare crystal which is in good agreement with q = 7 predicted theoretically. The signal from the nanostructures has q = 2.6. The power law of H9 is shown in Fig. 4.19(c). While at low intensities the signal of the nanostructures is stronger than the signal from the bare crystal, this ratio is inversed for intensities above $0.2 \, \mathrm{TW/cm^2}$. As was seen in Fig. 4.19(b) it is the luminescence that is enhanced at low intensities and not H9. H9 is weaker from the nanocones than from the bare crystal. If H9 was a perturbative harmonic, we would expect q = 9. But H9 is an above-bandgap harmonic. We extract q = 5.1 for the bare crystal. For the signal from the nanostructures which is a combination of both H9 and luminescence we get q = 2.2. Measurements of H11 (filter IV was used) and H13

103

(filter V was used) are shown in Figs. 4.19(d) and 4.19(e), respectively. Over the entire intensity range H11 and H13 are much stronger from the bulk crystal than from the nanostructures, no enhancement occurs. From the bare crystal we obtain q = 6.0 and from the nanostructures q = 5.1 for H11. For H13 it is q = 5.7 and q = 7.1, respectively. The luminescence is strongly enhanced in the nanocones over the entire intensity range. The generation of luminescence is a multiphoton process. Approximately 9 photons of 3.1 μm wavelength are needed to raise an electron from the valence band to the conduction band. Hence we expect q $\approx$ 9, which is in good agreement with the value obtained from the fit (q = 9.2). The luminescence from the nanocones has a value of q = 1.55. For below-bandgap harmonics and the luminescence from the bare crystal the value for q is close to the value predicted by eq. 2.3. For above-bandgap harmonics the situation is more complicated and no comprehensive theory is available yet. We saw that q has smaller value for the nanostructures than for the bare crystal for a given harmonic order (same for the luminescence). We believe that due to the local enhancement in the nanocones above-bandgap harmonic generation is in the saturation regime which leads to a smaller slope of the power law.

Camera measurements

We imaged the UV radiation on a CMOS camera in order to better understand the local enhancement behaviour. While the spectral measurements discussed earlier provide spectral information camera measurements allow to determine the local enhancement behaviour of an individual nanocone. Measurements employing filter II are shown in Fig. 4.20(a) for the nanocones and in Fig. 4.20(b) for the bare crystal at an intensity of 0.1 TW/cm^2. One can clearly see the 5 individual nanoemitters (the corresponding SEM-image is shown in Fig. 4.15). The boundaries of the array of nanocones are indicated by the white dashed lines. No signal at all could be detected from the bare crystal at the same intensity. Due to the spectral measurements discussed earlier we know that the signal from the nanocones is the enhanced tail of the luminescence. A similar behaviour is observed when employing filter III. No signal at all is observed from the bare crystal at 0.1 TW/cm^2. So neither H9 nor luminescence are generated. When moving on to the nanostructures, a strong signal is observed, which can be identified as the luminescence due to the spectral measurements.

(a) **Signal from nanocones meas. with filter II.**

(b) **Signal from bare crystal meas. with filter II.**

(c) **Signal from nanocones meas. with filter III.**

(d) **Signal from bare crystal meas. with filter III.**
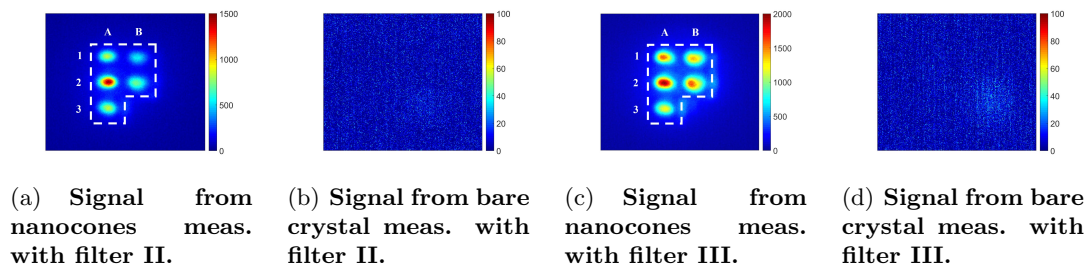
Figure 4.20.: Signal from nanocones and bare crystal generated at 0.1 TW/cm^2 **an measured with filters II and III, respectively.**

By comparing the camera measurements made with filter III from the nanocones and the bare crystal, we can extract approximate values of the local enhancement factors for the luminescence. The intensity-dependent enhancement factors of the luminescence in the nanocones are shown in Fig. 4.21. At low intensity the luminescence is strongly enhanced by more than three orders of magnitude. The enhancement decreases with increasing pump intensity and eventually saturates around $0.4\,\mathrm{TW/cm^2}$.
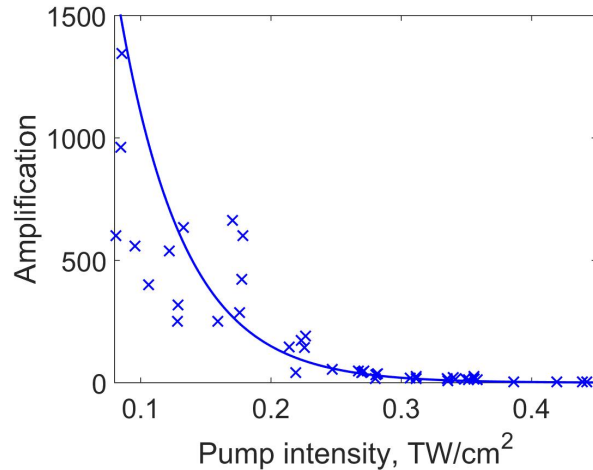
Figure 4.21.: Intensity-dependent enhancement factors of the luminescence measured with filter III.

Polarization measurements

The goal was to investigate the polarization dependence of H7 and H9. However, as was shown in the analysis above H7 and H9 are superposed by a luminescence signal. We will use the polarization measurements to discriminate between luminescence and harmonic signals and to evaluate their relative yield. For linear pump polarization a harmonic signal is linearly polarized and the luminescence unpolarized. However, for a circularly polarized pump beam harmonic generation vanishes but the luminescence yield and its polarization properties remain unchanged with respect to linear polarization. We use the CMOS camera for our measurements. For the measurements from the bare crystal and the nanostructures a pump intensity of $0.48\,\mathrm{TW/cm^2}$ and $0.025\,\mathrm{TW/cm^2}$ was used, respectively. We use a linearly polarized pump beam and measure the signal generated in the bare crystal with filter II (app. D). The result is shown in Fig. 4.22(a). For circular polarization (Fig. 4.22(b)), the signal decreases by more than two orders of magnitude with respect to linear polarization. The residual signal at circular polarization might come from the tail of the luminescence that is transmitted through filter II. But even an imperfect circular polarization could lead to a small residual of H7. For a linearly polarized pump beam, the signal measured from the nanocones with filter II is shown in Fig. 4.22(c). The signal emitted from the nanocones slightly decreases by around 20 % when moving to circular polarization.

105

(a) **Signal from bare crystal at $\epsilon = 0$.**

(b) **Signal from bare crystal at $\epsilon = 1$.**

(c) **Signal from nanocones at $\epsilon = 0$.**

(d) **Signal from nanocones at $\epsilon = 1$.**

(e) **Signal from bare crystal vs. ellipticity.**

(f) **Signal from nanocones vs. ellipticity ϵ.**
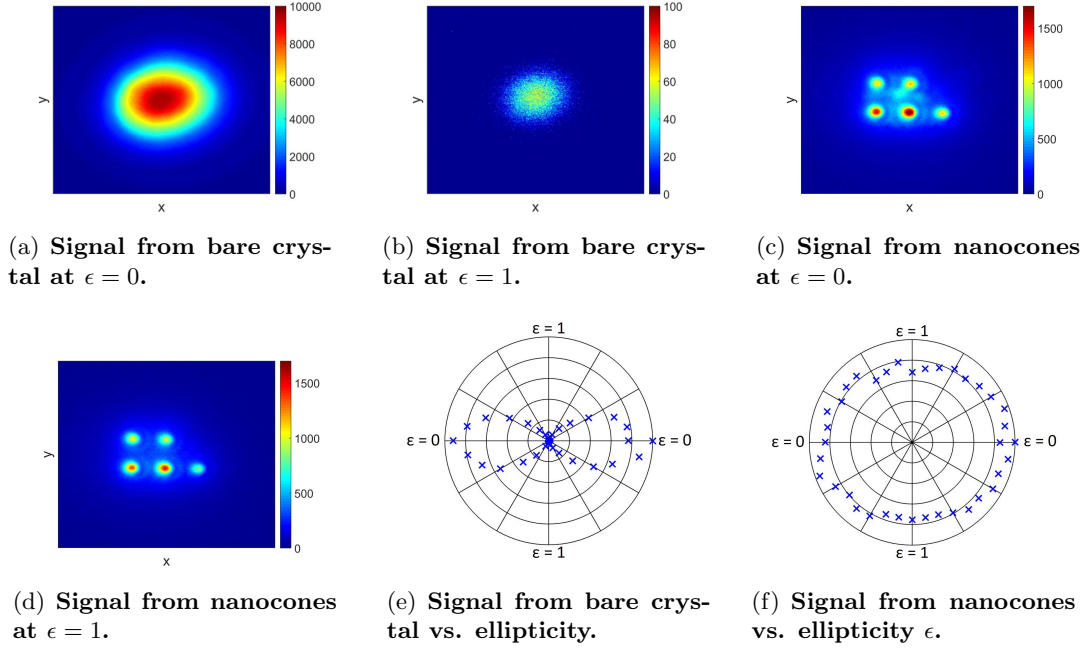
Figure 4.22.: Images taken from the bare crystal (a), (b) and the nanocones (c), (d) by employing filter II. Systematic measurements of the signal of the bare crystal and the nanocones in dependence on the ellipticity are shown in (e) and (f), respectively.

The signal emitted from the space between the nanocones visible at linear polarization decreases at circular polarization. In agreement with the spectral measurements, the polarization measurements indicate that it is indeed the luminescence that is strongly enhanced in the nanocones, rather than the harmonic radiation (Fig. 4.17). This explains the insensitivity of the signal from the nanocones to ellipticity. The small variation of the signal with ellipticity might be due to a small portion of H7 that is generated in the nanocones in addition to the luminescence. Polar plots of the signal from the bare crystal and the nanocones are shown in Figs. 4.22(e) and 4.22(f), respectively. Measurements with filter III (app. D) at linear polarization from the bare crystal are shown in Fig. 4.23(a). For circular polarization (Fig. 4.23(b)), the signal decreases by more than two orders of magnitude with respect to linear polarization. The signal is indentified to be H9. The residual signal might be due to the fact that the polarization is not perfectly circular. Another possibility is that it is luminescence. The signal measured at linear polarization with filter III from the nanocones is shown in Fig. 4.23(c). It does not change at all when moving on to circular polarization (Fig. 4.23(c)). As in the case for the measurement made with filter II, we deduce from the spectral measurements that it is mostly the luminescence that is emitted from the nanocone (Fig. 4.17). Polar plots of the signal from the bare crystals and the nanocones made with filter III are shown in Figs. 4.23(e) and 4.23(f), respectively.

In the next step, we analyze the polarization of the generated radiation. We use an

(a) **Signal from bare crystal at $\epsilon = 0$.**

(b) **Signal from bare crystal at $\epsilon = 1$.**

(c) **Signal from nanocones at $\epsilon = 0$.**

(d) **Signal from nanocones at $\epsilon = 1$.**

(e) **Signal from bulk ZnO vs. ellipticity.**

(f) **Signal from ZnO-nanocones vs. ellipticity.**
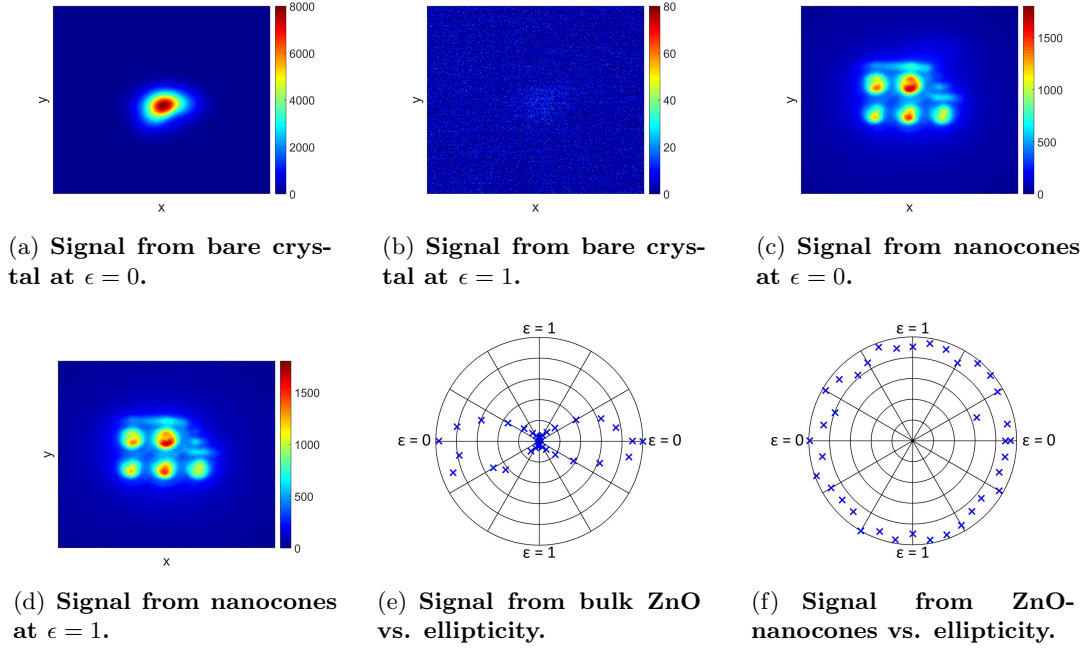
Figure 4.23.: **Images taken from the bare crystal (a), (b) and the nanocones (c), (d) by employing filter III. Systematic measurements of the signal of the bare crystal and the nanocones in dependence on the ellipticity are shown in (e) and (f), respectively.**

analyzer between sample and spectrometer to study the polarization of the generated radiation for four different ellipticity values of the pump beam ($\epsilon = 0, 0.27, 0.58, 1.0$). Fig. 4.24(a) shows the analysis of the polarization of the signal measured with filter II generated in the bare crystal at $\epsilon = 0$. It turns out the the beam is mostly linearly polarized. The ratio of maximum and minimum transmission of the harmonic beam through the analyzer is 30. However, at no angle of the analyzer the transmission disappears totally, indicating that the polarization is not purely linear. The unpolarized part of the signal might be the luminescence. Another possibility would be that the pump beam is not perfectly linear which leads to a H7 signal which is slightly elliptical. When increasing the ellipticity, the signal yield decreases (Fig. 4.22(e)). At the same time, the polarization properties change. The harmonic beam becomes elliptically polarized which leads to a decreasing ratio of maximum an minimum transmission through the analyzer. In addition to H7, we might generate a small amount of luminescence. This behaviour becomes more evident when increasing the ellipticity of the pump beam further (Fig. 4.24(c)). The signal yield decreases and it has almost an equal amount of polarization along x and y. This might be either a small residual of H7 with a high degree of ellipticity or the luminescence. The analysis of the polarization of the signal emitted from the nanocones at $\epsilon = 0$ is shown in Fig. 4.24(e). One part of the signal is unpolarized, which is ascribed to the luminescence which is strongly enhanced in the nanocones with respect to the bare crystal (Fig. 4.17). It is super-

(a) **H7 bulk,** $\epsilon = 0$. (b) **H7** **bulk,** $\epsilon = 0.27$. (c) **H7** **bulk,** $\epsilon = 0.58$. (d) **H7 bulk,** $\epsilon = 1.0$.

(e) **H7** **nanocone,** $\epsilon = 0$. (f) **H7** **nanocone,** $\epsilon = 0.27$. (g) **H7** **nanocone,** $\epsilon = 0.58$. (h) **H7** **nanocone,** $\epsilon = 1.0$.
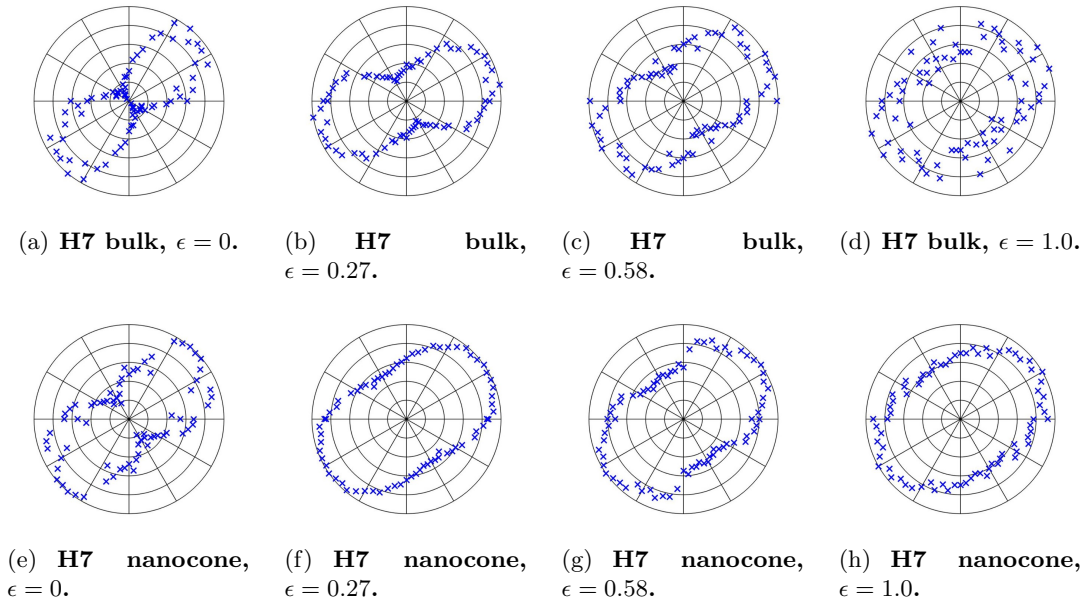
Figure 4.24.: Analysis of the polarization state of the signal measured with filter II from bulk and nanocones for different ellipticties $\epsilon = 0, 0.27, 0.58, 1.0$.

posed by the signal of H7 which is at least partially linearly polarized. For increasing ellipticity the ratio of maximum and minimum transmission through the analyzer decreases. At $\epsilon = 1$, the generated beam turns out to be not completely unpolarized, which suggests that there is another signal beside the luminescence (which is always unpolarized). So a small part of the detected signal should be H7. The fact that a circularly polarized pump beam allows for the generation of a harmonic signal in the nanocones might be explained by the fact that the nanocone is not perfectly rotation-symmetric which leads to an effective filtering of the polarization. Furthermore, even the edges of the array of nanocones can have a polarization-dependent enhancement which can lead to harmonic generation.

The polarization analysis of H9 is shown in Fig. 4.25. H9 from the bulk crystal for $\epsilon = 0$ is linearly polarized (Fig. 4.25(a)). In contrast to H7, H9 seems to be completely linearly polarized. At certain angles of the analyzer, no signal at all could be detected with the camera. From the bulk crystal, the behaviour of H9 is similar to H7 when increasing the ellipticity. The harmonic beam becomes elliptically polarized. The signal measured from the nanostructures generated from linear polarization (Fig. 4.25(e)) consists of an unpolarized part which is ascribed to the luminescence and a polarized part which is ascribed to H9. When increasing the ellipticity up to $\epsilon = 1$, the behaviour stays almost unchanged. Even though the total signal generated in the nanocones does not depend on the degree of ellipticity (Fig. 4.23(f)), which suggests that it is mostly luminescence, the signal is not totally unpolarized. This affirms the theory that in addition to the luminescence, H9 is generated in the nanocones from elliptical and circular polarization due to the polarization filtering mentioned above.

108

(a) **H9 bulk,** $\epsilon = 0$.   (b) **H9 bulk,** $\epsilon = 0.27$.   (c) **H9 bulk,** $\epsilon = 0.58$.   (d) **H9 bulk,** $\epsilon = 1.0$.

(e) **H9 nanocone,** $\epsilon = 0$.   (f) **H9 nanocone,** $\epsilon = 0.27$.   (g) **H9 nanocone,** $\epsilon = 0.58$.   (h) **H9 nanocone,** $\epsilon = 1.0$.
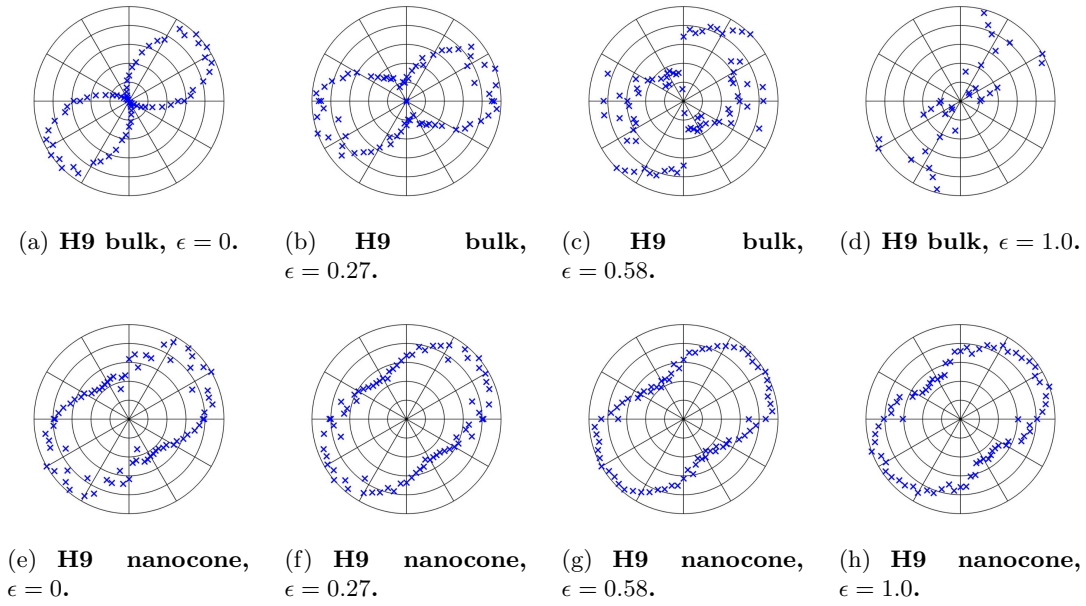
Figure 4.25.: Analysis of the polarization state of the signal measured with filter III from bulk and nanocones for different ellipticties $\epsilon = 0, 0.27, 0.58, 1.0$.

Discussion

We generated up to H15 in ZnO bulk and nanocones. Compared to the experiment described in sec. 4.2 we observed higher harmonic orders due to an improved detection system. FDTD simulations showed that the fundamental beam is enhanced at the output surface of the nanocones which is necessary for enhancing above-bandgap harmonics. All harmonics emitted by the nanostructures appear weaker with respect to the bulk when measured with the spectrometer. But this is be due to the fact that the spectrometer collects and sums up the total signal emitted from the sample. For extracting the local enhancement factor of an individual nanocone one needs to take into acount the effective emission surface. While the coupling area of 5 nanocones is $220\,\mu\mathrm{m}^2$ it is $3100\,\mu\mathrm{m}^2$ for the bare crystal (the diameter of the pump beam in the focus is $63\,\mu\mathrm{m}^2$). When normalizing the harmonic signal to the effective emission area of the nanocones, enhancement might be observed. We believe that the harmonics are mostly generated in the nanocones and much less in the space between the cones. As could be seen in the SEM-image of the nanostructures shown in Fig. 4.15, the crystal surface between the nanocones is rough (caused by FIB milling) and is supposed to scatter harmonic radiation such that it can not be detected. This justifies the suggested normalization. We saw that the luminescence from the band edge (385 nm) is strongly enhanced by several orders of magnitude at low pump intensity (without having applied the suggested normalization to the effective emission area). The enhancement decreases with increasing pump intensity and eventually saturates. In the experiment described in sec. 4.4 we exactly match the size of the laser focal spot to the nanocone surface entrance.

4.4. Experiment at CEA: Third design

In sec. 4.3 we observed the generation of up to H15 of a $3.1\,\mu$m pump beam in an array of ZnO nanocones. Only a small part of the beam interacted with the nanostructures which made it difficult to deduce enhancement factors of the nanocones with spectral measurements. In the experiment described in this section we investigate enhancement of HHG in truncated ZnO nanocones with a femtosecond fiber laser operating at $2.1\,\mu$m wavelength and 18.66 MHz repetition rate. In order to optimize the coupling geometry, we focus the entire pump beam into one single nanocone. The outcoupling efficiency of the harmonics is maximized by using truncated nanocones as a new design. The experiment was carried out at 'CEA Saclay' in Saclay in June/July 2017.

Laser system and setup

The laser used in this experiment is a fiber laser from NOVAE. The operating wavelength is $2.1\,\mu$m, the pulse duration 85 fs, the repetition rate 18.66 MHz and the maximum pulse energy 8.7 nJ. For more details about the laser system we refer to app. C. The laser is focused with an off-axis parabola (f = 25 mm) into the sample to
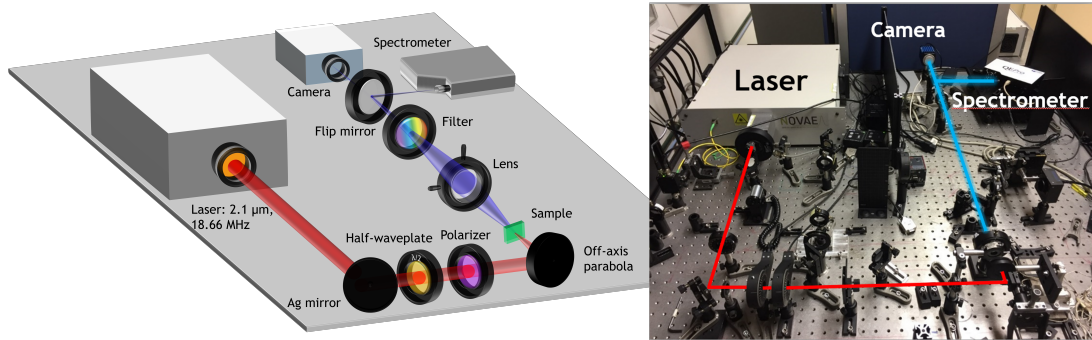
Figure 4.26.: Layout and picture of the experimental setup.

a spot size of $5.9\,\mu$m (FWHM). We work at normal incidence. Due to the small spot size almost the whole beam couples into the nanocone which has a base size of $4.1\,\mu$m. The pulse energy can be attenuated by means of a half-waveplate and a polarizer. The accessible intensity range used in this experiment is $0.02 - 0.2\,\mathrm{TW/cm^2}$. The beam is focused into the sample and the harmonic radiation is measured in transmission with a spectrometer or a CMOS camera. Different transmission filters are used to select different harmonic orders. Details about the filters can be found in app. D.

FDTD simulations and sample properties

We calculate the enhancement of a $2.1\,\mu$m beam in an isolated truncated ZnO nanocone by using FDTD simulations with Lumerical Solutions (app. B). The simulated intensity enhancement is shown in Fig. 4.27. The enhancement is very fragmented and

(a) **Enhancement in the x-z-plane.**

(b) **Enhancement in the y-z-plane.**

(c) **Enhancement in the x-y-plane at the height of maximum enhancement.**

(d) **Enhancement in the x-y-plane 50 nm below the output surface.**

(e) **SEM-image at $0°$.**

(f) **SEM-image at $60°$.**
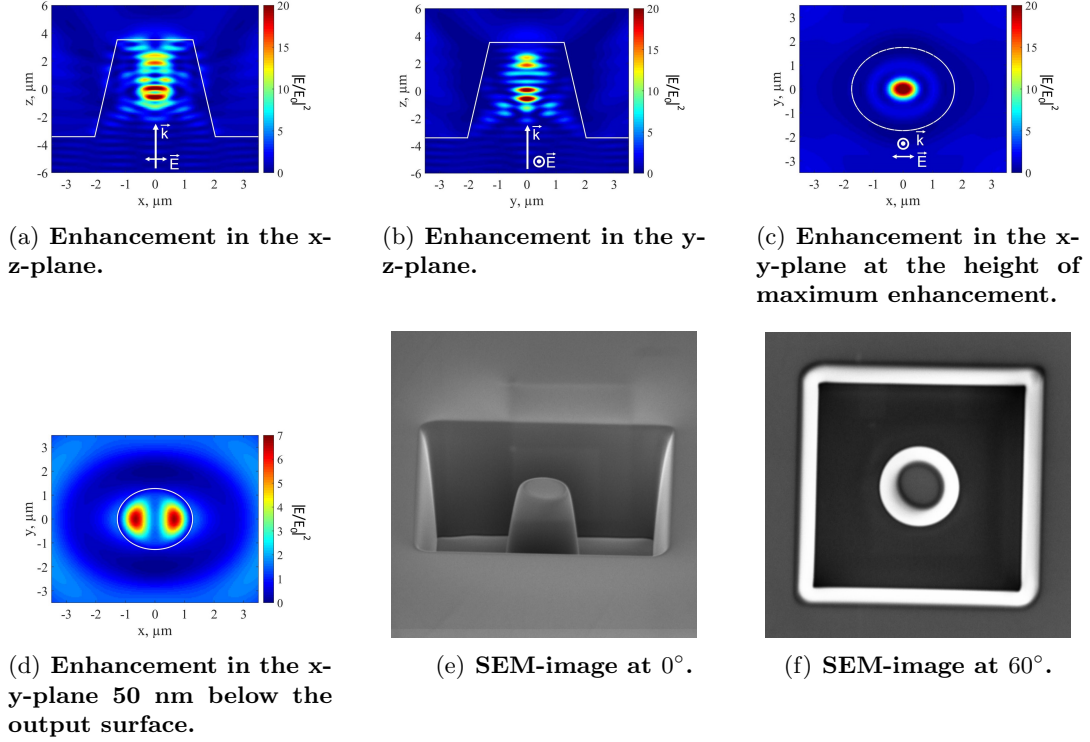
Figure 4.27.: Calculated intensity enhancement in an isolated truncated nanocone and SEM-images of the nanocone.

reaches a maximum value of 24 $2.8\,\mu$m above the base line. The maximum enhancement at the output surface is 8 which is favourable for efficient above-bandgap harmonic generation. SEM-images of the sample are shown in Figs. 4.27(e) and 4.27(f). The isolated nanocone is placed in a square-shaped hole with dimensions $12\,\mu$m x $12\,\mu$m.

Measurements

For all measurements, the coupling of the harmonic radiation to the spectrometer was optimized for H9. A complete spectrum from the nanocone at an intensity of $0.07\,\mathrm{TW/cm^2}$ is shown in Fig. 4.28(a) (red curve). We identify H3 (700 nm), H5 (420 nm), H7 (300 nm), H9 (233 nm), the luminescence from the band edge at 385 nm as well as the luminescence from defect states at around 500 nm. However, from the bare crystal (blue curve) we only detected H3. It is due to the local field enhancement in the nanocone that the intensity threshold for HHG is reached. Beside the harmonics, the luminescence is strongly enhanced in the nanocone. When increasing the intensity to $0.17\,\mathrm{TW/cm^2}$, the threshold for high harmonic generation from the bare crystal is reached (blue curve, Fig. 4.28(b)). We identify H3, H5, H7, H9 and the luminescence from defect states (500 nm). But the luminescence from the band edge (385 nm) could still not be detected at this intensity. When moving from the bare

(a) **Spectrum generated at** $0.07 \, \mathrm{TW/cm^2}$.

(b) **Spectrum generated at** $0.17 \, \mathrm{TW/cm^2}$.

(c) **H7 and H9 generated at** $0.02 \, \mathrm{TW/cm^2}$.

(d) **H7 and H9 generated at** $0.05 \, \mathrm{TW/cm^2}$.

(e) **H7 and H9 generated at** $0.07 \, \mathrm{TW/cm^2}$.

(f) **H7 and H9 generated at** $0.17 \, \mathrm{TW/cm^2}$.
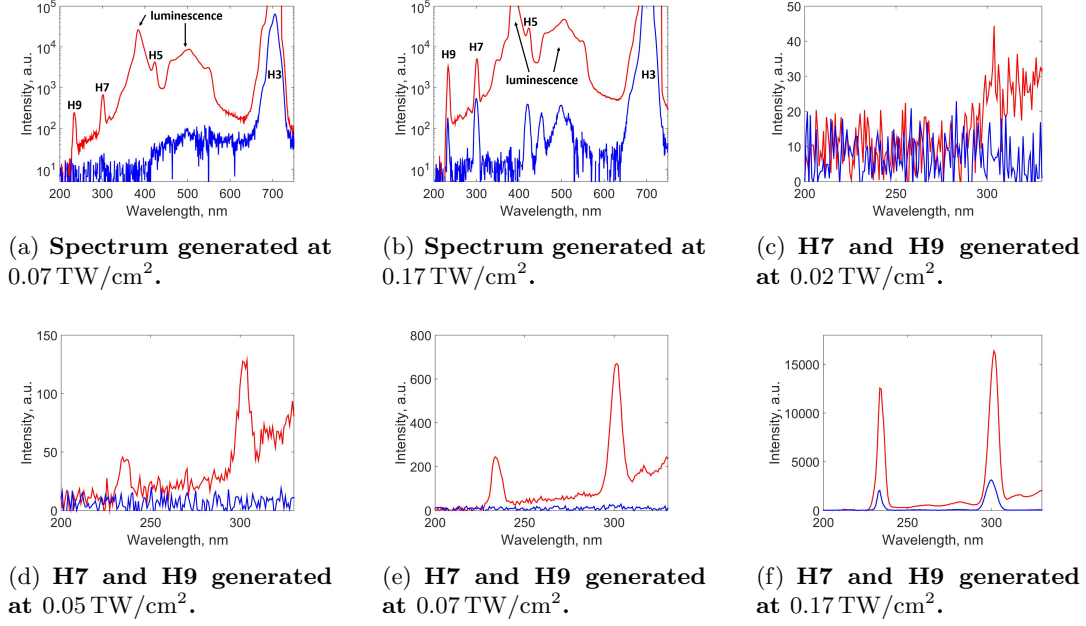
Figure 4.28.: Complete spectrum (a), (b) and H7 and H9 (c), (d), (e), (f) from the nanocone (red curve) and the bare crystal (blue curve).

crystal to the nanocone (red curve, Fig. 4.28(b)), all harmonics and the luminescence from defect states are strongly enhanced. The luminescence from the band edge is much stronger than the above-bandgap harmonics. We systematically study above-bandgap harmonic generation at different intensities. At $0.02 \, \mathrm{TW/cm^2}$ (Fig. 4.28(c)), no H7 and H9 is generated from the bare crystal (blue curve) and a weak H7 signal from the nanocones (red curve). When increasing the intensity to $0.05 \, \mathrm{TW/cm^2}$ (Fig. 4.28(d)) and $0.07 \, \mathrm{TW/cm^2}$ (Fig. 4.28(e)), H7 grows and H9 is now generated from the nanocone. However, both signals could still not be detected from the bare crystal at this intensity. At $0.17 \, \mathrm{TW/cm^2}$ (Fig. 4.28(f)), both H7 and H9 are efficienty generated from the bare crystal (blue curve). But both harmonics are by almost one order of magnitude stronger from the nanocone.

Fig. 4.29(a) shows the intensity-dependent yield of H7 from the nanocones (red curve) and the bare crystal (blue curve). The yield from the bare crystal can be fitted by a polynomial with q = 6.4 which is close to the value of q = 7.0 that one would expect if H7 was a perturbative harmonic (eq. 2.3). Fig. 4.29(b) shows a plot of the intensity-dependent yield of H9 from the nanocones (red curve) and the bare crystal (blue curve). The yield from the bare crystal can be fitted by a polynomal with q = 8.5 which is close to the value of q = 9.0 that would be expected for a perturbative harmonic. The perturbative scaling of H7 and H9 indicates that both harmonics might be generated due to multiphoton absorption even though they are above-bandgap harmonics. For both H7 and H9 the signal increases from the nanocone much slower than from the bare crystal. We believe that due to the local intensity enhancement the generation of H7 and H9 switches from a multiphoton process to HHG via interband and intraband pro-

112
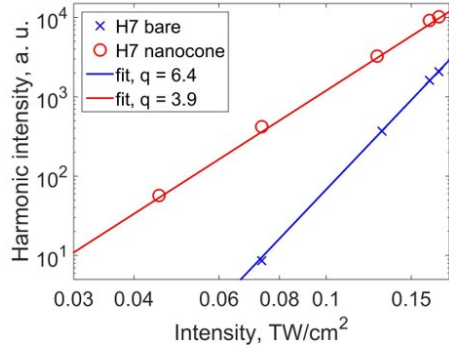
(a) **H7 from nanocone and bare crystal vs. pump intensity.**
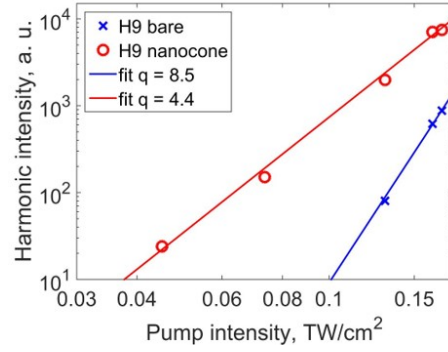
(b) **H9 from nanocone and bare crystal vs. pump intensity.**
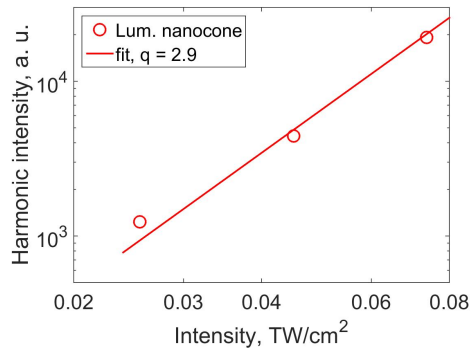
(c) **Luminescence from the band edge from nanocone vs. pump intensity.**
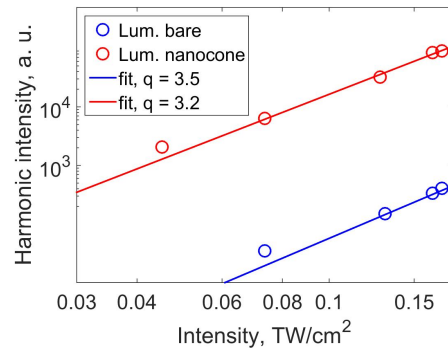
(d) **Luminescence from defect states from nanocone vs. pump intensity.**

Figure 4.29.: Intensity-scaling of H7, H9 and the luminescence.

cesses which explains the non-perturbative behaviour. At low intensity, the nanocone enhanced both H7 and H9 by at least two orders of magnitude. While no signal is observed from the bare crystal, a strong harmonic signal is generated in the nanocone. The intensity-dependent behaviour of the luminescence from the band edge is shown in Fig. 4.29(c). For the investigated intensity range it could only be detected from the nanocone and not from the bare crystal. It scales as q = 2.9. The intensity-scaling for the luminescence from defect-states (around 500 nm) is shown in Fig. 4.29(d). From the bare crystal q = 3.5 is consistent with the fact that approximately four photons need to be absorbed to generate luminescence from defect states. For the nanocones q = 3.2 which is close to the value from the bare crystal.

Discussion

In conclusion, we demonstrated enhancement of below-bandgap as well as above-bandgap harmonics of a 2.1 μm beam in nanocones. Compared to earlier experiments at ICFO (sec. 4.2) and IOGS (sec. 4.3) we improved our detection system and the

nanocone geometry. At low intensity, high harmonics were enhanced by several orders of magnitude with respect to the bare crystal. Since energies of 1 nJ are sufficient to trigger high harmonic generation in isolated truncated nanocones, high repetition rate oscillator pulses can be used without employing additional amplification stages such as chirped pulse amplification which is bulky and significantly decreases the repetition rate. This paves the way towards high-repetition rate applications of HHG. Beside the harmonics radiation we significantly enhanced the luminescence both from the band edge and from defect states in the nanocones with respect to the bare crystal. We found that the above-bandgap harmonics H7 and H9 scale almost perturbatively with pump intensity when generated in the bare crystal. When generated in the nanocones the value q (eq. 2.9) is significantly lower than for the bare crystal and the scaling is now non-perturbative. The damage of the nanocones is discussed in chapter 5.1.

Conclusion of chap. 4

We investigated the enhancement of HHG in ZnO nanocones. By improving the detection system, the experimental setup and the nanostructure design we demonstrated high enhancement of above-bandgap harmonics in ZnO nanocones at MHz repetition rate. In the first design (sec. 4.2) we used an array of ZnO nanocones and a $3.2\,\mu\text{m}$ pump beam and we demonstrated high enhancement of the signal selected with filter II (app. D). We were not able to determine whether it was H7 or the fluorescence that was enhanced. The enhancement is high at low intensities and decreases with increasing pump intensity. The nanocones suffered from resposition of milled matter during the FIB fabrication process. Nanocones with high redeposition have lower enhancement factors than nanocones that suffered from little redeposition. Having improved the detection system and the nanocone design and fabrication, we generated up to H15 from a $3.1\,\mu\text{m}$ beam (sec. 4.3). Spectral measurements of the radiation emitted from an array of 5 nanocones did not show enhancement with respect to the bare crystal. This is because the spectrometer collects and sums up the total signal emitted from the sample. For extracting the local enhancement factor of an individual nanocone one needs to take into account the effective emission surface. By normalizing the harmonic signal to the effective emission area of the nanocones, enhancement might be observed. The luminescence from the band edge was strongly enhanced. H7 and H9 were immersed in the red and blue tail of the luminescence, respectively. In order to increase the laser coupling, we came up with a new design and fabricated isolated truncated ZnO nanocones and coupled the pump beam completely inside one single cone. We use MHz repetition rate and nJ pulse energies (sec. 4.4). We observed strong enhancement of the luminescence (both from the band edge around 385 nm and from defect states around 500 nm). The enhancement factors for the luminescence were even higher than for the harmonics. H5 is immersed in the broadband luminesence. In 2017, The group of Paul Corkum [20] reported on the enhancement of H5 from a driving laser tunable in the range $2.0 - 2.3\,\mu\text{m}$ in ZnO nanostructures. However, in our experiment with very similar parameters (sec. 4.4) we saw that H5 is totally immersed in the luminescence. Even narrowband transmission filters as used by [20] cannot solve this issue. We demonstrated that the luminescence is enhanced and no evidence from the enhancement of H5 can be disentangled. Finally, we extended our study to H7 (300 nm) and H9 (230 nm) that were far from the luminescence. High enhancement factors of these above-bandgap harmonics in the nanostructures were observed leading to a real enhancement of the total harmonic signal as compared to bulk.

5. Applications of solid HHG

In comparison to high harmonic generation (HHG) in gases, HHG in solids offers additional degrees of freedom. The generation medium can be structured which allows to modify and tailor properties of the harmonic radiation. In this chapter, we study several applications of crystal HHG, namely the possibility to deduce the electric field distribution in nanostructures by analyzing the radiation-induced damage (sec. 5.1) and the possibility to generate solid harmonics that carry an orbital angular momentum (sec. 5.2). In addition, we image nanoscale objects with harmonic radiation from nanocones (sec. 5.3).

5.1. Mapping of the electric field through laser induced damage

In this section, we study radiation-induced damage and structural modifications of semiconductor nanostructures that were used for HHG experiments. Beside the high peak intensity the high average power can contribute to structural deformation. Huang et al. report on the creation of subwavelength apertures during ultrafast laser ablation of ZnO (Fig. 5.1) [134]. They used Ti:sapphire laser pulses and observed the formation of ripples at the ZnO surface with periodicities that depend on the laser parameters. Wang et al. investigated the ablation of matter from a silicon surface under the irradiation with an intense laser pulse. They observed the formation of subwavelength structures (SWS) and deep-subwavelength strucures (DSWS) [135]. They distinguish two cases:

- SWS are observed for a laser fluence above $170 \, \mathrm{mJ/cm^2}$ by pulse accumulation. SWS means structures with a period slightly (up to $50\,\%$) smaller than the wavelength.

- DSWS are observed for a laser fluence in the range $76 - 170 \, \mathrm{mJ/cm^2}$. SWS means structures with a period significantly (by around a factor of 10) smaller than the wavelength.

The laser can induce a plasma conductive layer that supports waves which in turn imprint SWS and DSWS by ablation. Surface plasmon polaritons (SPP) can be formed at the interfaces between air-plasma and plasma-substrate [135].
In the following, we show the damage that occured in the nanocones used in the experiments described in secs. 4.2, 4.3 and 4.4 and we relate the observed damage to the simulated field enhancement of the fundamental beam in the nanocones.

116
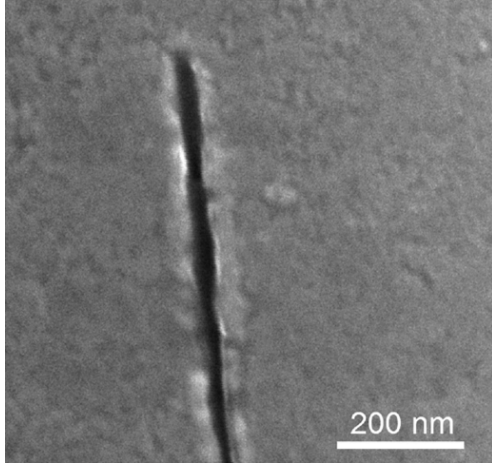
(a) **Subwavelength apertures created in ZnO during ultrafast laser ablation.**
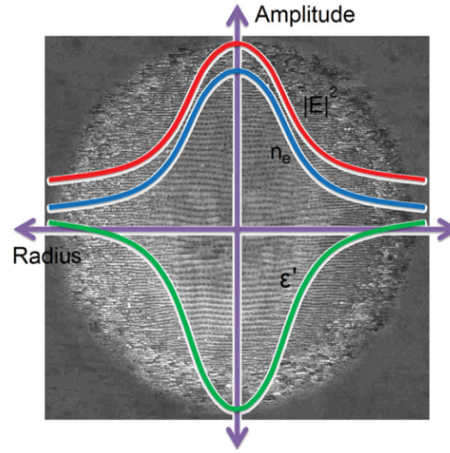
(b) **Gaussian field distribution (red) of a focusing laser spot, the free electron density (blue) and the real part of the relative dielectric constant (green) induced by the laser in a crater.**

Figure 5.1.: Damage of ZnO due to ultrafast laser ablation, pictures taken from [134].

Design I

Here we analyze the radiation induced damage of the nanocones used in sec. 4.2. Fig. 5.2(d) shows an SEM-image of the array of ZnO nanocones after irradiation. We see that peeling occured at the tip of the ZnO nanocones. While the global shape of the nanocones is unaffected by laser irradiation, a black spot appears at the tip of most of the nanocones. We worked at a laser repetition rate of 160 kHz and low intensity. Since the damage is visible only at the tips of the nanocones we believe that the damage is non-thermal but rather due to the high field enhancement in the nanocone. In Figs. 5.2(a) - (c) we see the formation of modulations on the bare ZnO crystal surface in the region around the nanostuctures with a periodicity of $2.3\,\mu$m. Each modulation consists of DSWS. They are an extension of the rows of nanocones and are parallel to the edge of the nanocone array. It was confirmed by simulations that even the edge of the array of ZnO nanocones can exhibit significant enhancement.

Beside ZnO, we tested GaAs as a material for nanocones. We produced an array of GaAs [1000] nanocones with $2\,\mu$m basis and $3\,\mu$m periodicity. Post-irradiation SEM-images are shown in Fig. 5.3. We see that at the tip some peeling occured and that some material is floating down the cone which reminds of the eruption of a volcano. We believe that due to the local enhancement inside the nanocones and due to the low melting temperature of GaAs (The melting temperature of GaAs is 1500 K, of ZnO it is 2250 K) a part of the nanocone was transformed into the liquid phase due to a temperature above the boiling point. For comparison, the intensity enhancement of a $3.2\,\mu$m laser in GaAs nanocones with the indicated dimensions is shown in Fig.
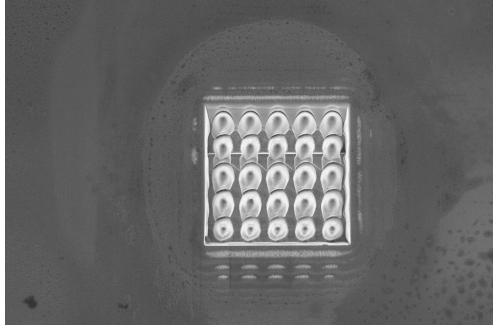
(a) **Array of ZnO nanocones after irradia-tion.**
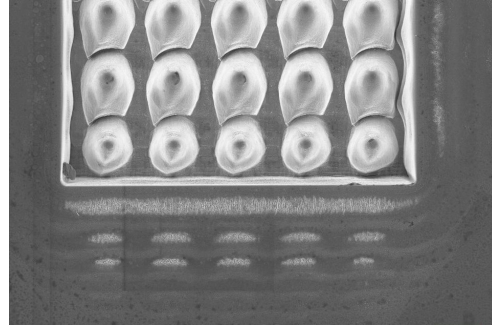
(b) **Array of ZnO nanocones after irradi-ation, zoom on the edge.**
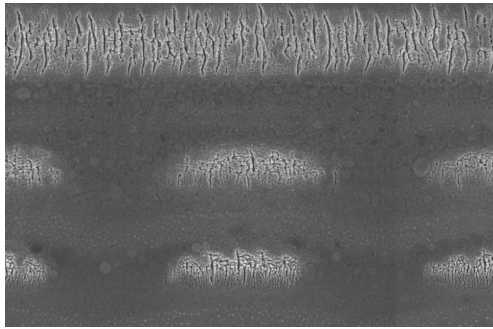
(c) **Array of ZnO nanocones after irradia-tion, zoom on the modulations beside the nanocone array on the ZnO surface.**
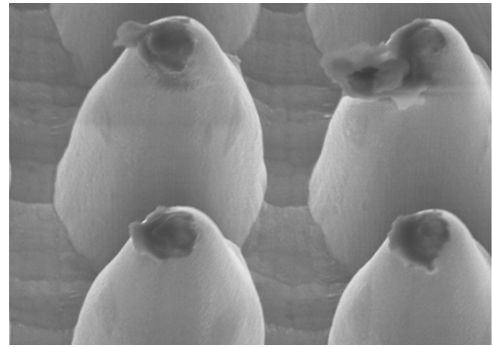
(d) **Ablation of ZnO nanocones at the tips.**

Figure 5.2.: Damage of ZnO nanocones.
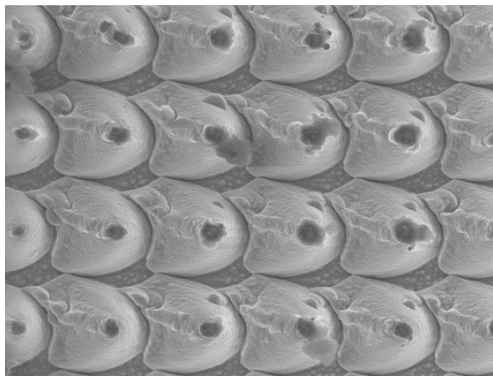
(a) **Array of nanocones.**
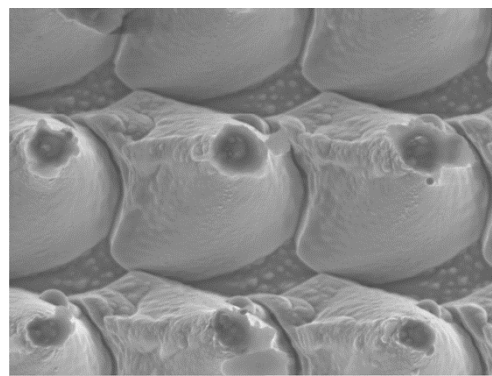
(b) **Zoom on one nanocone.**

Figure 5.3.: Radiation-induced damage of GaAs nanocones. We observe a peeling at the tip of the nanocone.

5.4. The enhancement leaks out of the nanocone. For an array of GaAs nanocones with $3\,\mu$m periodicity and a $2\,\mu$m broad basis the maximum enhancement is 16 and occurs at $4.4\,\mu$m height (Figs. 5.4(a) - 5.4(c)). The observation of HHG was not

(a) **Enhancement in x-z-plane.**

(b) **Enhancement in y-z-plane.**

(c) **Enhancement in x-y-plane at height of maximum enhancement.**
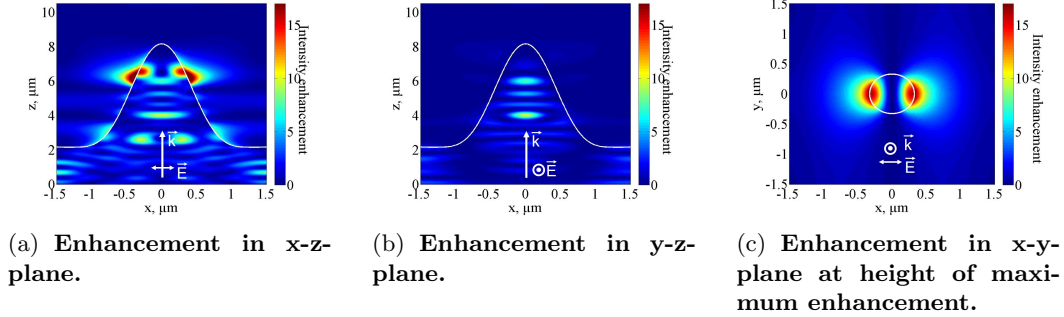
Figure 5.4.: Intensity enhancement of a $3.2\,\mu$m beam in an array of GaAs nanocones with a $2\,\mu$m basis, $6\,\mu$m height and $3\,\mu$m periodicity.

reported yet for GaAs. Second and fourth harmonic generation in GaAs was observed by [136, 137, 138] and [139], respectively and higher harmonics were predicted by [140]. We studied HHG with such GaAs nanocones. In the experiment, no harmonics higher than H5 were detected in the frame of this experiment. However, this might be due to the limited sensitivity of our detection system. H3 from GaAs nanocones was weaker than H3 from bare GaAs (Fig. 5.5). The nonlinear refractive index of GaAs n_2 is approximately $1 \cdot 10^{-13}\,\mathrm{cm}^2/\mathrm{W}$, which is a high value and can cause detrimental nonlinear effects which can inhibit harmonic generation. In addition, the low bandgap of GaAs makes this material easy to damage.
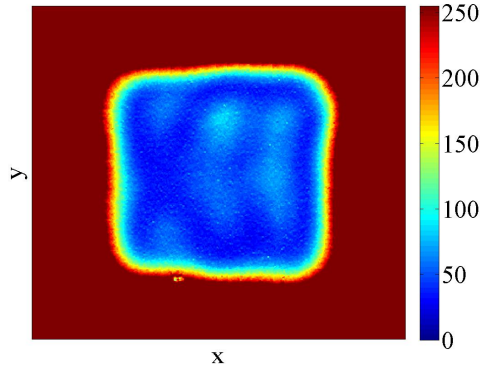
Figure 5.5.: Image of H3 generated in GaAs nanocones. The array of nanocones appears in blue and the surrounding bulk in red.

Design 2

We explore the damage that occured after irradiation in non-truncated and truncated ZnO nanocones with pulses at $3.1\,\mu$m wavelength (the experiment is described in sec. 4.3). Fig. 5.6 shows two different zooms on an array of non-truncated ZnO nanocones after irradiation. We see that the global shape of the nanocones stays unchanged. How-

(a) **Array of nanocones.**

(b) **Zoom on one nanocone.**
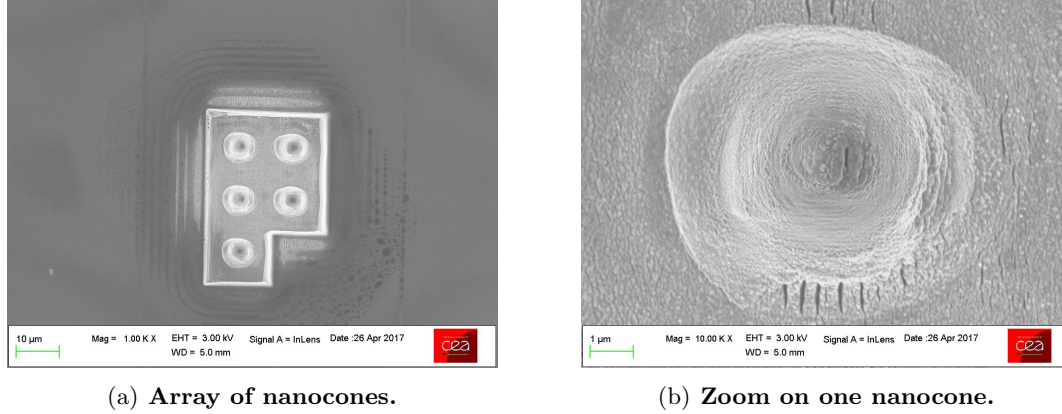
Figure 5.6.: Radiation induced damage in an array of ZnO nanocones.

ever, DSWS occured at the tips of the nanocones and at the bottom of the nanocones [135]. As was seen in the simulations of the intensity enhancement (Fig. 4.14), high enhancement occured at the output surface of the nanocone which might be related to the occurrence of the DSWS.

We investigate the ablation that occured in truncated ZnO nanocones during laser irradiation. A SEM-image taken at 0° of a truncated nanocone before radiation is shown in Fig. 5.7(a). The inset shows a perspective view taken at 60°. The nanocone has a conical profile a flat top. After irradiation, strong ablation occured at the flat output surface of the cones. In a zoom on two nanocones (Fig. 5.7(b)) we see that in the middle of the cone some ripples with a spacing of around 100 nm appeared (DSWS). They are aligned perpendicularly to the polarization direction. On the left and on the right part, matter has been ablated. The shape of the ablated matter reminds of the contours of the comic figure 'batman'. A zoom on one nanocone after irradiation is shown in Fig. 5.7(c). As an inset in Fig. 5.7(c), we show the intensity enhancement calculated via FDTD simulations for a truncated ZnO nanocone irradiated with radiation at $3.1\,\mu$m wavelength (more details about the enhancement can be found in Fig. 5.8). We see that the spots where matter has been ablated follow the shape of the calculated enhancement. While the right nanocone in Fig. 5.7(b) has symmetric ablation, the left cone has antisymmetric ablation. This antisymmetry might be due to a Gausian beam that is not centered on the nanocone (intensity gradient across the cone) or a tilted wavefront. We simulate the enhancement of a Gaussian beam that is not centered on the nanocone. The result is shown in Fig. 5.7(d). We obtain an asymmetric field enhancement that might explain the asymmetric ablation. Thermal damage could not be observed. This is due to the comparably low laser repetition rate

of 125 kHz and the low average power (Fig. 2.7).
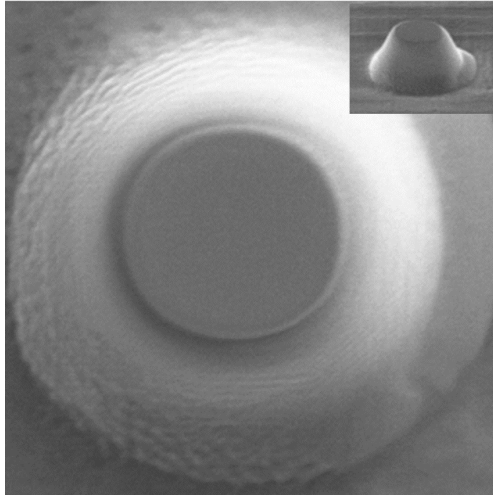
(a) **Pristine nanocone.**
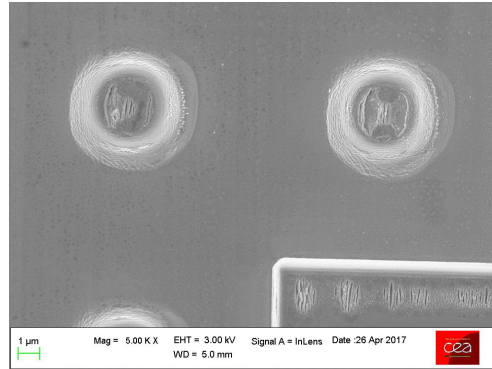
(b) **Zoom on two nanocones of the array. The right nanocone has symmetric and the left nanocone antisymmetric ablation.**
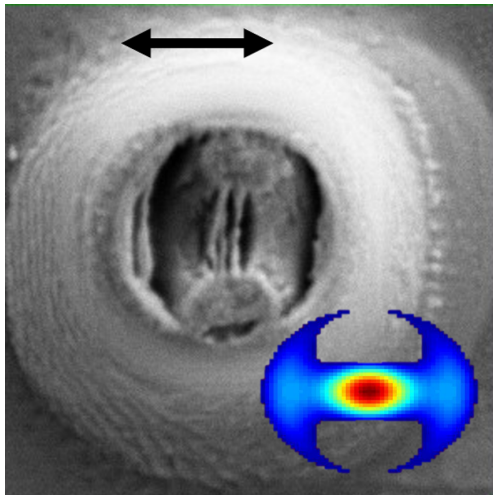
(c) **Zoom on one nanocone. The laser polarization is horizontal (black arrow). The inset shows the shape of the calculated intensity enhancement.**
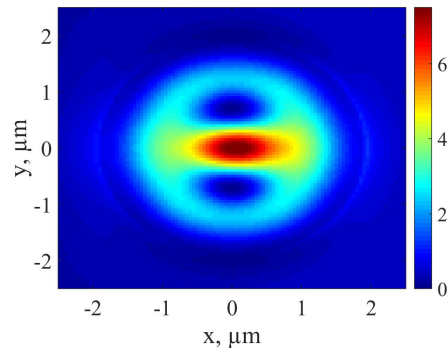
(d) **Simulations of the field enhancement at the cone output surface with a Gaussian beam that is not centered on the nanocone yields an asymmetric 'batman' shape.**

Figure 5.7.: (a) Truncated ZnO before irradiation, (b) Zoom on two nanocones after irradiation, (c) Zoom on one nanocone after irradiation (d) Asymmetric field enhancement.

(a) **Total intensity enhancement.**

(b) **Intensity enhancement along 'x'.**

(c) **Intensity enhancement along 'z'.**
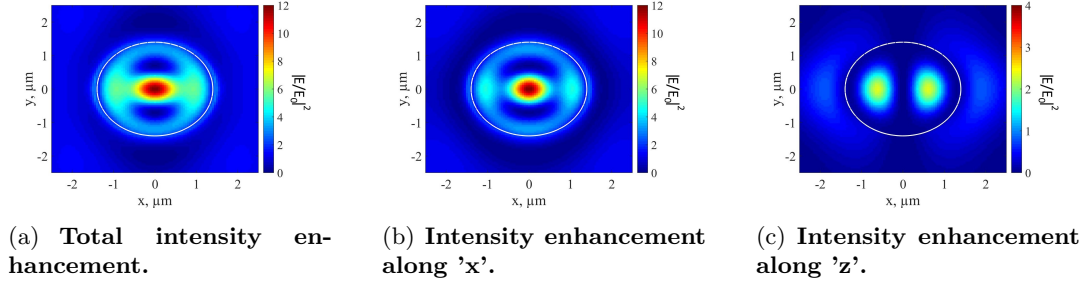
Figure 5.8.: Calculated intensity enhancement in the x-y-plane 50 nm below the output surface of the nanocone. The highest enhancement occurs in the cone center and reaches a value of 12. When analyzing the x- and z-component of the enhancement, we find that the central part is totally polarized along 'x'. However, at the location of the 'batman-wings', the field-enhancement is polarized perpendicular the cone surface, along 'z'.

Dynamic behaviour of radiation damages at $2.1\,\mu\mathrm{m}$ in truncated nanocones

We investigate the damage that occured after irradiation of truncated ZnO nanocones with pulses at $2.1\,\mu\mathrm{m}$ wavelength and 18.66 MHz repetition rate (the experiment is described in sec. 4.4). Due to the high repetition rate thermal effects might play a role (Fig. 2.7). We measure H7 from an isolated truncated nanocone at $0.06\,\mathrm{TW/cm^2}$ and we observe the signal over a time of 13 hours. The result is shown in Fig. 5.9(a). After irradiation the signal steeply rises. H7 increases by a factor of 4 within a time span of 80 minutes. A subsequent decrease of the signal which occurs much slower than the precendent steep increase is observed. Within 270 minutes the signal decreases by a factor of 4 and reaches a level close to the level at the beginning of the exposure. For better understanding this behaviour, we investigate changes occuring to the nanocone after different exposure times. We are interested in what happens when the signal is maximum, which is the case after two hours. We use another nanocone which is similar to the one used in the described measurement and expose it to the

(a) **Temporal evolution of H7.**

(b) **Top of the nanocone after an irration of 2 hours.**

(c) **Top of the nanocone after an irration of 13 hours.**

Figure 5.9.: Measurements of H7 at a peak intensity of $0.063\,\mathrm{TW/cm^2}$ and SEM-images of nanocones after laser irradiation.

122

laser during two hours. A SEM-image of the top of the nanocone after 2 hours of irradiation is shown in Fig. 5.9(b). Subwavelength structures appeared close to the center of the nanocone. After 13h (Fig. 5.9(c)), the structures are still visibile, but they are flattened. Due to the local field enhancement self-organized reshaping occured which yields a higher field enhancement than the pristine nanocone which explains the increase in H7. This reshaping continues which leads to a flattened surface which decreases the field enhancement which leads to a lower H7 yield. We perform a similar measurement at higher peak intensity ($0.18\,\mathrm{TW/cm^2}$) for H7 and H9. The result is shown in Fig. 5.10(a). As for the measurement at lower power (Fig. 5.9(a)), we first observe an increase of the signal and a subsequent decrease. However, the parameters are quite different. At $0.18\,\mathrm{TW/cm^2}$, H7 increased after exposure by a factor of 1.4 during 25 minutes. Then it decreases by a factor of 20 during 150 minutes. The temporal evolution of H9 (Fig. 5.10(d)) resembles the behaviour of H7. However, both the increase and the subsequent decrease of H9 are more pronounced than for H7. This suggests that the reshaping is different at high intensity. Indeed, when analyzing the SEM-images after different exposure times, we see that severe damage occured. After 30 min (Fig. 5.10(c)), two big cracks can be seen. In Figs. 5.10(e) and 5.10(f) we see

(a) **Temporal evolution of H7.**

(b) **Temporal evolution of H9.**

(c) **Top view of nanocone, after 30 min of exposure.**

(d) **Top view of nanocone, after 3 hours of exposure.**

(e) **Side view of nanocone, after 30 min of exposure.**

(f) **Side view of nanocone, after 3 hours of exposure.**
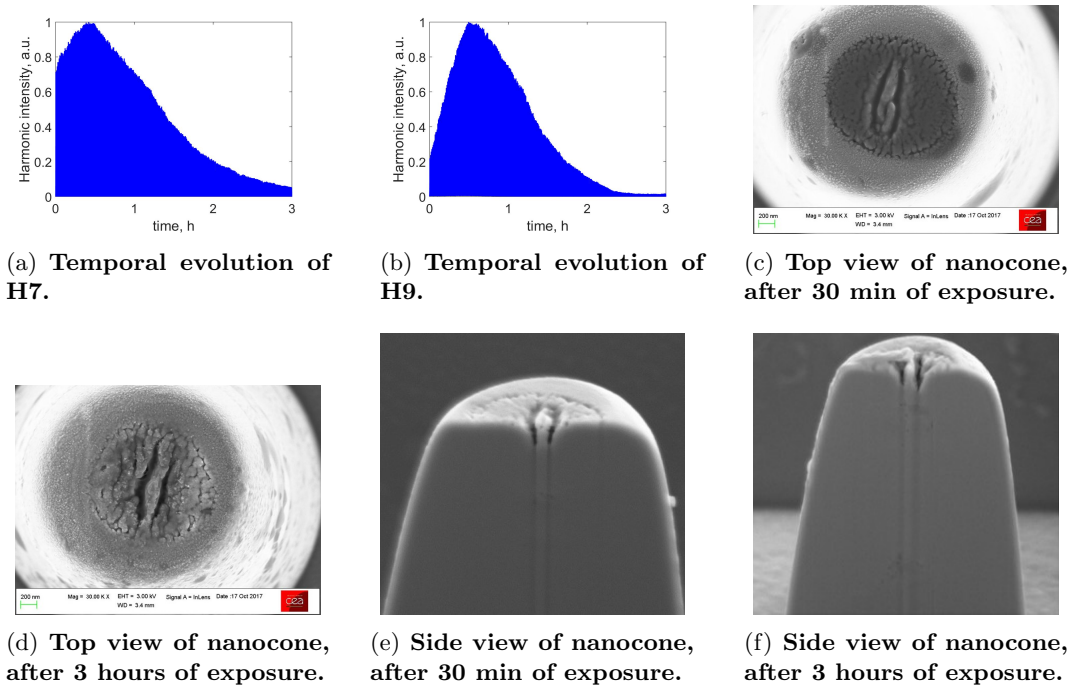
Figure 5.10.: Measurements of H7 and H9 at a peak intensity of $0.18\,\mathrm{TW/cm^2}$ and SEM-images of nanocones after laser irradiation.

that the damage does not only occur at the surface, but even deep inside the cone. The intensity enhancement in Fig. 4.27(c) shows that strong enhancement occurs in the center of the nanocone which should be related to the damage. No change in the harmonic yield from the bare crystal could be obsered during long-time measurements.

5.2. Generation of solid harmonics with an orbital angular momentum

In this section, we investigate the possibility to generate solid harmonics that carry an orbital angular momentum. The orbital angular momentum of light (OAM) is the component of a light beam that is dependent on the field spatial distribution, and not on the polarization. Beams carrying an OAM are called optical vortices and are in general Laguerre-Gauss modes. They have a helical wavefront around a phase singularity in their center and an annular intensity distribution. Their far-field profile is donut-shaped. The phase varies with respect to their azimuthal coordinate ϕ following $\exp(-il\phi)$ with l being the mode index. The principle of how to generate an OAM is explained schematically in Fig. 5.11. A Gaussian beam passes through a phase plate, the thickness of which varies azimuthally (along ϕ). The higher the thickness of the plate, the greater the retardance of the beam. Generation of harmonics carrying an orbital angular momentum was already demonstrated in gases: Laguerre-Gauss modes
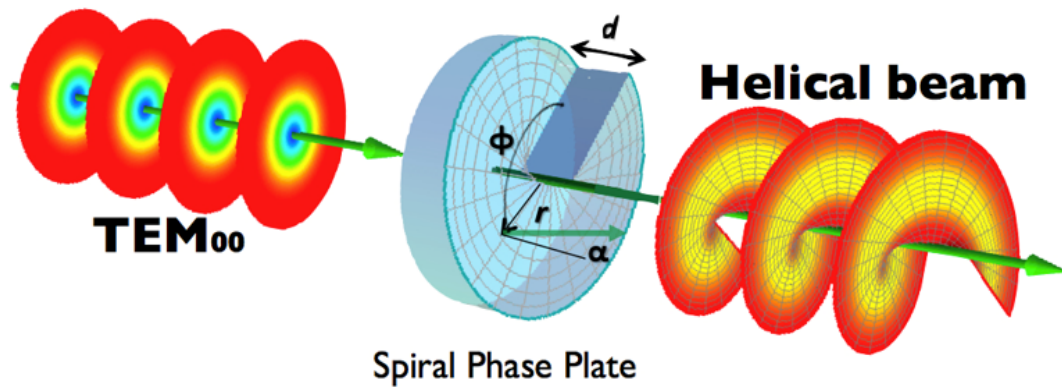
(a) **Principle of generation of solid harmonics that carry an OAM.**
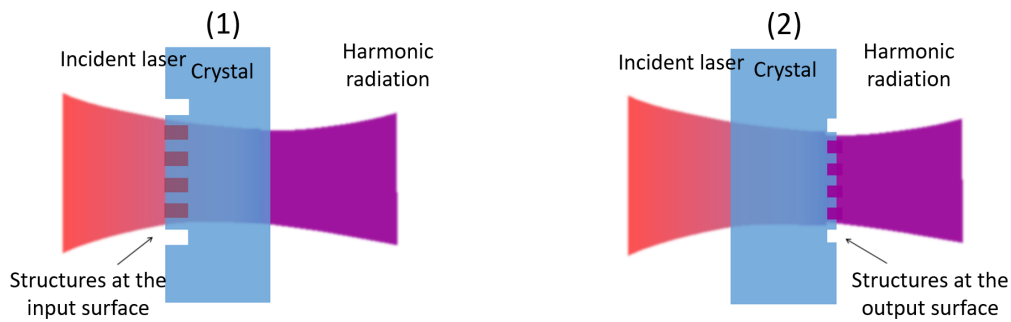
(b) **The phase plate can be at the input or at the output surface.**

Figure 5.11.: Schematic demonstration of the generation of an orbital angular momentum. A Laguerre-Gaussian beam is generated when a Gaussian beam passes through a phase plate and acquires an orbital angular momentum.

were generated by means of a phase plate, and then focused into a noble gas where high harmonics were generated. The OAM was transferred from the pump beam to the fundamental beam. Our idea is to generate high harmonics in crystals and to imprint the phase plate directly onto the generation medium. Two possibilities are imaginable:

1. The phase plate is imprinted on the input surface of the crystal. Like this, the pump beam acquires an OAM and transfers it to the harmonics during the harmonic generation process in the nonlinear crystal. The phase shift introduced by the phase plate needs to be adapted to the fundamental wavelength.

2. The phase plate is imprinted on the output surface of the crystal. Harmonics generated in the crystal travel through the phase plate at the exit surface of the crystal and acquire the OAM. Harmonics can be generated directly in the phase plate as well.

In the frame of this work we investigate the second possibility. The goal is to generate the fifth harmonic in a ZnO crystal that carries an orbital angular momentum.
The laser oscillator from NOVAE used for this experiment operates at $2.1\,\mu$m wavelength and 18.66 MHz repetition rate. We work in the sub-TW regime. The beam is focused into the sample and the harmonic radiation is measured in transmission. For more details about the experimental setup and the laser system we refer to sec. 4.4 and app. C.

Sample

Two different samples were prepared by focused ion beam milling (FIB, app. A). We prepared a binary zone plate (Fig. 5.12(a)) and a non-binary zone-plate (Fig. 5.12(b))
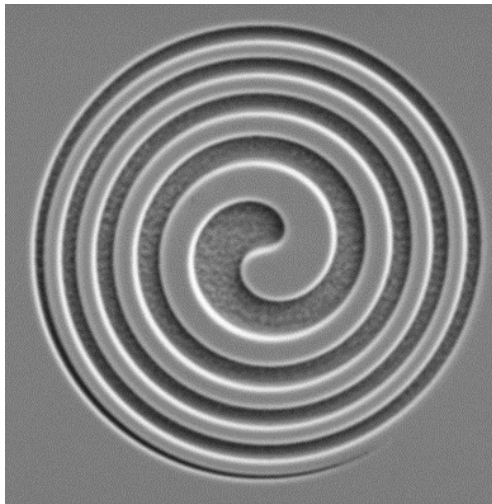
(a) **SEM-image of binary zone plate.**
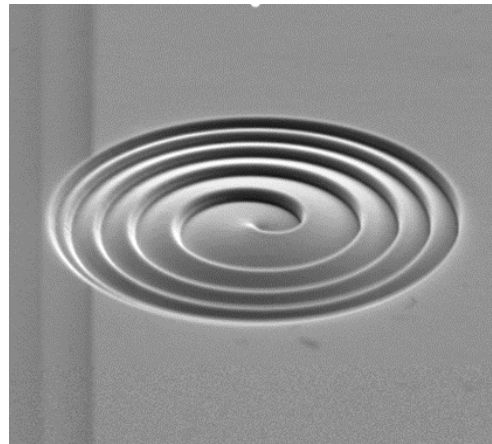
(b) **SEM-image of non-binary zone plate.**

Figure 5.12.: SEM-images of binary and non-binary zone plates.

which are designed to transfer an OAM with l = 1 to the fifth harmonic. While the depth of the binary zone plate varies between two different values, the depth of the non-binary zone plate varies continuously. The binary zone plate transfers the OAM by diffraction. However, the non-binary zone plate is a refractive optics. It is a Fresnel-lens with an azimuthally varying thickness.

Measurement

The measurement of the far-field emission of H5 from the binary zone plate is shown in Fig. 5.13(a). One can clearly see the annular intensity distribution, indicating that H5 carries an OAM with l = 1. However, the annular shape shows some deformations and aberrations due to imperfect design and fabrication of the binary zone plate. By taking into account the real shape of the zone plate and abberations of the pump beam we simulate the intensity profile of H5. The result is shown in Fig. 5.13(b). It agrees

(a) **Measurement: H5 from binary zone plate.**

(b) **Simulation: H5 from binary zone plate.**

(c) **Measurement: H5 from non-binary zone plate.**

(d) **Simulation: H5 from non-binary zone plate.**
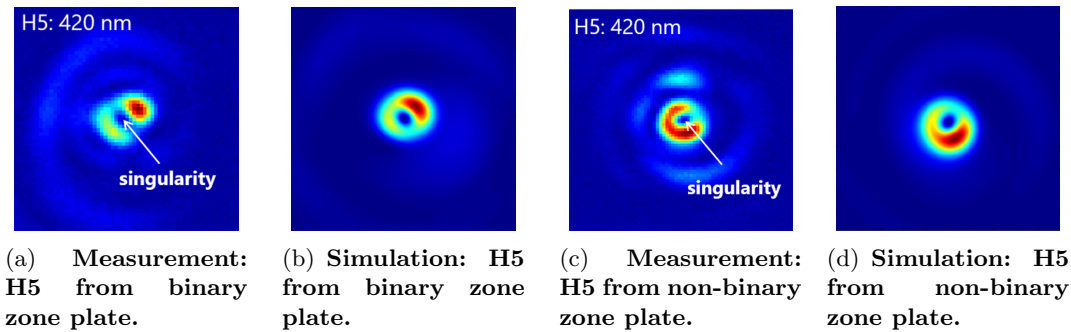
Figure 5.13.: Simulation and measurement of the far-field emission of H5 from binary and non-binary zone plates.

well with the measurement. The measurement of the far-field emission of H5 from the non-binary zone plate is shown in Fig. 5.13(c). The result is an improvement with respect to to the binary zone plate. The intensity profile exhibits an annular shape with very little imperfections. It is very well reproduced when simulating H5 by taking into account the real shape of the non-binary zone plate and the aberrations of the fundamental beam (Fig. 5.13(d)).

Discussion

In conclusion, we generated the fifth harmonic carrying an OAM of l = 1 of a $2.1\,\mu$m beam in a ZnO crystal. The zone plate that transferred the OAM to the harmonic beam was imprinted on the output surface of the crystal. We tested a binary and a non-binary zone plate. The non-binary zone-plate produced a fifth harmonic with an OAM of l = 1 with less imperfections than the binary zone plate.

126

5.3. Imaging with harmonic radiation and CDI reconstruction

In sec. 4.4, we demonstrated enhancement of below-bandgap and above-bandgap harmonics of a $2.1\,\mu$m laser in isolated truncated ZnO nanocones. HHG can be used to image nanoscale objects with femtosecond time resolution. We select one harmonic emitted from the nanocone by a transmission filter and focus it onto a sample that was produced by FIB milling. A SEM-image of the sample is shown in Fig. 5.14(a). The diffraction pattern is measured in transmission with a CMOS camera. Images of H3 and H5 are shown in Figs. 5.14(b) and 5.14(c), respectively. The diffraction of H7 and H9 was too weak to be detected. Both H3 (integration time 200 ms) and H5 (integration time 5000 ms) were measured at different integration times and the object was reconstructed by applying the method of coherent diffraction imaging (CDI) [141]. CDI is a lensless technique for 2D or 3D reconstruction of the image of nanoscale structures. The CDI-reconstruction of the measurement with H5 is shown in Fig. 5.14(d).
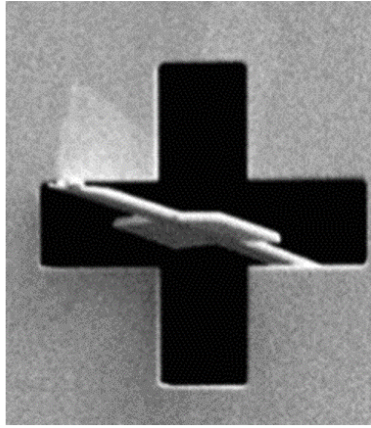
(a) **SEM-image of object.**
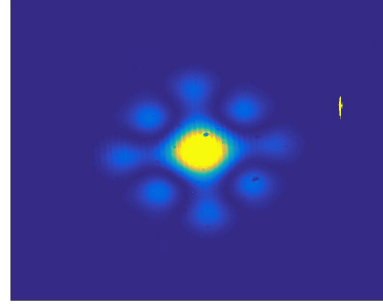
(b) **Diffraction of H3.**
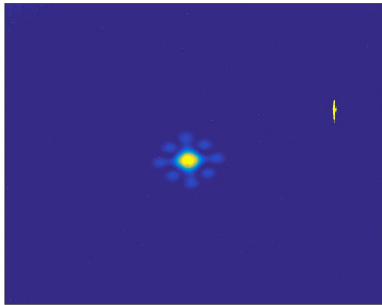
(c) **Diffraction of H5.**
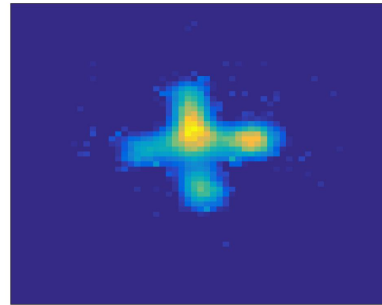
(d) **Reconstruction of the diffraction pattern of H5.**

Figure 5.14.: **SEM-image of a cross-shaped object, diffractions patterns measured with H3 and H5 and the reconstruction of H5.**

The cross-shape of the sample is well reconstructed. Further improvements in the nanocone geometry and the detection system might enable imaging experiments with even higher harmonics orders that allow high resolution and the imaging of even smaller objects at MHz repetition rate. This imaging experiment proves the coherence of the harmonics generated in the nanocone and that the source provides enough photons for applications.

Conclusion of chap. 5

In comparison to HHG in gases, HHG in solids offers the possibility to structure the generation medium which allows to modify and tailor properties of the harmonic radiation. We performed three applications with solid harmonics. First, we studied different kinds of laser-induced deformations in semiconductor nanocones. Nanocones of different materials show melting features, subwavelength cracks were observed for ZnO nanocones. We observed at a pump wavelength of $3.1\,\mu\mathrm{m}$ that the shape of the local field enhancement can be imprinted at the output surface of truncated nanocones. Truncated ZnO nanocones used at $2.1\,\mu\mathrm{m}$ pump wavelength lead to a quick increase of the high harmonic yield (this was studied for H7 and H9) over a time of a few tens of minutes with a subsequent slow decrease and saturation at a constant value. This change in harmonic yield is related to ablation and crack formation at the top surface of the truncated nanocones. In a second experiment, we studied the possibility to generate harmonics in a ZnO crystal that carry an orbital angular momentum. Therefore, we imprinted a phase plate at the output surface of the crystal. We measured H5 of a $2.1\,\mu\mathrm{m}$ beam that carries an OAM of $\mathrm{l}=1$. In a third experiment, we used harmonics generated in isolated truncated ZnO nanocones to image nanoscale objects.

6. Conclusion and perspectives

Conclusion

In this work we studied high-order harmonic generation (HHG) in crystals. Beside the generation process itself in 3D and 2D materials, we investigated HHG assisted by local field enhancement in metallic and semiconductor nanostructures.

In chap. 2, we studied different aspects of the process of HHG in 3D and 2D materials. In sec. 2.2, the role of different wavelengths and materials with respect to bandgap and lattice constants was investigated. We studied the wavelength dependence of HHG in a one-dimensional solid by solving the time-dependent Schrödinger equation. We found an extension of the high harmonic cutoff with increasing wavelength. However, in experiments we mostly worked in air and we were not able to access the harmonic cutoff due to absorption. We investigated HHG in $CaCO_3$ and we found that HHG strongly depends on the relative orientation of crystalline axes and polarization direction. The global polarization-dependent harmonic yield was well reproduced by TDDFT simulations. We analyzed the origin of the spectral fringes that were observed in third harmonic spectra in different experiments. It turned out that the fringes are due to the interference of a third harmonic pulse generated at the input surface and a third harmonic pulse generated in the bulk. Furthermore, we generated high harmonics in a ZnO crystal and investigated the power law. Beside the perturbative scaling of below-bandgap harmonics we studied the power law of above-bandgap harmonics. We found that the first three above-bandgap harmonics have a similar scaling law with values of q = 5.0 - 6.0 (eq. 2.9). Beside three-dimensional bulk crystals, the two-dimensional material graphene was studied in sec. 2.3. It turned out that high harmonic generation in graphene is strongly enhanced with respect to a bulk crystal. However, graphene damages quickly at high intensities. First studies were made with trilayer graphene on a quartz substrate. In order to investigate the effect of pure graphene without substrate that can lead to effects as bandgap opening we analyzed HHG in freestanding graphene on a TEM grid.

In chap. 3 we investigated the enhancement of HHG in different plasmonic nanostructures, namely bow ties, nanoholes, gratings and resonators. Due to detection issues we were mostly limited to the third harmonic. All investigated nanostructures were able to boost the efficiency of third harmonic generation. In sec. 3.2, we investigated harmonic generation of a $2.0\,\mu m$ beam in a ZnO crystal with gold gratings at its surface. We found that the harmonics yield strongly depends on the polarization of the pump beam. An effective enhancement could not be observed since the harmonic radiation was strongly attenuated due to the high thickness of the gold nanostructure. The third harmonic generated in ZnO due to local enhancement in a gold grating has a complex

polarization dependence. A great variety of effects such as polarization-dependent enhancement of the fundamental beam, polarization-dependent transmission of the harmonic beam through the grating as well as near-field effects have to be taken into account for understanding the polarization-dependent third harmonic. In sec. 3.3 we observed the enhancement of H3 of an 800 nm pump beam in gold nanoholes on a ZnO crystal by a factor of 12 after normalization to the effective emission area. In sec. 3.4 we studied the enhancement of H3 of an 800 nm pump beam in a metal-dielectric-metal (gold-SiO_2-gold) nanostructure and found and enhancement factor of 21 with respect to a bare gold-SiO_2 film after normalization to the effective emission area. In contrast to bow ties for example, which exhibit high enhancement in a small volume, resonators have high homogeneous enhancement in a broad volume. In sec. 3.5, we investigated enhancement of third harmonic generation in sapphire due to the local field enhancement in bow tie nanostructures at the crystal surface. Enhancement values by more than one order of magnitude with respect to a bare sapphire crystal were observed. We investigated the origin of third harmonic generation and found that the third harmonic mostly originates from the sapphire crystal and not from the gold itself. In sec. 3.6 we investigated the damage that occured in the nanostructures during laser irradiation. Damage can happen due to high average power, but other channels of nanostructure deformation due to high peak intensity are possible (Fig. 2.7). The third harmonic from a sapphire substrate with gold bow ties at its surface first increased and then decreased during laser exposure. This is due to a reshaping of the bow tie that follows the field enhancement. Bow ties with higher thickness are less susceptible to thermal damage. Higher peak intensity leads to stronger reshaping. A protective SiO_2 film that covers the bow ties helps to preserve the bow tie shape during laser irradiation. We found that the third harmonic from gold nanoholes (sec. 3.3) steadily decrease over time. This is due to a carbon deposit inside the holes that built up during irradiation and that followed the distribution of the near-field enhancement. The carbon deposit strongly absorbed third harmonic radiation. The shape of the nanoholes, however, remained unchanged.

In chap. 4, we investigated the possibility to boost the efficiency of HHG in crystals by the use of semiconductor nanostructures. While metallic nanostructures exhibit a small enhancement volume with often a steep electric field gradient and damage quickly, semiconductor nanostructures are more stable, have a higher enhancement volume with a smoother gradient. They turned out to be more adapted for boosting nonlinear processes. In particular, semiconductor nanocones were investigated. In different experiments we progressively improved the detection system and the nanocone geometry. Harmonics need to be generated close to the output surface of a crystal/nanostructure in order to be efficiently coupled out. In sec. 4.2, we investigated HHG of a $3.2\,\mu$m pump beam. We used filters to investigate the enhancement of different spectral regions and made systematic enhancement studies. Strong enhancement was observed at low pump intensity that saturated at high intensities. It turned out that the employed filter transmitted, beside the seventh harmonic, luminescence from the ZnO crystal. In the frame of this experiment it could not be determined whether the enhanced radiation was the luminescence or H7. Having improved the detection system and the nanocone geometry, we investigated HHG of a $3.1\,\mu$m laser

in ZnO nanocones in sec. 4.3. We observed up to H15 from the nanocones. Spectral measurements of the UV radiation emitted from an array of nanocones did not show enhancement with respect to the bare crystal. This is because the spectrometer collects and sums up the total signal emitted from the sample. For extracting the local enhancement factor of an individual nanocone one needs to take into acount the effective emission surface. While the coupling area of 5 nanocones is $220\,\mu m^2$ it is $3100\,\mu m^2$ for the bare crystal (the diameter of the pump beam in the focus is $63\,\mu m^2$). When normalizing the harmonic signal to the effective emission area of the nanocones, enhancement might be observed. The luminescence from the band edge was strongly enhanced. H7 and H9 were immersed in the red and blue tail of the luminescence, respectively. In sec. 4.4, we investigated HHG in isolated truncated ZnO nanocones. In order to increase the conversion efficiency from the pump beam to the harmonics, we coupled the total beam into one nanocone. We observed high enhancement by more than two orders of magnitude for above-bandgap harmonics. However, even in this arrangement the luminescence was strongly enhanced. It turned out that in all experiments the luminescence, which can have different origins such as a recombing exciton pairs or defect states, is enhanced much more than the harmonic radiation. This might have different reasons such as the effect that harmonic radiation is coherent and requires phase matching while the luminescence is incoherent. For the case of gases it was shown that a strong phase relation with the driver is needed for eficient HHG [52]. In experiments, coherence measurements can be used to discriminate both types of radiation. Dai et al. showed that different kinds of ZnO nanostructures can either favour second harmonic generation or the enhancement of luminescence [128]. Furthermore, they demonstrated that the ratio of harmonic generation and luminescence generation depends (at constant intensity) on the focal spot size. So it seems possible to reduce the relative amount of luminescence by ajusting in addition to the sample parameters the laser parameters such as the focusing conditions [129].

HHG in solids offers the possibility to structure the generation medium which allows to modify and tailor properties of the harmonic radiation. In chap. 5, we explore several applications of crystal HHG. In sec. 5.1, we observe different kinds of laser-induced deformations in semiconductor nanocones. ZnO and GaAs nanocones exhibit melting features and peeling at their tip. Furthermore, subwavelength cracks were observed for ZnO nanocones. We observed with truncated ZnO nanocones at $3.1\,\mu m$ that the shape of the local field enhancement can be imprinted at the output surface of the nanocone. Truncated ZnO nanocones used at $2.1\,\mu m$ pump wavelength lead to a quick increase of the high harmonic yield (this was studied for H7 and H9) over a time of a few tens of minutes with a subsequent slow decrease and saturation at a constant value. We find that this change in harmonic yield is related to ablation and crack formation at the top surface of the truncated nanocones. In sec. 5.2, we investigated the possibility to generate harmonics in a ZnO-crystal that carry an orbital angular momentum. Therefore, we imprinted a phase plate at the output surface of the crystal. We measured H5 of a $2.1\,\mu m$ beam that carries an OAM of l = 1. In sec. 5.3, we used harmonics generated in isolated truncated ZnO nanocones to image nanoscale objects.

Perspectives: Harmonic enhancement in 2D materials

It was shown that nanostructures have the potential to boost HHG from bulk crystals. A possible experiment, that was already investigated theoretically, is about the enhancement of high harmonic generation from 2D materials by exploiting the local plasmonic enhancement of metallic nanostructures [142]. We simulated and fabricated

(a) **Schematical layout of sample.**

(b) **SEM-image of sample, top-view.**

(c) **Simulated H3 from a graphene monolayer on nanoholes (red curve) and H3 from a bare graphene monolayer (blue curve).**

(d) **Total intensity enhancement.**

(e) **x-component of intensity enhancement.**

(f) **z-component of intensity enhancement.**
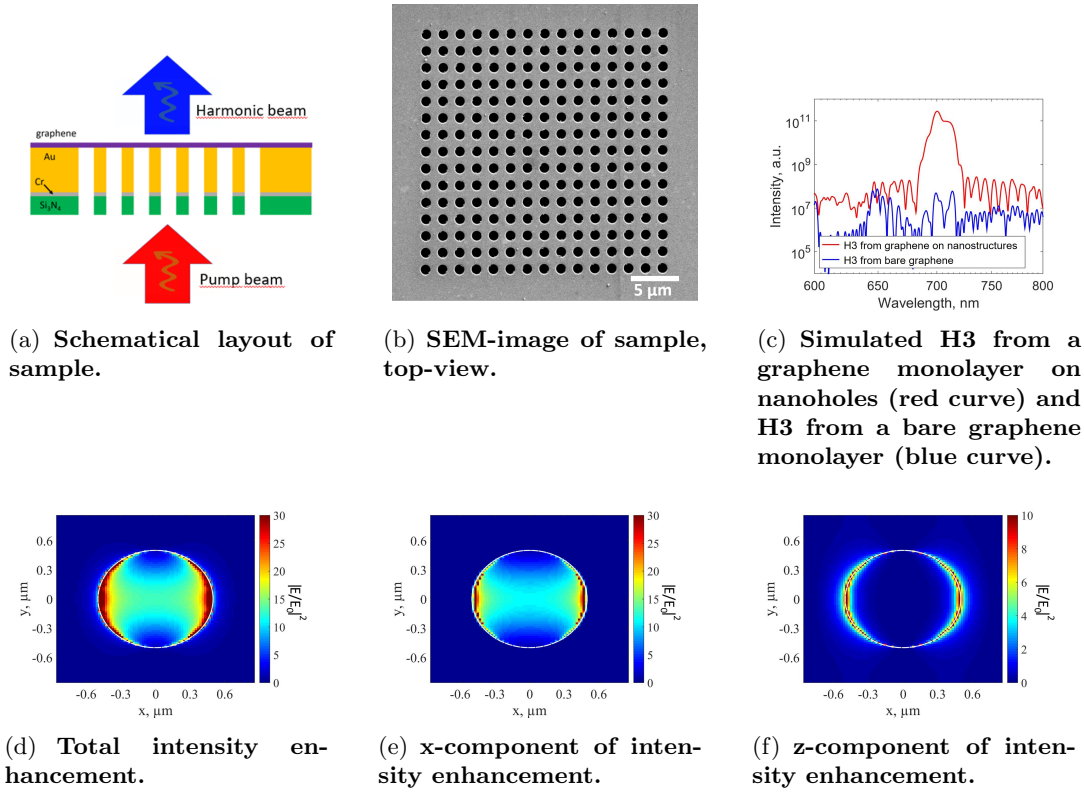
Figure 6.1.: Plasmonic nanoholes are proposed to enhance high harmonic generation in graphene. We show the sample (a), (b), the simulation of third harmonic generation (c) and the simulation of the local intensity enhancement of the fundamental beam (d) - (f).

plasmonic nanoholes in a gold-Si_3N_4 membrane. The sample is a TEM grid with square-shaped membranes with $500\,\mu$m x $500\,\mu$m size. Each of these membranes consists of $75\,$nm Si_3N_4 and $150\,$nm Au with a 4 nm thick adhesion layer of Cr between them (Fig. 6.1(a)). The membrane is perforated with nanoholes as shown in Fig. 6.1(b). The diameter of each nanohole is $1.0\,\mu$m and the periodicity is $1.7\,\mu$m. The sample is illuminated from the Si_3N_4-side and the harmonic radiation is collected in transmission. The graphene monolayer will be deposited on top of the gold nanoholes. The holes were optimized to have high enhancement at $2.1\,\mu$m at the gold-air-interface. The intensity enhancement inside the graphene monolayer calculated by FDTD simulations is shown in Fig. 6.1(d). The incident beam is enhanced by a factor of up to 150 in intensity. The hole boundaries are shown by a white solid line. The laser polar-

ization is along 'x'. Most of the enhancement occurs inside the hole on the left and the right edge. The part of the enhancement polarized along 'x' is shown in Fig. 6.1(e). The enhancement occurs due to localized surface plasmons and exclusively inside the hole on the left and the right side with a maximum enhancement factor of 50. The part of the enhancement polarized along 'z' is shown in Fig. 6.1(f). The enhancement occurs due to propagating surface plasmons on the left and on the right edge of the hole, inside and above the gold surface. The maximum enhancement factor along 'z' is 130. It turns out that when simulating a single hole, the 'x'-component of the enhancement is very similar to the one of a hole inside an array of holes. However, the 'z'-component only appears for an array of holes. So by tuning the periodicity of the array, the 'z'-component can be modified while keeping the 'x-component' constant. All experiments about HHG in graphene reported so far used a polarization parallel to the graphene layer, which causes in-plane oscillations of the electrons. The proposed nanostructures offer the posibility to study HHG for a polarization perpendicular to the graphene layer (Fig. 6.1(f)), which causes the electrons to oscillate perpendicular to the surface. The proposed experiment allows to investigate the role of in-plane and out-of-plane contributions to HHG (Fig. 6.2) [89]. Third harmonic generation was simulated from a bare graphene monolayer and from a graphene monolayer on nanoholes in the proposed geometry. Due to the extraordinary high nonlinearity of graphene ($\chi^{(3)} = 10^{-15}\mathrm{m}^2/\mathrm{V}^2$) weak intensities are sufficient for third harmonic generation. Laser intensities of $3\,\mathrm{MW/cm}^2$ are boosted to more than $300\,\mathrm{MW/cm}^2$ in the nanoholes which enhanced the third harmonic by four orders of magnitude. The combination of 2D materials with extremely high nonlinearities and plasmonic enhancement holds promise to provide efficient high harmonic generation from low-energy oscillator pulses in a compact setup.

In-plane polarization
=> Crystal like response

Out-of-plane polarization
=> Atomic/molecular like response
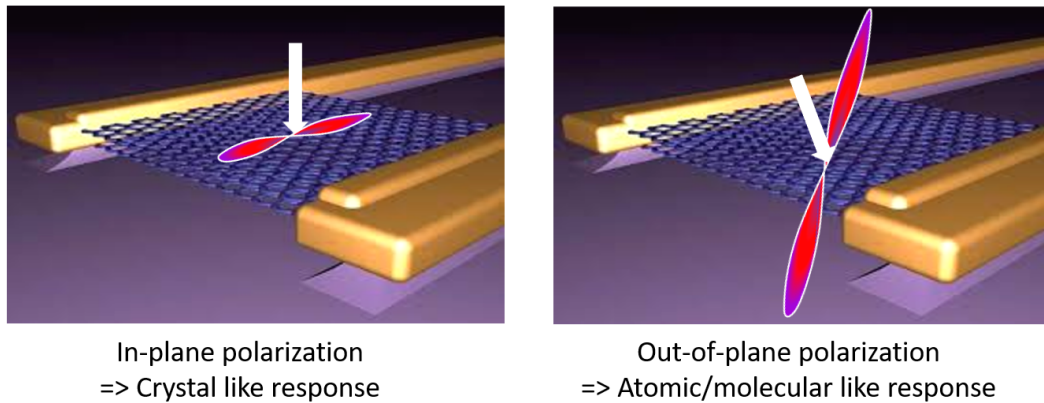
Figure 6.2.: In-plane an out-of-plane polarizations cause fundamentally different responses of graphene.

Appendices

A. Nanofabriation: Focused ion beam

Focused ion beam (FIB) uses a finely focused ion beam to pattern the surface of a material. When the high-energy ions strike the sample, they will sputter atoms from the surface. It allows for the fabrication of structures with a resolution of tens of nanometers. A scanning electron microscope (SEM) allows a simultaneous observation of the sample surface. A schematical layout is shown in Fig. A.1.

Most samples were milled at the sample CSNSM Laboratory in Orsay. The equipment consists of a LEO 1530 SEM (Field Effect Gun) equipped with an Orsay Physics Column. The energy of the ion beam (Ga^+) is set at 40 keV. Typical beam currents used are of the order of few nA leading to spot sizes of several hundreds of nm. Typical milling times for the nanostructure produced in the frame of this thesis are between several minutes up to one hour.
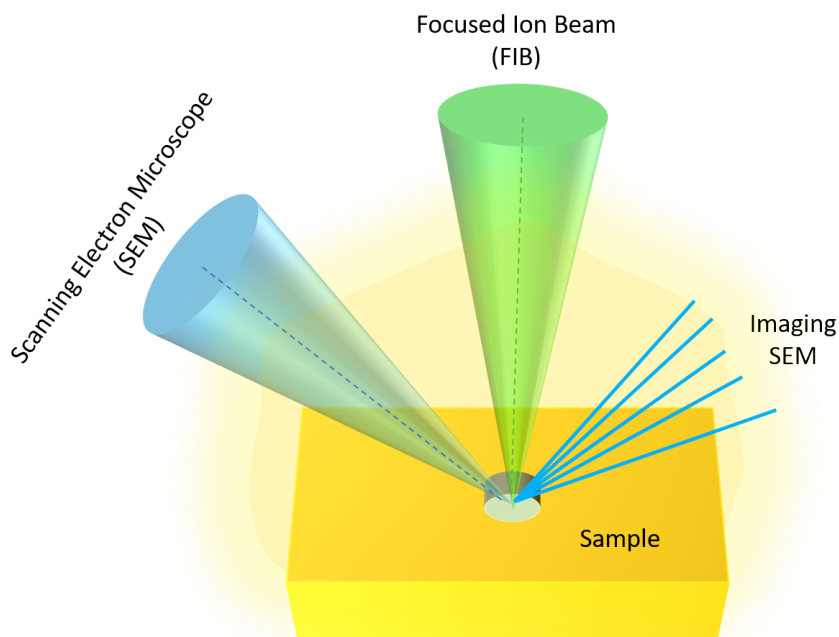
Figure A.1.: Layout of FIB.

136

B. Finite difference time domain calculations

Finite difference time domain (FDTD) calculations are an analysis technique that numerically solves Maxwell's equations. In this method, the time-dependent Maxwell equations are discretized by replacing space and time partial derivatives by central-difference approximations. These finite difference equations are solved in the so-called leapfrog manner: the electric field vector components in a spatial volume in space are solved at a given instant in time, then the magnetic field vector components in the same region are solved at the next instant in time. This process is repeated until the electromagnetic field has fully evolved. From Maxwell's equations it is known that a change of the E-field in time depends on a change of H-field across space. Hence at each point in space, the new value of the electric field in time is depends on the stored value of the electric field and the curl of the local distribution of the magnetic field in space. Likewise, the updated value of the magnetic field at any point in time is dependent on the previous value of the magnetic field and the curl of the local distribution of the electric field in space [143].

For most FDTD simulations in this thesis Lumerical Solutions was used [144]. In this software, a computational domain has to be established, which is the physical region over which the simulation will be made. Electric and magnetic fields are determined at every point in space within this region. Materials need to be specified. The most common ones are air, metals or dielectric materials. Any other material such as semiconductors can be use as long as permeability, permittivity and conductivity are specified. Furthermore, an appropriate light source needs to be chosen. The grid size must be chosen such that over one increment the electromagnetic field does not change significantly which means that the linear dimensions must be only a fraction of the wavelength. The output of the simulation is usually electric or magnetic fields in a region within the computational domain. In the frame of colaborations with the university of Hanover the open-source sofware-package MEEP [145] was used. The computer used was a bi-processor Intel Haswell 10C E5-2650V3 (10 cores, 20 threads, max. frequency 3 GHz, Bus speed 9.6 GT/s QPI, 768 Gb registered SDRAM (DDR4 2133, 68GB/s bandpass)).

C. Laser systems

Laser system ICFO

Here, the laser system used for the experiment used in sec. 4.2 is described. A schematics is shown in Fig. C.1. The clock for the system is a two-color Erbium-doped fiber laser (Toptica Photonics AG) which provides optically synchronized pulses at 1550 nm and 1050 nm.
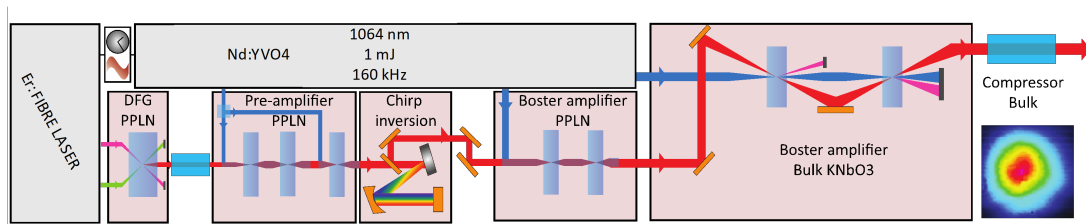
Figure C.1.: 3.2μm **OPCPA system.**

The Nd:Vanadate pump laser operates at 160 kHz and is electronically synchronized to the fiber laser with a jitter level below 300 fs. Mid-IR pulses at 3200 nm are directly generated from the fiber laser output via difference frequency generation (DFG). The mid-IR seed is amplified in 3 pre-amplifier stages, chirp inverted and then boosted further in 4 power amplifier stages. Finally, compression is achieved though dispersive propagation in 20 cm of sapphire with a final output of $118\,\mu$J and a duration of 97 fs (sub-9 optical cycles). The output corresponds to an average power of 21 W at $3.2\,\mu$m with a pulse-to-pulse output energy stability of 0.33 % rms over 30 min. More details about the laser system can be found in [132].

Laser system IOGS

Here, the laser system used for the experiment used in sec. 4.3 is described. The laser is an OPCPA system delivering a signal at $1.55\,\mu$m wavelength and $20\,\mu$J energy (Fig. C.2). The idler, which as few cycle pulse duration, $3.07\,\mu$m wavelength and an energy of $10\,\mu$J per pulse. The OPCPA is based on a high-energy femtosecond ytterbium-doped fiber amplifier pump delivering 400 fs, $400\,\mu$J pulses at 125 kHz repetition rate. A small fraction ($5\,\mu$J) of the pump pulse energy is focused into a 100 mm long YAG crystal where a spectrum from $1.4\,\mu$m to $1.7\,\mu$m is generated by supercontinuum generation [102], which is used as a seed for the first OPCPA stage. The rest of the fiber laser output is used to pump the three OPCPA stages. Idler and signal are compressed after the third stage to few-cycle pulse duration with $12\,$mm of Si and
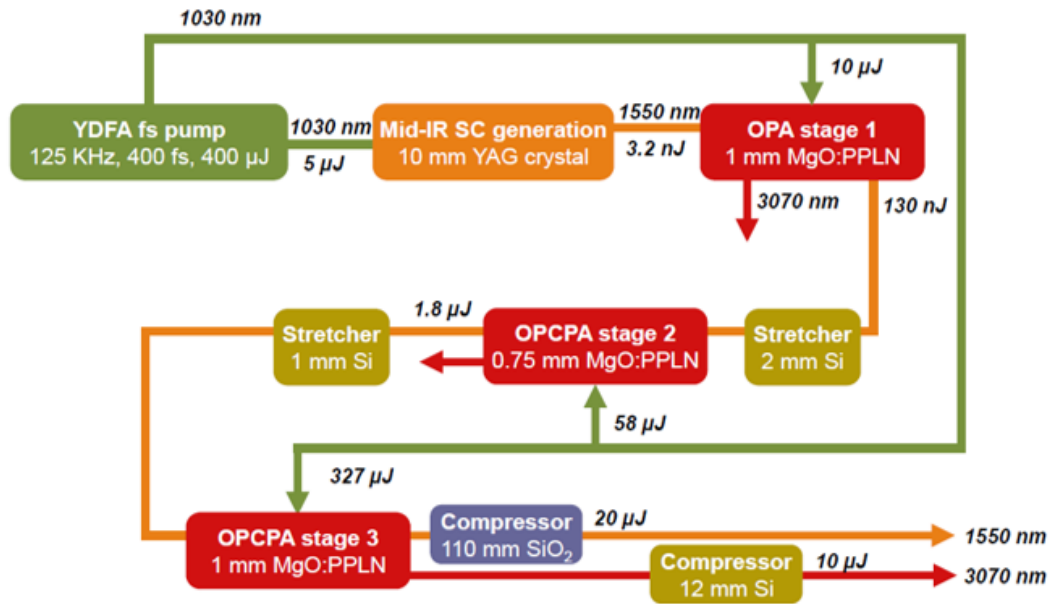
Figure C.2.: 3.1μm **OPCPA system.**

110 mm of SiO_2, respectively. For more details about the laser system we refer to [102].

Laser system NOVAE

Here, the laser system used in secs. 2.3, 4.4 and in subsec. 5.2 is described. The seed mode-locked oscillator delivers a train of 1.3 ps hyperbolic secant squared ($sech^2$) shaped pulses centered at 1910 nm with a repetition rate of 18.66 MHz (Fig. C.3). The average power is 4 mW, corresponding to E = 0.2 nJ. The pulses are further
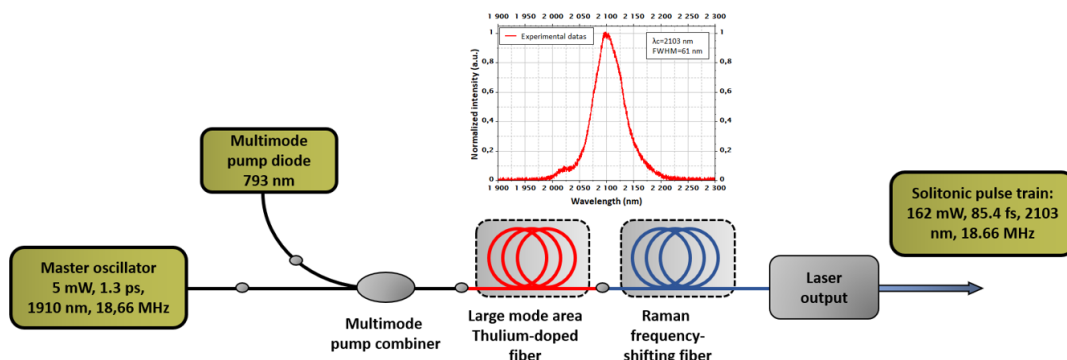
Figure C.3.: Layout of experimental setup and spectrum of laser.

amplified in a cladding-pumped amplifier based on LMA TDF to tens of nanojoules. Multisolitonic effects lead to the pulse fission followed by ejection of high-energy (8.7 nJ) pulses that are frequency-shifted to 2100 nm. In a Raman-active medium such as fused silica, the high-frequency part of sub-picosecond pulses is absorbed while the low-frequency part is amplified, yielding a continuous red-shift in the pulse carrier frequency. The spectrum with 2103 nm central wavelength was measured with an optical spectrum analyzer (AQ6375, Yokogawa, Japan) and is shown as an inset in Fig. C.3. The average power of the pulse train is 162 mW with a linear polarization state. The pulse duration was measured via autocorrelation to be 85.4 fs.

Laser system IOGS $1.0\,\mu$m

Here, the laser system used for the experiment used in subsec. 2.2.2 is described. The used optical source is a tangerine ultrafast fiber laser developed by Amplitude Systemes and Laboratoire Charles Fabry. The laser has a broadband spectrum of 30 nm centered at 1039 nm, a pulse duration under 50 fs with a repetition rate of 100 kHz. Spectral and temporal profiles are shown in Fig. C.4(a) and C.4(b), respectively. The maxiumum pulse energy is $15\,\mu$J. In the temporal profile, a second peak is observed few hundreds of femtoseconds before the main pulse at 3% of the maximum peak power. The pulse duration is 32 fs. A laser system similar to the one used in the frame of this experiment is described in [146].
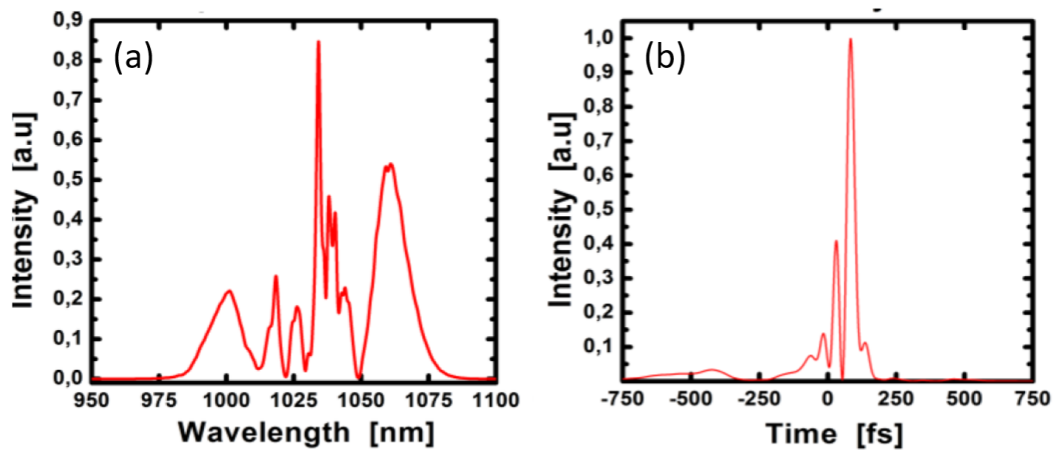
Figure C.4.: (a) The spectrum is centered at 1039 nm and has a bandwidth of 30 nm. (b) Temporal profile of the pulse.

D. Filters
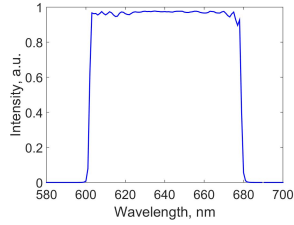
(a) **Filter I: 67036 (Edmund Optics), central wavelength: 640.5 nm, bandwidth: 75 nm.**
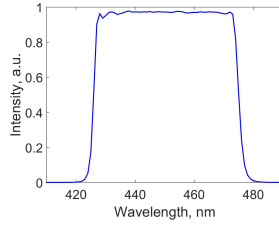
(b) **Filter II: 84782 (Edmund Optics), central wavelength: 450 nm, bandwidth: 50 nm.**
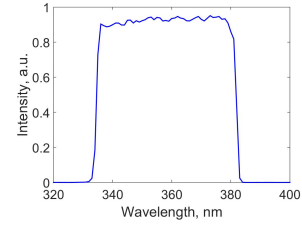
(c) **Filter III: 86973 (Edmund Optics), central wavelength: 357 nm, bandwidth: 44 nm.**
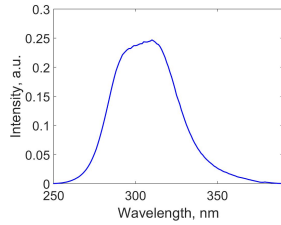
(d) **Filter IV: 67817 (Edmund Optics), central wavelength: 300 nm, bandwidth: 40 nm.**
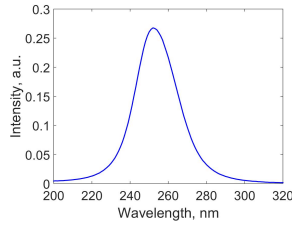
(e) **Filter V: 33013 (Edmund Optics), central wavelength: 248 nm, bandwidth: 26 nm.**
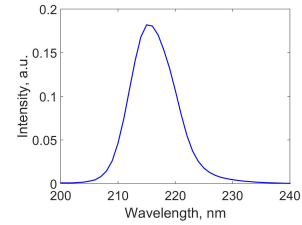
(f) **Filter VI: 67801 (Edmund Optics), central wavelength: 214 nm, bandwidth: 10 nm.**

Figure D.1.: Transmission filters.

List of Figures

142

143

144

145

146

147

148

149

Bibliography

[1] H. Yoneda, et al. Saturable absorption of intense hard X-rays in iron. *Nature Communications*, 5:5080, October 2014.

[2] T. Kimura, et al. Imaging live cell in micro-liquid enclosure by X-ray laser diffraction. *Nature Communications*, 5:3052, January 2014.

[3] M. F. Hantke, et al. High-throughput imaging of heterogeneous cell organelles with an X-ray laser. *Nature Photonics*, 8:943–949, December 2014.

[4] M. M. Seibert, et al. Single mimivirus particles intercepted and imaged with an X-ray laser. *Nature*, 470(7332):78, February 2011.

[5] B. Vodungbo, et al. Laser-induced ultrafast demagnetization in the presence of a nanoscale magnetic domain network. *Nature Communications*, 3:999, August 2012.

[6] A. McPherson, G. Gibson, H. Jara, U. Johann, and T. S. Luk. Studies of multi-photon production of vacuum-ultraviolet radiation in the rare gases. *Journal of the Optical Society of America B Optical Physics*, 4:595–601, April 1987.

[7] M. Ferray, et al. Multiple-harmonic conversion of 1064 nm radiation in rare gases. *J. Phys. B: At. Mol. Opt. Phys.*, 21(3):L31, 1988.

[8] S. Ghimire, et al. Observation of high-order harmonic generation in a bulk crystal. *Nat. Phys.*, 7(2):138–141, February 2011.

[9] A. Bouhelier, M. Beversluis, A. Hartschuh, and L. Novotny. Near-Field Second-Harmonic Generation Induced by Local Field Enhancement. *Phys. Rev. Lett.*, 90(1):013903, January 2003.

[10] C. C. Neacsu, G. A. Reider, and M. B. Raschke. Second-harmonic generation from nanoscopic metal tips: Symmetry selection rules for single asymmetric nanostructures. *Phys. Rev. B*, 71(20):201402, May 2005.

[11] B. Metzger, et al. Doubling the Efficiency of Third Harmonic Generation by Positioning ITO Nanocrystals into the Hot-Spot of Plasmonic Gap-Antennas. *Nano Letters*, 14(5):2867–2872, May 2014.

[12] T. Hanke, et al. Efficient Nonlinear Light Emission of Single Gold Optical Antennas Driven by Few-Cycle Near-Infrared Pulses. *Phys. Rev. Lett.*, 103(25):257404, December 2009.

[13] S. Nie and S. R. Emory. Probing Single Molecules and Single Nanoparticles by Surface-Enhanced Raman Scattering. *Science*, 275(5303):1102–1106, February 1997.

[14] E. Cubukcu, S. Zhang, Y.-S. Park, G. Bartal, and X. Zhang. Split ring resonator sensors for infrared detection of single molecular monolayers. *Appl. Phys. Lett.*, 95(4):043113, July 2009.

[15] T. Shaaran, R. Nicolas, B. Iwan, M. Kovacev, and H. Merdji. Nano-plasmonic near field phase matching of attosecond pulses. *Scientific Reports*, 7(1):6356, July 2017.

[16] S. Kim, et al. High-harmonic generation by resonant plasmon field enhancement. *Nature*, 453(7196):757–760, June 2008.

[17] S. Han, et al. High-harmonic generation by field enhanced femtosecond pulses in metal-sapphire nanostructure. *Nature Communications*, 7:13105, October 2016.

[18] M. Sivis, M. Duwe, B. Abel, and C. Ropers. Nanostructure-enhanced atomic line emission. *Nature*, 485(7397):E1–E3, May 2012.

[19] G. Vampa, et al. Plasmon-enhanced high-harmonic generation from silicon. *Nat. Phys.*, advance online publication, April 2017.

[20] M. Sivis, et al. Tailored semiconductors for high-harmonic optoelectronics. *Science*, 357(6348):303–306, July 2017.

[21] L. V. Keldysh and others. Ionization in the field of a strong electromagnetic wave. *Sov. Phys. JETP*, 20(5):1307–1314, 1965.

[22] F. A. Ilkov, J. E. Decker, and S. L. Chin. Ionization of atoms in the tunnelling regime with experimental evidence using Hg atoms. *J. Phys. B: At. Mol. Opt. Phys.*, 25(19):4005, 1992.

[23] N. H. Burnett, H. A. Baldis, M. C. Richardson, and G. D. Enright. Harmonic generation in CO2 laser target interaction. *Applied Physics Letters*, 31:172–174, August 1977.

[24] S. Ghimire, et al. Strong-field and attosecond physics in solids. *Journal of Physics B: Atomic, Molecular and Optical Physics*, 47(20):204030, October 2014.

[25] S. Ghimire, et al. Observation of high-order harmonic generation in a bulk crystal. *Nat. Phys.*, 7(2):138–141, February 2011.

[26] G. Farkas, C. Tóth, S. D. Moustaizis, N. A. Papadogiannis, and C. Fotakis. Observation of multiple-harmonic radiation induced from a gold surface by picosecond neodymium-doped yttrium aluminum garnet laser pulses. *Phys. Rev. A*, 46(7):R3605–R3608, October 1992.

[27] T. T. Luu, et al. Extreme ultraviolet high-harmonic spectroscopy of solids. *Nature*, 521(7553):498–502, May 2015.

[28] M. F. Pereira, et al. Theory and measurements of harmonic generation in semi-conductor superlattices with applications in the 100 GHz to 1 THz range. *Physical Review B*, 96(4), July 2017.

[29] A. Borot, et al. High-harmonic generation from plasma mirrors at kilohertz repetition rate. *Opt. Lett.*, 36(8):1461–1463, April 2011.

[30] H. G. Kurz, et al. High-order-harmonic generation from dense water micro-droplets. *Phys. Rev. A*, 87(6):063811, June 2013.

[31] B. H. Shaw, et al. High-peak-power surface high-harmonic generation at extreme ultra-violet wavelengths from a tape. *Journal of Applied Physics*, 114(4):043106, July 2013.

[32] P. A. Franken, A. E. Hill, C. W. Peters, and G. Weinreich. Generation of Optical Harmonics. *Physical Review Letters*, 7:118–119, August 1961.

[33] A. H. Chin, O. G. Calderón, and J. Kono. Extreme Midinfrared Nonlinear Optics in Semiconductors. *Phys. Rev. Lett.*, 86(15):3292–3295, April 2001.

[34] M. Hentschel, et al. Attosecond metrology. *Nature*, 414(6863):509–513, November 2001.

[35] M. Lewenstein, P. Balcou, M. Y. Ivanov, A. L'Huillier, and P. B. Corkum. Theory of high-harmonic generation by low-frequency laser fields. *Phys. Rev. A*, 49(3):2117–2132, March 1994.

[36] J. L. Krause, K. J. Schafer, and K. C. Kulander. High-order harmonic generation from atoms and ions in the high intensity regime. *Phys. Rev. Lett.*, 68(24):3535–3538, June 1992.

[37] G. Cirmi, et al. Cut-off scaling of high-harmonic generation driven by a femtosecond visible optical parametric amplifier. *J. Phys. B: At. Mol. Opt. Phys.*, 45(20):205601, 2012.

[38] J. Tate, et al. Scaling of Wave-Packet Dynamics in an Intense Midinfrared Field. *Phys. Rev. Lett.*, 98(1):013901, January 2007.

[39] A. D. Shiner, et al. Wavelength Scaling of High Harmonic Generation Efficiency. *Phys. Rev. Lett.*, 103(7):073902, August 2009.

[40] K. S. Budil, P. Salières, A. L'Huillier, T. Ditmire, and M. D. Perry. Influence of ellipticity on harmonic generation. *Phys. Rev. A*, 48(5):R3437–R3440, November 1993.

[41] V. V. Strelkov, M. A. Khokhlova, A. A. Gonoskov, I. A. Gonoskov, and M. Y. Ryabikin. High-order harmonic generation by atoms in an elliptically polarized laser field: Harmonic polarization properties and laser threshold ellipticity. *Phys. Rev. A*, 86(1):013404, July 2012.

[42] A. Flettner, et al. Ellipticity dependence of atomic and molecular high harmonic generation. *Eur. Phys. J. D*, 21(1):115–119.

[43] E. J. Takahashi, Y. Nabekawa, and K. Midorikawa. Low-divergence coherent soft x-ray source at 13 nm by high-order harmonics. *Appl. Phys. Lett.*, 84(1):4–6, December 2003.

[44] E. Constant, et al. Optimizing High Harmonic Generation in Absorbing Gases: Model and Experiment. *Phys. Rev. Lett.*, 82(8):1668–1671, February 1999.

[45] E. Takahashi, Y. Nabekawa, T. Otsuka, M. Obara, and K. Midorikawa. Generation of highly coherent submicrojoule soft x rays by high-order harmonics. *Phys. Rev. A*, 66(2):021802, August 2002.

[46] J.-F. Hergott, et al. Extreme-ultraviolet high-order harmonic pulses in the microjoule range. *Phys. Rev. A*, 66(2):021801, August 2002.

[47] P. Rudawski, et al. A high-flux high-order harmonic source. *Review of Scientific Instruments*, 84(7):073103, July 2013.

[48] A. Rundquist, et al. Phase-Matched Generation of Coherent Soft X-rays. *Science*, 280(5368):1412–1415, May 1998.

[49] C. G. Durfee, et al. Phase Matching of High-Order Harmonics in Hollow Waveguides. *Phys. Rev. Lett.*, 83(11):2187–2190, September 1999.

[50] Y. Niu, et al. Pressure-dependent phase matching for high harmonic generation of Ar and N2 in the tight focusing regime. *Optics Communications*, 397, August 2017.

[51] H.-W. Sun, et al. Extended phase matching of high harmonic generation by plasma-induced defocusing. *Optica*, 4(8):976–981, August 2017.

[52] T. Shaaran, R. Nicolas, B. Iwan, M. Kovacev, and H. Merdji. Nano-plasmonic near field phase matching of attosecond pulses. *Scientific Reports*, 7(1):6356, July 2017.

[53] M. Blanco, et al. Phase matching effects in high harmonic generation at the nanometer scale. *Optics Express*, 25(13):14974–14985, 2017.

[54] A. Husakou. Quasi-phase-matched high harmonic generation in corrugated micrometer-scale waveguides. *JOSA B*, 34(1):137–141, 2017.

[55] H. Kim, S. Han, Y. W. Kim, S. Kim, and S.-W. Kim. Generation of Coherent Extreme-Ultraviolet Radiation from Bulk Sapphire Crystal. *ACS Photonics*, 4(7):1627–1632, July 2017.

[56] Y. S. You, et al. High-harmonic generation in amorphous solids. *Nature Communications*, 8(1):724, September 2017.

[57] H. Liang, et al. High-energy mid-infrared sub-cycle pulse synthesis from a parametric amplifier. *Nature Communications*, 8(1), December 2017.

[58] N. Yoshikawa, T. Tamaya, and K. Tanaka. High-harmonic generation in graphene enhanced by elliptically polarized light excitation. *Science*, 356(6339):736–738, May 2017.

[59] M. Taucer, et al. Nonperturbative harmonic generation in graphene from intense midinfrared pulsed light. *Phys. Rev. B*, 96(19):195420, November 2017.

[60] M. Baudisch, et al. Ultrafast nonlinear optical response of Dirac fermions in graphene. *Nature Communications*, 9(1):1018, March 2018.

[61] H. Liu, et al. High-harmonic generation from an atomically thin semiconductor. *Nature Physics*, 13(3):262–265, November 2016.

[62] G. Ndabashimiye, et al. Solid-state harmonics beyond the atomic limit. *Nature*, 534(7608):520–523, June 2016.

[63] T. Apostolova and B. Obreshkov. High harmonic generation from bulk diamond driven by intense femtosecond laser pulse. *Diamond and Related Materials*, 82:165–172, February 2018.

[64] Y. S. You, D. A. Reis, and S. Ghimire. Anisotropic high-harmonic generation in bulk crystals. *Nature Physics*, 13(4):345–349, April 2017.

[65] G. Vampa, et al. Linking high harmonics from gases and solids. *Nature*, 522(7557):462–464, June 2015.

[66] M. Lindberg and S. W. Koch. Effective Bloch equations for semiconductors. *Phys. Rev. B*, 38(5):3342–3350, August 1988.

[67] D. Golde, T. Meier, and S. W. Koch. High harmonics generated in semiconductor nanostructures by the coupled dynamics of optical inter- and intraband excitations. *Physical Review B*, 77(7), February 2008.

[68] D. Golde, M. Kira, T. Meier, and S. W. Koch. Microscopic theory of the extremely nonlinear terahertz response of semiconductors. *physica status solidi (b)*, 248(4):863–866, April 2011.

[69] P. Földi. Gauge invariance and interpretation of interband and intraband processes in high-order harmonic generation from bulk solids. *Physical Review B*, 96(3):035112, 2017.

[70] M. Wu, S. Ghimire, D. A. Reis, K. J. Schafer, and M. B. Gaarde. High-harmonic generation from Bloch electrons in solids. *Physical Review A*, 91(4), April 2015.

[71] Y. S. You, et al. Laser waveform control of extreme ultraviolet high harmonics from solids. *Optics Letters*, 42(9):1816, May 2017.

[72] G. Vampa, et al. Theoretical Analysis of High-Harmonic Generation in Solids. *Physical Review Letters*, 113:073901, August 2014.

[73] A. A. Lanin, E. A. Stepanov, A. B. Fedotov, and A. M. Zheltikov. Mapping the electron band structure by intraband high-harmonic generation in solids. *Optica*, 4(5):516, May 2017.

[74] N. Tancogne-Dejean, O. D. Mücke, F. X. Kärtner, and A. Rubio. Impact of the Electronic Band Structure in High-Harmonic Generation Spectra of Solids. *Physical Review Letters*, 118(8), February 2017.

[75] X. Liu, et al. Wavelength scaling of the cutoff energy in the solid high harmonic generation. *Opt. Express, OE*, 25(23):29216–29224, November 2017.

[76] Z. Wang, et al. The roles of photo-carrier doping and driving wavelength in high harmonic generation from a semiconductor. *Nature Communications*, 8(1):1686, November 2017.

[77] C. R. McDonald, G. Vampa, G. Orlando, P. B. Corkum, and T. Brabec. Theory of high-harmonic generation in solids. *Journal of Physics: Conference Series*, 594:012021, March 2015.

[78] N. Tancogne-Dejean, O. D. Mücke, F. X. Kärtner, and A. Rubio. Ellipticity dependence of high-harmonic generation in solids originating from coupled intraband and interband dynamics. *Nature Communications*, 8(1):745, September 2017.

[79] D. E. Aspnes and A. A. Studna. Dielectric functions and optical parameters of Si, Ge, GaP, GaAs, GaSb, InP, InAs, and InSb from 1.5 to 6.0 eV. *Phys. Rev. B*, 27(2):985–1009, January 1983.

[80] S. Gholam-Mirzaei, J. Beetar, and M. Chini. High harmonic generation in ZnO with a high-power mid-IR OPA. *Applied Physics Letters*, 110(6):061101, February 2017.

[81] T. T. Luu and H. J. Wörner. High-order harmonic generation in solids: A unifying approach. *Physical Review B*, 94(11), September 2016.

[82] S. Ghimire, et al. Generation and propagation of high-order harmonics in crystals. *Physical Review A*, 85(4), April 2012.

[83] T. Derrien. *Nanostructuration de cellules photovoltaïques par impulsion laser ultracourte. : étude numérique des mécanismes de formation.* Aix-Marseille, February 2012.

[84] H. Kim, S. Han, Y. W. Kim, S. Kim, and S.-W. Kim. Generation of Coherent Extreme-Ultraviolet Radiation from Bulk Sapphire Crystal. *ACS Photonics*, 4(7):1627–1632, July 2017.

[85] K. F. Lee, et al. Harmonic generation in solids with direct fiber laser pumping. *Optics Letters*, 42(6):1113–1116, March 2017.

[86] N. A. Savostianova and S. A. Mikhailov. Third harmonic generation from graphene lying on different substrates: Optical-phonon resonances and interference effects. *Optics Express*, 25(4):3268, February 2017.

[87] E. Hendry, P. J. Hale, J. Moger, A. K. Savchenko, and S. A. Mikhailov. Coherent Nonlinear Optical Response of Graphene. *Phys. Rev. Lett.*, 105(9):097401, August 2010.

[88] I. Al-Naib, J. E. Sipe, and M. M. Dignam. High harmonic generation in undoped graphene: Interplay of inter- and intraband dynamics. *Physical Review B*, 90(24), December 2014.

[89] N. Tancogne-Dejean and A. Rubio. Atomic-like high-harmonic generation from two-dimensional materials. *Science Advances*, 4(2):eaao5207, February 2018.

[90] C. R. Dean, et al. Boron nitride substrates for high-quality graphene electronics. *Nature Nanotechnology*, 5(10):722–726, October 2010.

[91] Q. Cui, R. A. Muniz, J. E. Sipe, and H. Zhao. Strong and anisotropic third-harmonic generation in monolayer and multilayer ${\mathrm{ReS}}_{2}$. *Phys. Rev. B*, 95(16):165406, April 2017.

[92] X. Zhou, et al. Strong Second-Harmonic Generation in Atomic Layered GaSe. *J. Am. Chem. Soc.*, 137(25):7994–7997, July 2015.

[93] F. Ladieu, P. Martin, and S. Guizard. Measuring thermal effects in femtosecond laser-induced breakdown of dielectrics. *Appl. Phys. Lett.*, 81(6):957–959, July 2002.

[94] K. F. Lee, et al. Harmonic generation in solids with direct fiber laser pumping. *Opt. Lett., OL*, 42(6):1113–1116, March 2017.

[95] Y. S. You, D. A. Reis, and S. Ghimire. Anisotropic high-harmonic generation in bulk crystals. *Nature Physics*, 13(4):345–349, April 2017.

[96] M. Mlejnek, E. M. Wright, J. V. Moloney, and N. Bloembergen. Second Harmonic Generation of Femtosecond Pulses at the Boundary of a Nonlinear Dielectric. *Phys. Rev. Lett.*, 83(15):2934–2937, October 1999.

[97] N. Garejev, et al. Third- and fifth-harmonic generation in transparent solids with few-optical-cycle midinfrared pulses. *Physical Review A*, 89(3), March 2014.

[98] n. Ranka, n. Schirmer, and n. Gaeta. Observation of Pulse Splitting in Nonlinear Dispersive Media. *Phys. Rev. Lett.*, 77(18):3783–3786, October 1996.

[99] A. H. Chin, O. G. Calderón, and J. Kono. Extreme Midinfrared Nonlinear Optics in Semiconductors. *Phys. Rev. Lett.*, 86(15):3292–3295, April 2001.

[100] Measurement of the Refractive Indices of Several Crystals. *Journal of Applied Physics*, 36(5):1674–1677, May 1965.

[101] M. G. Brik, V. Nagirnyi, and M. Kirm. Ab-initio studies of the electronic and optical properties of ZnWO4 and CdWO4 single crystals. *Materials Chemistry and Physics*, 134(2):1113–1120, June 2012.

[102] P. Rigaud, et al. Supercontinuum-seeded few-cycle mid-infrared OPCPA system. *Opt. Express, OE*, 24(23):26494–26502, November 2016.

[103] S. A. Maier. *Plasmonics: Fundamentals and Applications*. Springer US, 2007.

[104] S. Babar and J. H. Weaver. Optical constants of Cu, Ag, and Au revisited. *Applied Optics*, 54(3):477–481, January 2015.

[105] B. Lahiri, A. Z. Khokhar, R. M. D. L. Rue, S. G. McMeekin, and N. P. Johnson. Asymmetric split ring resonators for optical sensing of organic materials. *Opt. Express, OE*, 17(2):1107–1115, January 2009.

[106] P. Genevet, et al. Large Enhancement of Nonlinear Optical Phenomena by Plasmonic Nanocavity Gratings. *Nano Lett.*, 10(12):4880–4883, December 2010.

[107] S. Han, et al. High-harmonic generation by field enhanced femtosecond pulses in metal-sapphire nanostructure. *Nat. Commun.*, 7:13105, October 2016.

[108] I.-Y. Park, et al. Plasmonic generation of ultrashort extreme-ultraviolet light pulses. *Nat. Photon.*, 5(11):677–681, November 2011.

[109] S. Kim, et al. High-harmonic generation by resonant plasmon field enhancement. *Nature*, 453(7196):757–760, June 2008.

[110] G. Vampa, et al. Plasmon-enhanced high-harmonic generation from silicon. *Nat. Phys.*, 13(7):659–662, July 2017.

[111] H. Liu and P. Lalanne. Microscopic theory of the extraordinary optical transmission. *Nature*, 452(7188):728–731, April 2008.

[112] F. B. Van, et al. Quasi-cylindrical wave contribution in experiments on extraordinary optical transmission. *Nature*, 492(7429):411–414, December 2012.

[113] M. A. Jensen and G. P. Nordin. Finite-aperture wire grid polarizers. *J. Opt. Soc. Am. A, JOSAA*, 17(12):2191–2198, December 2000.

[114] T. Shibanuma, G. Grinblat, P. Albella, and S. A. Maier. Efficient Third Harmonic Generation from Metal-Dielectric Hybrid Nanoantennas. *Nano Lett.*, March 2017.

[115] L. Shi, et al. Self-optimization of plasmonic nanoantennas in strong femtosecond fields. *Optica*, 4(9):1038–1043, September 2017.

[116] H. Kim, S. Han, Y. W. Kim, S. Kim, and S.-W. Kim. Generation of Coherent Extreme-Ultraviolet Radiation from Bulk Sapphire Crystal. *ACS Photonics*, June 2017.

[117] L. Shi, et al. Investigating the origin of third harmonic generation from diabolo optical antennas. *Appl. Phys. Lett.*, 111(17):173102, October 2017.

[118] T. Grosjean, M. Mivelle, F. I. Baida, G. W. Burr, and U. C. Fischer. Diabolo Nanoantenna for Enhancing and Confining the Magnetic Optical Field. *Nano Lett.*, 11(3):1009–1013, March 2011.

[119] X. Xiong, et al. Polarization-dependent perfect absorbers/reflectors based on a three-dimensional metamaterial. *Phys. Rev. B*, 88(11):115105, September 2013.

[120] R. L. Kelly. Program of the 1972 Annual Meeting of the Optical Society of America. *J. Opt. Soc. Am., JOSA*, 62(11):1336–1336, November 1972.

[121] J. Renger, R. Quidant, and L. Novotny. Enhanced nonlinear response from metal surfaces. *Opt. Express, OE*, 19(3):1777–1785, January 2011.

[122] T. Utikal, et al. Towards the Origin of the Nonlinear Response in Hybrid Plasmonic Systems. *Phys. Rev. Lett.*, 106(13):133901, March 2011.

[123] L. Shi, et al. Resonant-Plasmon-Assisted Subwavelength Ablation by a Femtosecond Oscillator. *Phys. Rev. Applied*, 9(2):024001, February 2018.

[124] M. Mesch, B. Metzger, M. Hentschel, and H. Giessen. Nonlinear Plasmonic Sensing. *Nano Lett.*, 16(5):3155–3159, May 2016.

[125] L. Shi, et al. Impact of Plasmon-Induced Atoms Migration in Harmonic Generation. *ACS Photonics*, February 2018.

[126] R. H. Fowler and L. Nordheim. Electron Emission in Intense Electric Fields. *Proceedings of the Royal Society of London Series A*, 119:173–181, May 1928.

[127] L. O. Herrmann, et al. Threading plasmonic nanoparticle strings with light. *Nature Communications*, 5:4568, July 2014.

[128] J. Dai, J.-H. Zeng, S. Lan, X. Wan, and S.-L. Tie. Competition between second harmonic generation and two-photon-induced luminescence in single, double and multiple ZnO nanorods. *Opt. Express, OE*, 21(8):10025–10038, April 2013.

[129] J. Dai, et al. Controllable color display induced by excitation-intensity-dependent competition between second and third harmonic generation in ZnO nanorods. *Appl. Opt., AO*, 53(2):189–194, January 2014.

[130] T. Ning, et al. Efficient second-harmonic generation in silicon nitride resonant waveguide gratings. *Optics Letters*, 37(20):4269–4271, October 2012.

[131] M. Sivis, et al. Tailored semiconductors for high-harmonic optoelectronics. *Science*, 357(6348):303–306, July 2017.

[132] M. Baudisch, B. Wolter, M. Pullen, M. Hemmer, and J. Biegert. High power multi-color OPCPA source with simultaneous femtosecond deep-UV to mid-IR outputs. *Opt. Lett.*, 41(15):3583–3586, August 2016.

[133] N. S. Han, et al. Defect states of ZnO nanoparticles: Discrimination by time-resolved photoluminescence spectroscopy. *Journal of Applied Physics*, 107(8):084306, April 2010.

[134] Huang Min and Xu Zhizhan. Spontaneous scaling down of femtosecond laser-induced apertures towards the 10-nanometer level: the excitation of quasistatic surface plasmons. *Laser & Photonics Reviews*, 8(4):633–652, April 2014.

[135] L. Wang, et al. Competition between subwavelength and deep-subwavelength structures ablated by ultrashort laser pulses. *Optica*, 4(6):637–642, June 2017.

[136] C. Yamada and T. Kimura. Anisotropy in second-harmonic generation from reconstructed surfaces of GaAs. *Phys. Rev. Lett.*, 70(15):2344–2347, April 1993.

[137] S. Buckley, et al. Below Bandgap Second Harmonic Generation in GaAs Photonic Crystal Cavites in (111) and (001) Crystal Orientations. In *CLEO: 2014 (2014), paper SW3M.8*, page SW3M.8. Optical Society of America, June 2014.

[138] F. B. P. Niesler, et al. Second-harmonic generation from split-ring resonators on a GaAs substrate. *Opt Lett*, 34(13):1997–1999, July 2009.

[139] Y.-S. Lee, M. H. Anderson, and M. C. Downer. Fourth-harmonic generation at a crystalline GaAs(001) surface. *Opt. Lett., OL*, 22(13):973–975, July 1997.

[140] D. P. Adorno, G. Ferrante, and M. Zarcone. Generation of even harmonics of sub-THz radiation in bulk GaAs in the presence of a static electric field. *J Comput Electron*, 6(1-3):31–34, September 2007.

[141] J. Miao, P. Charalambous, J. Kirz, and D. Sayre. Extending the methodology of X-ray crystallography to allow imaging of micrometre-sized non-crystalline specimens. *Nature*, 400(6742):342–344, July 1999.

[142] J. D. Cox, A. Marini, and F. J. G. d. Abajo. Plasmon-assisted high-harmonic generation in graphene. *Nature Communications*, 8:14380, February 2017.

[143] K. S. Yee. Numerical solution of initial boundary value problems involving Maxwell's equations in isotropic media. *IEEE Trans. Antennas and Propagation*, pages 302–307, 1966.

[144] Lumerical Inc. | Innovative Photonic Design Tools, https://www.lumerical.com/.

[145] MEEP Documentation, https://meep.readthedocs.io/en/latest/.

[146] F. Guichard, et al. Nonlinear compression of high energy fiber amplifier pulses in air-filled hypocycloid-core Kagome fiber. *Opt. Express, OE*, 23(6):7416–7423, March 2015.

Titre : Génération d'harmoniques d'ordre élevé dans des cristaux assistée par exaltation locale du champ dans des nanostructures

Mots clés : Génération d'harmoniques d'ordre élevé, nanostructures, exaltation du champ

Résumé : Des radiations ultraviolettes et rayons X sont utilisées en médecine, biologie, dans des applications d'imagerie et dans la recherche fondamentale. La génération d'harmoniques d'ordre élevé (HHG, en anglais high-order harmonic generation) est un processus bien établi pour générer une telle radiation. Dans la HHG, un laser infrarouge intense interagit avec un milieu nonlinéaire et génère des multiples de la fréquence du faisceau générateur. Des tels lasers amplifiés ont des limitations qui empêchent une diffusion de la HHG. Dans cette thèse, nous étudions la HHG dans des solides en exploitant l'exaltation locale du champ dans des nanostructures résonantes. Nous utilisons l'exaltation plasmonique dans des nanostructures métalliques et le confinement du champ dans des nanostructures sémiconductrices pour rendre possible la HHG avec des lasers à basse intensité et haute cadence. Nous démontrons l'exaltation de la radiation harmonique par plusieurs ordres de grandeur. Nous performons les premières applications à l'imagerie nanométrique sans lentille et démontrons la capabilité de structuration des cristaux afin de contrôler les propriétés d'émission.

Title : High harmonic generation in crystals assisted by local field enhancement in nanostructures

Keywords : High harmonic generation, nanostructures, field enhancement

Abstract : Coherent ultraviolet and X-ray radiations are widely used in medicine, biology, imaging applications and fundamental research. High-order harmonic generation (HHG) is a well-established process that generates such radiation. In HHG, an intense infrared driving laser interacts with a nonlinear medium and generates multiples of the driving laser frequency. Such amplified infrared driving lasers have limitations that prevent HHG democratization. In this thesis, we investigate HHG in solids by exploiting local field enhancement in resonant nanostructures. We exploit plasmonic enhancement in metallic nanostructures and field confinement in semiconductor nanostructures to enable HHG with low-intensity, high repetition rate lasers. We demonstrate enhancement of harmonic radiation by several orders of magnitude. We perform the first applications to nanometer scale lensless imaging and demonstrate the capability of crystal structuring to control the emission properties.